Experimental and Modelling Methods for High-Accuracy Performance Characterisation of Chain Drives

George C. Barnaby

A dissertation submitted to the University of Bristol in accordance with the requirements for award of the degree of Doctor of Philosophy in the Faculty of Engineering.

April 2023

Word count: 52,154

or

"Testing Chains for Marginal Gains"

Abstract

In recent years there has been a growing interest in measuring and predicting the performance of chain drives in applications such as elite cycling and industrial drives since improvement in the life-time performance of transmission promotes efficient use of finite energy sources. This thesis investigates and develops testing and modelling methods for achieving high-accuracy estimation of transmission power efficiency of chain drives.

At present many test rigs used in industry are not able to replicate real-world loading and have limited accuracy in torque measurements. To address these limitations a dynamometer test rig was developed at the University of Bristol which has the capability of testing in representative boundary and loading conditions. This thesis contributes to the development of this dynamometer rig with new testing protocols and applying advances in data processing.

A significant area of uncertainty in measurements on the test apparatus was the power losses in the support bearings on the shafts. To isolate the performance of the transmission system, the friction in the bearings must be accurately compensated. Analytical methods from the literature were evaluated and found to poorly predict frictional moment in light lubrication regimes at low operating range relative to the bearing rated loads and speeds. A purpose-built bearing test rig was developed to test identical bearings in similar conditions, and empirical results used to compensate bearing friction in the dynamometer test rig. The remaining uncertainty of the power loss measurand was determined, encompassing the combined uncertainty of measured variables across two test rigs.

High frequency chain dynamics from polygonal action and chain span resonance were measured in torque data on the test apparatus. Tested transmissions were shown to have unique vibration signatures across the test envelope. Chains with smaller pitch were seen to have reduced measured dynamics. On a bicycle, these measured disruptions are sensed as vibrations in the crank by a rider and smoother transmissions are more desirable for maximal effort exertion.

In power loss measurements, a transmission with a cyclic driving torque profile incurred more losses when compared with the same transmission at constant torque. Results showed the greater the variation about a mean torque, the greater the transmission losses. This is important because a cyclist delivers cyclic torque during cycling and until now test rigs have applied a constant torque based on the assumption that this gives the same result. Results also demonstrate that a cyclist with smoother pedal action will incur reduced transmission losses.

The primary application of this research has been to inform decision making in the development of a novel small-pitch chain drive by Renold Plc for British Cycling at the 2020 Tokyo Olympics.

Acknowledgements

I am grateful to my supervisors Stuart Burgess, Robert Wragge-Morley and Jason Yon for their guidance and support in the course of this project. Tom Hill, too; our annual check-ins were always engaging and helpful.

For financial and in-kind support particularly early in the project, many thanks to those from Renold PLC and British Cycling: Detlef Ragnitz, Tony Purnell, Oliver Caddy, and particularly to Adam Bonser for generously lending equipment and giving the opportunity to swap notes on interesting test parallels between riding and rig. Bradley Greenwood and Chris Lodge: I have been very pleased to catch up regularly with your research and work in industry more recently, which has greatly helped me contextualise my own work.

To my friends and family, I aspire to redevelop a personality over the coming months. Thank you for putting up with it all, Isobel more than any.

This thesis is dedicated to my Grandpa. I hope that you would have thought some of this was alright.

Author's declaration

I declare that the work in this dissertation was carried out in accordance with the requirements of the University's *Regulations and Code of Practice for Research Degree Programmes*, and that it has not been submitted for any other academic award. Except where indicated by specific reference in the text, the work is the candidate's own work. Work done in collaboration with, or with the assistance of, others, is indicated as such. Any views expressed in the dissertation are those of the author.

SIGNED: .....

DATE: .....

Publications

Barnaby, G. C., Yon, J., & Burgess, S. (2020). Sprocket Size Optimisation for Derailleur Racing Bicycles. Journal of Science and Cycling, 9(2), 36-36.

Prepared for the 2020 Science & Cycling Congress, Nice - June 2020. [APPENDIX B]

Barnaby, G., Yon, J., & Burgess, S. (2021). Mapping whole-event drive losses: studying the impact of race profile and rider input on bicycle transmission efficiency. *Journal of Science and Cycling, 10*(2).

Presented at the 2021 Science & Cycling Congress, Leuven - September 2021. [APPENDIX C]

Contents

List of Figures

List of Tables

Chapter 1

Introduction: Performance in Chain Drive Transmission Systems

1.1 Introduction

A chain drive transmits useful work between parallel rotating shafts through positive engagement of a chain with two or more toothed sprockets. Such drives are widely used in manufacturing industries, mechanical infrastructure, automotive applications and in motorcycles and pedal powered bicycles.

Modern engineering solutions demand efficient use of material and energy resources and so the performance of chain transmission drives is now of particular interest to industry. In the case of bicycle racing applications, there is great effort in accumulating marginal gains for cyclists to give them a performance advantage in elite competition where race outcomes depend on very fine margins. The performance of a transmission system is central to these efforts since it directly influences the deliverable power from a driving machine or cyclist.

The performance of a chain drive is particular to its application, and may vary significantly with different drive types, designs, sizes, boundary conditions and operating environment. Understanding and characterising the performance of a transmission must be set in these contexts, and is a central theme in this thesis.

Whereas past chain testing methodologies have tended to favour simplified loading or measurement to overcome fundamental practical issues in their construction, this work seeks to promote realism of testing environment. A newly commissioned test rig, pictured in Figure 1.1, is the starting point of the research project described in this thesis.

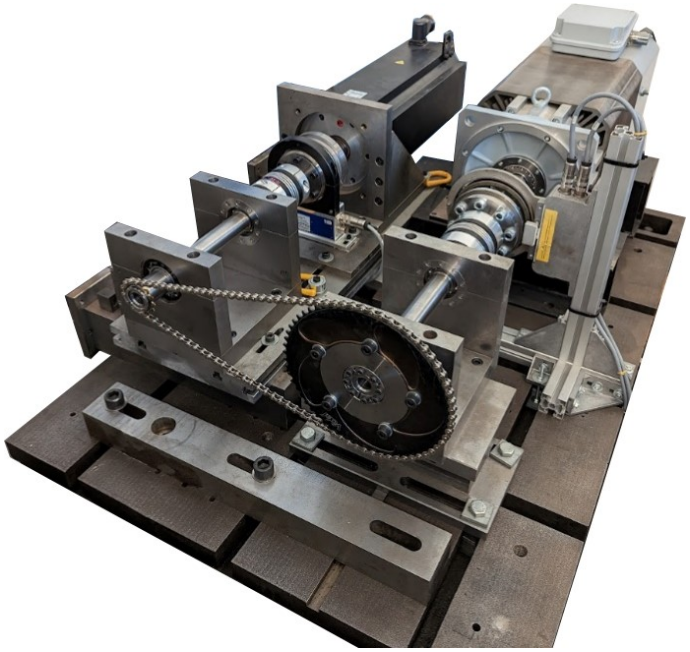

Figure 1.1: Dynamometer experimental apparatus for testing chains with representative loading and boundary conditions.

1.2 Chain drives as transmission systems

Transmission chains operate to deliver torque between two rotating shafts. Other useful work done by chains may be for lifting applications, such as in a fork-lift or sluice gate; for conveying, such as carrying load on a factory floor; or in timing applications, such as in automobile engines.

A modern transmission chain is also known as a bush roller chain, and is an assembly of components illustrated in Figure 1.2. An inner link is comprised of two inner plates and two push-fitted bushings. An outer link is similar with longer pins push fitted into outer plates. The pin has a diameter smaller than the inside of the bushing to allow for free rotation between (often) lubricated surfaces. The roller exists on the outside of the bushing, with a clearance fit again to allow for relative movement between them.

The design of the bush roller chain was first patented by Hans Renold in 1880 [66], following development of a roller chain by James Slater in 1864 [72]. Previously, chains operated with plates and pins only and high wear made them very poor in transmission applications. The introduction of the roller-chain improved sprocket engagement, but it was not until the addition of Renold's solid bush that the wear characteristics were improved sufficiently that a practical transmission chain was developed. The design of the bush roller chain remains largely unchanged today.

The geometry of a transmission chain is scaled depending on its application. The chain pitch, measured as the distance between the pin centres on a link, varies from 9.525 mm (3/8") to upwards

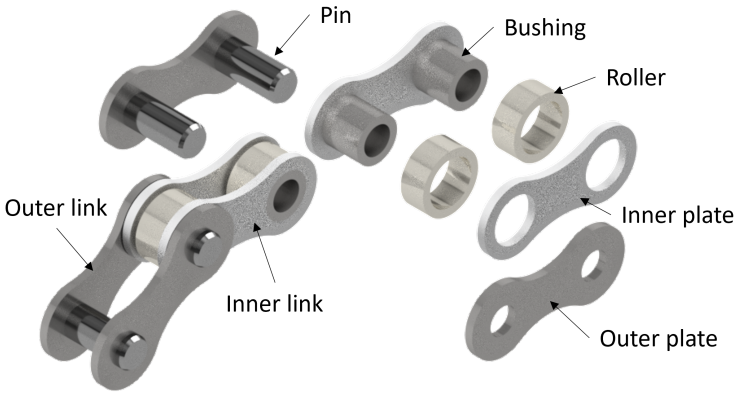

Figure 1.2: Components in bush roller chain.

of 50 mm (2”) on commonly used transmission chain. The chain may also be multi-strand, such that it engages with multiple sprockets on the driving and driven shafts. All examples discussed in this thesis are single strand (simplex) though double strand (duplex) and triple stand (triplex) are used in certain high torque industrial applications.

1.2.1 Chain drives in cycling transmission

Renold’s bush roller chain was significant in the development of the ‘safety bicycle’ in the 1880’s, and a Renold chain was used in the John Kemp Starley’s Rover Safety Bicycle in 1885.

This bicycle design replaced direct drive bicycles, which needed large wheels for favourable gearing such as in a penny-farthing. With the bush roller chain, the gear ratio could be defined in the size of the sprockets and so the wheel size was decoupled from intended riding cadence and bicycle speed. Furthermore, by driving the rear wheel via a chain transmission the front was used for steering only. By reducing the wheel size and decoupling the pedalling plane from steering direction the bicycle was safer for users, hence its name.

The bush roller chain is still standard in dual-sprocket configurations on bicycles. The 1/2-inch pitch bush roller chain has an internal width of either 1/8-inch or 3/32-inch, defined by the internal clearance between inner plates. When properly configured, the chainring and rear sprocket operate in the same plane to maintain a straight ‘chain-line’ – the angle of the chain span relative to the sprocket plane. These drive types are present in fixed gear (e.g. velodrome track bikes) and single speed (e.g. bicycle motorcross, or BMX) bicycles, or those with internal hub gearing.

In multi-speed cycling, the most common transmissions feature front and rear derailleurs which allow the chain to be disengaged and re-engaged with a parallel sprocket in a set. There are typically between 1 and 3 driving sprockets (chainrings) in a front set and between 5 and 13

driven sprockets on a rear cassette. As transmissions have been developed with more sprockets, the bicycle frame geometry has not greatly changed and gears and chains have become narrower to accommodate increased gear options.

The wide range of sprockets in a derailleur drive invariably means that the chain often runs between front and rear sprockets which are misaligned. Traditional bush roller chains cannot operate properly with significant misalignments which are now commonplace in derailleur drives, and a different chain design is used which was first widely-sold by French chain manufacturer Sedis in 1981 [4]. The Sedisport chain was based on a design patented by Guy Dupoyet [20], and this 'bushing-less' design is now used for all multi-speed derailleur drives. This chain does not have a separate bushing in its assembly, but instead has shoulders integrated with the inner plate, illustrated in Figure 1.3.

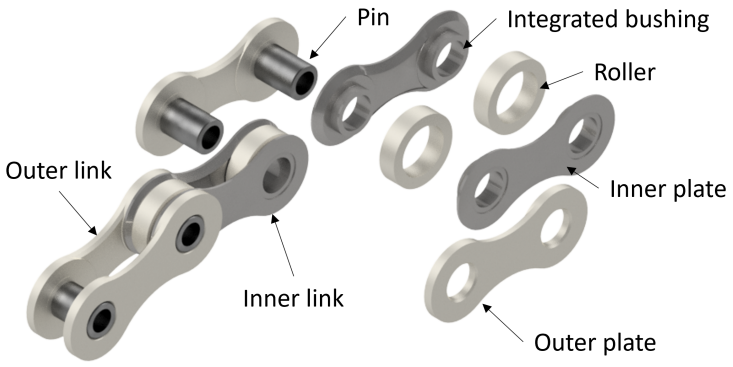

Figure 1.3: Integrated bushing design chain for derailleur bicycles.

With fewer components, the bushing-less chain could be manufactured both quicker and with reduced material and overhead costs. Crucially, it also allowed a degree of lateral compliance in chain strands such that transmission can operate with an imperfect chain-line. The sliding surfaces, and hence wear characteristics, friction and behaviour of lubrication, change for this case.

To improve performance of shifting the chain between sprockets using the derailleur mechanisms, the inner and outer surfaces of the outer link plates feature chamfered edges and grooves, as do the teeth on the sprockets. Various sprocket manufacturers have their own patented technologies for this purpose.

The typical 'waisted' profile of the plates on chain links is to reduce the necessary material and mass of the chain while maintaining appropriate tensile strength characteristics. Further removal of material is seen across bicycle chains, such as the use of hollow pins, or letter-box outer plates. In very narrow chains, such features may reduce tensile strength properties below a safe standard,

and some modern chains may not include typical weight saving features such as double-waisted outer plates to achieve necessary strength properties for a safe narrow chain.

Bicycle chain drives are driven by the torque of a cyclist rotating the driving sprocket via a crank and pedals, against loads associated with aerodynamic drag, friction and inertial loads acting against acceleration. Additional driving load may come from an electric motor in modern pedal-assist bicycles. The torque application from a rider is not constant during crank rotation because application of leg force from a rider is mainly directed downwards during the cycling cadence. 'Clipless' systems, where a cyclist's shoe is mechanically attached to the pedal, enable force to be applied throughout the drank rotation but the resulting torque application tends to be a fluctuating in the form of a sinusoid peaking twice per pedal rotation. With selection of gears and variations in physiological outputs of torque and speed, loading conditions in transmission change quite significantly during use.

1.3 Characterising performance of chain drives

The metrics used to judge the performance of transmission are highly dependent on the context of its operation in-use. Optimisation in one performance criterion can be at the expense of another, and so the use-case of transmission must be considered when evaluating performance.

Three areas of performance are introduced:

1. Wear characteristics.
2. Transmission power efficiency.
3. Noise, vibration, and harshness (NVH).

While they can be separated into broadly different phenomena, there is significant inter-dependency, represented in Figure 1.4.

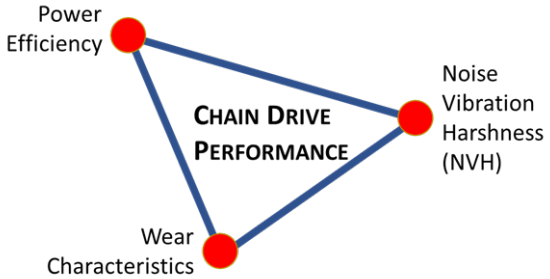

Figure 1.4: Inter-dependent performance characteristics in chain drives.

1.3.1 Wear characteristics

Historically, wear characteristics of a chain transmission has been the most fundamental limit to performance. A mechanical solution that wears out quickly is not viable for reasons of practicality, safety or financial viability. If a meaningful lifespan is expected of the transmission components, wear is the primary concern in performance.

Wear primarily occurs by degradation of material in the pin and bushing due to friction at this interface. This causes 'stretch' or elongation in the chain, illustrated in Figure 1.5. In fixed sprocket systems with fixed centre distance, chain elongation introduces more slack into the transmission which eventually causes the chain to ride over the sprocket teeth. The effective pitch of the chain is also lengthened relative to the pitch of the sprocket, leading to improper meshing and additional wear on the sprocket teeth.

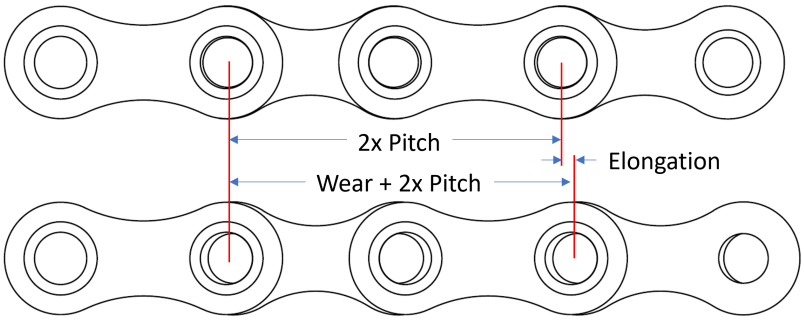

Figure 1.5: Removal of pin surface from wear causing chain elongation.

Chain transmissions are designed to tolerate an amount of wear, and may have some active response to wear such as re-tensioning the system which increases the lifetime of components.

1.3.2 Power efficiency

The power efficiency of a drive is the ratio of output power from the transmission and input power to the transmission. Where peak performance is more vital than life-time performance (such as in cycle racing applications), efficiency of the system including the transmission can be the most important performance metric.

Energy is consumed in transferring power via a chain drive, such that the usable power from the driven shaft is less than the input power at the driving shaft. Energy is primarily consumed in overcoming friction in the transmission, largely from the sliding surfaces in the chain links undergoing articulation. Sliding occurs between the sprocket tooth and roller, and at the pin-bushing and bushing-roller interface illustrated in Figure 1.6. Efficiency is linked with wear as the

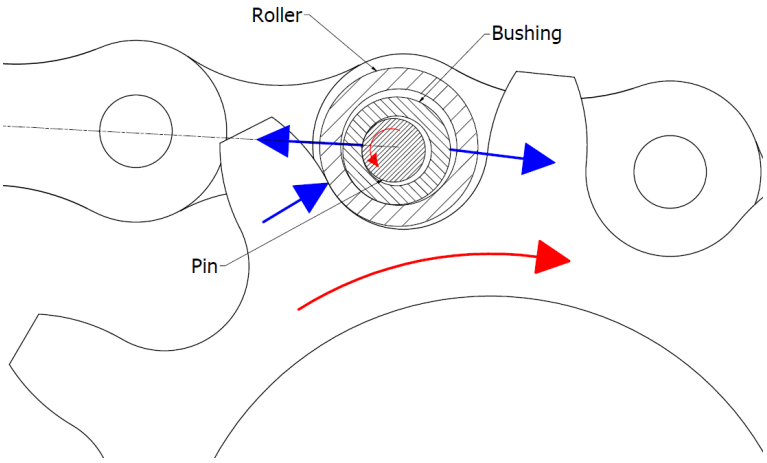

Figure 1.6: Sliding surfaces in a chain link during articulation onto a sprocket.

same friction which accelerates the removal of material will increase the mechanical losses of the chain articulation. Furthermore, worn components can exhibit additional friction due to greater movement from improper meshing.

The efficiency of chain drives has been a subject of academic interest since the 19^{th} century with early experimental work conducted by G. D. Mack [49] in 1897, which is commented on by a number of academics including R. C. Carpenter had who conducted similar experimental work independently. Over 100 years later, there is still wide interest, and conflicting experimental results, in efficiency of chain drives particularly in the context of human powered vehicles compiled by D Wilson [85], with notable commentary from J Papadopoulos who describes his desire for an absolute arbiter of transmission efficiency still lacking in the field.

Frictional losses representing inefficiencies in a chain drive are dissipated as heat energy, which can be an important metric in performance of a transmission system in its own right as neighbouring systems may be sensitive to changes in temperature.

1.3.3 Noise, vibration, and harshness (NVH)

The dynamics induced by a transmission can be an important performance metric in applications where vibration or noise must be minimised. Roller chains are inherently dynamic systems since there is regular shock and excitation of a multi-degree-of-freedom system from mechanical impact between chain roller and sprocket teeth. Further effects are caused by polygonal action. The chain makes a polygon, not a circle, on a sprocket and the roller at the end of a chain span engaged with a sprocket tooth is moved through a changing effective radius, illustrated in Figure 1.7. Depending on the relative inertia on the two drives, this can result in a changing chain speed or a changing sprocket speed.

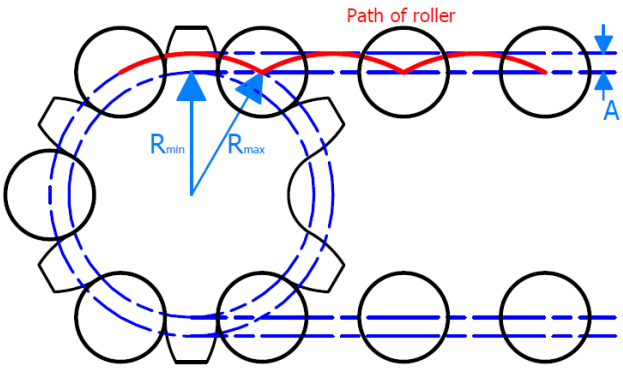

Figure 1.7: Polygonal action of a chain on a sprocket causing transverse excitation in the span and changing torque radius during articulation.

Polygonal action causes transverse movement of a chain strand as it leaves a sprocket, introducing harmonic excitation to a tight chain span. This is illustrated in Figure 1.7 by the path of the roller as it leaves the sprocket. Resultant vibrations can be significant if aligned with resonant frequencies in the system, increasing tension and articulation, which may cause increased wear and reduced efficiency. Furthermore, vibration can affect the dynamics of the output from the transmission by inducing a harmonic component, or affect the input by non-constant resistance to its driving torque. Vibration will have more effect on compliant and low-inertia systems.

1.3.4 Limitations of current methods to characterise performance of chain drives

The experimental assessment of transmission performance in academic and industrial settings is a narrow field of research, and solutions tend to simplify loading to isolate the performance metric of interest. Characterisation of wear, power efficiency and vibration of transmission are considered as abstracted phenomena. This is done to promote accuracy of measurement, repeatability of loading, and to minimise the cost of apparatus and of testing.

There is a gap in literature considering performance from a holistic standpoint, with an appreciation of the wider implications of a single performance metric, and the effect of a transmission's performance on the wider system. This is of particular note in real-world cases such as pedal cycling where loading cases, environmental factors and boundary conditions of the system are changeable in use and driving 'machines' (cyclists) are sensitive to performance of the transmission. A whole system approach will seek to maximise the efficiency of the physiological input of the rider (as much as it pertains to transmission), alongside the efficiency of the transmission over a full race distance.

To consider the holistic performance of a transmission system in real world use-cases it must be subjected to the closely replicated conditions of loading and boundary states. This presents several challenges, which are summarised:

1. Sophisticated control of loading conditions is required – loading and driving torque characteristics are wide ranging in cycling application and a number of parameters must be considered to create conditions which cover an envelope of typical use.
2. Uncertainty of measurement is high – previous test apparatus simplify loading conditions to simplify measurement and uncertainty is reduced. This is not possible when focus in on creating realistic conditions. Torque measurement based on strain gauge technologies is rated based on transmitted torque, and has an absolute uncertainty quoted as a percentage of the rated torque. With such a rating, the measurement of small differences in measurement from small frictional behaviours has inherently high error associated with measurement.
3. Parasitic losses must be minimised and compensated – well-made and properly configured transmission systems have losses and wear characteristics in the same order of magnitude as common components on test rigs, which presents a challenge for testing as the parasitic effects contribute significantly to the measurement of transmission performance. They need to be limited and compensated. This inherent issue has not been directly addressed in literature.

1.4 Aims and Objectives

- To appraise the current methodology for practical testing of chains drives in the literature.
- To examine parasitic influence on torque measurement in dynamometer test apparatus and develop methods for mitigation and compensation.
- To characterise the uncertainty of performance measurands on test apparatus, including the uncertainty of compensation methods.
- To develop new performance testing methods addressing the use-case of elite track cycling.
- To demonstrate parametric influences on performance of chain drive transmissions.
- To develop analytical methods for the assessment of whole-life performance of chain drive transmissions.

1.5 Research Methods

In order to develop high accuracy performance characterisation of chain drives with novel experimental apparatus and modelling methods, several threads of research will be addressed.

1.5.1 Evaluate experimental apparatus from the literature

A number of designs of experimental test apparatus are addressed in the literature and synthesised in a literature review. Two key designs of dynamometer have become popular in the assessment of performance of bicycle transmission. These will be appraised to consider their relative merits with qualitative and quantitative comparisons.

1.5.2 Determine parasitic influences on test measurands

Literature will be appraised where mitigation and compensation methods on dynamometer test stands are specifically addressed, most notably in the case of frictional moment from support bearings. The applicability of analytical models of bearings frictional moment to compensate for parasitic influence in dynamometer test rig will also be evaluated in effort to find an accurate solution to mitigating and compensating parasitic influence on the test measurand (power loss in the transmission under test). The uncertainty of compensation methods will also be determined.

Further parasitic influences on the loading and boundary conditions of transmission under test will be discussed and mitigation explored through design of test protocol and post processing techniques. Further determination of the indirect influence of parasitic effects on the test measurand is a research area to be addressed in further work.

1.5.3 Develop efficiency tests on dynamometer test rig

Testing protocols will be developed on the dynamometer test apparatus to consider relevant parameters and their influence on performance. Test envelopes will be designed consider typical loading regimes in a defined use-case, specifically related to elite level velodrome track cycling. Testing protocols will promote uncertainty where changes are not detrimental to the realism of loading.

1.5.4 Assess the uncertainty of measurands on existing test rig

To quantify the validity of results from the dynamometer test rig, the uncertainty of measured variables will be considered to determine the combined uncertainty of the performance measurand of transmission power loss. The parametric dependency of uncertainty and relative impact of sources of uncertainty will allow for recommendations on improvement for future work.

1.5.5 Apply methods for characterising high frequency dynamics in transmissions to existing test rig

Literature addressing methods of measuring high frequency dynamics in chain drive transmission systems will be assessed. Suitable measurement and processing methods with be adapted from the literature to examine fluctuations in the measured parameters on the dynamometer test rig. The influence of the experimental hardware on high frequency dynamics will be investigated as a measure of parasitic influence on the measured variables from the method of loading. Fluctuations from transmissions which would be seen in use will be isolated and characterised, with comparisons made between different transmission types and gearing options.

1.5.6 Explore performance metrics in whole-life-cycle context

Metrics describing aggregate performance of transmission will be explored analytically to appreciate the changing loading and configurations of a chain transmission in use. The case study of an elite cycling road race will be addressed, since environmental, loading and configuration parameters might all vary significantly during a single event.

1.6 Summary of Chapter 1

- The use of chain drives as transmission systems was introduced, and expanded upon for pedal powered bicycles.
- The performance of transmission systems was introduced in three areas: wear characteristics, power efficiency, and NVH (noise, vibration and harshness).
- The shortcomings of isolating individual parameters when evaluating the performance experimentally were addressed.
- The research required to address these shortcomings was presented, setting the context for this thesis, with aims and objectives summarised.
- Research methodologies were outlined to address each of the stated aims.

1.6.1 Thesis structure

Part One: Chapters 2 and 3 will introduce the setting for the research, highlighting the context in which the performance characterisation fits, evaluating the literature and appraising current methodology of chains testing using analytical models from the literature.

Part Two: Chapters 4, 5, 6, and 7 will address development of performance tests on a new dynamometer test rig, and represent the bulk of the work conducted in this research project. The

experimental rig is introduced for completeness in Chapter 4 ; the novel research in this thesis starts from a point of this rig being commissioned and used for testing. Characterisation of bearing losses and evaluation of overall uncertainty are key areas of research which are necessary to measure efficiency of inherently low-loss systems. A method for assessing vibration performance of the transmission system is developed with key results shown to demonstrate its use as a tool for assessing the performance and health monitoring of the test rig, as well as quantifying a further performance metric of the test subject. Results from several test transmissions are presented in Chapter 8.

Part three: Chapter 9 presents an analytical approach to whole-life-cycle analysis of transmission performance with a case study of road race. This chapter extends the limits of the duty cycles possible on the test rig by considering the expected efficiency during the entirety of a road race with a derailleur drive.

Part Four: Chapter 10 summarises the thesis and addresses the research impact, conclusions and suggested further work. The primary application of this research has been to inform decision making in the development of a novel small-pitch chain drive by Renold Plc for British Cycling at the 2020 Tokyo Olympics. The technology was used in winning 7 Olympic medals, including 3 gold medals, seeing Team GB top the medal table for track cycling.

Chapter 2

Literature Review: Analytical and Experimental Methods to Assess Performance of Chain Drives

2.1 Introduction

This chapter summarises the existing literature which bears relevance to the work conducted in this thesis. It serves to identify the gaps in the current field related to the assessment of chain drive performance as transmission systems and to synthesise relevant published materials.

All areas of literature addressed are related to characterising the performance of a chain drive transmission, both directly and indirectly. This includes both analytical and experimental assessment of chain drive performance, and auxiliary areas of literature related to experimental methods such as loss mechanisms in support bearings and assessment of measurement uncertainty.

2.1.1 Structure of chapter

Four main sections of literature are addressed. First, analytical methods to describe transmission performance. Kinematic modelling of chain drives is introduced, followed by load distribution around links in a chain drive. These modelling techniques are central to several models of frictional losses and modelling dynamics of the chain drive in the literature, which are described finally.

Secondly, literature addressing experimental methods of determining transmission performance is addressed. Experimental apparatus in the literature has been designed and implemented to validate analytical work, to determine specific parametric inputs for analytical models discussed,

or to directly measure empirical performance of test transmissions. Equipment developed to test chain wear, isolated friction, vibration testing, and system level tests are addressed.

Thirdly, literature pertaining to the performance of rolling element bearings is addressed. Rolling element bearings are common components in rotational test apparatus in the literature. They have a 'parasitic' influence on the test, in that their mechanical behaviour impacts the measured performance of the test subject which must be mitigated or compensated. This is commonly addressed in literature describing rotational test machines and further research is addressed which considers the performance of rolling element bearings directly.

Finally, a key area in the use of experimental apparatus is the appreciation of the uncertainty of measurement. Literature is addressed relevant to quantifying and reducing the uncertainty of experimental determination of performance.

2.2 Analytical methods to describe transmission performance

Analytical models can be used to describe parametric dependence of performance in chain drives. Several broad categories of model exist in the literature:

1. Kinematic models, where geometry and quasi-static movement of chain drives has been described with impact of accelerations, loads and contact mechanics neglected.
2. Load distribution, where forces between links under tension in a chain strand or a complete drive have been determined.
3. Transmission efficiency, where frictional and secondary loss mechanisms have been determined to evaluate the power losses in transmission.
4. Transmission dynamics, where models have described dynamics in chain strands under tension and the implications on the transmission system, including predictions of resonant behaviour.

2.2.1 Kinematic modelling of chain drives

Several kinematic models exist in literature and have been used as starting points for tension and dynamic modelling from the geometry of a transmission and the lie of a chain between sprockets. Kinematic analysis also allows for determination of relative velocities of sprockets linked by a chain, where polygonal effects result in accelerations of chain or sprockets.

Kinematics of roller chain drive (Chen and Freudenstein, 1988 [11])

Chen and Freudenstein developed a strategy for kinematic analysis of a dual-sprocket drive to evaluate the effect of polygonal action, impact, and chain motion fluctuation on angular velocity and acceleration of sprockets.

The derived kinematic model assumed straight spans, that pitches of sprocket and chain were equivalent, and that there was negligible friction. Angular velocity, acceleration and impact velocity of links joining sprockets was shown to be dependent on centre distance, shown in Figure 2.1.

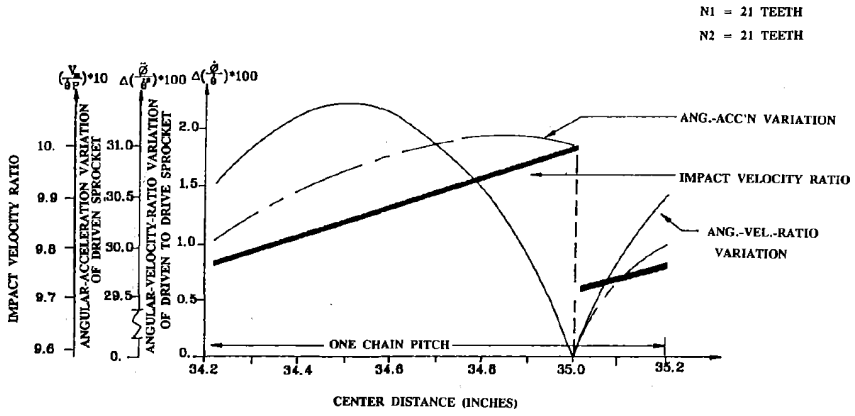

Figure 2.1: Results from kinematic modelling of a chain drive demonstrating the effect of varying centre distance over a chain pitch on angular acceleration, impact velocity ratio, and angular velocity ratio [11].

Geometric model of chain drive (Lodge, 2002 [47])

In his thesis, Lodge presented a geometric model as the starting point of a chain force model and chain vibration model. It described the quasi-static position of rollers in a chain drive, solved for incremental movements of a chain pitch so that full rotation of the transmission can be approximated.

The model described a dual-sprocket transmission with driving and driven sprockets in the same plane. The chain's driving span was approximated as a straight line and the slack span was solved by resolving force balance from link weight. The slack span was approximated initially as a catenary curve to improve computational speed. The model was capable of describing either top or bottom spans as the high tension driving span.

Sprocket teeth were not modelled. As seen in Figure 2.2, chain rollers were defined as either seated (black) or free (white), and change when they joined or left the sprocket pitch circle. The model approximated the elastic response of the tight span to force.

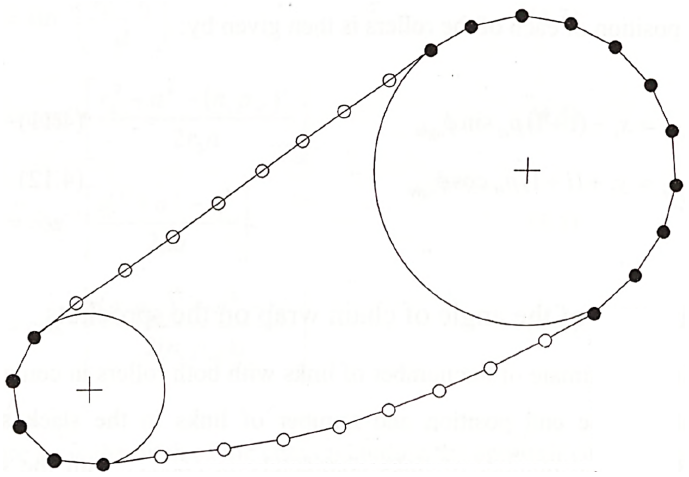

Figure 2.2: Link position modelled in the transmission. Rollers were defined to be engaged with the sprocket when they fall on the pitch circle (coloured black), or in the tight or slack span (coloured white) [47].

The relative position of the rollers calculated in this model were used in determination of the quasi-static forces between them, further described in Section 2.2.2.

Kinematic model with multi-body simulation validation (Fuglede, 2014 [25], Fuglede and Thomsen, 2016 [27])

Fuglede and Thomsen developed a complete kinematic model to predict wrap length, and sprocket angular velocities and accelerations. It is also the basis on which a dynamic model is proposed in a further study [26] (described in Section 2.2.4). The drive is not fully described, with slack span neglected. The tight span is modelled as a four-bar mechanism shown in Figure 2.3.

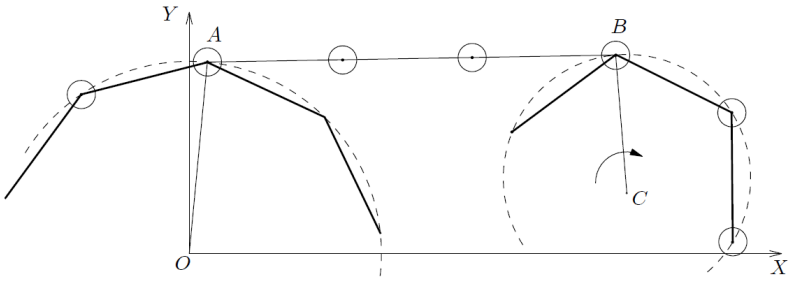

Figure 2.3: Kinematic modelling of a tight span in a chain drive as a four-bar mechanism [25]

.

The kinematic model is used to predict angular position, velocity and acceleration for sprockets and the resultant influence on the transverse movement of rollers in the tight span due to polygonal

action. A multi-body simulation serves as validation for the kinematic prediction, with good agreement.

Summary of kinematic modelling of chain drives

Kinematic modelling is a computationally efficient method of predicting chain link positions in a multi-sprocket transmission system. From these, wrapping length may be calculated and the effect of polygonal action in varying rotational speed of the sprockets [11].

The validity of a kinematic model is limited since the neglected inertial, gravitational and frictional effects will influence movement in real-world use. However, they were shown to be a necessary basis on which to build analytical models of link forces [47, 48] and of chain dynamics [47, 25].

2.2.2 Load distribution in transmission

The tension between links in chain transmission is the basis on which there is friction, vibration, and wear. Several descriptions of these performance metrics begin with analytical determination of the loads in a drive as a chain travels between driving span, sprocket, and slack span.

Mechanics of roller chains (Binder, 1956 [5])

Binder published a book with a complete evaluation of the mechanics of chain drives. Part of this was to provide seminal work in describing the forces in a chain as it rests on a sprocket. His analysis was based on solving static force balance for each roller, illustrated in Figure 2.4, with friction effects neglected and no distinction between roller and pin links.

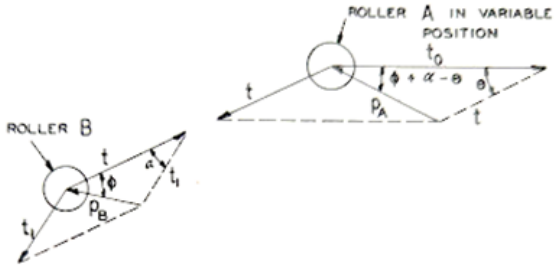

Figure 2.4: Force triangles for rollers in variable position [5].

Sprocket load distribution with elastic links (Marshek, 1979 [53])

Marshek developed a spring model analysis of a chain wrapped over a sprocket, expanding on work from Binder [5] by including elastic properties of the chain links.

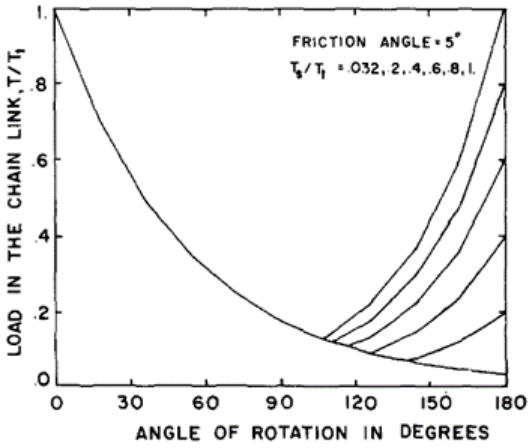

Figure 2.5: Load distribution on a driver sprocket predicted by the Geometric Progressive Load Distribution (GPLD) model for changing span tension ratios [59].

Using an example of a 180° wrap over a 31 tooth sprocket, the study demonstrated that the load on the first tooth in a sprocket was largest, and increased with sprocket material with higher Young's modulus, while this causes tension in the chain link to decrease. Increasing coefficient of friction has the same effect: increasing load in the tooth and reducing it in the chain. While friction and elastic effects were approximated in this analysis, deflections were not considered.

Geometric Progressive Load Distribution model (GPLD) with experimental validation (Naji and Marshek, 1983 [59, 60])

Naji and Marshek published several studies in analysis of the load in a chain around a sprocket following work of Naji in developing a Geometric Progressive Distribution Load (GPLD) model in their thesis [58].

The modelling work included the effect of frictional and elastic properties of both the chain and sprocket. In their analysis, pitches were equal, rollers were seated (no mechanical tolerances were present), and weight of chain was assumed to be negligible. The load in the links around the sprocket was calculated for known span tensions. An example of the output of their GPLD model is shown in Figure 2.5 for a variety of span tension ratios.

Where a chain is more compliant than a sprocket, elastic properties were determined not to have an effect on load distribution. A sprocket with low elastic modulus results in a more uniform load distribution. The former is more typical and, based on the analysis, maximum load on sprocket tooth is determined by:

- Pressure angle.

- Articulation angle.
- Friction angle.
- Tight side tension.

Experimental results show good agreement and clearly demonstrate the difference between driving and driven sprocket due to reversal of the friction forces. This is described within the GPLD by the friction angle increasing or decreasing the pressure angle depending on direction of rotation.

The GPLD model was further applied to consider the effect of difference between sprocket pitch and chain pitch on sprocket load distribution [61]. An increased chain pitch relative to the sprocket pitch is typical in chain drives due to elongation from wear. Pitch elongation causes movement of rollers during sprocket rotation and is a source of additional friction. Higher stresses were demonstrated in the teeth where the first link engages with the first tooth on the tooth flank as opposed to being seated.

Forces in chain during articulation (Hollingworth and Hills, 1986) [38]

Hollingworth and Hills described the forces in the links at span ends during articulation. In their analysis, frictional effects were included, highlighted as significant in the context of heavy duty chain drives which were not necessarily well lubricated. Distinction was made between open-end-forward and narrow-end-forward articulations, seen in Figure 2.6.

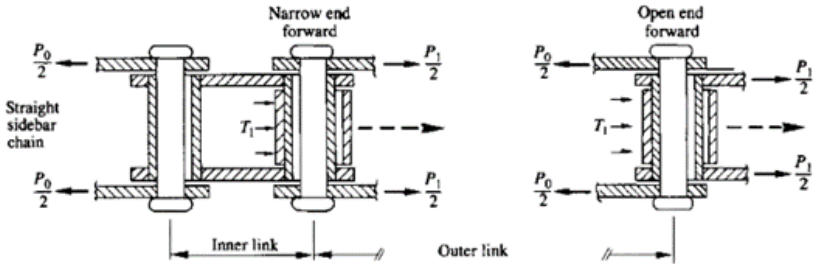

Figure 2.6: Roller-bushing-pin contacting during open-end-forward and narrow-end-forward articulations during chain articulation onto sprocket [38].

Forces in articulating links described analytically were presented with good agreement from experimental results. Hollingworth and Hills concluded that the distinction between open- and narrow-end forward articulation made a significant difference to normal contact forces due to the Coulomb friction, which was shown to be important in consideration of heavy duty applications.

Static load distribution in a complete drive (Troedsson and Vedmar, 1999 [77])

Troedsson and Vedmar modelled the static load distribution in a whole drive to determine the changing tension in a chain link on its travel around a dual-sprocket transmission. The roller position was calculated along with the forces between the rollers and sprockets, plotted in Figure 2.7.

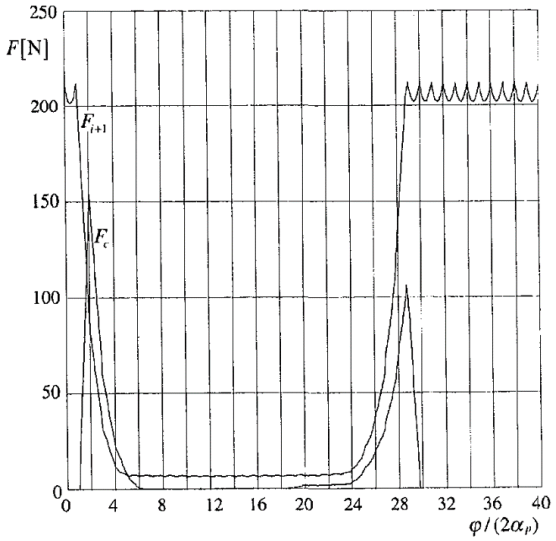

Figure 2.7: Link tension around a drive as modelled by Troedsson and Vedmar [77].

The geometry of the sprocket tooth is defined within the model to determine the unique point of contact between tooth flank and roller. Hence, Troedsson and Vedmar defined chain pitch and sprocket pitch independently and the effect of this on normal contact of seated rollers is defined. Further, geometry and tension models were iterated together to determine the effect of elasticity on contact points. The effect of friction on contact points is neglected.

Load distribution is shown to have dependency on:

- Chain pitch.
- Sprocket pitch.
- Elastic deformation.
- Driving/driven torque.

Tension in bush roller chain drive (Lodge and Burgess 2002 [48], Lodge 2002 [47])

Lodge and Burgess developed a model independently from Troedsson and Vedmar following similar analysis. Tension is defined for the whole drive based on geometry defined by their kinematic model described in Section 2.2.1. The tension around a chain drive is plotted as in Figure 2.8.

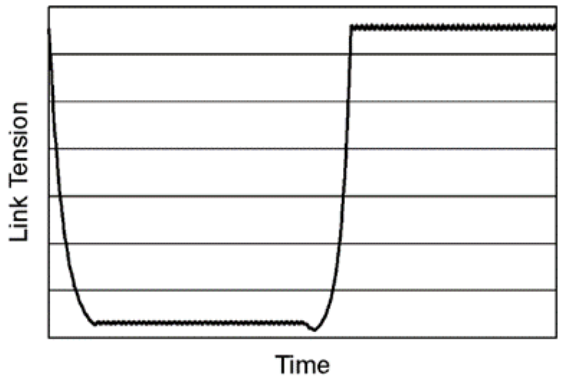

Figure 2.8: Link tension around a drive for 19T-19T chain drive [48].

Lodge used several existing models to define the chain tension in a sprocket based on different parameters, and introduced a novel description of sprocket load distribution in a low-slack span chain drive:

1. Static roller model, based on analysis by Binder [5].
2. High-slack span tension model, based on the GPLD model from Naji and Marshek [59].
3. Low-slack span tension model.

The choice of model was made based on the slack span/tight span tension ratio which changes the effective pressure angle between the teeth and rollers.

The elastic extension of the chain was estimated for the chain strand in the tight span, though neglected in the rest of the drive. As defined by the geometric model, the interaction between rollers and chain teeth was not described; rollers were defined as fully seated or part of the chain span between sprockets. This made for a computationally faster solution than the method proposed by Troedsson and Vedmar [77] since geometry was not reiterated with the modelled forces. Lodge also considered the implication of friction in the model, with distinction made between chain forces around a driver sprocket and those around a driven sprocket due to the opposing sliding friction direction.

A key contribution from this research was experimental validation from data collected by Stephenson et al. [76], seen in Figure 2.9.

The link tension described in this model was the starting point for analysis to determine friction in articulating links (described in Section 2.2.3), and to predict selected dynamic behaviours (described in Section 2.2.4).

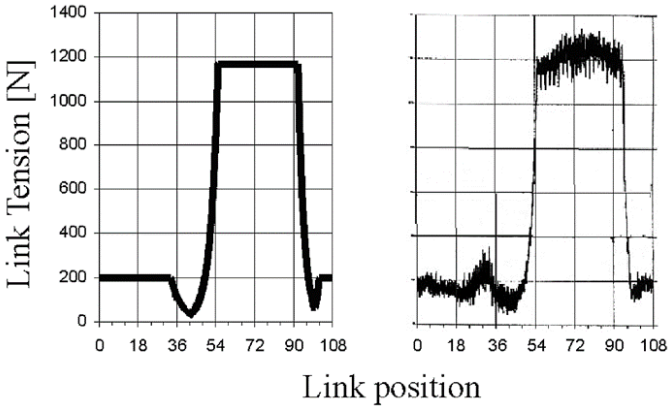

Figure 2.9: Modelled link tension compared with experimental results from Stephenson et al. [76], showing good agreement with approximate tension values. Dynamic effects seen in experimental data were not considered in the model [48]).

Summary of analytical descriptions of load distribution

The literature addressing the analytical description of tension in links around a chain drive began with static force balance of links engaged with a sprocket by Binder [5] in 1956, with significant work done by Naji and Marshek [53, 58, 59, 60, 61] in further consideration of interaction between chain rollers and sprocket teeth including elastic, frictional and geometric analysis.

Hollingworth and Hills [38] highlighted the role of friction in chain forces between articulating links which is significant in heavy duty chains.

Troedsson and Vedmar [77] and Lodge and Burgess [48] independently developed modelled descriptions of a full drive, including the effect of a slack chain span. Lodge and Burgess used experimental data from Stephenson et al. [76] to validate their model with good agreement.

2.2.3 Analytical description of transmission efficiency in literature

The power efficiency of a chain drive transmission is central in analysing performance since it directly relates to the required power input for given output, or a reduction in performance (e.g. bicycle velocity) for given input. Several strategies for analytical descriptions of efficiency are proposed in the literature.

Frictional model of cranked link chain (Hollingworth and Hills, 1986 [39])

Hollingworth and Hills considered the Coulomb friction in articulating links at either end of a tight span in a cranked link chain drive transmission. A distinction was made between open end articulation and narrow end articulation, illustrated in Figure 2.10. In open end articulation, the

pin moves relative to a stationary bush and roller; relative sliding surfaces are between pin and bush in this articulation, pivoting at radius of the inside of the bushing, R_{bi}. In narrow end forward articulation, the bushing moves relative to a stationary pin and roller and there is relative sliding at two surfaces at the inside and outside of the bushing, R_{bo}.

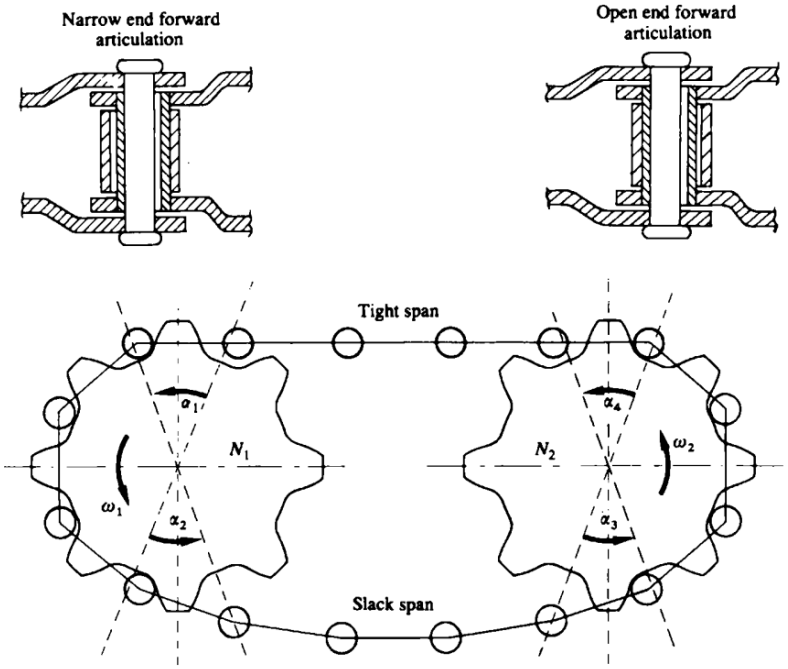

Figure 2.10: Articulation types in cranked link chain transmission. Locations and angles were shown in basic transmission [39].

Energy consumed in open-end articulation, E_o, was described by Equation 2.1.

$$E_o = \frac{P_o \mu_1 \alpha_o R_{bi}}{(1+\mu_1^2)^{1/2}} \tag{2.1}$$

Where P_o is tight span tension, μ_1 is pin-bush coefficient of friction, α_o is articulation angle (open end forward), and R_{bi} is the bush internal radius.

Energy consumed in narrow-end articulation, E_n, was described by Equation 2.2.

$$\begin{aligned} E_n = {} & \frac{P_o \mu_1 R_{bi} \cos\Psi_1}{\sin(\varphi_n + \alpha_n)} \{\cos\varphi_n - \cos(\varphi_n + \alpha_n)\} + \\ & P_o \mu_2 R_{bo} \cos\Psi_2 \left[\sin(\varphi_n + \alpha_n) \times \ln\left\{ \frac{\sin(\varphi_n + \alpha_n)}{\sin\varphi_n} - \alpha_n \cos(\varphi_n + \alpha_n) \right\} \right] \end{aligned} \tag{2.2}$$

Where μ_2 is bush-roller coefficient of friction, Ψ_1 and Ψ_2 were angle of repose for pin-bush and bush-pin contact (equivalent to previously defined friction angle), and φ_n is pressure angle of the sprocket tooth.

The efficiency of the drive was estimated as in Equation 2.3.

$$\eta = 1 - \frac{E_o + E_n}{P_o p_t} \tag{2.3}$$

Efficiency calculated thus was shown to increase with number of teeth in both driving and driven sprockets. Although there was dependency on chain forces in the energy consumed in articulations, the tight span term, P_o, cancelled in the calculation of efficiency and hence there was no dependence on load expressed. No experimental validation of the model was offered.

Simple frictional model of roller chain (Burgess, 1998 [8])

In a study examining the performance improvement of using larger sprockets, Burgess derived a simple model of chain transmission efficiency based on Coulomb friction between sliding surfaces which were equivalent for all articulations. A simplified chain construction was used, considering links to be joined by a single pin rotating within a sleeve. Efficiency was described as in Equation 2.4.

$$\eta_c = \frac{R - \left(\frac{r_p \mu_c}{2}\right)\left(1 + \frac{1}{N}\right)}{R} \tag{2.4}$$

The model illustrated the dependency of transmission efficiency on the radius of the driving gear, R, the radius of the pin, r_p, the coefficient of friction, μ_c, and gear ratio, N. Validation of the principle of improved efficiency from enlarged gears was demonstrated through static tests; however, this analytical model was not directly validated.

Frictional model of cycling chain with auxiliary gears (Kidd, 2000 [42])

In their thesis, Kidd developed a model based on analysis from Binder [5] and Coenen and Peeken [12] to describe frictional losses in a transmission for road bicycles, featuring auxiliary gears in the slack span as part of a rear derailleur.

Coulomb friction was considered at articulations around the drive, occurring at 8 locations shown in Figure 2.11. Kidd distinguished between pin-link and roller-link articulation, and forward and rear links. Slack span tension, F_s, was constant and non-zero.

The relative contribution to losses from 8 articulations and lateral offset for an example case is illustrated in 2.12. P_{f1-4} were associated with the top span articulations (between chain pin and bush, and between bush and roller); P_{f5-6} and P_{f8-9} were associated with bottom span articulations; and P_{f7} was due to the lateral offset.

The transmission efficiency was described by Equation 2.5.

$$\eta = 1 - \frac{\pi N_L \sum_{i=1}^{9} P_{fi}}{\omega_1 Z_1 p F_t \left(1 - \frac{F_s}{F_t}\right)} \tag{2.5}$$

Kidd offered no direct experimental validation of this model.

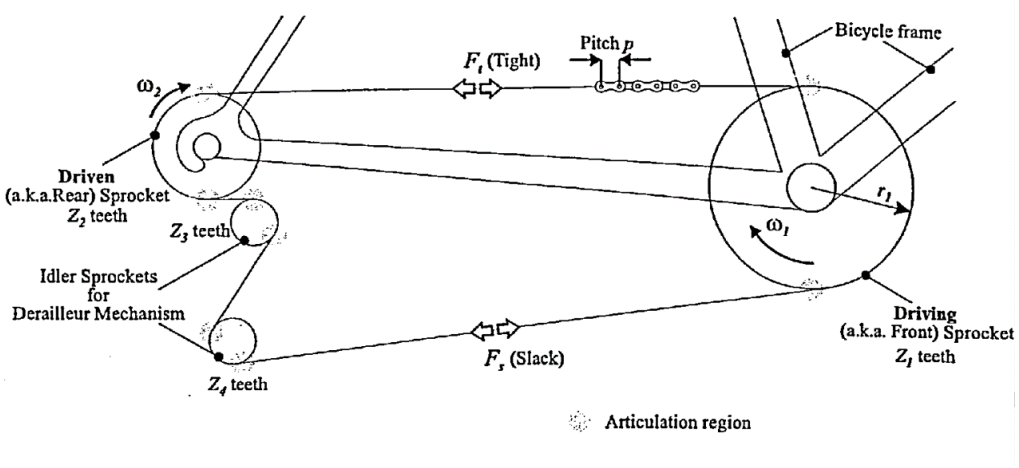

Figure 2.11: Transmission of a road bicycle with auxiliary sprockets, articulation region highlighted at entry to and exit from each sprocket [42].

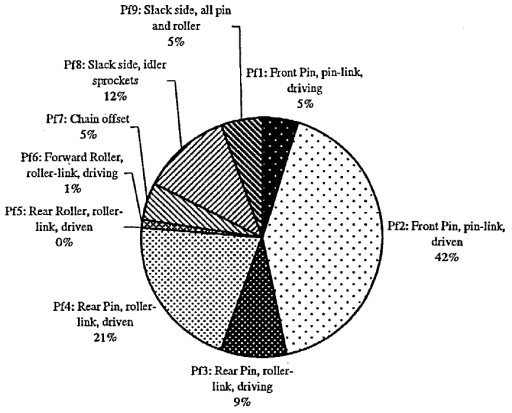

Figure 2.12: Contribution to friction in cycle chain transmission with rear derailleur acting to tension the lower span from 9 sources of Coulomb friction [42].

Frictional model of cycling chain (Spicer, 2001 [74, 75])

Spicer et al., developed an analytical description of transmission efficiency in cycle chain in a derailleur configuration. Friction from relative movement between chain links was described from three sources:

- Case I: Relative sliding between bush and pin.
- Case II: Chainline offset.
- Case III: Relative sliding between tooth-roller and roller-bush.

In all cases, only Coulomb friction was considered. The descriptions for power losses during chain articulation for each case were described as in Equations 2.6 - 2.8.

$$P_{f_I} \approx N_1 \omega_1 \mu_I \rho \left(\frac{\pi}{2} T_0\right) \left[\frac{1}{N_1} + \frac{1}{N_2}\right] \tag{2.6}$$

$$P_{f_{II}} \approx N_1 \omega_1 \mu_{II} \left(T_0 r_0 \sin\gamma\right) \left[\frac{1}{N_1} + \frac{1}{N_2}\right] \tag{2.7}$$

$$\begin{aligned} P_{f_{III}} \approx \mu_{III} T_0 r_{R_i} \frac{N_1 \omega_1}{4\pi} \sum_{j=1}^{2} \left[\left(N_1 \psi_1 \pi - 1\right) \delta_{1j} + \left(N_2 \psi_2 \pi - 1\right) \delta_j\right] \\ \times \left[\frac{2\pi}{N_i} \cos\varphi_i - \sin\varphi_i \ln\left(\cos\left(\frac{2\pi}{N_i}\right) + \sin\left(\frac{2\pi}{N_i}\right) \cot\varphi_i\right)\right] \end{aligned} \tag{2.8}$$

Spicer suggested that cases I and III should dominate in expected operating conditions, and total power loss was expressed as in Equation 2.9.

$$\begin{aligned} P_{f_{Total}} = \mu T_0 \frac{N_1 \omega_1}{2\pi} \Bigg\{ \frac{\pi}{2} \rho \sum_{i=1}^{2} \sin\left(\varphi_i\right) \ln\left|\frac{1 + \tan\left(\alpha_i 2\right)\tan\left(\varphi_i 2\right)}{1 - \tan\left(\alpha_i 2\right)\tan\left(\varphi_i 2\right)}\right| \\ + \frac{r_{R_i}}{2} \sum_{j=1}^{2} \left[\left(2\psi_1 \alpha_1 - 1\right) \delta_{1j} + \left(2\psi_2 \alpha_2 + 1\right) \delta_{2j}\right] \times \left[\alpha_j \cos\varphi_j - \sin\varphi_j \ln\left(\cos\alpha_j + \sin\alpha_j \cot\varphi_j\right)\right] \Bigg\} \end{aligned} \tag{2.9}$$

Efficiency was expressed by Equation 2.10.

$$\eta = 1 - \frac{P_{f_{total}}}{\left(pT_0 \omega_1 \alpha_1\right)} \tag{2.10}$$

Though the study addressed the context of bicycle transmission with auxiliary gears and a tensioned bottom span, only articulations in the high tension span were considered. Extensive experimental data was collected in the same study though Spicer et al. did not successfully validate the model with experimental results. There was significant disagreement in the dependency of efficiency on chain tension, prompting a subsequent investigation into non-frictional losses in roller chains.

Model of non-frictional losses in roller chain (Spicer, 2013 [73])

In an later study, Spicer addressed the discrepancy between modelled friction in articulation and experimentally measured loss in their previous research [75] and examined non-frictional sources of loss in the form of non-linear elastic effects. This study sought to describe the harmonic generation and dispersion in the chain span by modelling the span as a series of masses linked with springs with linear and nonlinear stiffness coefficients, illustrated in Figure 2.13.

The chain span was made up of N masses, and the force on the N^{th} mass was determined based on the stiffness of link contact and the displacement from equilibrium position. Spicer derived equations of motion for chain links to describe their relative movement and hence articulation between neighbouring links. These articulations describe irrecoverable losses based on combining effects of fundamental and second harmonic waves in the span.

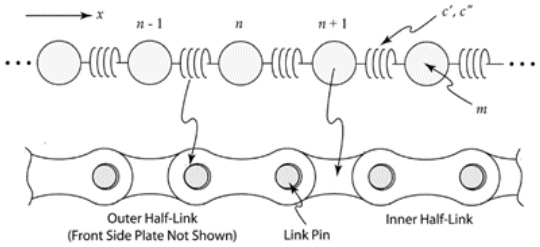

Figure 2.13: Links modelled as lumps of mass m. Contact between links has stiffness described by linear and nonlinear coefficients (c', c'') [73].

The ratio of average usable power at the span end, $\langle P_N \rangle$, and span start, $\langle P_0 \rangle$ was defined as in Equation 2.11.

$$\frac{\langle P_N \rangle}{\langle P_O \rangle} \approx 1 - N^2 \mu m^{\frac{1}{2}} c''^2 c'^{-\frac{5}{2}} \left(1 - \frac{N-1}{2} N \mu m^{\frac{1}{2}} c''^2 c'^{-\frac{5}{2}} \right) \tag{2.11}$$

Where N is the number of half-links in the span, m is the mass of each link, c' and c'' are linear and nonlinear stiffness coefficients for the chain spring based on Hertzian contact in pin-bushing interactions. These are defined in Equations 2.12 and 2.13. μ is a factor defined by a number of constants of proportionality $\mu = \frac{3\eta a_0^2}{2}$.

$$c' = \{a\,[b - \ln(P)]\}^{-1} \tag{2.12}$$

$$c'' = c' \left\{ 2aP\,[b - \ln(P)]^2 \right\}^{-1} \tag{2.13}$$

Within the deceptions of stiffness coefficients, b is a factor defined by the sprocket sizes, length of contact, viscosity and Young's modulus of chain link, and is described by Equations 2.14 and 2.15.

$$b = \ln \left[\frac{l^3}{V} \frac{(R_2 - R_1)}{R_1 R_2} \right] \tag{2.14}$$

$$V = \frac{2\left(1 - \upsilon^2\right)}{\pi E} \tag{2.15}$$

Spicer combined this new analysis with their previous description of loss due to Coulomb friction [75]. Transmission efficiency was shown to decrease with the reciprocal of chain tension and with increased pin/bushing Young's modulus. The new combined model was compared with experimental data from their previous study [75]. With μ used as a fitting parameter, good agreement was seen.

Frictional model of bush-roller chain (Lodge and Burgess, 2002 [48])

Lodge and Burgess considered Coulomb friction in links articulating on entry to, and exit from, each sprocket in a dual-sprocket bush-roller chain transmission. Chain forces were calculated

with the chain tension model previously described in Section 2.2.2. Chain link articulations were considered in both spans.

Distinction was made between pin- and bush-articulations in similar analysis to Hollingworth [39]. Lodge also considered the centripetal forces from high speed rotation as defined originally by Binder [5], as described in Equation 2.16.

$$F_{cf} = \frac{mR_s^2\omega_s^2}{p} \tag{2.16}$$

The energy consumed in pin- and bush-articulations defined by Lodge are described in Equations 2.17 and 2.18.

$$W_{pin} = \frac{F_c + F_{cf}}{\sqrt{1+\mu_p{}^2}}\mu_p r_{bi}\alpha_m \tag{2.17}$$

$$W_{bush} = \begin{cases} \frac{F_c\mu_p r_{bi}[\cos\theta_{RA} - \cos(\theta_{RA}+\alpha_m)]}{\sqrt{1+\mu_p{}^2}\sin(\theta_{RA}+\alpha_m)} + \frac{F_{cp}\mu_p r_{bi}\alpha_m}{\sqrt{1+\mu_p{}^2}} + \frac{F_c\mu_r r_{bo}(1-\cos\alpha_m)}{\sin(\theta_{RA}+\alpha_m)} & \textit{High tension} \\ \frac{F_c\mu_p r_{bi}[\cos\theta_{RA} - \cos(\theta_{RA}+\alpha_m)]}{\sqrt{1+\mu_p{}^2}\sin\theta_{RA}} + \frac{F_{cp}\mu_p r_{bi}\alpha_m}{\sqrt{1+\mu_p{}^2}} + \frac{F_c\mu_r r_{bo}(1-\cos\alpha_m)}{\sin(\theta_{RA})} & \textit{Low tension} \end{cases} \tag{2.18}$$

With energy consumed in bush articulations, a distinction was made between a high tension and low tension environment. The articulations in the transmitting span were defined to be high tension; the slack span articulations were in a low tension state below a threshold span force ratio.

The efficiency was determined by Equation 2.19, based on known output power, P_o.

$$\eta = \frac{P_o}{P_o + N_s\omega_s\Sigma W} \tag{2.19}$$

Experimental measurements were made with varying sprocket configurations of driving and driven gears (19/19, 26/26, 52/26, and 26/13), varying rotational speed between 50 RPM and 300 RPM, a range of output torques between 0 Nm and 25 Nm, and with two different chain types (industrial 1/2-inch pitch, and bicycle chain 1/2-inch pitch). Within the uncertainty of the measurement, experimental data demonstrated good agreement with theory across the parameters tested.

Frictional model of bush-roller chain including viscous damping (Zhang and Tak, 2020 [91])

Zhang and Tak derived a new expression for transmission efficiency which considered Coulomb friction in articulating links in a chain drive and included the effect of lateral offset between two sprockets. Work done against Coulomb friction in sliding surfaces in chain links was, again, distinguished for different articulation types. Work done in pin articulation, W'_{pin}, and bush articulation, W_{bush}, was described as below.

$$W'_{pin} = 2\cdot\left(\frac{1}{\sqrt{1+\mu_1{}^2}}\cdot T_c\right)\cdot\mu_1\cdot R_{bi}\cdot\theta \tag{2.20}$$

$$W_{bush} = \frac{\pi}{2}\cdot\frac{1}{\sqrt{1+\mu_1{}^2}\cdot\sin(\beta-\theta)}\cdot T_c\cdot\cos(\gamma)\cdot\mu_2\cdot R_{bo}\cdot\theta \tag{2.21}$$

Further to work done against Coulomb friction, Zhang and Tak highlighted damping force as an important characteristic in the tight span of the chain. Damping force, F_d, was described to be proportional to the relative velocity between end points of the tight span of the chain as in Equation 2.22.

$$F_d = D_{chain}\left[R_{s,1}\dot{\sigma}_1 \cdot \cos\left(\sigma_1 - \theta_{in,1}\right) - R_{s,2}\dot{\sigma}_2 \cdot \cos\left(\sigma_2 - \theta_{in,2}\right)\right] \tag{2.22}$$

Where D_{chain} is the constant of proportionality. Efficiency, η', was described by Equation 2.23.

$$\eta' = \frac{T_o \cdot \omega_{s,2}}{T_o \cdot \omega_{s,2} + N_{s,1} \cdot \omega_{s,1} \cdot (W'_{pin} + W_{bush}) + F_d \cdot \omega_{s,1} \cdot R_{s,1}} \tag{2.23}$$

Zang and Tak offered experimental validation of this model for a 32/32 dual-sprocket chain drive with low-power input parameters (rotational speed 40-80 RPM, offset angle 0-3 degrees, torque 5-9 Nm, sprockets centre distance 0.45-0.55 metres). The error between theoretical and experimental results was reported in the range 0.35-1.81%, with highest deviation at low speed and high offset angle.

Frictional model of bush-roller chain with roller-sprocket losses (Lanaspeze et al., 2022 [46])

Lanaspeze et al. considered Coulomb friction in bush roller chain, distinguishing between the 'meshing' losses from chain articulation, and 'roller' losses from relative movement between the roller and tooth flank as the pressure angle changes for seated chain links during sprocket rotation.

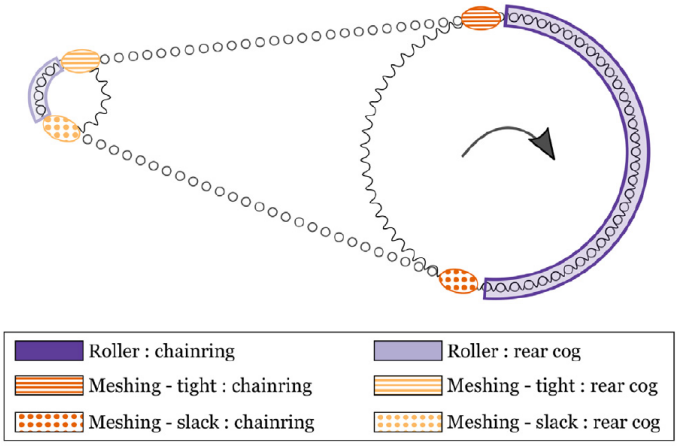

Figure 2.14: Sources of sliding friction on the path of a chain around a dual sprocket transmission system. Meshing between chain links and sprockets occurs at either end of the tight and slack spans. Rolling due to imperfect seating of a roller on a sprocket occurs between meshing points [46].

A description for energy lost to friction in meshing was provided by the authors and is described in Equation 2.24.

$$W_{mesh} = \mu_{pb}\alpha R_{pin} T \tag{2.24}$$

Where T is tension in the link, α is the sprocket angle, R_{pin} is the radius of the pin and μ_{pb} is friction coefficient between pin and bushing.

Further friction induced from the movement of the roller in the sprocket tooth as the tension changes from one side to the other was also defined. Two extreme cases were considered:

- Case (a): Pure sliding at roller/sprocket contact, and relative sliding between roller and bush
- Case (b): pure rolling at roller/sprocket contact, and sliding between roller and bush.

The two cases are defined in Equation 2.25.

$$\begin{cases} Case(a): & W_{roller} = \mu_{rp}\bar{P}_j L_{travel} \\ Case(b): & W_{roller} = \mu_{br}\bar{P}_j \theta_{roller} R_{bush} \end{cases} \tag{2.25}$$

A mean value of contact force, P, was used based on modelled tension in links around each sprocket.

With estimated parameters, meshing losses and roller losses around the sprocket were shown to be of similar order of magnitude, suggesting that roller losses should not necessarily be neglected in analysis, as was the case in previous analytical methods in the literature. No experimental validation was presented.

Summary of analytical descriptions of chain transmission losses

The literature addressing analytical descriptions of chain transmission power efficiency presented a number of different sources of energy losses. All presented literature identify Coulomb friction in articulating links at either end of a tight span in a dual-sprocket transmission as the primary source of energy consumption. Losses due to sliding friction is described with simplified chain link geometry, or with consideration of several different sliding surfaces in a bush-roller chain.

Several models include the secondary effects of losses in the bottom span, which depending on the application may still be significant. In their thesis, Kidd addresses additional losses in the bottom span of a bicycle transmission with a tensioning derailleur [42]. Several studies also consider the additional friction from planar offset typical in bicycle chain drives [75, 91].

Beyond sliding friction, several other sources of energy loss were described such as non-linear elastic effects and viscous damping due to lubrication [73, 91] , and losses due to changing contact of the roller on sprocket tooth on its path between spans [46]. Different sources of energy consumption were highlighted as important for the specific context for the tested transmission.

Where experimental results were presented, they show agreement to suggest that the principles of frictional losses were broadly correct, though no experimental data is sufficiently detailed or accurate to demonstrate that the subtle choices in what effects were modelled were correct.

2.2.4 Modelling dynamic behaviour in chain spans

Dynamic behaviour in chain transmissions is inherent due to polygonal action caused by wrapping of chain pitches around a sprocket, compliance in chain and sprocket, and inconsistent driving and driven loads in operation. Various analytical descriptions of dynamic effects were proposed in the literature, from static modelling of a chain span as a string to full description of the transmission and interaction of chain, sprockets, and driving and driven inertial mass.

Moving heavy string (Mahalingam, 1957 [50])

Seminal work by Mahalingam presented equations of motion to describe a travelling chain span approximated as a heavy string, illustrated in Figure 2.15.

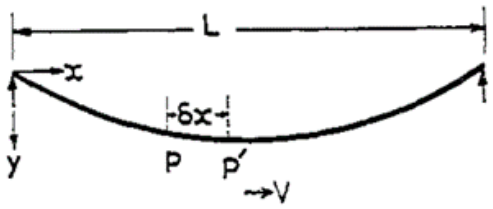

Figure 2.15: Displacements of travelling chain approximated as a string [50].

Mahalingam's analysis included consideration of centrifugal effects increasing the span tensions, and forced vibration due to both transverse excitation (from polygonal action) and longitudinal excitation (from torsional vibration in the sprocket).

Mahalingam demonstrated that the amplitude of transverse vibrations in a chain span decreases with increasing longitudinal velocity of the chain span, tending to zero as velocity approaches infinity.

Resonance from heavy string model (Lodge, 2002 [47])

In his thesis, Lodge proposed an extension to the quasi-static force model, as described in Section 2.2.2, to consider some dynamic influences of a chain transmission. A description of natural frequency in chain span was proposed based on simple harmonic analysis approximating a chain span as a heavy string with fixed ends, seen in Equation 2.26.

$$f_k = \frac{k\sqrt{\frac{F_t p}{m}}}{2n_t p} \tag{2.26}$$

Dynamic modelling with inertial effects (Troedsson and Vedmar, 2000 [78])

Troedsson and Vedmar presented a new method for dynamic modelling of a dual-sprocket transmission which included consideration of the drive geometry and inertial forces. The modelled system is shown in Figure 2.16. The inertial effects of driving and driven systems illustrated were also modelled (shown as flywheels) with given torque acting to drive and brake the transmission.

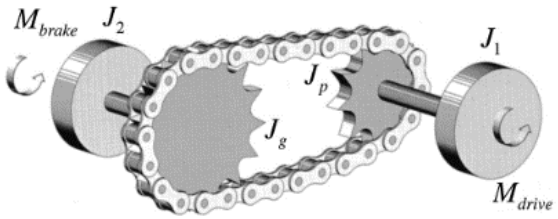

Figure 2.16: Chain drive transmission system modelled with inertial effects of the driving and driven systems, J_1 and J_2 [78].

To determine the dynamic forces, friction and damping were considered for the chain, sprockets, driving and driven systems. The results for dynamic tension in chain links is demonstrated in Figure 2.17 for movement of one chain pitch. Impact forces from chain pick-up were shown reflecting along the span in the tight span with tension peaks in antiphase due to the wave travelling between ends while diminishing. This effect was almost eliminated when chain mass approached zero.

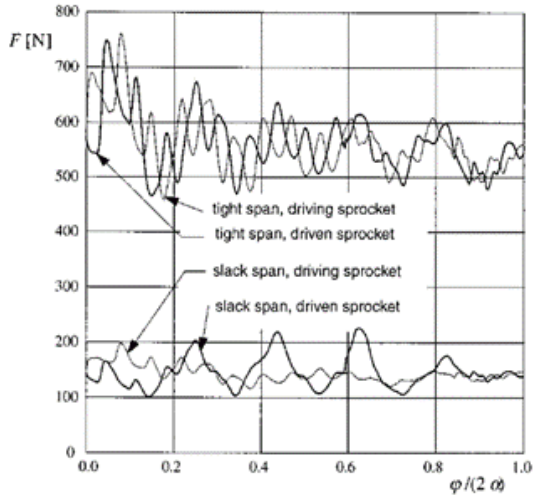

Figure 2.17: Tension force in the chain for links at end of each span [78].

Modal approach to determining chain harmonics (Xu et al., 2011 [89])

Work by Xu et al. offered a new method of determining the expected resonant behaviour of a chain span in tension. Equations of motion were derived with Lagrangian mechanics, defining the

kinetic and potential energy of chain links. The resonant, rather than driven, properties of a chain span were described.

A long chain span (40 links, 15.875mm pitch) was modelled with a lumped mass on the strand. Natural frequencies of transverse vibration were determined as a function of chain velocity, chain force, and lumped mass weight up to a 5^{th} resonant mode. Figure 2.18 shows frequency and shape of resonant mode 1 and 2 as a function of tension.

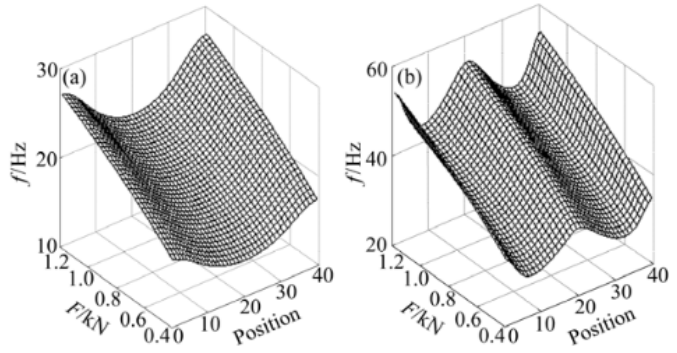

Figure 2.18: Shape and frequency of mode 1 and mode 2 resonance [89].

Key conclusions from Xu et al. were:

1. With increased tension force, natural frequencies increased.
2. With increase of mass, natural frequencies decreased but the magnitude of load fluctuation increased.
3. Mode shapes changed with location of lumped mass.

Chain span dynamics with moving boundary conditions (Fuglede and Thomsen, 2016 [26])

Fuglede and Thomsen developed a dynamic model as an extension to the kinematic model of a dual-sprocket chain drive [27], described in Section 2.2.1. With end conditions defined by the previous model, chain span was modelled as a heavy string with moving boundaries, changing length, and defined axial stiffness and mass per unit length, illustrated in Figure 2.19.

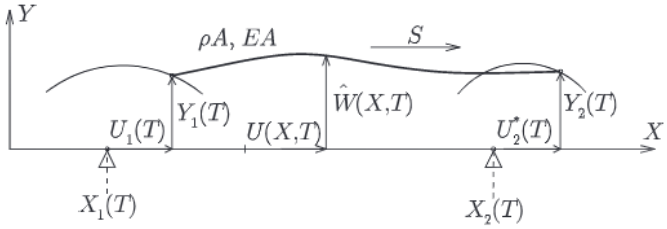

Figure 2.19: Tight span of chain drive transmission is modelled as a dynamic string with moving boundaries at each sprocket [26].

Equations of motion were solved for the chain spans and driving sprocket, from which solutions described the longitudinal displacement and axial tension of the chain span. Resonance was evaluated in the spans, sprocket, and a combined resonance between them both.

This study concluded that large span vibrations can occur due to compliance in the driven sprocket due to potential for aligned resonance, demonstrating the interaction between dynamics in the driving sprocket and chain.

Summary of dynamic modelling

Analytical approaches to evaluating dynamic behaviours in high-tension chain spans in literature have been presented. Several studies consider a chain span approximated as a heavy string with fixed ends [51, 47, 26], or computationally more involved approach of modelling multi-link strands [78, 89]. In the case of Troedsson and Vedmar [78], the whole transmission is modelled which offers the most modelled complete system of the summarised literature. Predicting resonance in the chain span and wider system is a common theme from both a modal approach [89] and from a heavy string model [47]. Large responses can be expected if excitation frequencies match resonance frequencies. The resonance has dependency on chain mass, compliance, chain force, and presence of a lumped mass.

2.3 Experimental methods to determine transmission performance

Various experimental apparatus has been used in the literature to validate theoretical effects of transmission performance, or to directly assess transmission performance in specific test conditions. Experimental work may focus on key parameters, such as determining the coefficient of friction between sliding surfaces or by inducing dynamic effects. Alternatively, a more direct method of evaluating transmission efficiency was carried out through experimental apparatus which drives a complete transmission while measuring power lost to the transmission, which has been done by various means.

2.3.1 Experimental wear characterisation in chain drives

Literature addressing experimental methods to determine wear in chain drives is summarised here. Modern chain drive transmissions have good wear characteristics, and experimental methods in the literature are largely adapted to long-duration or accelerated loading testing, while maintaining loading conditions related to those in real-world conditions so that results bear relevance to typical use.

Four-square sprocket test machine (Ross and Marshek, 1982 [67])

Ross and Marshek developed experimental apparatus based on the four-square testing principle, where two transmission systems were tensioned against one another statically and linked such that they drive one another. The input power to the system was then only required to top up the losses. Their design was patented in 1983 [68]. Two chain drives were run as a test pair on the apparatus illustrated in Figure 2.20. Tight and slack span were oppositely orientated in the pair of chains.

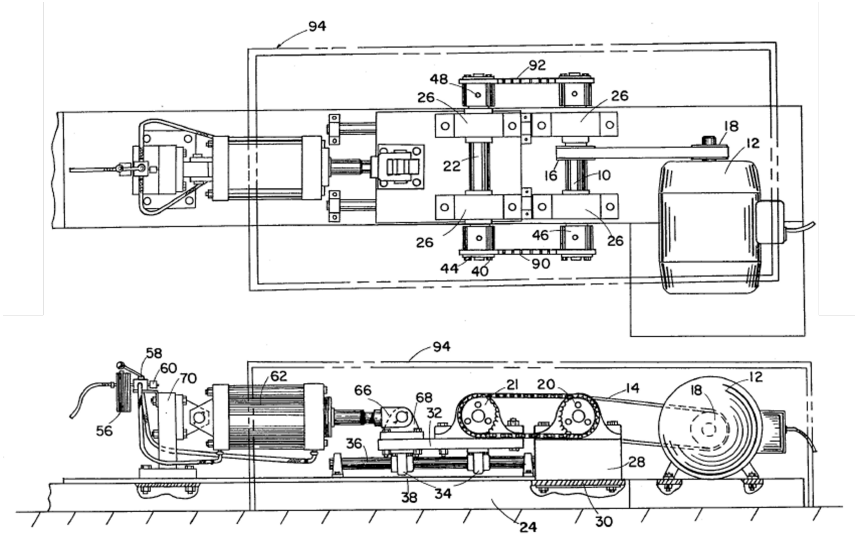

Figure 2.20: Schematic of Ross and Marshek's four-square sprocket test rig [67].

The design featured a translational platform connected to a pneumatic cylinder to adjust centre distance and pre-tension in the chain spans. Long duration tests were run continuously until failure of chain components. Wear rate was determined by recording the number of cycles-to-failure of test specimens.

Low- and high-torque test stands (Peeken and Coenen, 1985 [64])

Peeken and Coenen conducted a large study into the effect of lubrication type and regularity of application on wear rate in roller chains. They developed two test stands for their work: a high power stand for applied torques greater than 100 Nm, and a smaller test stand for torques less than 100 Nm. These were denoted Test Stand I and Test Stand II respectively.

Test Stand I is illustrated in Figure 2.21. A high torque driving motor drove a shaft with two sprockets and support bearings. A test chain pair were linked to a driven shaft which drove against an electro-hydraulic torque unit acting as brake.

The secondary experimental apparatus, Test Stand II, tested a single chain and is illustrated in Figure 2.22. A small motor drove a gear transmission which stepped down the speed and increased

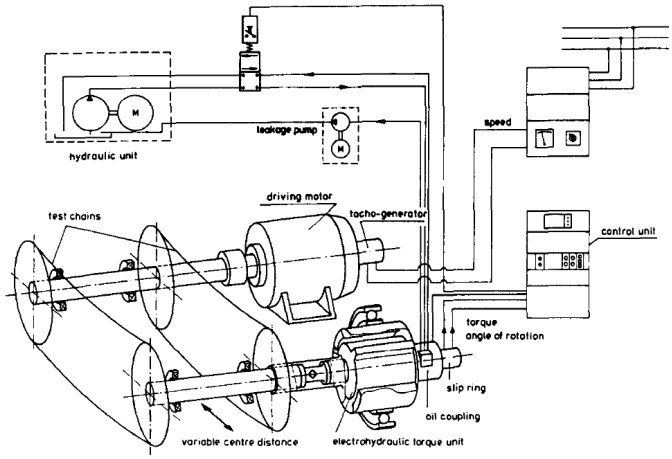

Figure 2.21: Schematic of Peeken and Coenen's Test Stand I [64].

torque for the driving sprocket on the test chain. A secondary 're-conducting' chain was used to recirculate the power. This operated on the other side of the gears and so travelled at high speed and low load, hence it was not a second test chain. It was necessary that the gear ratio in the chain transmissions was equivalent to the gear ratio in the gear box. The schematic illustrated in Figure 2.22 appears to show a friction clutch to connect the test driven sprocket shaft to the re-conducting chain.

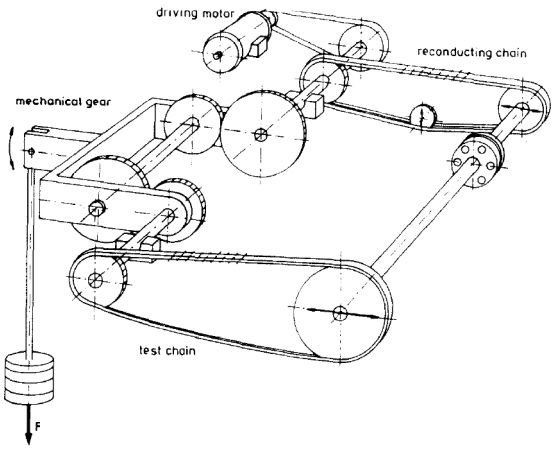

Figure 2.22: Schematic of Peeken and Coenen's Test Stand II [64].

Both test rigs were intended to induce wear over long duration tests (greater than 500 hours). Chains were removed periodically and wear determined with measurement of chain elongation.

New four-square design (Hollingworth, 1987 [37])

Hollingworth developed a novel rig to induce wear in a chain based on the four-square method. Rather than tensioning two test chains against one another as previously, the chain spans of a single

chain in a dual-sprocket configuration were tensioned against one another. The schematic for the rig is illustrated in Figure 2.23.

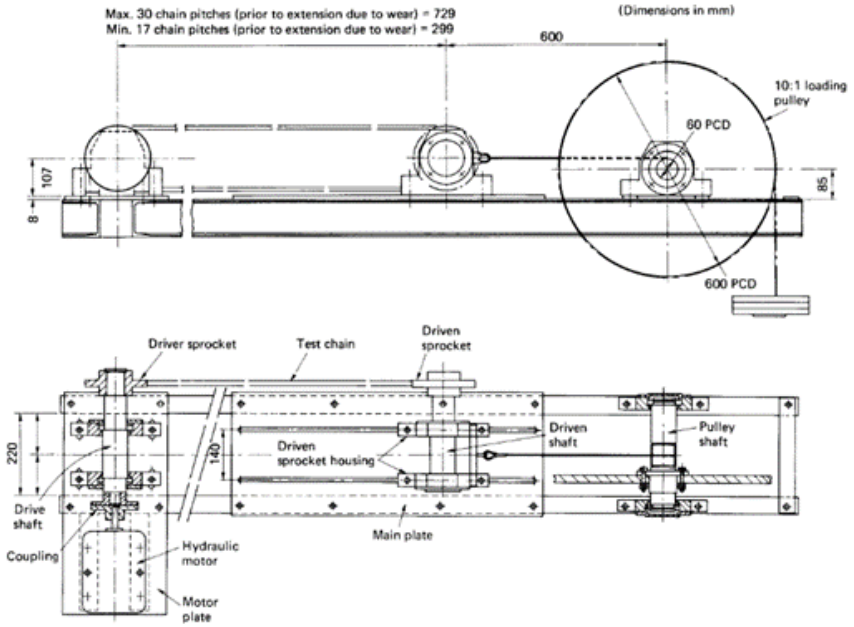

Figure 2.23: Four-square chain wear rig by Hollingworth [37].

To tension the chain spans against one another, the driven shaft was forced away from the driving shaft. The driven shaft was mounted on a translational platform and a mass-pulley system was attached, inducing load in each chain span equal to approximately half the tension in the cable.

Since the centre distance was not fixed, the tested configurations had to ensure that the movement of the chain around the sprockets did not introduce transient dynamics. The test apparatus was limited to equivalent driving and driven sprockets (1:1 gear ratio) with an even number of teeth to achieve this.

The motor was relatively low power since it needed to overcome friction power only. Wear was determined by removing the test chain and accurately measuring its mass over time to estimate the material lost to wear.

Linear actuated rig for accelerated wear (Pyper, 2008 [65], Burgess et al, 2014 [9])

Pyper developed an accelerated wear test apparatus with non-rotating actuation in their thesis [65], with design published in a later paper [9]. The design, illustrated in Figure 2.24, tensioned a short chain strand between two cantilevered leaf springs and induced articulations with a pneumatic linear actuator.

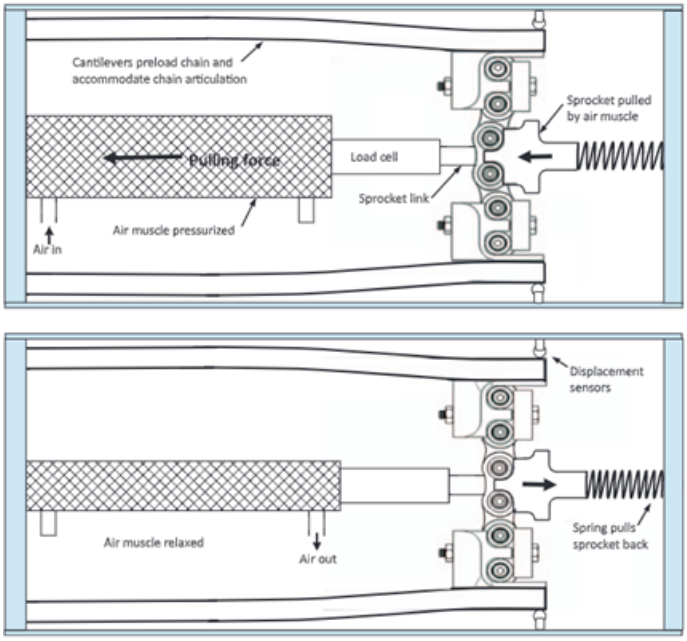

Figure 2.24: Schematic of linear actuated wear test apparatus [9].

The pneumatic air muscle operated at high frequencies, applying a pulling force on a chain link to induce articulation in four pin-bush and bush-roller interfaces. The air muscle acted against a tension spring which returned the link to its original position during relaxation.

Measurement of wear in the test piece was determined in-situ by measuring displacement of the cantilevered leaf spring over time, measured with high accuracy linear displacement transducers (with quoted accuracy of 0.06 μm). The elongation of the chain strand was recorded at a frequency of up to 4000 samples per second.

New four-square rig and chain joint tribometer for wear characterisation (Sappok & Sauer, 2015 [70], Becker et al., 2019 [3])

Researchers at the Institute of Machine Elements, Gears & Transmissions at the University of Kaiserslautern, Germany have developed significant capability in experimental determination of wear in automotive timing chains in recent years. One area of development was in determination of wear by examining the roundness of worn components after periods of continuous running, and the development of a new four-square style experimental test rig by Sappok & Sauer [70].

The four-square test rig followed the design intention of Ross and Marshek's apparatus [67, 68]. A new tensioning clutch was designed for loading the two chains against one another, and torque was measured with strain gauges on the bearing support shaft, seen in Figure 2.25. The design also allowed for varying centre distance during operation by up to 2 mm to counter elongation in the test chains due to temperature and wear, and maintain tension during tests.

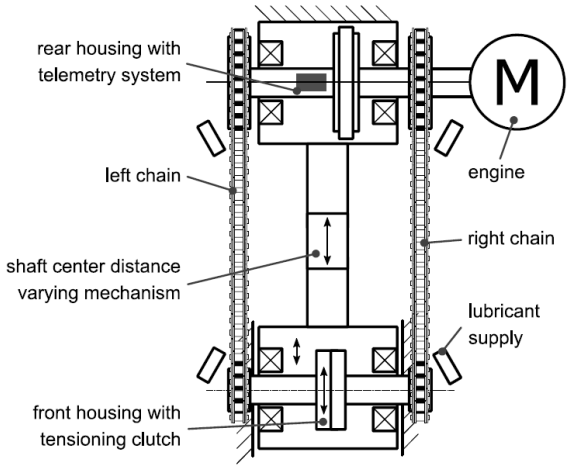

Figure 2.25: Test schematic of new four-square test rig [3].

Becker et al. [3] also presented a novel design for a chain joint tribometer test rig. This was designed to test an individual link in articulation by driving a controlled articulation of a bush roller chain without a sprocket. The dynamic loading was motivated by results from multibody simulations of a chain link around a transmission path. With the test apparatus illustrated in Figure 2.26, both wear and frictional effects in the link were determined.

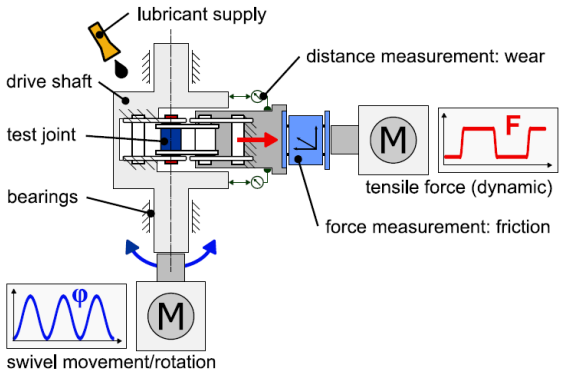

Figure 2.26: Test schematic of chain joint tribometer test rig [3].

A normal force equivalent to the span tension was applied by a linear actuator between the chain links, and a rotationally reciprocating shaft induced articulation. Over a large number of cycles, the wear of the link surfaces was determined in-situ by linear measurement of travel in the actuator. Further force and moment measurement data was collected to determine frictional effects, discussed in Section 2.3.2.

The wear measured on the single link in-situ on the chain joint tribometer were compared with results from a four-square test rig. While the two back-to-back chains on the four-square test rig were almost identical, more wear was seen on the link tested on the chain joint tribometer with

nominally similar conditions. The difference was attributed to the differing contact conditions, highlighted as area for further investigation.

Summary of experimental wear apparatus

Experimental apparatus used to determine wear in chain transmission is quite varied. Many designs were influenced by the inherent low wear rate of bush-roller chains, and the need for long or accelerated testing. The dynamometer design used in Test Stand I by Peekan and Coenen [64] is unique among those summarised since it is the only example of a full chain loop which does not recirculate power and long tests become prohibitively expensive.

Measurement of wear may be done in situ on the test rig by accurately determining the elongation of a chain sample [65, 9, 3], though in many cases requires breaks in testing to measure elongation [64], loss of mass with a well adjusted balance [37], or measurement of roundness to determine lost material [70]. The simplest measurement used in the literature is cycle counters of test-chains which were run to failure [67], though this gives very limited insight into the wear characteristics over time of particular test specimens - only an average lifetime wear rate.

2.3.2 Experimental assessment of coefficient of sliding friction

The coefficient of sliding friction is the ratio of frictional force to normal force in relative movement between materials. It is a key parameter in the determination of frictional forces in analytical models discussed in Section 2.2.3. Several different experimental methods of inferring friction coefficient in chain links are seen in literature.

Chain pin on plate (Kidd, 2000 [42])

In their thesis, Kidd described several tests used to evaluate performance in bicycle chains. The simplest was a pin-on-plate method of determination of friction coefficient by application of a standard tribological test to the specific case of a sample bush roller chain.

Kidd's pin on plate test is illustrated in Figure 2.27. The test involved forcing a stationary pin against a plate which is on a reciprocating carriage, inducing pure sliding between the two materials. A pin from a deconstructed chain joint was used and a plate made from material closely matching the chain bushing. The normal force between pin and plate was controlled by choice of masses, and the friction force was measured by a load cell. The coefficient of friction was defined by the ratio between friction force and normal force, Equation 2.27.

$$\mu = \frac{F}{N} \tag{2.27}$$

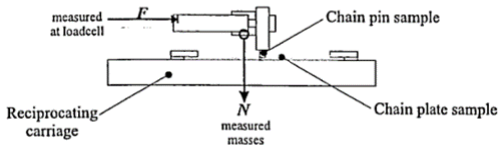

Figure 2.27: Pin-on-plate test apparatus used by Kidd [42].

Kidd tested with a number of different lubricants and recorded friction coefficients in the range of 0.1 - 0.6.

Pendulum test for single chain link (Kidd, 2000 [42])

Secondary to the pin on plate method, Kidd also evaluated friction coefficient in chain links by testing an assembled chain link as the pivot point for a decaying pendulum. The pendulum, illustrated in Figure 2.28, was initially displaced and its time-dependent displacement during its decay was recorded via a Linear Variable Differential Transformer (LDVT).

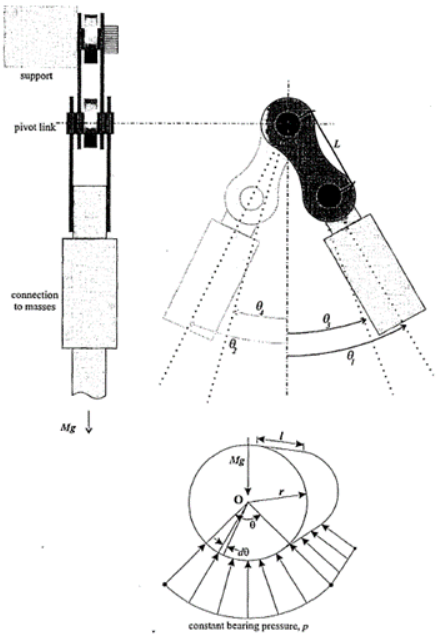

Figure 2.28: Test schematic of pendulum rig from Kidd [42].

The decay of the pendulum was recorded with displacement data captured by the LDVT. Kidd noted the effect of both exponential decay from viscous effects (Figure 2.29a) and linear decay from Coulombic friction (Figure 2.29b).

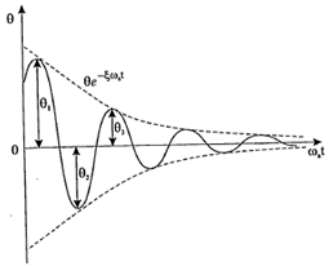

(a) Exponential decay from viscous drag.

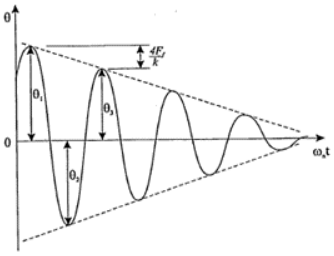

(b) Linear decay from Coulombic friction.

Figure 2.29: Distinction between decay types in pendulum tests [42].

Kidd proposed evaluation of friction friction, μ by three methods, shown in Equation 2.28.

$$\mu\left(\frac{\pi r}{L}\right) = \begin{cases} \frac{\cos\theta_3 - \cos\theta_1}{\theta_1 + \theta_3} & Energy \\ \frac{1}{4}\ln\frac{\theta_1}{\theta_3}\left(\theta_1 + \theta_3\right) & Viscous \\ \frac{1}{2}\left(\theta_1 - \theta_3\right) & Coulomb \end{cases} \tag{2.28}$$

In captured data the change in displacement angle was sufficiently small that all results agreed closely (within 2%); no further comment was made on the role of different sources of friction.

Friction coefficient was calculated for different scenarios (22 N / 44 N ; new / worn ; dry / lubricated ; with / without angular displacement), with inferred values between 0.001-0.016. The results suggested lower friction coefficient than when tested with the pin-on-plate method. Kidd hypothesised that the chain link was predominantly rocking and there was not significant sliding between inner surfaces of the chain link. Hence, a coefficient of rolling friction, not sliding friction, dominated the decay characteristics.

High accuracy single link pendulum test (Wragge-Morley et al., 2018 [88])

A new pendulum test was developed by Wragge-Morley et al. following the same basis as in previous literature but with renewed focus on minimising and quantifying measurement uncertainty of the inferred friction coefficient. A schematic for their test apparatus is shown in Figure 2.30. A Doppler laser vibrometer was used to measure angular velocity of the decaying pendulum without need to mount equipment to the pendulum. An aerodynamic model was used to compensate losses due to air resistance.

The recorded decay profiles, illustrated in Figure 2.31, demonstrated two different frictional regimes: during large oscillations there was sliding between chain components; during small oscillations the chain was rocking only and friction is reduced, shown by the long decay time in this second pe-

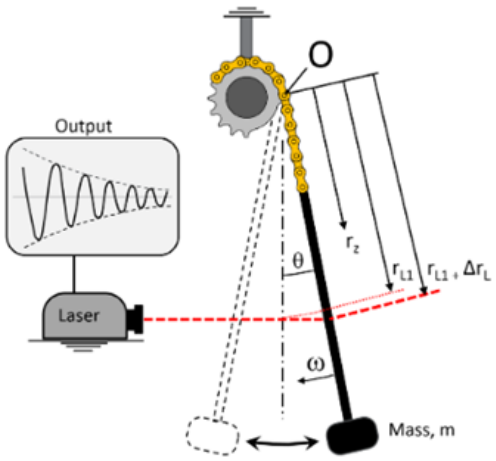

Figure 2.30: Test schematic of pendulum rig from Wragge Morley et al. [88].

riod. By making this distinction, coefficient of sliding friction and coefficient of rolling friction were determined from the same test.

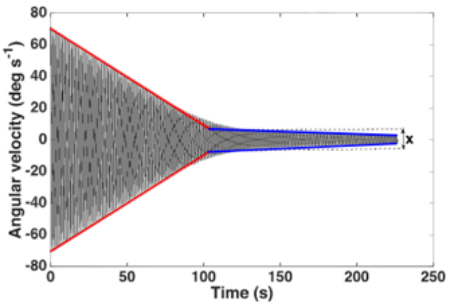

Figure 2.31: Recorded data of decaying angular velocity of pendulum with sliding (red) and rocking (blue) phases [88].

The coefficient of sliding friction was calculated as in Equation 2.29

$$\mu_p = \frac{X}{\sqrt{1-X^2}} \tag{2.29}$$

Where parameter X is defined in Equation 2.30.

$$X = \frac{\Delta T - W_{Aero}\Big|_{t_0}^{t_1}}{r_{bi}\alpha_m} \tag{2.30}$$

Wragge-Morley et al., distinguished between the sliding and rocking phase of decay to infer the correct coefficient for the sprocket size. Coefficient of sliding friction in the quoted results was measured as 0.1066-0.1090 in repeat tests.

Chain joint tribometer for friction characterisation (Becker et al., 2019 [3], Meffert et al., 2021 [57])

Test apparatus developed at the Institute of Machine Elements, Gears & Transmissions at the University of Kaiserslautern, Germany was introduced in the context of its wear characterisation capability in Section 2.3.1. It was simultaneously capable of measuring frictional effects and inferring coefficient of friction in a single chain link.

As seen in Figure 2.26, frictional moment in the link under test was measured with a torque transducer and normal force (link tension) measured with a load cell. The coefficient of friction was calculated from the ratio of normal and frictional force within the chain link, Equation 2.31.

$$\mu = \frac{T}{F_{x,\ sensor}\,(l + r_{pin})} \tag{2.31}$$

In tests, amplitude and frequency of articulation was a controlled input and data recorded at high sample rate. In a test with triangular movement, data is captured shown in Figure 2.32.

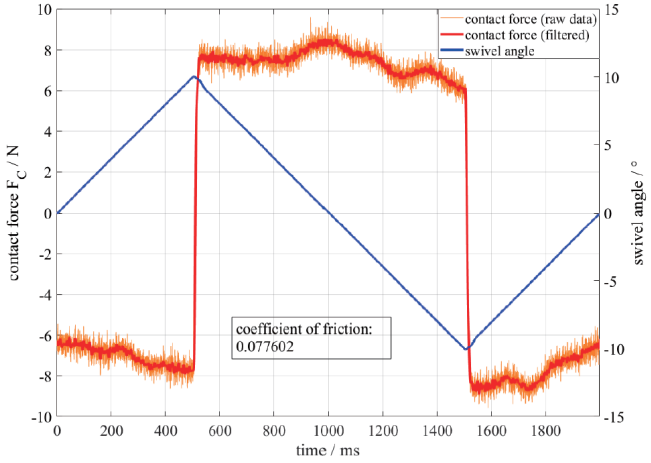

Figure 2.32: Experimental results of measured contact force and angle during articulation [57].

From time-averaged forces over a full articulation, coefficient of friction was calculated for a number of samples in this study. Motorcycle chains were tested (15.875mm pitch) and friction coefficients shown to be in range 0.04-0.08. Measurement uncertainty was not examined in detail, but was quite significant from presented error bars in data. In determination of friction coefficient, standard deviation of collected data was approximately 10-50% of the average value.

Summary of friction coefficient test rigs

In experimental determination of friction coefficient, all test apparatus presented from the literature were based on the principle of applying a normal force and inferring frictional force between

sliding materials. Novel test designs were based on articulation of chain links [42, 88, 57], where forces, contact surfaces and hence friction in the test chain were representative of those in application. Measurement of frictional forces was inferred from either decay characteristics, in the case of pendulum tests [42, 88], or from torque measurement [57]. A weakness of measuring friction by decay was that rotational speeds were not constant and not typical of chain articulations in their intended application. Furthermore, through both rocking and sliding of the chain joint different friction effects were induced during the experiment, necessitating the separation of these effects [88].

2.3.3 System-level friction testing

System level testing is carried out by inferring power losses in a drive which is a complete looped series of chain links connecting a driving sprocket to a driven sprocket (with or without auxiliary sprockets). Loading conditions may still be simplified in tests of complete transmission, and various measurement techniques were used to infer the mechanical losses.

A popular style of test rig follows a dynamometer design, where a transmission is driven continuously against a brake and independent measurements of input and output power were compared to infer the power lost in the transmission. These have appeared regularly in literature with some subtle differences in implementation.

Dynamometer for bicycle derailleur transmission (Spicer et al., 2000, 2001 [74, 75])

Spicer et al. developed a dual measurement dynamometer for testing bicycle chains in transmission configurations typical of road bicycles. A schematic of the developed test apparatus is illustrated in Figure 2.33. The driving and brake machines were electric motors with variable rotational rate and an electromagnetic brake respectively. Rotary torque sensors measured input and output torque, and the test setup also included infrared cameras to examine the effect of friction on temperature in chain links.

The test result was expressed as power efficiency, calculated by Equation 2.32 from the measurement variables recorded by torque sensors.

$$\%Efficiency = \frac{\tau_2 \omega_2}{\tau_1 \omega_1} \times 100 \tag{2.32}$$

With this test equipment, test results were published from a bicycle chain in a transmission with multi-speed cassette and derailleur system with auxiliary sprockets. Test parameters were varied in parameters below:

1. Gear configuration (ratio).

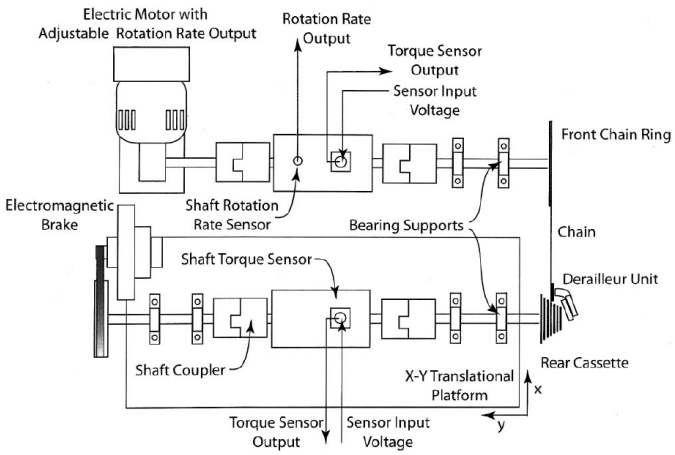

Figure 2.33: Schematic of test apparatus for bicycle chain dynamometer [75].

2. Input power.
3. Lubrication types.
4. Planar offset (chainline).

Published results showed measured efficiency in the range 81.0 - 98.6%. Higher efficiency was measured for larger gear ratio, increasing power (for same speed), and decreasing speed (for same power). There was also some difference in efficiency between different lubrication states.

Results of infrared measurements showed components increased in temperature with increasing input power and the chain pin is the source of most heat. However, these results did not align with the expected losses based on inferred efficiency of these tests.

No comment was made of the uncertainty of the torque and speed measurement, and neither was there analysis of the parasitic influence of the support bearings on measurement.

Dynamometer for bicycle derailleur transmission (Kidd, 2000 [42])

Following the pin-on-plate and pendulum tests discussed in Section 2.3.2, a dynamometer for bicycle chains and sprockets was the final test apparatus developed by Kidd in their thesis, though a version seemingly existed since 1995 as is mentioned in a previous publication [43]. A schematic of the apparatus is illustrated in Figure 2.34. The test transmission was driven by a 0.55 kW motor with a step down belt arrangement (8:1.75). Varied with a controller, speeds up to 350 RPM were tested and measured with a hall effect sensor mounted to the pulley wheel on the driving shaft.

Torque was measured with non-contacting torque sensors which were developed by Kidd [42]. Mounted directly to the input and output shaft respectively, the strain gauges were situated between

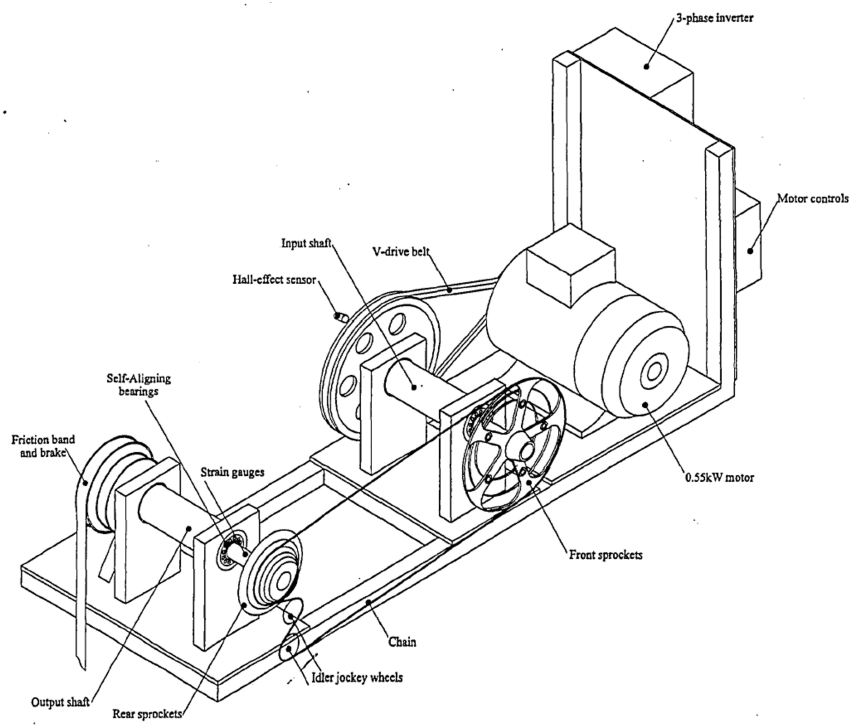

Figure 2.34: Schematic of test apparatus developed by Kidd [42].

the self-aligning support bearings and the transmission-under-test, neglecting parasitic friction from bearings in measurements.

Performance of the chain on the rig was expressed as output power P_o as a fraction of input power P_i, expressed in Equation 2.33. Output torque, T_o, and input torque, T_i, is used in this calculation, and the sprocket teeth ratio replaces the speed measurements since speed is measured only on input.

$$\frac{P_o}{P_i} = \frac{T_o \alpha_o}{T_i \alpha_i} = \frac{T_o}{T_i} \frac{N_1}{N_2} \tag{2.33}$$

Kidd conducted tests to determine efficiency for varying parameters:

1. Gear configuration (ratio).
2. Chain quality.
3. Lubricant.
4. Power, speed, time.
5. Presence of derailleur.
6. Planar alignment (chain-line).

Measured chain efficiency varied between 51% and 97% across the changes to the above parameters. Kidd presented results which demonstrate improvement in chain efficiency from increased power, higher wear state and better lubrication. Increased speed and sprocket ratio were shown to decrease efficiency. Chain efficiency was shown to be directly proportional to chain tension, and

presence of rear derailleur in the slack span reduces the efficiency by between 1.5 and 5 % depending on power input. Reduced efficiency was also seen for increased misalignment (2% reduction at 3.5 degree chain-line). Uncertainty of the efficiency measurand or torque measurements was not assessed.

Dynamometer for bicycle derailleurs and hub gears (Kyle & Berto, 2001 [45])

Kyle and Berto developed a cradle dynamometer test apparatus for testing derailleur and hub gear transmissions from bicycles pictured in Figure 2.35. A variable speed DC motor was mounted on a gimbal, and a load cell measured the linear force necessary to prevent the motor rotating from which the input torque was inferred. A bicycle rear hub was linked to a ergometer wheel with a secondary chain drive which was mechanically braked with a calibrated weight-pulley system.

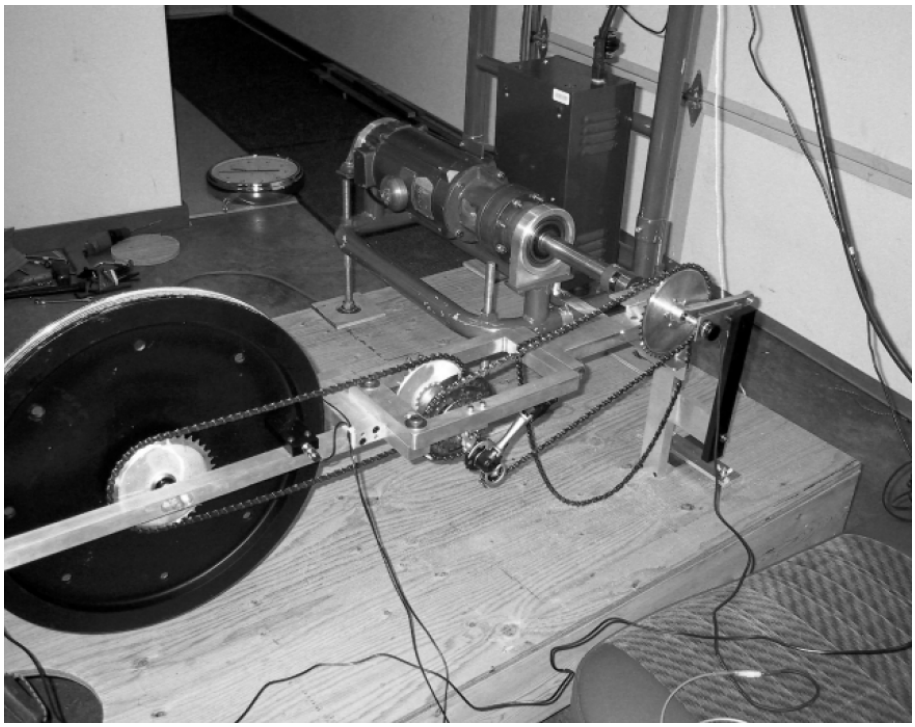

Figure 2.35: Photograph of dynamometer by Kyle and Berto [45].

Since the apparatus was designed with a bicycle rear hub, several different multi-speed transmission systems could be tested. In the published study, efficiency was determined for two Browning automatic transmissions, a Shimano derailleur type transmission, and planetary gear rear hub transmissions by Sachs, Sturmey Archer, Shimano, and Rohloff. In each instance, three loads were tested at fixed speed (75 RPM input), equivalent to 80W, 150W, and 200W input.

To isolate the measurement of transmission efficiency, losses in the secondary ergometer drive nedded to be compensated. Kyle and Berto comment on this, and conducted tests of this transmis-

sion in isolation to determine an estimate for compensation. The ergometer drive was rotated at 75 RPM only, while in testing the ergometer rotational speed will change depending on the engaged gear ratio. The authors to not apply this flawed compensation, and instead results are quoted with the caveat that the absolute values would change by 2% - 2.5%, and that presented data is valid for inferring comparative results between transmission configurations at equivalent test points.

Dynamometer for industrial chain (Lodge, 2002 [47])

In their thesis, Lodge further developed a dual measurement dynamometer for testing industrial and bicycle chains in two-sprocket configurations to validate published models of transmission efficiency [48]. The dynamometer test rig was constructed by project students initially. A schematic of the test apparatus is shown in Figure 2.36. The test rig featured two electric machines to act as driver motor and brake with rated capability of 35 Nm and 360 RPM. Both machines were controlled with variable frequency drives. Torque and speed was measured by torque transducers at input and output to the system under test.

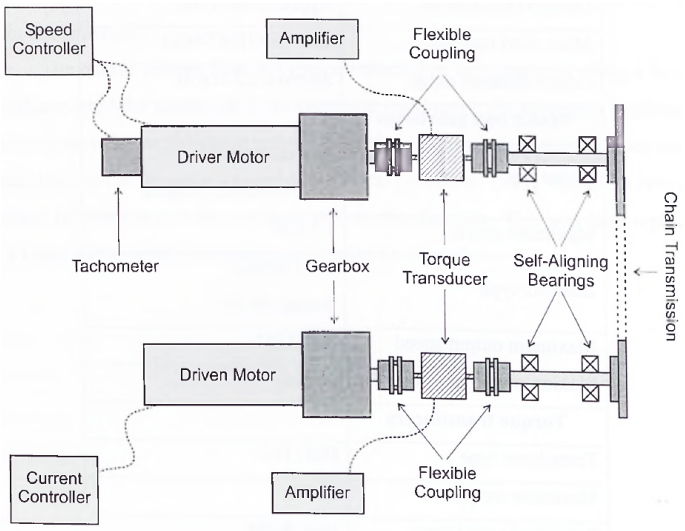

Figure 2.36: Schematic of test apparatus used by Lodge [47].

The torque and speed data for each shaft was recorded on a multi-meter, and efficiency was calculated for chain and low friction bearings. The parasitic influence of the bearings was accounted for by running tests with no transmission to determine the speed-dependent frictional torque as measured by the transducers. Speeds between 50 RPM and 360 RPM were tested, with no axial or radial load applied (only self-weight of shafts). The load-dependent losses were expected to be small since the bearings were oversized for their application.

Results with a number of variable test parameters were published:

1. Output torque.

2. Gear configuration (ratio and diameter).
3. Chain type.
4. Rotational speed.

Efficiency was shown to increase for increased torque due to the fixed contribution of the tension in the bottom span from the test chain's self-weight. There was very little dependence of efficiency on rotational speed. Larger gear sizes had measurably higher efficiency.

The uncertainty of torque measurements in the transducers was quoted as +/- 0.25%.

Full Tension Tester (FTT) for lubrication testing (Friction Facts, 2012 [24])

A Full Tension Tester (FTT) was an apparatus design developed by Jason Smith of 'Friction Facts', a company which tested chain drives to determine the performance of bicycle chain lubricants to inform consumers. The principles of the rig were identical to the novel four-square solution for wear testing developed by Hollingworth [37], discussed in Section 2.3.1. Its design is now widely used in bicycle drive component industries.

The experimental apparatus, shown in Figure 2.37, featured a small motor driving a two sprocket transmission. The driven sprocket's shaft was housed in a hinged block which was forced away from the driving sprocket by a lever arm with hung masses, thus inducing load in the spans. The induced load was designed to induce equivalent losses to a real-world case with torque-induced tension.

The torque required to drive the transmission at constant speed overcame the friction in the system, which was dominated by the articulation of the chain in the tensioned spans. An appropriately rated torque transducer between the motor and driving sprocket measures input torque and speed.

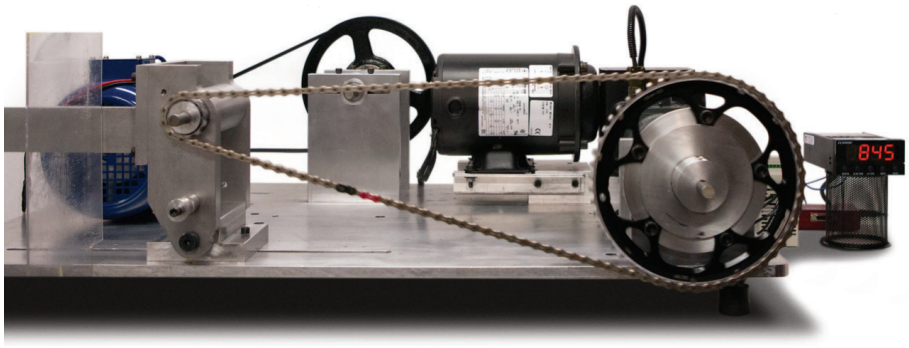

Figure 2.37: Photograph of test hardware for the Full Tension Tester by Friction Facts [23].

Full Tension Test rigs have since been adopted by a number of cycling equipment test houses in recent years, including lubricant and hardware manufacturers 'MucOff' and 'Ceramic Speed' who now own the 'Friction Facts' brand.

Dual-sprocket Pendulum Test (Wragge-Morley et al., 2018 [88])

In addition to the developed single link pendulum tests by Wragge-Morley et al., a dual-sprocket pendulum test was introduced where the pendulum drives articulation in a full drive connecting two sprockets, illustrated in Figure 2.38.

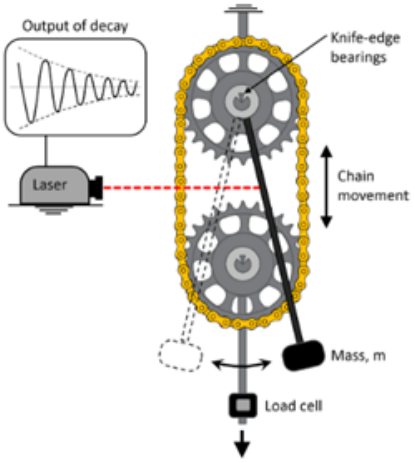

Figure 2.38: Schematic of dual-sprocket Pendulum Test proposed by Wragg Morley et al. [88].

The friction in the whole system could be assessed by the decay characteristics of the pendulum, with the spans loaded independently from the mass on the pendulum. No results were published, though the benefit of testing a complete transmission was highlighted: test subjects can be expanded to belts, or other chain types such as inverted tooth chains.

Though a complete drive is tested in this configuration, it is not tested with typical loading. The transmission is atypical is several ways: it was loaded evenly in both spans, orientation was vertical, and rotational speeds were very low and oscillating between positive and negative.

Inertia decay test rig (Kozlov et al., 2018 [44])

A test rig proposed and developed by Kozlov et al. measured the decay characteristics of a full transmission by its retardation from a set speed point. In operation, a transmission was driven by an electric motor at a target speed and input torque then reduced instantaneously to zero. The retardation of the system was measured by an encoder recording the angular acceleration, and

retardation due to friction in the chain transmission isolated from other sources. A schematic is shown in Figure 2.39.

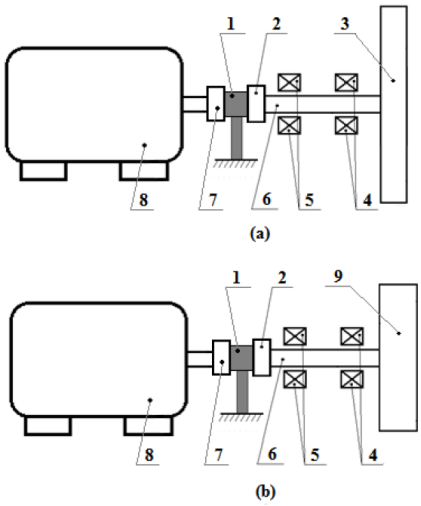

Figure 2.39: Schematic of test apparatus used by Kozlov et al [44].

Two experimental configurations, (a) and (b), were used to run tests with different inertial masses attached to the driving shaft, labelled 3 and 9 in Figure 2.39. These were of equivalent mass to maintain parasitic friction between cases, though different rotational inertia. The effect of the change in inertia on the acceleration behaviour allowed the effect of drive friction to be determined.

Initial tests were also conducted with no transmission linked to determine the parasitic influence on retardation, M_{BTB}.

$$M_{BTB} = J_{\Delta}\frac{\varepsilon_1\varepsilon_2}{\varepsilon_2 - \varepsilon_1} \tag{2.34}$$

Where ε_1 and ε_2 were average angular acceleration for tests with rotary body of inertia J_1 and J_2 respectively, where $J_{\Delta} = J_1 - J_2$.

With chain drive attached, a new frictional moment was described for this system, M_{BTBCT}.

$$M_{BTBCT} = J_{\Delta}\frac{\varepsilon_3\varepsilon_4}{\varepsilon_4 - \varepsilon_3} \tag{2.35}$$

Where ε_3 and ε_4 were measured retardation for two further tests with rotary bodies as described above. The frictional influence of the transmission was inferred from the difference between the two results (i.e. the full system compensated for the parasitic influence).

$$M_{BCT} = M_{BTBCT} - M_{BTB} \tag{2.36}$$

The transmission ran with constant direction of both angular velocity (positive throughout) and angular acceleration (negative throughout). The measurement of angular acceleration was made with a rotary encoder. The motor required no control, and was specified based on its rated speed.

For the parasitic compensation to be valid, the chain drive must have had negligible pretension since this would introduce new radial loads and increase parasitic losses. As a result, this method was quite restricted in the range of transmission loading conditions which can be examined.

Low-torque dynamometer (Zhang and Tak, 2020 [91])

Zhang and Tak developed a small dual-measurement dynamometer to validate a new model of transmission efficiency, detailed in Section 2.2.3. Their design featured a driving electric motor (1700 rpm, 13 Nm rated) and a friction brake to regulate speed and torque on the driven side of test transmission, illustrated in Figure 2.40. Two torque transducers measured input and output speed and torque to the test system including support bearings.

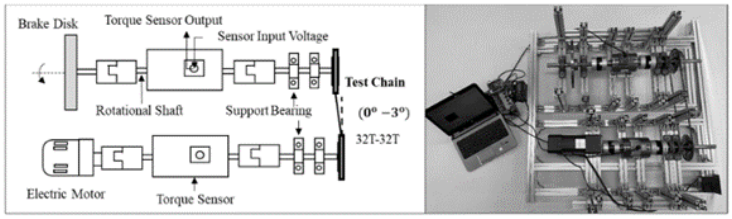

Figure 2.40: Schematic and photograph of test apparatus used by Zhang and Tak [91].

The parasitic influence of the support bearings was evaluated by running tests with no transmission to bearing frictional torque at various speeds (50 RPM - 280 RPM). No comment was made on the effect of radial load on parasitic loss, though the low torques result in small span forces and shaft weight might be expected to dominate the radial load.

Transmission efficiency was determined for a 1:1 drive (32T) with test envelopes covering changing parameters as below:

1. Torque (5 Nm - 9 Nm).
2. Speed (40 RPM - 80 RPM).
3. Angular offset (0 degrees - 3 degrees).
4. Distance between sprockets (0.45 m - 0.55 m).

Experimental results were in the range 86.3% - 93.1%, with increased efficiency demonstrated for higher torque, lower angular speed, lesser angular offset and reduction in centre distance. The measurement uncertainty of the torque transducer was quoted (+/- 0.3%), though no comment made on the combined uncertainty of the efficiency measurement.

Summary of system level testing

Across system level testing apparatus, various configurations have been summarised. By definition, all systems tested were continuous chain loop between at least two sprockets. A dual-sprocket design was most common, while some designs allow for auxiliary sprockets to tension the slack span [75, 42, 45] or even testing alternative multi-speed transmission such as planetary hub gears [4]. In some cases the configuration was limited by the action of the test rig, with even numbers of sprocket teeth [24] and equivalent driving and driven sprocket teeth for matched spans [88].

Transmissions see quite different loading regimes across the apparatus discussed. In decay rigs the system was decelerating with no input to the system during test [88, 44]. In contrast, steady state tests were run in a continuous direction [75, 42, 45, 47, 24, 91]. Tension in the chain spans came from various sources: high torque against braking load, or tension induced in spans from hanging masses.

The measured variable across system-level test apparatus was either torque (in steady-state tests) or decay characteristics. Most commonly, torque was measured at input and output, and measurements compared to understand the energy consumed in the transmission-under-test [75, 42, 47, 91]. Alternatively, a single torque measurement was made where only frictional energy is measured [24], or input torque measured against a calibrated braking torque[45].

2.3.4 Vibration characterisation in chain drives

Several experimental rigs were developed in the literature to specifically investigate the effect of dynamic chain behaviours on system vibration. The dynamic response of chain transmissions come from a combination of transverse and longitudinal accelerations which may be excited by either kinematic effects (physical displacement from polygonal action) or forcing effects (acceleration from roller impact) at constant running speed. Accelerations of driving machines, such as firing pulses in internal combustion engines, can interact with chain dynamics and so practical testing is of great interest to appreciate the performance of a whole-system.

Four-square rig design to determine vibration at constant speed and load (Turnbull, 1974 [80])

In their thesis, Turnbull developed a test rig to determine the vibration induced in a chain drive during constant speed and load. It is later used and referenced in a study by Fawcett and Nicol [22]. Their experimental rig, illustrated in Figure 2.41, aimed to test chain transmissions at high span loads and a range of speeds.

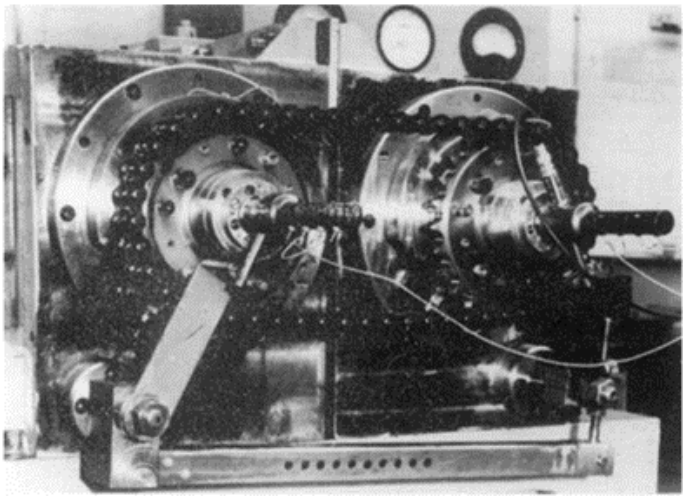

Figure 2.41: Photograph of constant velocity high tension vibration test apparatus [22].

The vibration test rig decoupled tension from driving torque based on a four-square method. The dual-sprocket chain drive transmission was connected to a secondary gear train transmission, forming a power circulating arrangement. The connection was via torsion rods on both driving and driven sprockets. The chain was loaded to its rated tension (5000 N) by disconnecting the gear train and applying torsional pre-load to the torsion rods. The gear train was reconnected and a variable speed motor drove the rig at given speed, overcoming the frictional torque across the two transmission systems.

The angular acceleration of both sprockets was measured using piezo-electric accelerometers mounted 180° apart, arranged to measure tangential acceleration of sprocket. The two results were summed to remove effects due to transverse vibration of shaft centres. Results were collected as acceleration/time trace data and as frequency spectra of time domain signals.

Rotational speeds up to 1100 RPM were tested with up to 5000 N chain tension. Centre distance was also varied to vary the span length between two integer number of links. Experimental results demonstrated:

1. There were peaks in time domain data as a roller was removed from the span by the driving sprocket.
2. There was some evidence of impact when a roller was removed from the unloaded span at low loads (< 500 N).
3. Transverse vibrations were observed at low rotational speeds when tooth frequency aligned with its fundamental frequency (100-140 RPM, varying with chain tension). However, this had little effect on the measured accelerations.

4. There was resonance of longitudinal spring action of the span observed at around 440 RPM, where sprockets vibrated in antiphase.
5. Acceleration at impact dominated at higher speed.

Measuring vibration with orthogonal load cells (Conwell and Johnson, 1995, 1996 [14, 15])

Conwell and Johnson designed a dynamometer style test rig to measure the effect of regular impact forces from chain pick up at the sprocket [14, 15]. In their design, a driving sprocket was linked to a driven sprocket with an auxiliary sprocket acting to tension the transmission with a defined pre-load, illustrated in Figure 2.42.

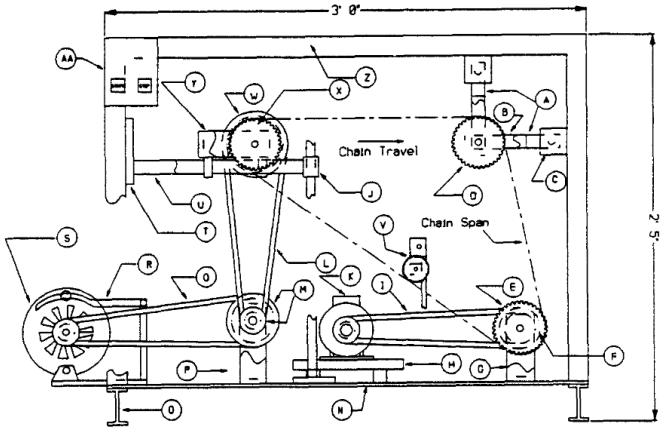

Figure 2.42: Dynamometer test rig by Conwell and Johnson with vibration measurement of auxiliary sprocket [15].

The force in the chain was measured on its path around the transmission by a strain gauge mounted on a single link. In this data, peaks in tension at points of rapid changes in link tension were seen and attributed to dynamic impact forces.

Further measurements were made by load cells affixed to the auxiliary sprocket support, measuring forcing in orthogonal directions parallel to the plane of the transmission. The study concluded the following points:

1. Tension in link increased rapidly as the link exits driven sprocket, and decreased rapidly when entering the driven sprocket.
2. For a chain travelling horizontally, the vertical component of impact force was much larger than the horizontal component.

Link tension during continuous operation (Stephenson et al., 2000 [76])

Apparatus designed by Stephenson et al. was built to measure forces in a chain link during typical operating conditions of an internal combustion engine timing chain. The force was measured with a strain gauge mounted on an individual link which wirelessly transmitted data. This was achieved by running service chains in parallel to the test timing chain, which housed a telemetry unit in close proximity to the instrumented link on the timing chain. Data from the telemetry unit was transmitted to a fixed receiver. The configuration of timing chain and service chains is illustrated in Figure 2.43.

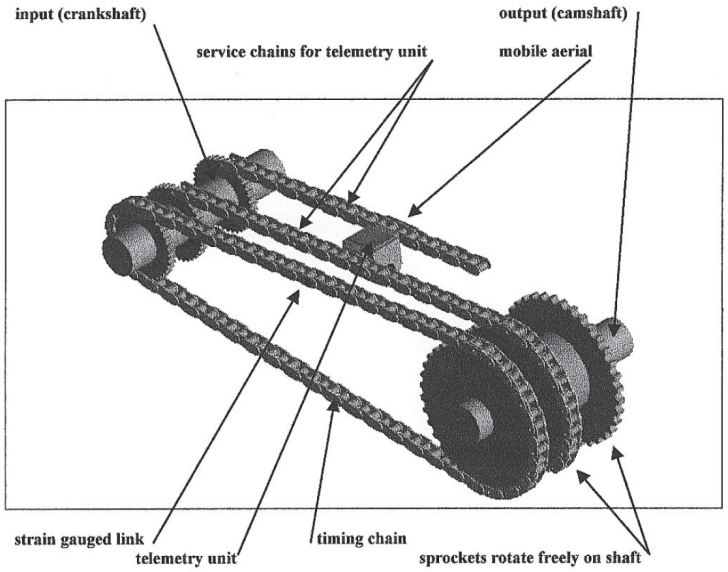

Figure 2.43: Arrangement for timing chain under test and two further service chains with mounting for telemetry unit [76]

Alongside strain in the instrumented link, Stephenson's rig also determines link position, inferred from a shaft encoder on the driven shaft, torque and torsional vibration. Torsional vibration is measured with diametrically opposing accelerometers in a similar arrangement to that employed by Turnbull, Fawcett and Nicol [80, 22].

Results for the dynamic changes in link tension around the tested drive are illustrated in Figure 2.44. Pronounced variations in both the torque and tension are observed at a frequency equal to the tooth-roller contact frequency of the transmission.

Static chain span vibration rig (Alexander et al., 2017 [1])

An experimental test rig was developed for an undergraduate group project at the University of Bristol by Alexander et al. [1] which examined the resonant response of static loaded chain spans excited with transverse accelerations. The rig apparatus, pictured in Figure 2.45, featured a chain

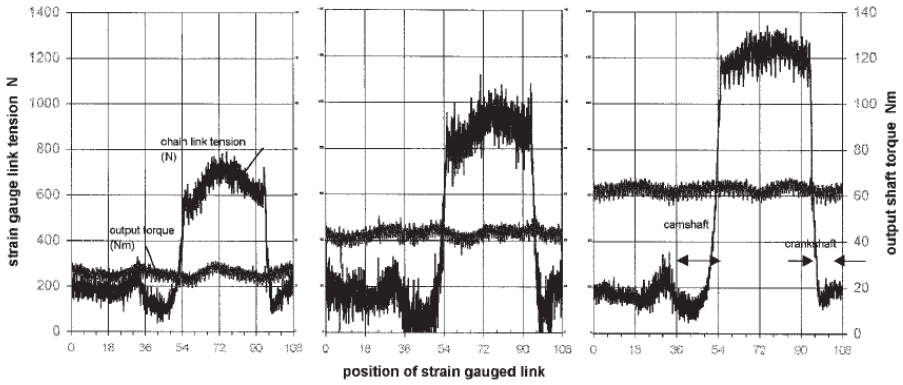

Figure 2.44: Chain tension and output torque for different torque input at 900 RPM [76]

sample anchored at one end and tensioned with hanging weights over an axially fixed sprocket. With tension induced, the chain span was excited with transverse displacement at fixed frequency, intended to mimic the transverse effect of polygonal action. An industrial shaker with power oscillator was used to achieve this.

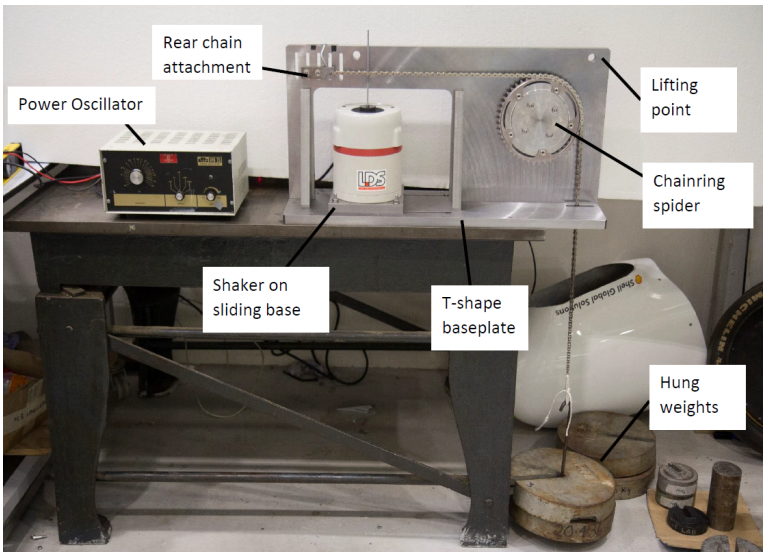

Figure 2.45: Configuration of test rig for static vibration of chain spans [1]

The experimental apparatus was used to determine the magnitude and frequency of resonant points of the chain span, and its dependence on tension in the span. Mode 1 resonance was observed as is shown in long exposure photograph in Figure 2.46. The investigation also observed resonant frequencies on a dynamometer test rig.

Summary of vibration test rigs

Literature addressing experimental assessment of vibration in chain strands shows similar rig arrangements to those used in testing other performance phenomena such as wear and efficiency.

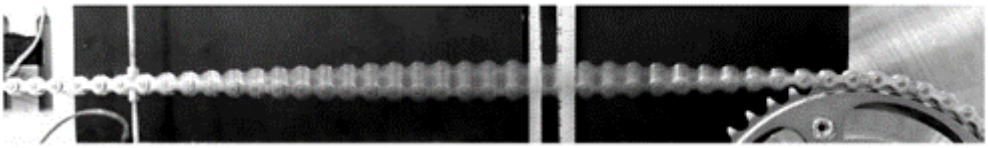

Figure 2.46: Long exposure photograph of mode 1 transverse resonance of chain span [1].

The determination of vibration in test rigs was done by both observation, using high-speed camera technologies to capture high frequency dynamics [1], and measurement [80, 22, 14, 15, 76]. Various parameters were measured, including strain gauges mounted on a chain link [14, 15, 76] and load cells on shaft supports [14, 15] to measure dynamic effects on chain tension, and accelerometers [80, 76] to measure sprocket angular acceleration.

The influence of polygonal action on sprocket acceleration developed by Turnbull [80] used data recorded as a function of time, and further analysed the frequency spectra to accurately determine the vibrational influences on the measured signal. Similar data was subsequently captured by Stephenson et al. [76] in both link-mounted strain gauges and torque signals.

2.4 Performance of rolling element bearings for use in rotating experimental test rigs

In rotating and oscillating experimental test rigs, support bearings are required to facilitate shaft rotation and hence are a feature of all experimental apparatus for determining chain losses described in Section 2.3. Bearings include a number of rolling elements which induce a frictional moment on the shaft, retarding the direction of rotation. Without compensation of the parasitic energy consumed in the bearings, there is error induced in the measured performance of the transmission-under-test.

In compensating for parasitic influence including bearing losses it can be possible to use empirical data from tests in-situ using the same experimental instrumentation without the transmission-under-test connected, a method employed in several studies introduced previously. A weakness of this method is that only speed-dependent frictional moment is measured. Further means for determining the influence of bearings on experimental measurement of transmission losses were addressed in literature and presented in this section.

2.4.1 Modelling frictional moment

There are several models describing frictional moment in rolling element bearings commonly used in literature and industry. One was developed by Harris [30] as part of a full analysis of rolling element bearing mechanics. The model built on an existing method by Palmgren [63]. More latterly, bearing manufacturer SKF developed a model of frictional moment [71] as a design tool. Both models were derived with a combination of analytical descriptions of frictional drag and empirical data from undocumented testing.

Harris model of bearing friction torque, 1991 [30]

The Harris model was built on previous work by Palmgren [63]. Total frictional moment in a rolling element bearing was described by the sum of three independent sources of friction according to Equation 2.37.

$$M = M_1 + M_v + M_f \tag{2.37}$$

Where M is total frictional moment [Nmm], M_1 is frictional moment due to applied load, M_v is speed dependent moment and M_f is moment due to end-flange friction. Each of these is considered in turn.

Several parameters in the Harris model were dependent on the style of bearing used. Calculations are restated for the most common variety seen in test rigs with predominantly radial loading: deep groove ball bearing, and cylindrical roller bearings.

M_1 - Torque due to applied load

Torque due to applied load was described by Equation 2.38.

$$M_1 = f_1 F_\beta d_m \tag{2.38}$$

Where f_1 is a dimensionless factor dependent on bearing design and relative bearing load, defined in Equation 2.39; F_β is the load variable [N] and changes with magnitude and direction of applied load, defined in Equation 2.41; and d_m is the pitch diameter [mm] of the rolling elements in the bearings.

For cylindrical roller bearings, f_1 was empirically derived where greater values were for higher series bearings. For ball bearings, it was the ratio of static equivalent load F_s [N] and basic load rating C_s [N] with fitting parameters z and y, empirically derived and dependent on ball bearing type. For light series deep groove ball bearings (with 0° nominal contact angle), $z = 0.006 - 0.004$,

$y = 0.55$.

$$f_1 = \begin{cases} z\left(\frac{F_s}{C_s}\right)^y & for\ ball\ bearings \\ 0.0002 - 0.0004 & for\ radial\ cylindrical \end{cases} \tag{2.39}$$

In the literature, an empirically derived range of z values were quoted for ball bearings and f_1 values for cylindrical roller bearings, dependent on whether the modelled bearings were light series or heavy series. An exact definition of what value is most appropriate was not provided, and so some interpretation is required.

Static equivalent load, F_s $[N]$, was a function of radial load F_r $[N]$ and axial load F_a $[N]$, with fitting variables X_s and Y_s, defined in Equation 2.40.

$$F_s = max \begin{bmatrix} X_s F_r + Y_s F_a \\ F_r \end{bmatrix} \tag{2.40}$$

Load variable, F_β $[N]$ is defined as below.

$$F_\beta = max \begin{bmatrix} 0.9 F_a \cot\alpha - 0.1 F_r \\ F_r \end{bmatrix} \tag{2.41}$$

M_v - Viscous Friction Torque

Viscous friction torque was derived from Palmgren and determined empirically. A distinction was made between friction modes either side of a threshold defined by the product of rotational speed and kinematic viscosity of the lubricant in the bearings, again determined empirically. The two regimes come from changing hydrodynamic effects.

$$M_v = \begin{cases} 160 \times 10^{-7} f_0 {d_m}^3 & \nu_0 n < 2000 \\ 10^{-7} f_0 \left(\nu_0 n\right)^{\left(\frac{2}{3}\right)} {d_m}^3 & \nu_0 n \geq 2000 \end{cases} \tag{2.42}$$

Where ν_0 is kinematic viscosity of lubricant $[mm^2 s^{-1}]$ and n is rotational speed $[RPM]$. f_0 is an empirically derived factor and depended on bearing type and type of lubrication, summarised in Table 2.1. As previously, where there was range for f_0 the value was dependent on light or heavy series bearings.

M_f - End-flange friction

End flanges were present in radial cylindrical roller bearings only, since ball bearings were constrained by the spherical contact between ball and race. Frictional moment from end flanges is described by Equation 2.43.

$$M_f = f_f F_a d_m \tag{2.43}$$

Where f_f is a variable based on cylindrical roller bearings type and lubrication, F_a is the axial load $[N]$ on bearing and d_m is the pitch diameter of the rolling elements $[mm]$. Values for f_f for single

Table 2.1: Values of f_0 for typical bearings and lubrication in dynamometer test rig applications [30].

Bearing type	f_0	
	Grease lubricated	**Oil mist lubricated**
Deep groove ball	0.7 – 2	1
Cylindrical roller (with cage)	0.6 – 1	1.5 – 2.8
Cylindrical roller (full complement)	5 – 10	∼

row cylindrical roller bearings were given in Table 2.2. 'Optimum design' is not well defined and this is open to interpretation.

Table 2.2: Values of f_f for cylindrical roller bearings with different lubrication types [30].

Bearing type	f_f	
	Grease lubricated	**Oil lubricated**
With cage, optimum design	0.003	0.002
With cage, other designs	0.009	0.006
Full complement, single row	0.006	0.003

SKF model of frictional moment, 2018 [71]

Bearing manufacturers SKF developed an analytical model with empirically derived parameters. Similar to the Harris model, distinct sources of frictional moment were defined and summed to describe the total frictional moment, Equation 2.44.

$$M = M_{rr} + M_{sl} + M_{seal} + M_{drag} \tag{2.44}$$

Where M is total frictional moment $[Nmm]$, M_{rr} is rolling frictional moment, M_{sl} is sliding frictional moment, M_{seal} is frictional moment of seals, and M_{drag} is frictional moment of drag losses, churning and splashing of lubricant. Each is described in turn below.

M_{rr} - Rolling frictional moment

Rolling frictional moment M_{rr} was described as below.

$$M_{rr} = \Phi_{ish}\Phi_{rs}G_{rr}\left(\nu n\right)^{0.6} \tag{2.45}$$

Where Φ_{ish} is the inlet shear heating reduction factor and described below, dependent on rotational speed, n $[RPM]$, bearing mean diameter, d_m $[mm]$, and operating viscosity of the lubricant, ν

$[mm^2 s^{-1}]$.

$$\Phi_{ish} = \frac{1}{1 + 1.86 \times 10^{-9} (n d_m)^{1.28} \nu^{0.64}} \tag{2.46}$$

Φ_{rs} is the kinematic replenishment/starvation reduction factor is and described below, dependent on replenishment/starvation constant K_{rs} (3×10^{-8} for low level oil bath lubrication, 6×10^{-8} for grease and oil-air lubrication), operating viscosity of lubrication ν $[mm^2 s^{-1}]$, rotational speed n $[RPM]$ bearing bore diameter d $[mm]$, bearing outside diameter D $[mm]$, and bearing type related geometric constant K_z.

$$\Phi_{rs} = \frac{1}{e^{\left[K_{rs} \nu n (d+D) \sqrt{\frac{K_Z}{2(D-d)}}\right]}} \tag{2.47}$$

Rolling frictional variable G_{rr} is dependent on geometric constant R_1 (which changes with bearing type), bearing mean diameter d_m $[mm]$, radial load F_r $[N]$, and exponent fitting parameters, themselves dependent on bearing type seen in Equation 2.48.

$$G_{rr} = \begin{cases} R_1 {d_m}^{1.96} {F_r}^{0.54} & (deep\ groove\ ball\ bearings) \\ R_1 {d_m}^{2.41} {F_r}^{0.31} & (cylindrical\ roller\ bearings) \end{cases} \tag{2.48}$$

Values of R_1 for typical bearings are shown in Table 2.3. The range of values demonstrates the quoted range, though exact values pertaining to specific bearing types are defined in the literature.

Table 2.3: Values of R_1 for bearings typical in dynamometer rig applications [71].

Bearing type	R_1
Deep groove ball bearings	$3.6 \times 10^{-7} - 5.4 \times 10^{-7}$
Cylindrical roller bearings	$1 \times 10^{-6} - 1.63 \times 10^{-6}$

M_{sl} - Sliding frictional moment

Sliding frictional moment M_{sl} was described as below.

$$M_{sl} = G_{sl} \mu_{sl} \tag{2.49}$$

Where G_{sl} is the sliding frictional variable, dependent on geometric constants for sliding frictional moments S_1 and S_2, the bearing mean diameter d_m $[mm]$, the radial load F_r $[N]$, the axial load F_a $[N]$.

$$G_{sl} = \begin{cases} S_1 {d_m}^{-0.26} {F_r}^{\left(\frac{5}{3}\right)} & (deep\ groove\ ball\ bearings) \\ S_1 {d_m}^{0.9} F_a + S_2 d_m F_r & (cylindrical\ roller\ bearings) \end{cases} \tag{2.50}$$

Typical values for geometric constants S_1 and S_2 are shown in Table 2.4, which were defined by specified SKF bearing series.

Table 2.4: Values of S_1 and S_2 for bearings typical in dynamometer rig applications [71].

Bearing type	S_1	S_2
Deep groove ball bearings	$2\times10^{-3}-6.5\times10^{-3}$	$3.6-198$
Cylindrical roller bearings	$0.16-0.17$	0.0015

The sliding friction coefficient μ_{sl} was defined as below.

$$\mu_{sl} = \Phi_{bl}\mu_{bl} + (1-\Phi_{bl})\,\mu_{EHL} \tag{2.51}$$

Where μ_{bl} is a constant depending on movement (0.12 for $n \neq 0$, 0.15 for $n = 0$), sliding friction coefficient in full–film conditions μ_{EHL} depends on bearing type and lubrication (see Table 2.5), and the weighting factor for the sliding friction coefficient is Φ_{bl}, described below.

$$\Phi_{bl} = \frac{1}{e^{2.6\times10^{-8}(n\nu)^{1.4}d_m}} \tag{2.52}$$

Table 2.5: Values of μ_{EHL} for bearings and lubrication typical in dynamometer rig applications [71].

Bearing/lubrication type	μ_{EHL}
Cylindrical roller bearings	0.02
Other bearings, lubrication with mineral oils	0.05
Other bearings, lubrication with synthetic oils	0.04
Other bearings, lubrication with transmission fluids	0.1

M_{seal} - Frictional moment of seal losses

To minimise contaminants entering the raceway of a bearing in dirty environments and contain lubricant, bearings are commonly fitted with seals on both sides. Friction associated with the seals can be significant and was described in the SKF model as in Equation 2.53.

$$M_{seal} = K_{S1}{d_s}^{\beta} + K_{S2} \tag{2.53}$$

Constants K_{S1} and K_{S2}, and exponent β are dependent on bearing type and size and the seal type. Values were summarised in Table 2.6. d_s is the seal counterface diameter [mm] and dependent on bearing type.

M_{drag} - Frictional moment of drag losses

Table 2.6: Variables in frictional moment of seal losses [71].

Bearing type	β	K_{S1}	K_{S2}
Deep groove ball bearings	$0-2.25$	$0-0.023$	$0-20$
Cylindrical roller bearings	2	0.032	50

Where bearings were lubricated by partial or full submergence in an oil bath, there were significant drag losses for rolling bearing elements. In continuous rotating applications an oil bath can be vital in maintaining lubrication to maximise wear life and minimise maintenance and replacement costs and down-time for machinery. However, in relatively short experiments on test apparatus to determine performance of chain drive transmissions, such lubrication is not necessary and induces too much loss, such that losses in the bearings can become more significant than that measured in the test subject. This significantly increases the uncertainty of measurement. Hence, the drag losses are not described here for applying the SKF model in this context.

Summary of analytical description of bearing frictional moment

The presented analytical approaches by Harris [30] and SKF [71] were broadly similar in their consideration of separate influences on the overall bearing frictional moment, though achieve this with quite different degrees of complexity. Both used parametric fits to empirical data within analytical descriptions of drag losses, such that they each featured fitting parameters in factors and exponents. The SKF model included calculations for hydrodynamic losses associated with rotating elements in oil bath which were not considered for the application to chain dynamometer test rigs.

2.4.2 Experimental determination of bearing frictional moment in radial load applications

A number of experimental solutions for testing deep groove ball bearings and cylindrical roller bearings have been developed in the literature to determine performance. Literature is summarised which considers rolling element bearings in radial load applications.

Combined load bearing test rigs by SKF (Harris, 1991 [30])

Several experimental test rigs built by SKF were referenced in Harris' work. Test apparatus for conducting endurance tests of bearings with combined radial and axial load is illustrated in Figure 2.47.

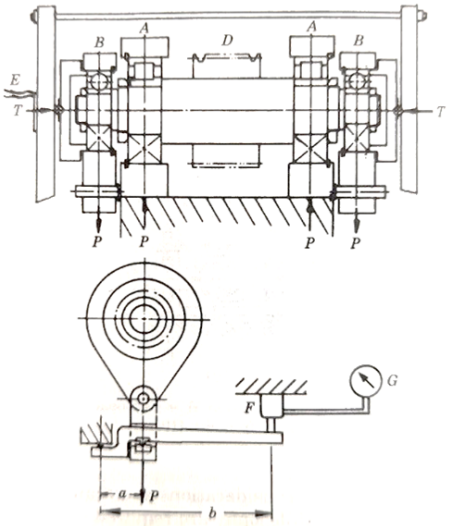

(a) Schematic of combined axial-radial application test rig.

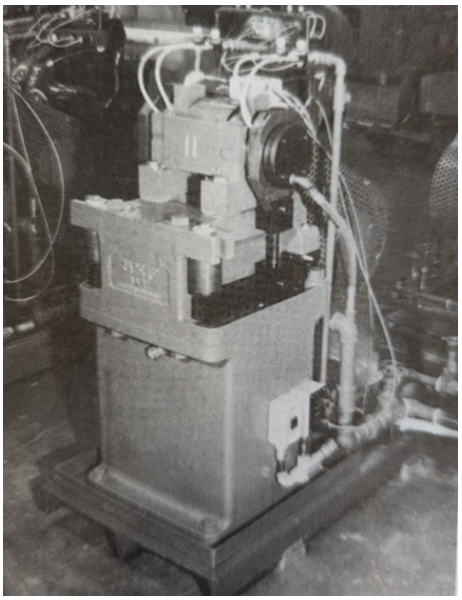

(b) Photograph of combined loading test rig.

Figure 2.47: SKF combined loading experimental test apparatus used by Harris [30].

A test shaft was driven by electric motor at specified rotational speed. Four test bearings were arranged on a shaft with option for various lubrication regimes. Shown in Figure 2.47a, radial load was applied by a hydraulic actuated lever applying force P on the outer bearings, B. This is measured with a pressure gauge, G.

Friction in radial loading of cylindrical roller bearings (Tu, 2016 [79])

Tu developed test apparatus for applying pure radial loads on bearings under test, shown in Figure 2.48.

Four bearings were fitted to a common shaft. The two outer bearings were fixed in grounded housing, and the inner pair were housed within a square sleeve which was connected to the end of a lever arm. Radial load was applied downwards to the inner bearing pair by lifting the lever with an overhead crane, providing between 0.6 and 9 kN of force on the bearing pair.

Frictional moment across all test bearings was measured with a rotating torque sensor connected to the common shaft. With the bearings close together bending in the shaft was minimised, though access problems for lubrication were introduced.

Experimental results were shown against predictions from Palmgren [63], Harris [30] and SKF [71] models with best agreement from the Harris model.

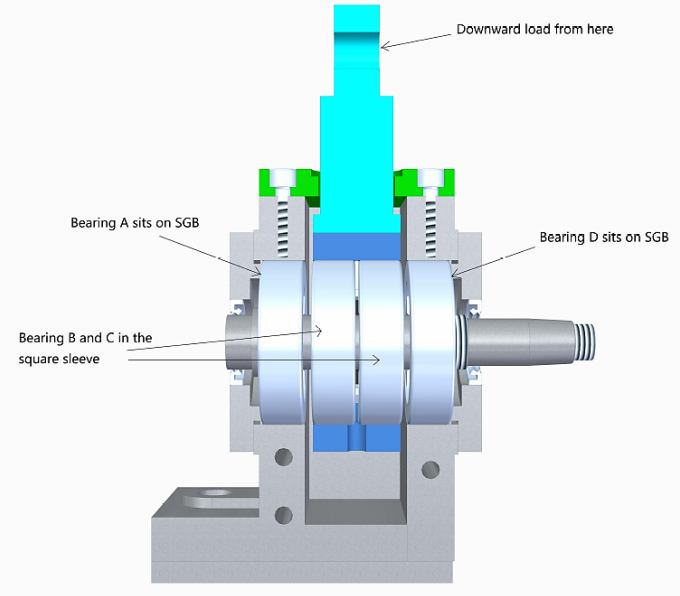

Figure 2.48: Test rig by Tu with radial load applied on central bearings [79].

Benchtop test rig for frictional moment in test bearing (Geonea et al., 2017 [29])

A benchtop design test rig was developed by Geonea et al. for measuring frictional moment in ball bearings. The test apparatus applied radial load to an individual test bearing by hanging masses from a lever, shown in Figure 2.49. The shaft was turned by an electric motor with nominal speed of 1450 RPM.

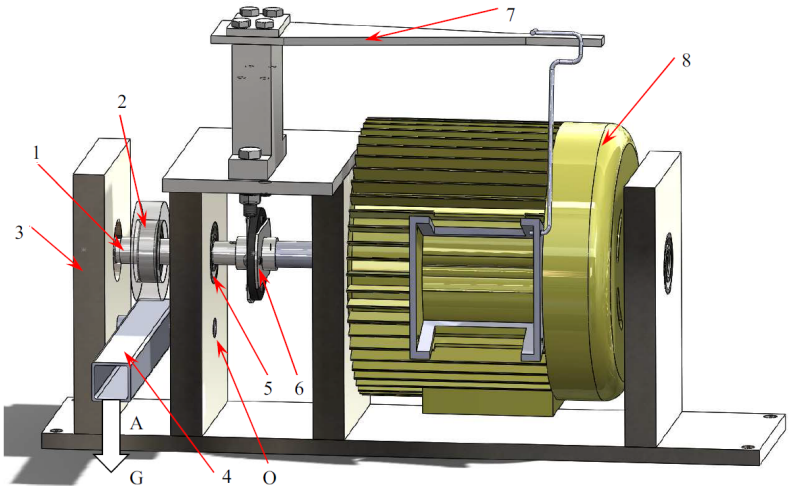

Figure 2.49: Schematic of test apparatus for testing bearing under radial load by Geonea et al. [29].

Further bearings were used to support the shaft, labelled 3 and 5 in Figure 2.49. Frictional torque induced static bending in beam, 7, measured by strain gauges. The frictional moment as a func-

tion of radial load was compared with analytical predictions computed with the Harris model of frictional torque [30] with fairly good agreement.

Multi-sensor, run-to-failure rig with screw load applicator (Kan, 2017 [40])

A 'run-to-failure' radial load applicator bearing test rig was developed by Kan in their thesis. There was no measurement of frictional moment, but novel application of radial load and condition monitoring with various sensors. The test apparatus is shown in Figure 2.50.

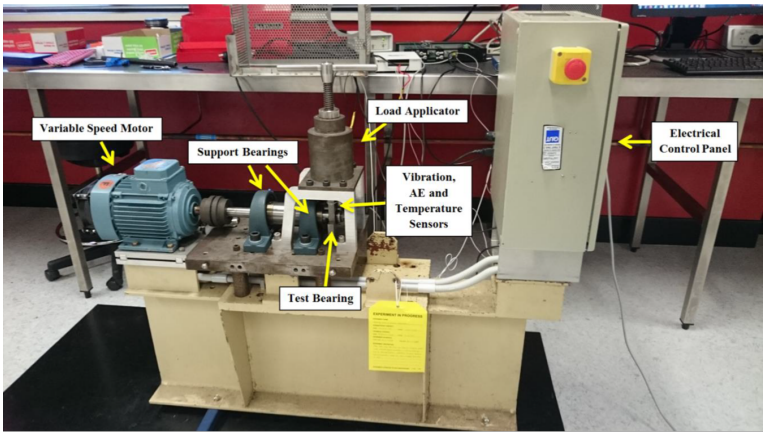

Figure 2.50: Kan run-to-failure experimental test apparatus [40].

A shaft was supported with large support bearings, with an individual (smaller) bearing under test. Radial load was applied by hand screw which compressed a large compression spring. Vibration (accelerometer), acoustic emission and temperature data was collected as the test bearing was run over extended tests.

Unlike in previous experimental set-ups, the arrangement of bearings was asymmetrical with a single bearing-under-test on a cantilevered shaft. This was necessary for this design since support bearings were much larger than the test bearing with larger bore diameter and so required a larger shaft diameter.

Friction during dynamic radial loads on bearing (Blomstedt, 2017 [7])

Blomstedt described a test rig in their thesis which was developed over a number of years. This test apparatus was designed for the specific case of creating dynamic radial loading of bearings to mimic those on a crankshaft in an internal combustion engine. The apparatus is illustrated in Figure 2.51.

A large steel frame supported equi-spaced hydraulic loading cylinders around a rotating shaft. These were capable of applying 10-100 kN radial force dynamically at up to 50 Hz. The shaft had

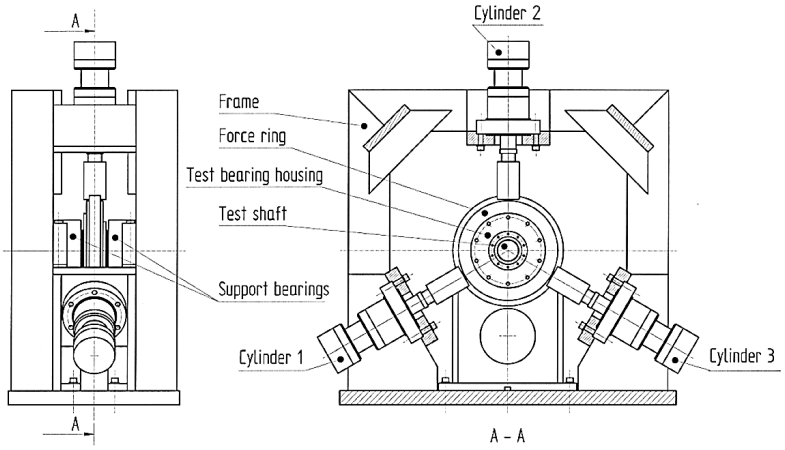

Figure 2.51: Schematic of test apparatus developed by Blomstedt for testing bearings with dynamic radial loads [7].

a test bearing in housing connected to the cylinders, with support bearings either side in housing fixed to the test bed.

Elgeti commercial test apparatus (Yadav and Elgeti, 2019 [90])

Engineering company Elgeti offer several experimental test rigs to their customers of various loading types, and published a white paper which detailed their capability. The design for their radial load applicator is shown in Figure 2.52. This was recommended for measurement of frictional torque, equilibrium temperature testing or endurance testing.

Four test bearings were fitted to a common shaft driven by electric motor. Housing for outer bearings was fixed to the test bed, while the central pair were held in floating housing and radial load applied by hydraulic cylinders. The radial load was measured by either pressure gauge or load cell.

Summary of radial load bearing test rigs

There are common themes across the experimental apparatus presented for testing bearings with applied radial load. All had a single shaft driven by electric motor, and generally had a symmetrical array of bearings with the exception of the design from Kan [40].

Differentiation between support bearings and test bearings was made in several test rigs [29, 40]. Support bearings were of much higher load rating than the test bearings to limit their load-dependent performance during testing. These were a necessary design choice for tests to failure for reasons of safety (test bearings failing must not have caused the apparatus to break apart) and of time (a single test bearing should fail more quickly for given load). In determination of ac-

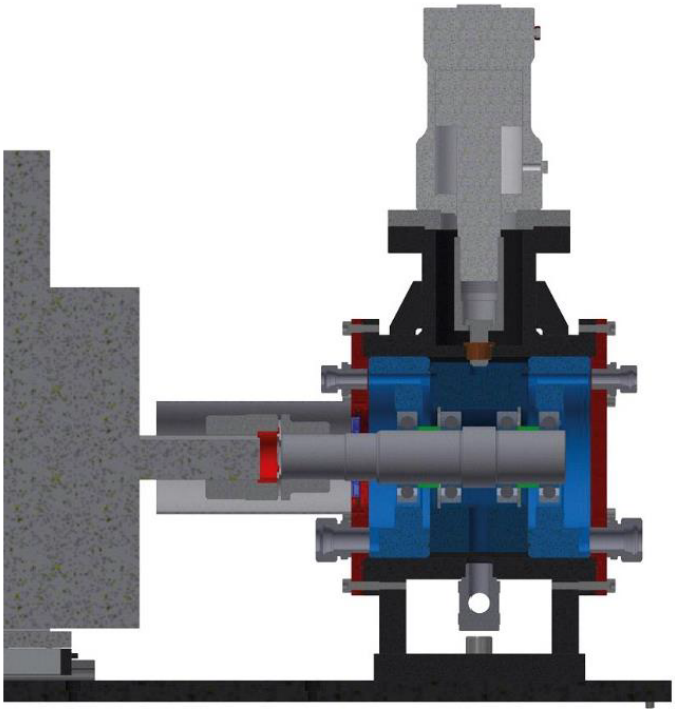

Figure 2.52: Radial load application test rig offered by Elegeti [90].

curate assessment of frictional moment, support bearings introduced additional source of friction and dynamics which had an influence on experimental results.

Application of radial load was carried out by a variety of means, often achieved using mechanical advantage with a lever [30, 79, 29]. Force was applied directly and indirectly by hydraulic pressure [30, 7, 90], hanging masses [29], tension from winch action (overhead crane) [79], or from compressing a spring [40].

Where frictional moment was measured, rotating strain gauges were most commonly employed [79, 7, 90]. Static methods were also used, demonstrated by Geonea [29] in measuring bending strain. Further condition monitoring of bearings was demonstrated with a variety of sensors in Kan's thesis [40].

2.5 Characterising measurement uncertainty of experimental measurement

Chain transmission systems are shown to be highly efficient in optimal loading conditions. In measurement of the relatively small frictional losses, the uncertainty of measurements is increasingly important to understand, quantify and reduce where possible. Seminal and applicable literature

relating to the measurement uncertainty in relevant measurement equipment is detailed in this section.

2.5.1 General principles of uncertainty

The *Guide to the expression of uncertainty in measurement* [6] is the accepted standard of uncertainty assessment and its central themes where they were applied in this work are summarised. In experimental assessment of a metric, it can be said that its true value, Y, is a function of the true values of multiple measurands:

$$Y = f(X_1, X_2, \ldots, X_N) \tag{2.54}$$

Since all measurement has an associated uncertainty, Y can only be estimated as value y, described as a function of input estimates:

$$y = f(x_1, x_2, \ldots, x_N) \tag{2.55}$$

Repeated observations of y will fall within a Gaussian probability density function (PDF) according to the central limit theorem (CLT). The standard deviation of the PDF produced from repeated observations of y is its uncertainty, $u_c(y)$. It may be written as the combined uncertainty of its inputs' uncertainties.

$$u_c(y) = f(u_c(x_1), u_c(x_2), \ldots, u_c(x_N)) \tag{2.56}$$

Uncertainties are combined as variances such that measures of standard deviation of each input is summed in quadrature.

$$u_c(y)^2 = u_c(x_1)^2 + u_c(x_2)^2 + \ldots + u_c(x_N)^2 \tag{2.57}$$

$$u_c(y) = \sqrt{u_c(x_1)^2 + u_c(x_2)^2 + \ldots + u_c(x_N)^2} \tag{2.58}$$

One standard deviation about a mean represents 68.27% coverage according to a normally distributed variable. The quoted uncertainty may require greater coverage in safety-critical applications, for example. An expanded uncertainty is defined, $U_c(y)$, where:

$$U_c(y) = k_p \, u_c(y) \tag{2.59}$$

The coverage factor, k_p, is the coverage defined as the number of standard deviations from the mean. To achieve 95% coverage, the coverage factor must be 2.576. Common values were summarised in Table 2.7.

The uncertainty of a variable may be determined by two distinct methods:

- Type A evaluation of uncertainty: statistical analysis of repeated observation.
- Type B evaluation of uncertainty: assessment by means other than statistical analysis of repeated observation.

Table 2.7: Level of confidence and associated coverage factor for expanded uncertainty.

Level of confidence p [%]	**Coverage factor** k_p
68.27	1
90	1.645
95	1.960
95.45	2
99	2.576
99.73	3

Type A evaluation of uncertainty

Repeated observations of a measured value q, describing a true value Q, can describe the uncertainty of the measured value through statistical analysis. The arithmetic mean of repeated observations described the result of repeated measurements, $\bar{q}$.

$$\bar{q} = \frac{1}{n}\sum_{k=1}^{n} q_k \tag{2.60}$$

The variance is a measure of the difference of values from the mean, where the variance of a sample about the sample mean is described as below.

$$s^2(q_k) = \frac{1}{n-1}\sum_{j=1}^{n} (q_j - \bar{q})^2 \tag{2.61}$$

The estimate of variance of a sample mean about a population mean is described as below.

$$s^2(\bar{q}) = \frac{s^2(q_k)}{n} \tag{2.62}$$

Type B evaluation of uncertainty

Type B evaluation of uncertainty is broadly defined by the GUM [6] as a method other than statistical analysis of repeated measurement. Several methods were suggested:

1. Uncertainty is based on previously measured data (historical type A analysis).
2. Experience with measurement equipment.
3. Manufacturer's specifications or calibration data.
4. Uncertainties of reference data.

A general approach to type B evaluation of uncertainty for analytical models is defined by GUM where a measurement y is described analytically by n measurands. The combined variance of

measurement y is defined as below:

$$u_c^2(y) = \sum_{i=1}^{n} \left(\frac{\partial f}{\partial x_i} \right)^2 u^2(x_i) \tag{2.63}$$

The partial derivative $\left(\frac{\partial f}{\partial x_i} \right)^2$ is known as a sensitivity factor, where f is the function described in Equation 2.55. It works to scale the influence of variance in measurand x_i on the combined variance $u_c^2(y)$.

2.5.2 Monte Carlo methods as Type B evaluation of uncertainty

Monte Carlo methods [16] offer a versatile approach to defining an expanded uncertainty of a measurand defined analytically by a number of measurements with known probability density functions (PDFs).

$$y = f(x_1, x_2, x_3) \tag{2.64}$$

Repeated observations of measurand y were simulated based on a large number of pseudo-randomised inputs of measurements in function f. The variables were produced based on a defined PDF in each case, illustrated in Figure 2.53. The output represents the PDF of the measurand y and the expanded uncertainty can be evaluated from the spread.

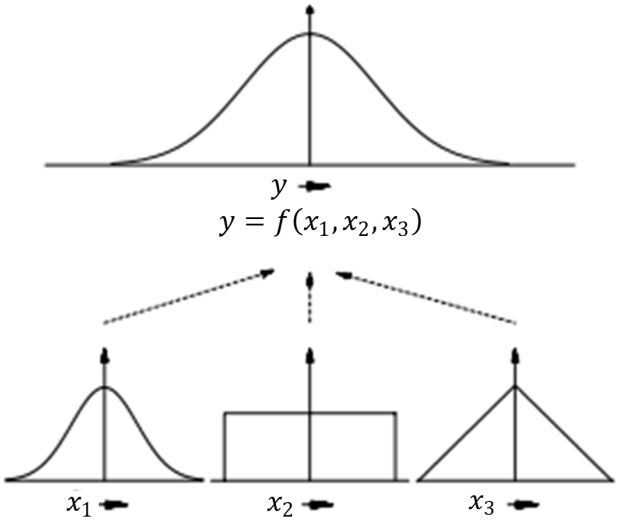

Figure 2.53: Gaussian probability density function (PDF) of measurand y is determined from mixed PDFs of measurements x_1, x_2 and x_3 (adapted from [16]).

This is versatile as PDFs may be described by any combination of distributions: central limit theorem dictates that the resultant PDF will tend to a normal distribution in the case of the measurand y. Any scaling of the impact of uncertainties is dealt with in the impact of the variable in the analytical description.

2.5.3 Uncertainty of rotating torque transducers

A Type B analytical approach to evaluation of uncertainty of measurement in rotating torque transducers is presented by Wegener and Andrae [83]. This analysis is repeated by HBM in online webinars which have received some updates and clarifications on equation terms [2]. Furthermore, a study by Wegener et al. [84] explored the uncertainty of torque measurement when used in partial load ranges. Torque transducers were calibrated in their nominal range but many in many uses do not regularly measure to this extreme. They concluded that contribution to measurement uncertainty from linearity deviation and hysteresis may be downscaled linearly by the applied load as proportion of nominal load.

Individual influences on uncertainty were defined based on nominal data published on the data sheet for the corresponding torque transducer hardware. Variables used in calculation of uncertainty are shown in Table 2.8.

Table 2.8: Parameters in calculation of uncertainty of torque measurement.

Variable	Description	Source
M_{nom}	Nominal (rated) torque	Data sheet
M_{max}	Maximum torque in application	Application
ΔM	Torque range in application	Application
ΔT	Temperature range in operation	Application
d_{CS}	Uncertainty of sensitivity	Data sheet
d_{lh}	Linearity incl. hysteresis	Data sheet
TK_0	Temperature effect on the zero signal	Data sheet
TK_C	Temperature effect on the sensitivity	Data sheet
k	Coverage factor ($\frac{1}{\sqrt{3}}$ for rectangular dist.; 1 for normal dist.)	$\sim$
σ_{rel}	Standard deviation of repeatability	Data sheet
d_{para}	Combined parasitic loads in application relative to limit loads	Application + Data sheet
L_{para}	Maximum parasitic load	Application
$L_{para,ref}$	Limit load	Data sheet
x_{para}	Measuring error relative to M_{nom} due to permitted parasitic bending moments	Data sheet

The combined uncertainty is defined as the quadrature sum of uncertainties described in Table 2.9.

$$U_{total} = \sqrt{{U_C}^2 + {U_{lh}}^2 + {U_{TK0}}^2 + {U_{TKC}}^2 + {U_{b'}}^2 + {U_{para}}^2} \tag{2.65}$$

Table 2.9: Uncertainty contributions from properties defined on data sheet (no further calibration).

Uncertainty source	Equation
Sensitivity tolerance	$U_C = k \cdot M_{max} \cdot d_C$
Linearity incl. hysteresis	$U_{lh} = k \cdot M_{max} \cdot d_{lh}$
Temperature effect on zero signal	$U_{TK0} = k \cdot M_{nom} \cdot TK_0 \cdot \Delta_{T10K}$
Temperature effect on the sensitivity	$U_{TKC} = k \cdot M_{max} \cdot TK_C \cdot \Delta_{T10K}$
Standard deviation of repeatability	$U_{b'} = k \cdot \Delta M \cdot \sigma_{rel}$
Allowable load limits	$U_{para} = k \cdot x_{para} \cdot M_{nom} \cdot d_{para} \cdot \frac{L_{para}}{L_{para,ref}}$

2.5.4 Uncertainty of force measurement

A Type B assessment of uncertainty of force measurement in load cells is described by HBM in online customer literature [32]. Uncertainty on measurement due to various effects were described separately and scaled based on nominal data published on the data sheet of associated hardware. Variables are summarised in Table 2.10.

Table 2.10: Parameters in calculation of uncertainty of force measurement.

Variable	Description	Source
F_{appl}	Applied force	Experimental measurement
F_{nom}	Nominal (rated) force	Data sheet
ΔT	Temperature change	Experimental measurement
d_C	Deviation of the rated output	Data sheet
d_{lin}	Linearity deviation	Data sheet
$v_{0.4}$	Hysteresis error at 0.4 F_{nom}, relative to full scale value	Data sheet
TC_S	Temperature coefficient of the rated output	Data sheet
TC_0	Temperature coefficient of zero signal	Data sheet
d_{cr}	Relative creep	Data sheet

The contributions to uncertainty are shown in Table 2.11.

Uncertainty of different parts is combined as the quadrature sum in Equation 2.66.

Table 2.11: Uncertainty of load cell force measurement from various sources.

Uncertainty source	Equation
Tolerance of rated output	$\Delta_{dC} = d_C \cdot F_{appl}$
Linearity deviation	$\Delta_{dlin} = d_{lin} \cdot F_{nom}$
Hysteresis	$\Delta_{hys} = v_{0.4} \cdot F_{nom}$
Influence of changes in temperature on sensitivity	$\Delta_{TKC} = TC_S \cdot F_{appl} \cdot \frac{\Delta T}{10K}$
Influence of changes in temperature on zero point	$\Delta_{TK0} = TC_0 \cdot F_{nom} \cdot \frac{\Delta T}{10K}$
Creep	$\Delta_{cr} = d_{cr} \cdot F_{appl}$

$$U_{ges} = \sqrt{\Delta_{dC}^2 + \Delta_{dlin}^2 + \Delta_{hys}^2 + \Delta_{TKC}^2 + \Delta_{TK0}^2 + \Delta_{cr}^2} \tag{2.66}$$

2.6 Summary of Chapter 2

Literature has been summarised which bears relevance to the work conducted in this thesis. The relevant literature was wide ranging due to the breadth of areas which this work has addressed, though in some areas there are not a great number of individual studies and hence limited published material. It is likely that a significant amount of research and development in the industrial and cycling chain industries has been conducted and is unpublished due to its proprietary nature and the protection of intellectual property.

The four broad topics of literature addressed and their relevance to the remainder of this thesis are summarised:

1. **Analytical description of transmission performance.** Kinematic modelling and analytical determination of tensions in a chain drive are readdressed in Chapter 3, while analytical assessment of transmission efficiency is relevant to the research described in Chapter 9.
2. **Experimental determination of transmission performance.** Literature in this area is directly appraised in Chapter 3, and the literature sets the context for the experimental dynamometer described in Chapter 4. Gaps in the literature addressing parasitic friction of support bearings are addressed in Chapter 5. Methods for measuring high frequency dynamics in the literature are reapplied in Chapter 7.
3. **Performance of rolling element bearings, where relevant to their use in rotating test apparatus.** This is directly readdressed in Chapter 5 in the context of the dynamometer test rig introduced in Chapter 4.

4. **Measurement uncertainty (general principals and particular applications).** This is readdressed in Chapter 3 for a Type B approach to uncertainty of torque measurement, and is the sole focus of Chapter 6 where uncertainty of measurands in experimental setups are expanded on in detail.

THIS PAGE IS INTENTIONALLY LEFT BLANK.

Chapter 3

Analytical Appraisal of Dynamometer Test Rigs

3.1 Introduction

This chapter appraises two common dynamometer designs implemented to test chain drives in cycling and industrial applications: one most prevalent in literature, and one most prevalent in testing cycle components in the industry.

Experimental testing of chain performance in literature is summarised in Section 2.3 in the previous chapter. There are a number of tests presented which isolate key parameters and measure them specifically and accurately by reducing the chain drive to key components and simplifying loading cases. Such tests have significant benefits, allowing precise measurement of metrics (such as friction coefficient in chain links, or chain link materials) which can give broad understanding of improvements to performance. Contextual extrapolation of results is required to determine the power losses or efficiency of a full transmission in realistic duty cycles, for instance by applying a measured coefficient of friction in analytical models such as those introduced in Section 2.3.2.

Analysing performance in this way neglects phenomena which may be vital to performance in use. Dynamic behaviours in chain transmissions is introduced in Chapter 1 and analytical and experimental techniques to assess their influence demonstrate significant vibration is possible even at constant speed due to polygonal action and system resonance.

Chain drive dynamometers such as those introduced in Section 2.3.3 recreate a transmission with realistic boundary and loading conditions. Experimental methods induce the same vibration as in use, and thereby account for it in their measurements. This type of test equipment is designed and

scaled appropriately to recreate the conditions of the particular real-world context of the intended use of the transmission-under-test. The driving side of the transmission is turned continuously against active or passive resistance on the driven side. Resistive torque may be provided by sliding friction, electromagnetic, or hydraulic means. Power is measured at input and output, with the difference defining the rate at which energy is dissipated in the test system. With current technology, experimental apparatus of this design offer the most representative solution to contextual testing of chain transmissions. A schematic of the hardware is shown in Figure 3.1.

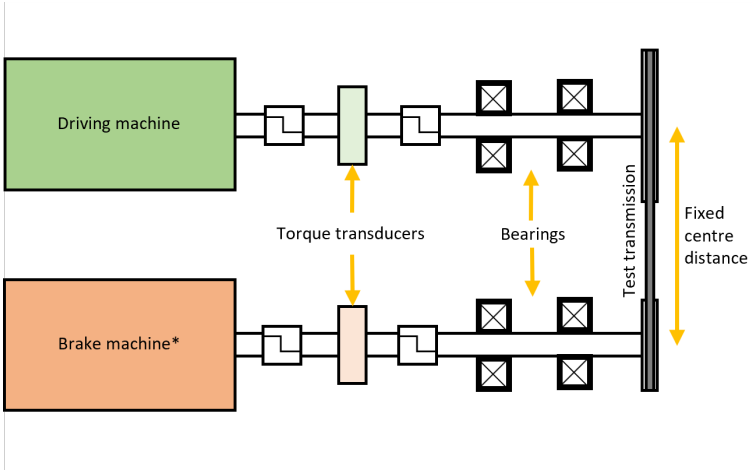

Figure 3.1: Transmitted Power Measurement (TPM) dynamometer test rig schematic.

A dual measurement dynamometer is described in this work as a Transmitted Power Measurement (TPM) test rig, since a central measure of performance is how much power is transmitted as a proportion of the power input:

$$P_{loss,TPM} = \{P_{in} - P_{out} - P_{bearings}\}_{TPM} \tag{3.1}$$

A chain or belt drive is a low-loss, high-efficiency systems and so the transmitted power is large relative to the power lost. To accurately determine the performance of the test transmission, very high quality measurement of input and output power is required.

An alternative design dynamometer is used commonly in testing of cycling transmission which is introduced in Section 2.3.3: the Full Tension Tester [24]. In this test rig, the loading of the chain span is decoupled from the driving torque similarly to the concept introduced by Hollingworth [37] . Chain tension is induced in spans by forcing the sprockets apart, inducing tension in both spans such that friction in four articulations is equivalent to friction in two articulations in only one span. With decoupled tensioning, the driving torque is acting against friction in the system

and so only one measurement is required to describe the power loss:

$$P_{loss,FPM} = \{P_{in} - P_{bearings}\}_{FPM} \tag{3.2}$$

This rig can be described as a Frictional Power Measurement (FPM) dynamometer, since there is no transmitted power and only frictional power is overcome. A schematic of the general design of a FPM dynamometer is shown in Figure 3.2.

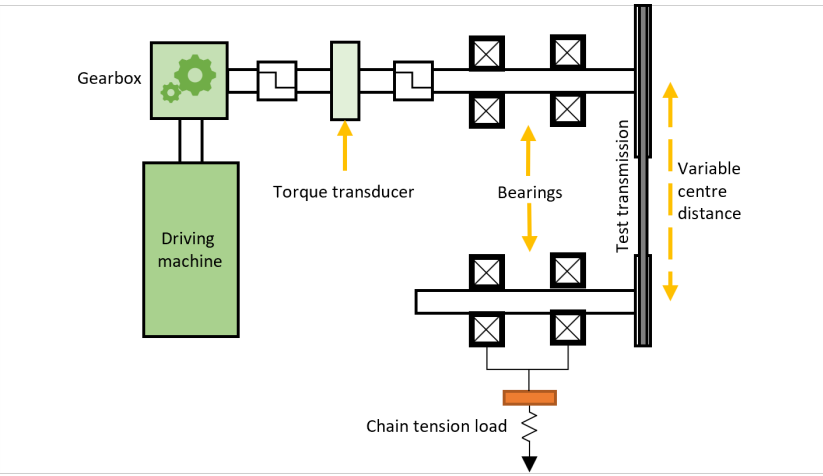

Figure 3.2: Frictional Power Measurement (FPM) dynamometer test rig schematic.

The measurement on an FPM dynamometer is more precise since the friction is determined in a single measurement with equipment rated for that order of magnitude. This is a clear benefit over a TPM dynamometer. However, while span loads are designed to be broadly equivalent between the two rigs in inducing similar friction, the loading and boundary conditions are not equivalent between TPM and FPM dynamometers.

This chapter aims to offer an appraisal of the two designs in both qualitative and quantitative terms. Quantitative analysis is possible by modelling the loading conditions and boundary conditions to challenge the assumption of equivalent loading. Furthermore, estimates of efficiency can be analytically determined from the tension in the articulating links. This gives some insight into the quality of equivalence of conditions between the tests. A further area of consideration is the uncertainty of measurement, which may be determined using Type B uncertainty analysis of theoretical measurement equipment.

3.1.1 Structure of chapter

The practical challenges of implementing TPM and FPM dynamometers are discussed, describing differences in:

1. Hardware utilised.
2. Loading conditions for transmission-under-test.
3. Boundary conditions for transmission-under-test.

Next, analytical modelling from the literature is used to examine the effect of these differences on equivalent test transmissions using:

1. Kinematic modelling.
2. Quasi-static link tension modelling.
3. Model of friction in articulation.

Models are used from literature with some adaptations to consider the different loading and boundary conditions for each dynamometer.

Finally, the measurement uncertainty of inferred power loss is calculated with an established Type B assessment of measurement uncertainty for each rig design.

With quantitative and qualitative comparisons, the benefits and detriments of each dynamometer type is summarised, and the case put forward for a Transmitted Power Measurement dynamometer as preference for academic studies into the holistic assessment of transmission performance.

3.2 Qualitative comparison of dynamometer test rigs

3.2.1 Dynamometer hardware

An example of a TPM dynamometer test rig is shown in Figure 3.3. This style of test rig is a traditional dynamometer, with driving and braking load independently applied. Loading and braking attempts to be representative of those in conditions use. In the context of bicycle transmission, typical loading involves large torques, relatively low speed and geometry of the dual sprocket system matches that on a bicycle. Power is transmitted between a driving and driven sprocket via the top span of a chain drive. The chain's return path is via a low-tension slack span.

Several examples of TPM dynamometers in the literature use a driving motor with speed control, with a friction brake [42, 91] or electromagnetic brake [75] acting on the driven shaft. Designs both with and without gearboxes are demonstrated. The use of a simple brake and gearbox conflicts with an aim to replicate representative transmission conditions which the TPM design lends itself to. A mechanical gearbox can introduce additional dynamics and backlash to the test system, influencing measurement and loading conditions. Furthermore, speed and torque changes are intrinsic to transmission in cycling and industrial applications.

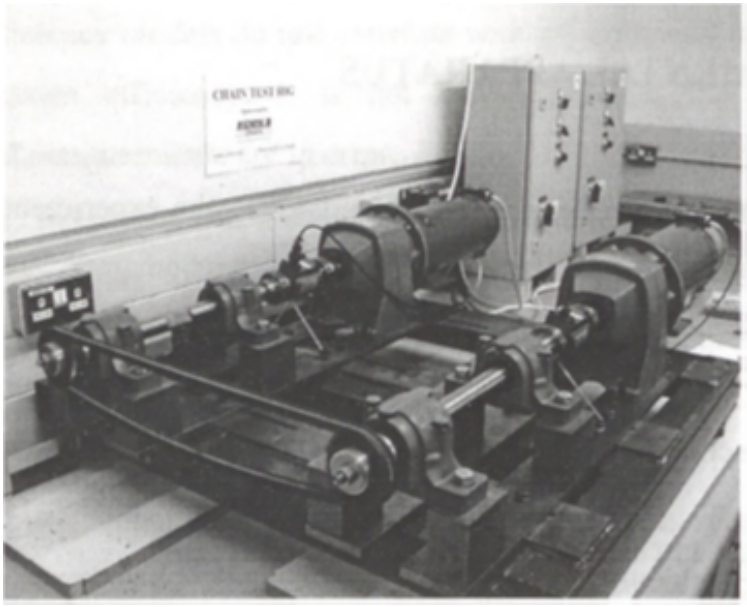

Figure 3.3: Photograph of TPM dynamometer test rig developed by Lodge for industrial chain testing [47].

A sophisticated TPM dynamometer is presented in the literature [47] which utilises with a second electric machine as brake allows for close control of the resistive torque in the system. With appropriate motor sizing and control of torque and speed with a Variable Frequency Drive (VFD), gearboxes can be eliminated. The rotational speed of the transmission may be controlled by the driving or driven motor with a VFD, while the other motor drives with or is driven at defined torque. Typically, the driving machine defines the rotational speed and the driven machine or brake provides resistive torque.

The cost of manufacture is significant in building a rig of this design. Multiple units are required of expensive components such as VFDs, electric machines and torque transducers. Furthermore, the power re-circulation system requires expertise and existing laboratory infrastructure to be in place to implement the TPM dynamometer.

An FPM dynamometer is a variation on a traditional dynamometer, where the high tension induced in the chain is decoupled from the driving motor turning the transmission. By inducing the load in the chain span through other means, similar frictional forces can be induced with a simpler and smaller test rig. The original example of a rig following this design was built by Friction Facts to test the effect of lubricants [24]. Their original FPM dynamometer is illustrated in Figure 3.4.

In an FPM dynamometer, a fixed driving sprocket is linked via a chain to a 'floating' driven sprocket. The floating sprocket is forced away from the driving shaft by some means, inducing high tension in the spans of the chain. Due to variable wrap on the sprockets from polygonal action

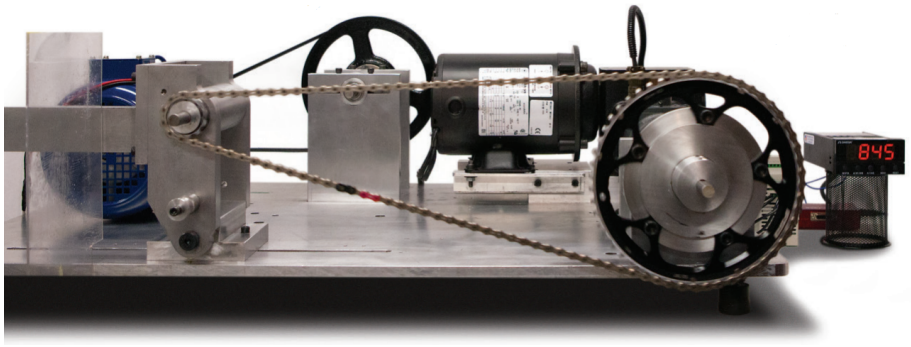

Figure 3.4: Photograph of FPM dynamometer test rig developed by Friction Facts [23].

and the presence of two tight spans, there will either be additional forces in the chain spans or a subtly changing distance between sprockets, depending on where the compliance is designed in the system.

A single motor turns the driving sprocket at fixed speed, which is driving not against a brake, but against the frictional forces in the system. A step-down gear box is used with a variable speed AC motor. A single torque transducer measures the torque necessary to overcome resistance in the system.

The FPM dynamometer pictured in Figure 3.4 includes a hinged shaft housing for the driven sprocket with sprung tensioning masses such that there is compliance in the system allowing for non-constant wrap in the chain spans. A version with fixed centre distance is possible, though must have equivalent and even-numbered teeth in the gear ratios else the chain will stretch to accommodate the changing wraps and incur additional forces and hence frictions. For cycling ratios, the type shown is the only feasible type, and there is no scope for testing systems with auxiliary gears due to two high tension spans.

The hardware of TPM and FPM dynamometer designs are summarised in Table 3.1.

3.2.2 Boundary and loading conditions for transmission-under-test

The conditions for the transmission-under-test can appear similar for both dynamometer types: both feature a driving sprocket, which rotates a transmission in a continuous direction linked to a secondary sprocket via a chain.

However, there are very important differences. Whereas the TPM transmits power with a slack span and fixed centre distance, the FPM does not have these conditions. In practice, industrial

Table 3.1: Summary of characteristics of hardware in dynamometer types.

Hardware characteristic(s)	Dynamometer type	
	Transmitted Power Measurement (TPM)	Frictional Power Measurement (FPM)
Span load source	Driving torque against braking torque	Weighted lever arm
Driving load source	High-torque electric machine	Low-torque electric machine
Speed control	Driving/Driven machine	Driving machine
Braking load source	Electric machine / Brake (electro-mechanical / hydraulic / friction)	System friction
Configuration with aux. sprockets	Yes/No	No
Loss measurement	2 high-rated torque transducers	1 low-rated torque transducer
Bearing(s)	Ball/roller bearings	Ball bearings
Cost to build ROM (£)	$> 10^5$	10^4
Relative cost to run	1	0.05

drives tend to have the boundary conditions of the TPM not the FPM. The extent to which this affects the chain link forces, and hence impact the frictional losses, are now examined.

A TPM dynamometer has the capability of recreating loads as expected in use, where independent torques drive the transmission at input and brake its output. When operating in positive direction, useful power is transmitted in the top span of the transmission-under-test and the bottom span is a low-tension return path of the chain. The span tension is induced by the torque from the electric machines acting at the sprocket pitch radius. The construction is stiff and centre distance between sprockets is fixed. The loading conditions are shown in Figure 3.5.

One way in which a TPM may emulate the boundary conditions for a transmission in use is to match the inertial effects acting on each shaft. In a cycling application at steady state, it might be expected that the bulk mass the bulk mass of a rider at high speeds results in relatively much higher inertia of the rear wheel when compared with the rider pedalling. This subtle change means fluctuations in speed due to dynamic effects will more readily manifest in changes to the speed on the driving shaft than the driven shaft. This boundary condition can be recreated on a TPM

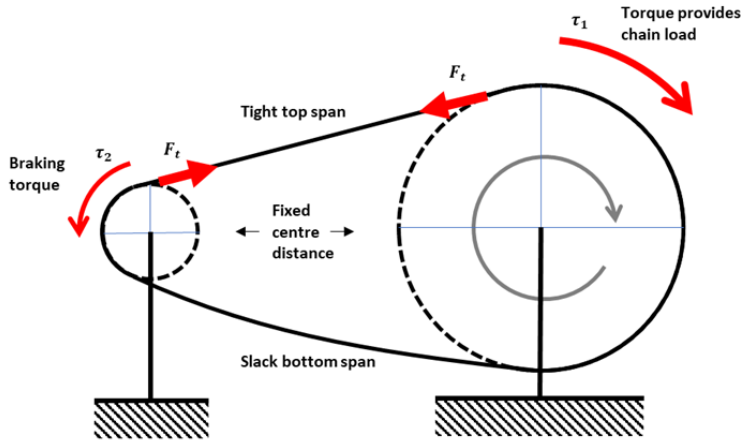

Figure 3.5: Annotated image of TPM dynamometer test rig showing boundary and loading conditions resulting from its construction and control.

dynamometer by breaking convention from the literature and controlling speed via the driven machine.

The conditions for transmission-under-test on a FPM dynamometer rig is quite different and illustrated in Figure 3.6. The decoupled tensioning system induces significant span tension in top and bottom chain spans. Changing centre distance means that polygonal behaviours in the chain are dampened. With speed control on the driving shaft and very little rotating mass on the driven shaft, the relative inertia of the driving sprocket is much larger (opposite to the TPM dynamometer). This means that fluctuations in speed due to dynamic effects will more readily manifest in changes to the speed on the driven shaft.

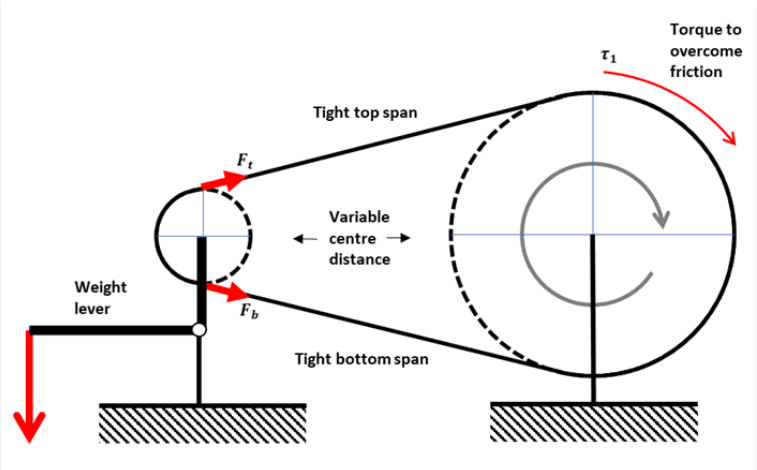

Figure 3.6: Annotated image of FPM dynamometer test rig showing boundary and loading conditions resulting from its construction and control.

The differences in conditions for transmission-under-test between TPM and FPM dynamometers are summarised in Table 3.2.

Table 3.2: Summary of boundary and loading conditions in dynamometer types.

Loading characteristic(s)	**Dynamometer type**	
	Transmitted Power Measurement (TPM)	**Frictional Power Measurement (FPM)**
Centre distance	Fixed	Compliant to account for changing chain wrap
Speed control	Driven machine	Driving machine
Relative effective shaft inertia	$J_{driven} \gg J_{driving}$	$J_{driving} \gg J_{driven}$
Loaded chain span	Top	Both
Span loading source	Driving and braking torque	Applied pre-tension
Driving torque	High, from driving electric machine	Low, from driving electric machine
Braking torque	Medium, from driven electric machine	From resistance only
Useful power transmitted	Yes	No

3.3 Modelling boundary and loading conditions

The differences in hardware, and in boundary and loading conditions have been summarised in Section 3.2. These affect the conditions seen in the transmission-under-test. Analytical models are used to describe the resultant effect on loading and expected power loss in the transmission-under-test.

3.3.1 Choice of model

The effects of changing boundary conditions and loading scenarios on chain forces can be investigated by modelling link tension around a drive. The losses in the drive are highly dependent on these forces. By considering the full modelled drive, the loading equivalence between TPM and FPM cases can be assessed.

As introduced in Section 2.2.2, there are several models in the literature which might serve to describe the loading of the chain links around the sprockets and in the spans. The model proposed by Lodge [48] is the only which considers the distinction between high-tension and low-tension

bottom span; given this is a key difference between test cases in this appraisal it is deemed the most suitable model.

Lodge and Burgess also propose a model of transmission efficiency from the estimated chain joint forces [48] which was also used to predict frictional power losses from equivalent test subjects on different dynamometer style test rigs. This considers losses due to sliding friction only, and so may be valid only for steady and smooth operation.

Several adaptations are required in the modelling assumptions for its application to the specific loading and boundary cases of the two dynamometers discussed.

3.3.2 Changes to model for TPM dynamometer test rig

The original model considers a transmission with driving and driven sprockets with defined output power. It is most like the loading case in a TPM dynamometer, and so the model can be applied with limited changes. There are several subtle alterations which are made.

1. Where the model defines driving torque from the deliverable output power, it is now defined from the input power. Applied torque is calculated directly from the input power.
2. The geometry of the drive is calculated in the first instance and parameters saved; from here, the link tension is calculated for a range of torque and speed inputs using the same geometric data. This improves computational efficiency, though comes at a disadvantage of not including a term for chain stretch.
3. The quasi-static step-wise movement of the drive is calculated based on regular rotational steps of the high-inertia driven sprocket, not constant rotation of the driving sprocket as is used in the original model. As a result, variable chain speed due to polygonal action causes variability in the rotational speed of the driving sprocket. This is an effort to better reflect the bicycle case in typical use, where the inertia of the rear wheel includes the bulk mass of the rider moving at speed: significantly higher than the rider driving the cranks. This assumption becomes invalid at low speeds, for example in specific hill climbing applications.

3.3.3 Changes to model for FPM dynamometer test rig

Modelling the boundary and loading conditions for an FPM dynamometer test rig requires some adaptations to the original model previously described.

1. Chain links in the slack span are assumed to lie on a straight line and solved similarly to the tight span.

2. The distance between the sprocket centres is not fixed, and is determined by a pivoting arm which provides compliance in the system necessary to solve the geometry as the drive travels.

3. The load in the spans is from three sources: the induced load from masses hanging from the pivot; the additional load from the mass of the chain held in tension; and the load in the top span from the driving torque overcoming the friction in the system. The first requires new equations, the second is already considered in the original model, the third requires some iteration with calculation of the efficiency where the frictional torque dictates the necessary driving torque.

3.3.4 Modelled drive rotational speeds

Lodge's link tension model begins with a geometric model of the rollers in the transmission, described in Section 2.2.1. Here, it is used as a kinematic model to consider how the different boundary conditions affect the rotational speed of driving and driven shafts, and the implications of this in tests.

The boundary conditions which impact the relative shaft movement are the centre distance and the relative inertia of shafts. In the TPM modelled case, the centre distance is fixed and the driven shaft is high inertia. As a result, changing speed due to polygonal action manifests purely in the driven shaft, as can be seen in Figure 3.7a. In the modelled FPM case, the centre distance changes to solve the transmission with spans held in tension and the driven shaft is low inertia. Seen in Figure 3.7b, the effects of polygonal action is seen in changing speed of the driven shaft. The expected half sinusoids are disrupted due to the changing centre distance and hence the amplitude is reduced.

3.3.5 Equivalence of loading

For a TPM dynamometer, the driving power, P_1, and driven rotational speed, ω_2, are defined. The driving torque, τ_1, is described from this according to Equation 3.3.

$$\tau_1 = \frac{P_1}{\left(\frac{N_1}{N_2}\right)\omega_2} \tag{3.3}$$

The tension induced in the top span from this torque is estimated as in Equation 3.4.

$$F_t = \tau_1 \left[\frac{p}{2\sin\left(\frac{N_1}{\pi}\right)}\right]^{-1} \tag{3.4}$$

On an FPM dynamometer, the load applied to the floating sprocket, F_w, is intended to be equivalent to this estimate of the 'real-world' top span tension [24]. The load F_w is shared in the top and

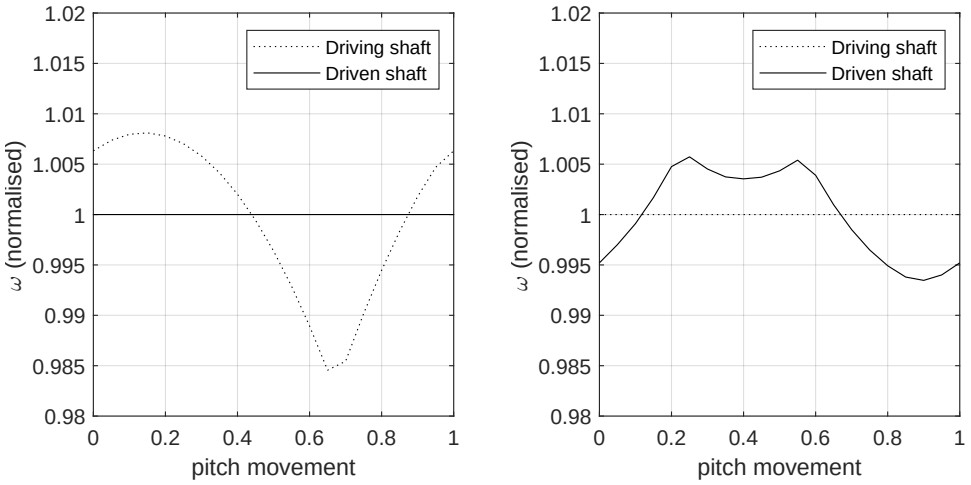

(a) TPM dynamometer.

(b) FPM dynamometer.

Figure 3.7: Rotational speed kinematically modelled for rotation of driving shaft. Rotational speed fluctuations are relative to nominal rotational speed ($N_1/N_2 = 42/14$).

bottom spans, and four articulations at half the link force are assumed to have broadly equivalent friction to two articulations at full link force. F_w can be defined in terms of an equivalent input power to emulate by means of the tensioning system, P_{eqlt}, as in Equation 3.5.

$$F_w = \frac{P_{eqlt}}{\omega_1} \left[\frac{p}{2\sin\left(\frac{N_1}{\pi}\right)} \right]^{-1} \tag{3.5}$$

3.3.6 Modelled link tension

The tension in the links in the drive are modelled for all positions in the transmission. Figure 3.8 shows the tension between links plotted for the path around the drive, where the position of a link is plotted on the x-axis and the tension on the y-axis. The link position starts at the first link engaged with the driving sprocket, showing decreasing tension in the links towards the bottom span.

Figure 3.9 shows the calculated link tension around a transmission for three different cases at equivalent driving torque with loading and boundary conditions aligned with a TPM dynamometer. In each case, different sized sprockets are used; the gear ratio is maintained.

There are several points demonstrated across all three cases plotted in Figure 3.9:

1. Tension drops off quickly around the driving sprocket.
2. Tension is very low in the bottom span.
3. Tension increases quickly around the smaller driven sprocket.
4. Tension is high in the top span.

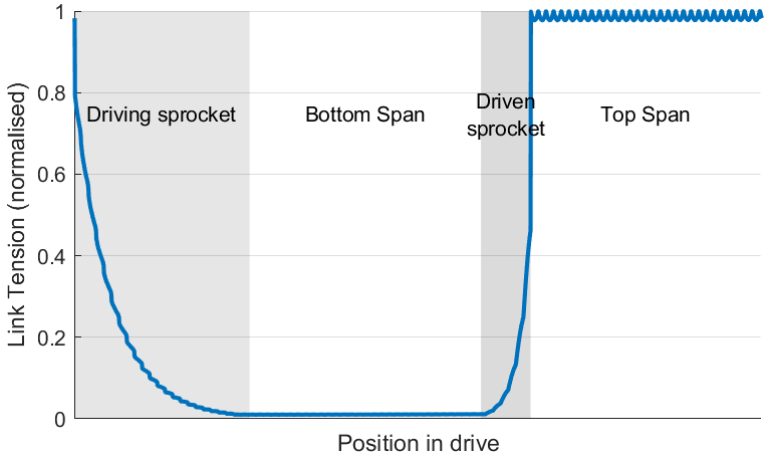

Figure 3.8: Sequence for link's path around drive, inducing changing tension: engaged with driving sprocket, travelling through the bottom span, engaged with driven sprocket, and travelling through the top span.

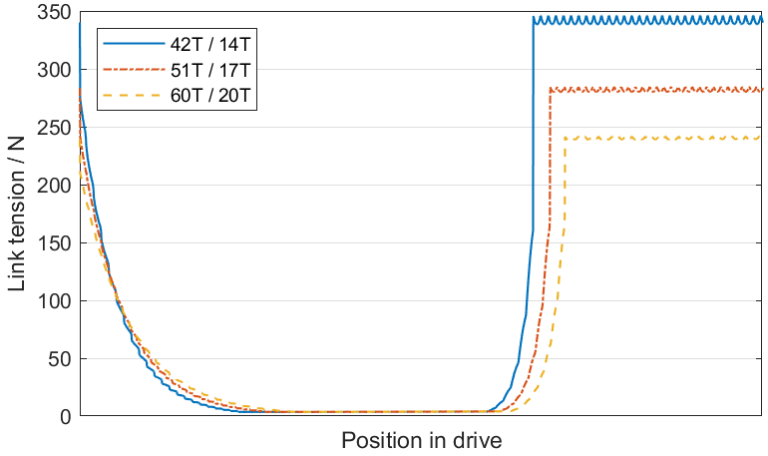

Figure 3.9: Transmission-under-test on TPM dynamometer test rig. Link tension changing with position in drive for 3 gear sizes of same ratio ($N_1/N_2 = 3, P_{in} = 250W, n = 95RPM$).

5. Polygonal action from changing torque radius of driving sprocket causes harmonic changes to top span tension.

Between the different cases plotted in Figure 3.9, there are several key distinctions in link tension around the drive:

1. There is lower tension in the top span for larger sprockets.
2. There is a more gradual increase in tension around driven sprocket for larger sprockets.
3. Polygonal action is more pronounced for smaller sprockets.

An equivalent loading scenario is created for the FPM dynamometer case, where induced tension is designed to match the tension in the top span. The same gear options are plotted in Figure 3.10.

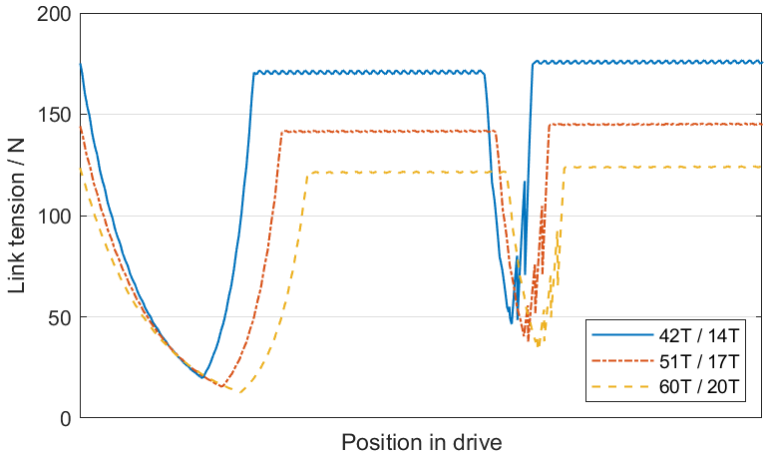

Figure 3.10: Transmission-under-test on FPM dynamometer test rig. Link tension changing with position in drive for 3 gear sizes of same ratio ($N_1/N_2 = 3, P_{eq't} = 250W, n = 95RPM$).

For all cases plotted in Figure 3.10, several general observations are made:

1. Tension of links travelling around the driving sprocket reduces to a minimum from the tight span and increases again to bottom span tension.
2. Bottom span tension is high.
3. Links around the driven sprocket experience large changes in tension to a minimum before climbing to top span tension again. The increase in tension is not smooth.
4. Top span tension is slightly higher than bottom span tension.
5. Both spans see harmonic fluctuations in tension.

Between the different gearing options plotted in Figure 3.10, key differences are:

1. Span tensions are reduced for larger sprockets.
2. Tension between links reaches lower value around larger sprockets.
3. Fluctuation in span tension is reduced for larger gears.

To better show the differences between 'equivalent' loading cases, the equivalent transmission is plotted for both TPM and FPM loading in Figure 3.11. Link tension is normalised relative to the maximum tension in TPM dynamometer case.

The tension in the spans of the FPM rig are approximately half that of the TPM rig, as expected. The bottom span of the TPM rig has very low tension. There is slightly more tension in the top span than the bottom in the FPM test rig, which is indicative of the rig being driven by the chainring in a forwards direction.

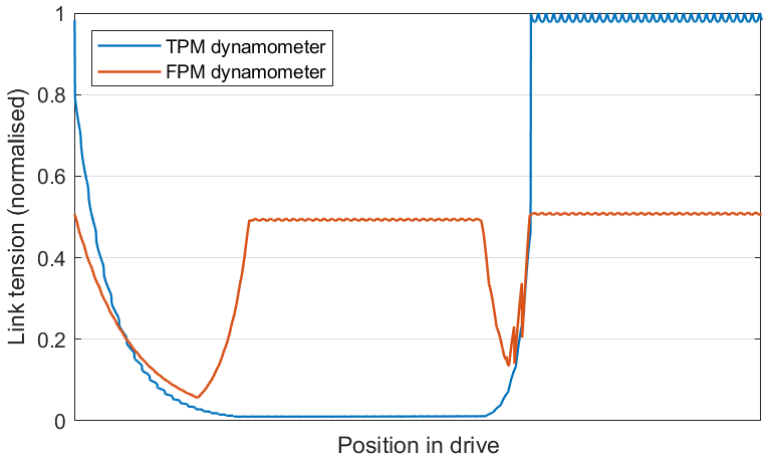

Figure 3.11: Normalised link tension changing around drive for two dynamometer types. Same equipment choices are modelled for both.

The effect of polygonal action is very pronounced in the TPM test rig. The polygonal effect here comes from the tension in the top span changing as the gear radius changes where the torque is acting, seen as half-sinusoids in the fluctuation of tension in the top span.

There are different fluctuations in the spans of the transmission on a FPM test rig which originate from the changing angle of spans due to movement of the floating sprocket. Furthermore, there are inconsistencies in the tension of links released from the driven sprocket into the top span. Within the model, this is due to the sporadic release of rollers into the span since the driven sprocket does not move at constant speed (shown in Figure 3.11).

3.3.7 Modelled power losses

The power lost during the rotation of the transmission on TPM and FPM dynamometer is modelled with Lodge's model of sliding friction [47, 48], detailed in Section 2.2.3.

Power loss may be expressed as the sum of frictional work done in the four articulating links, W, multiplied by the rate of articulation, adapted from Equation 2.19.

$$P_{loss} = \frac{N_s \omega_s}{2\pi} \sum_{i=1}^{4} W_i \tag{3.6}$$

The articulation of inner and outer links results in relative sliding of different surfaces between the pin and bushing. Since they must alternate, an average is taken of the two to define work done for one articulation, Equation 3.7. W_{pin} and W_{bush} are described in Equations 2.17 and 2.18.

$$W = \frac{W_{pin} + W_{bush}}{2} \tag{3.7}$$

Power loss is calculated for a range of input power with TPM loading conditions and equivalent input power for FPM loading conditions, based on equivalence described in Section 3.3.5. It is shown for the gear ratios illustrated previously in Figure 3.12.

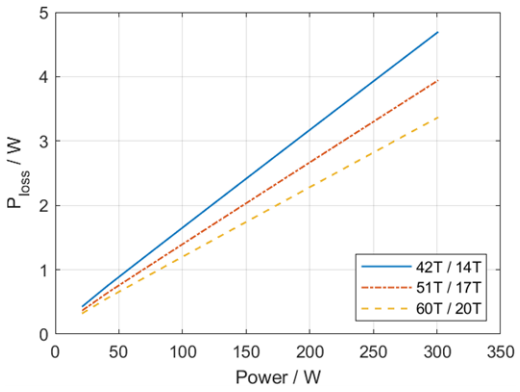

(a) TPM dynamometer.

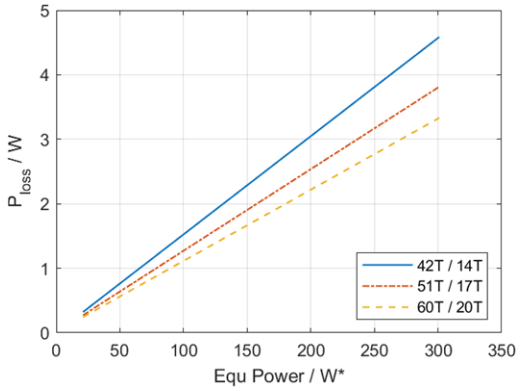

(b) FPM dynamometer.

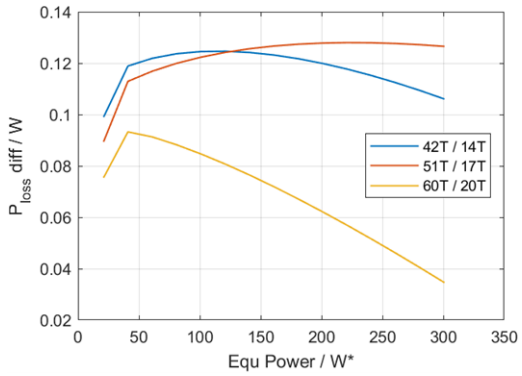

(c) Difference between modelled power loss on TPM and FPM dynamometer.

Figure 3.12: Modelled power loss [W] as function of input power at fixed speed (95 RPM driving) and similar nominal centre distance, with different number of chain links.

There is a subtle difference in power loss across all gear ratios, illustrated in Figure 3.12c. The trends between different gear ratios are in part from the geometry of centre distance and number of links in the drive. Fewer links in the slack span, which is the case for the 60/20 gear ratio, results in reduced tension contribution from self weight in TPM dynamometer. At increasing torque, increased stretch in the high tension spans also changes the links in the low tension span for the TPM case and changes centre distance in the FPM dynamometer case. The sensitivity to configuration and modelling strategy suggests further work is required in this area.

A subtle difference in power loss makes for significant relative difference in inferred or equivalent efficiency of the drive. When considering how efficiency changes across speed and torque map

which envelopes typical range in cycling application, the two dynamometer types produce quite different results, seen in Figure 3.13.

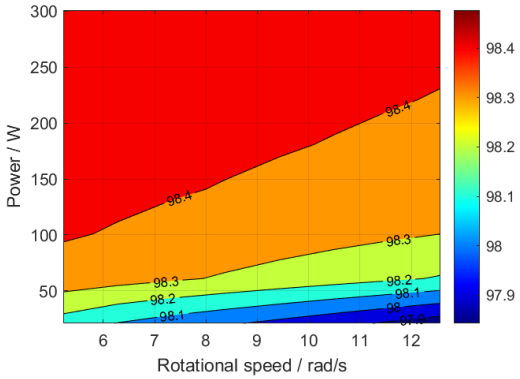

(a) TPM dynamometer modelled power efficiency [%] across test envelope.

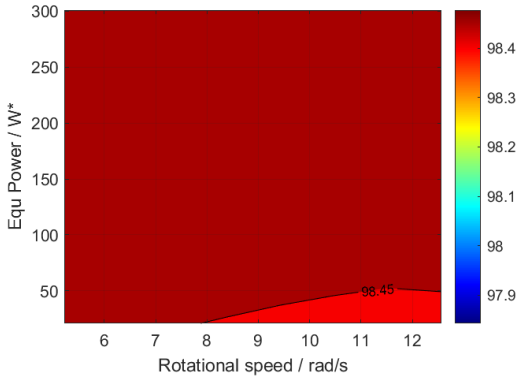

(b) FPM dynamometer modelled power efficiency [%] across test envelope.

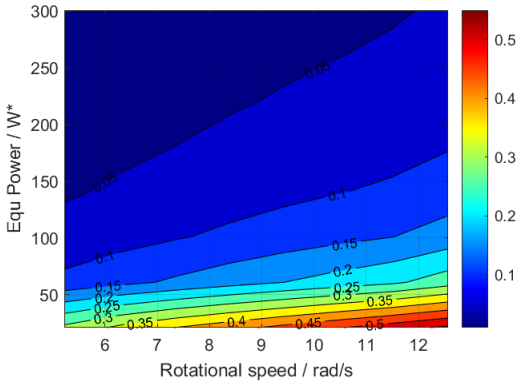

(c) Difference in modelled efficiency between TPM and FPM [%-pt] across test envelope.

Figure 3.13: Modelled power efficiency [%] of TPM and FPM test rig for nominally equivalent loading for changing speed and torque/equivalent torque.

Figure 3.13 shows there is very little speed and power dependence on efficiency in the FPM dynamometer case when compared with the TPM dynamometer. This is due to the effect of the lower-tension slack span, which essentially has constant losses so at low power transmitted these are proportionally higher. Even at higher load, the efficiency is over-predicted in the FPM dynamometer relative to the TPM dynamometer. At low loads, there is not good equivalence between the two loading cases, with an error in inferred efficiency of up to 0.5 %-pts, seen in Figure 3.13c. At high loads, the reduced error could be corrected by adjustment to the calculation of load equivalence.

3.4 Loss measurement and associated uncertainty

3.4.1 Inferred loss from transducer measurements

In TPM dynamometer test rigs, system losses are inferred from the difference between input and output power.

$$P_{loss',TPM} = \left\{ \tau_{in} \cdot \omega_{in} - \tau_{out} \cdot \omega_{out} \right\}_{TPM} \tag{3.8}$$

In FPM dynamometer test rigs, the power measured at the input is a direct measure of the losses, since the resistance to driving is entirely from system friction. Again, this friction does include bearings which must be compensated to describe the isolated transmission losses.

$$P_{loss',FPM} = \left\{ \tau_{in} \cdot \omega_{in} \right\}_{FPM} \tag{3.9}$$

In both cases, transmission loss P_{loss} differs from system loss $P_{loss'}$ since the support bearings and associated friction exist within the measurement loop. Given the same radial loads and speeds are induced in each shaft in both apparatus designs, these are neglected for simple comparison between the two test rigs.

3.4.2 Measurement uncertainty

Differences in measured variables and transmitted power between the TPM and FPM dynamometer test rigs impacts the uncertainty of the common measurand: power loss in the transmission-under-test.

As estimate of the uncertainty of torque measurements is made from the product of the quoted accuracy class A_C from the best available equipment and its rated nominal torque τ_{nom}.

$$u_{\tau,i} = A_{C,i} \cdot \tau_{nom,i} \tag{3.10}$$

The uncertainty of rotational speed measurement is not readily quoted, and a resolution of 0.1 RPM is assumed. This results in a rectangular distribution of $\pm 0.05 RPM$, which is expressed as an uncertainty rad/s according to Equation 3.11 .

$$u_{\omega} = \frac{0.05}{\sqrt{3}} \cdot \frac{2\pi}{60} = 0.003 \tag{3.11}$$

The resultant uncertainties of measured variables are calculated for suitable transducers in Table 3.3.

The uncertainty of the measurands, $U_{P_{loss}}|_{TPM|FPM}$, is calculated by methods described by the Guide to Measurement Uncertainty [6], introduced in Section 6.2. Equation 2.63 is applied to the

Table 3.3: Uncertainty performance of best available torque measurement equipment based on quoted ratings.

Dynamometer type	Shaft	τ_{appl} / Nm	τ_{nom} / Nm	A_C / %	u_τ / Nm	u_ω / rad/s
Transmitted Power Measurement (TPM)	Driving	100	200	0.02	0.04	0.003
	Driven	30	50	0.02	0.01	0.003
Frictional Power Measurement (FPM)	Driving	3	5	0.1	0.01	0.003

description of TPM power loss in Equation 3.8.

$$U_{P_{loss,TPM}}{}^2 = \left\{ \left(\frac{\partial P_{loss}}{\partial \tau_{in}}\right)^2 u_{\tau_{in}}{}^2 + \left(\frac{\partial P_{loss}}{\partial \tau_{out}}\right)^2 u_{\tau_{out}}{}^2 + \left(\frac{\partial P_{loss}}{\partial \omega_{in}}\right)^2 u_{\omega_{in}}{}^2 + \left(\frac{\partial P_{loss}}{\partial \omega_{out}}\right)^2 u_{\omega_{out}}{}^2 \right\}_{TPM} \tag{3.12}$$

Where uncertainties are those described in Table 3.3 and partial derivatives are calculated below.

$$\begin{aligned} \frac{\partial P_{loss,TPM}}{\partial \tau_{in,TPM}} &= \omega_{in,TPM} & \frac{\partial P_{loss,TPM}}{\partial \tau_{out,TPM}} &= \omega_{out,TPM} \\ \frac{\partial P_{loss,TPM}}{\partial \omega_{in,TPM}} &= \tau_{in,TPM} & \frac{\partial P_{loss,TPM}}{\partial \omega_{out,TPM}} &= \tau_{out,TPM} \end{aligned} \tag{3.13}$$

The uncertainty of power loss measurand on an FPM dynanometer is calculated similarly, applying Equation 2.63 again to the description of FPM power loss in Equation 3.9.

$$U_{P_{loss},FPM}{}^2 = \left\{ \left(\frac{\partial P_{loss}}{\partial \tau_{in}}\right)^2 u_{\tau_{in}}{}^2 + \left(\frac{\partial P_{loss}}{\partial \omega_{in}}\right)^2 u_{\omega_{in}}{}^2 \right\}_{FPM} \tag{3.14}$$

Uncertainty of torque and rotational speed measured variables are summarised in Table 3.3 and weighting factors, described by partial derivatives, are calculated below.

$$\frac{\partial P_{loss,FPM}}{\partial \tau_{in,FPM}} = \omega_{in,FPM} \quad \frac{\partial P_{loss,FPM}}{\partial \omega_{in,FPM}} = \tau_{in,FPM} \tag{3.15}$$

The calculated uncertainty of power loss measurands for TPM and FPM dynamometer tests is shown for a range of input parameters in Figure 3.14, assuming 3:1 gear ratio. Absolute uncertainty is similar between TPM and FPM cases at low speed. Uncertainty of power loss in TPM has more dependency on speed and increases to roughly twice the value of FPM at high speed.

The estimated absolute uncertainty demonstrates better performance in the FPM dynamometer despite the inferior accuracy class of the measurement equipment. This is because the transducer is rated for lower torques and directly measures frictional losses. Furthermore, despite the quality of the measurement devices in TPM application the inference of power loss from two independent measurements multiplies uncertainty.

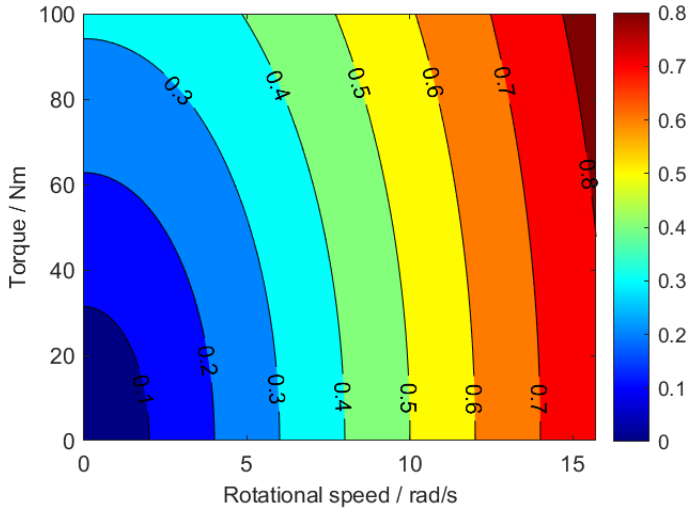

(a) $U_{P_{loss},TPM}$ $[W]$.

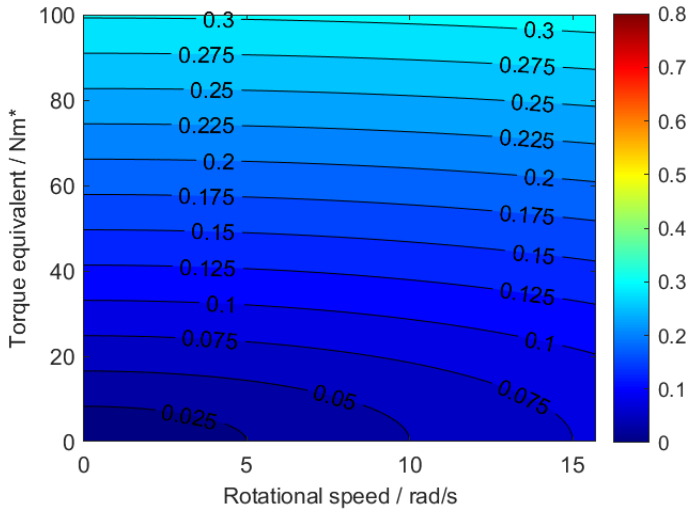

(b) $U_{P_{loss},FPM}$ $[W]$.

Figure 3.14: Absolute uncertainty of power loss test measurands across test envelope for different dynamometer types [W].

3.5 Summary of dynamometer types

The physical loading sources, boundary conditions and configurable hardware are summarised for dynamometer types in Table 3.4, including rough order of magnitude (ROM) monetary costs of building and running test apparatus of these designs.

3.6 Conclusions and further work

A Frictional Power Measurement (FPM) test dynamometer is beneficial in its cost of manufacture and replicating a broad range of span loads with relatively basic equipment. Its construction

Table 3.4: Key parameters of the TPM and FPM dynamometer types, with numerical examples from modelled cases.

Parameter	Dynamometer type	
	Transmitted Power Measurement (TPM)	**Frictional Power Measurement (FPM)**
Span loading source	Constant torque	Pre-tension
Loaded chain span	Top	Both
Derailleur pulleys	Yes/No	No
Cost to build ROM [£]	10^5	10^4
Cost to run (relative)	1	0.05
η [%] range	$97.84 - 98.47$	$98.4 - 98.48$
η [%] (90 RPM | 250W)	98.4	98.5
$U_{P_{loss}}$ [W] range	$0.16 - 0.80$	$0.02 - 0.46$
$U_{P_{loss}}$ [W] (90 RPM | 250W)	0.491	0.147

principles can be applied to tests of chains of any size by simply scaling the hardware. Its operation is also low cost, overcoming frictional losses only requiring relatively little power. In measuring the losses in the system, it also performs well due to small absolute uncertainty of measurement.

However, for replicating real loads there are some shortcomings, some of which are immediately apparent and some of which are shown with the modelling work addressed in this chapter:

1. The absence of a slack span changes the distribution of loading around the sprocket and due to the effect of the bottom span, there is error in loading equivalence between dynamometer types (most significant for systems with pretension or heavy chains).
2. Compliance in the centre distance from sprung mass loading will dampen dynamic behaviour in the transmission, shown by the reduced effect of polygonal action.
3. There is limited scope for conducting parametric testing (no auxiliary gears, no varying pre-tension, no varying speed).
4. The torque dependency of efficiency at low torque is not equivalent due to absence of a slack span.
5. The chain span is not subjected to the full tension of the 'equivalent' test, relying on losses always being linearly dependent on tension. This also means that chain links are not tested at maximum tension. Applying double tight span tension and halving the friction may be a

preferred method, although note there would be double the load on the bearings and hence increased parasitic friction.

A Transmitted Power Measurement (TPM) test rig offers opportunity for more complete parametric testing, including representing dynamic behaviours of transmission at particular loading cases. The difference in potential for dynamic excitation is demonstrated in the manifestation of the effect of polygonal action on the span tension. However, there are some considerations for testing bicycle-specific transmission which are not directly considered in previous incarnations of TPM dynamometers in literature:

1. Very signitficant torque in fixed gear track applications. Where riders perform standing starts in very significant gear ratios, the tension in the span is very high.
2. Non-constant torque in application.
3. Variable inertia.

For fundamental studies into the holistic performance of transmissions, particularly in cases where various configurations and loading considered to understand the parametric influence on performance, a FPM test rig is not appropriate. The development of the FPM test rig was made to measure accurate losses with relatively low cost hardware; the dependence of the TPM design dynamometer on expensive equipment remains.

Where more specified studies are required, the FPM dynamometer is attractive, and perhaps preferred. For instance, having both spans in tension is a form of accelerated test relative to conditions in use, so this could be an attractive option for creating low-cost rigs for determining wear characteristics. Indeed, this is the original test case for a rig of this type first developed by Hollingworth [37]. Given the presented FPM measures power losses, not wear, some adaptation would be required in this case.

The illustrative modelling done in this chapter is useful in demonstrating the expectation in link forces from different loading conditions, though is by no means exhaustive in its assessment. In particular, the differences in predicted power loss are shown to be sensitive to the transmission configuration and modelling choices, which should be further investigated. More complete analysis will be possible by collecting direct measurement of chain forces from rigs of this type to validate the work done here. With good confidence in such models, a more accurate model of loading equivalence may be applied to better align the expected loss measurement between TPM and FPM dynamometer test rigs.

There are interesting implications of changes in speed control and relative inertia of driving and driven shafts. Section 2.2.1 demonstrates how fluctuations in shaft speed come about due to chang-

ing chain speed and changing centre distance in the case of dynamometers with floating sprockets. Practical testing should be used to examine to what extent this modelled effect manifests.

3.7 Summary of Chapter 3

Two types of dynamometer test rigs were introduced as solutions for system level testing to complement and validate isolated tests discussed in Section 2.3.2 and advance understanding of holistic performance characterisation.

Key differences in their loading and measurement of losses are identified and the hardware necessary to create this identified. The main advantage of the TPM is that it is representative of the boundary conditions found in industrial and cycle applications. A key trade-off in creating these conditions is the monetary cost of manufacture and use. An FPM dynamometer is significantly cheaper in its realisation and operation. This stems from the difference in source of span tension in the transmission, although this fundamentally changes the operation of the transmission.

The effect of differences to the loading conditions are examined with models for chain link tension and frictional losses. These are presented as a platform for discussion, showing the influence of boundary condition on polygonal action and the difference in distribution of load around sprockets.

Uncertainty of inferred transmission losses is determined and shown to be better in FPM dynamometers due to torque transducer being rated for the power loss, not the power transmitted as is the case in TPM dynamometer.

In conclusion, the TPM dynamometer is demonstrated to be more appropriate for holistic performance characterisation with particular merit made of the representative dynamic behaviours and loading cases. The issue of uncertainty is a consideration for this research project and addressed in full in Chapter 6. The FPM dynamometer is shown to have strengths in different cases such as in system-level accelerated wear testing, for which is was originally developed.

THIS PAGE IS INTENTIONALLY LEFT BLANK.

Chapter 4

A New Dynamometer Test Rig: Design Summary

4.1 Introduction

A new dynamometer test rig has been designed and built at the University of Bristol to expand the scientific understanding of chain drive transmissions with particular focus on the context of track bicycle racing in elite competition. This is specifically intended to offer system-level testing of novel transmissions at real-world loads to complement isolated-variable testing which has been conducted in previous projects at the University in the form of Single Link Pendulum Tests [88]. System-level testing at real-world loads is of significant interest for testing of novel equipment, since there is confidence in the applicability of results compared with more abstracted testing methods discussed in Section 2.3.2. The built experimental apparatus is a Transmitted Power Measurement (TPM) dynamometer test rig, described in detail in Chapter 3. The experimental apparatus is shown in Figure 4.1.

A TPM dynamometer test rig offers capability which is important in complex loading cases and duty cycles seen in use-case of human-powered bicycles. The reasons are summarised:

1. Well defined boundary conditions.
2. Sprocket configuration of transmission-under-test is not fundamentally limited by rig design (range of gear ratios, presence of auxiliary gears).
3. Wide range of loading cases may be tested, with control over torque, speed, and inertial effects.
4. Dynamic, non-linear and hysteretic effects are induced in tests.

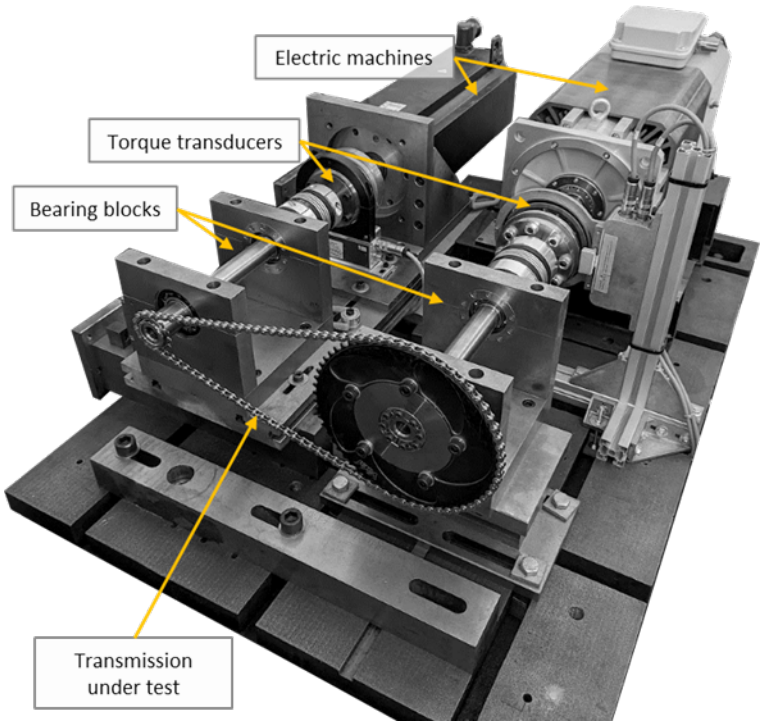

Figure 4.1: Photograph of the Transmitted Power Measurement (TPM) dynamometer test rig at the University of Bristol.

The previous chapter highlights weaknesses of a TPM dynamometer are not well addressed in the literature, which are true for this test apparatus:

1. Presence of parasitic influences on loss measurement, particularly in support bearings necessary to isolate the torque measurement devices from radial loads resulting from high span loads in the test transmission.
2. Uncertainty of measurement is relatively high and poorly understood.

This chapter serves to summarise the design choices and realisation of the dynamometer rig as built. The work summarised this chapter is based on the work done in an internal report [87], and is the original design work of its author which concluded in 2017. Following this introduction, Chapter 5, 6 and 7 address developments of testing capability and procedures on the described test apparatus. In particular, understanding of parasitic influences and uncertainty of measurement are developed in detail.

4.1.1 Structure of chapter

This chapter details the design of a novel dynamometer test rig for elite track cycling and its realisation. The structure is as follows:

1. The basis of the design is outlined with note made of its fundamental limitations.

2. A detailed requirement capture is presented per subsystem. The realisation of these requirements is demonstrated by showing the rig as built with specific hardware choices noted.
3. The capability of the rig is detailed with different configurations to allow a variety of loading cases to be addressed.

4.2 Basis of design

The dynamometer rig was built following a TPM design, based on the dual measurement dynamometers detailed in Section 2.3.3. A prototype mock-up of the experimental apparatus during design phase is illustrated in Figure 4.2. Two sprockets linked by transmission-under-test are independently driven and braked with opposing torque from two electric machines. On input and output to the transmission, torque and speed are measured with torque transducers. power lost on the path between the transducers can be determined by calculating the difference between the measured powers, and the efficiency of the system inferred. Bearings support the shaft and protect the torque transducers from parasitic shear and bending loads induced by the transmission spans.

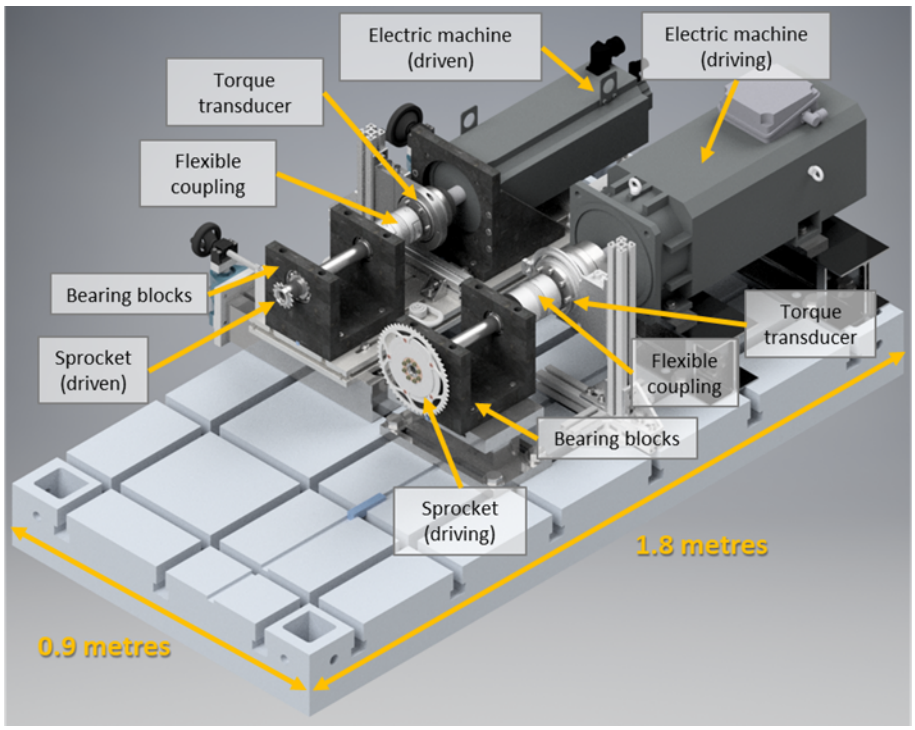

Figure 4.2: CAD render of prototype design of TPM dynamometer test rig [87].

Where the dynamometer offers novelty is in its realisation of cycling-specific boundary conditions and loading conditions such that the system-level performance of a Transmission-Under-Test (TUT) can be characterised and its dependence on numerous parameters tested. To achieve this,

capable machines are used with sophisticated control and the construction of the test bed is closely toleranced with high stiffness to ensure all loading is transferred via the TUT.

While the design aims to replicate conditions which are representative of real world use, there are fundamental limitations which exist in the current design:

1. A bicycle frame is not perfectly stiff and will flex in use. This cannot be incorporated into the current design, though active variable pitch and yaw could be considered in future rigs based on this design.
2. Air moving over transmission will impact aerodynamics and damping due to buffeting air in real world use. Air speed is zero in laboratory conditions, though this could be integrated into future rigs based on this design by using a wind tunnel in the test arrangement.
3. Introducing contaminants requires further consideration to isolate the transmission from the mechanics of the rig (e.g. with an isolated environmental chamber).
4. Centripetal effects from cornering which will increase forces on transmission cannot be recreated. This is most notable on a banked velodrome circuit, where regular tight corners are negotiated at high speeds.
5. Changing relative height of the sprocket centres occurs on a bicycle due to changes in gradient, which alters the angle of chain spans relative to gravity; this is not possible on this test apparatus.

These limitations are noted and comment made on the potential impact of changing conditions between test and real-world.

4.3 Specific requirement capture

The motivation for this design is to test cycling transmission with loading and configuration representative of that in typical use at elite level competition, while minimising the uncertainty of measurement and thus maximising accuracy of rig measurement. A comprehensive requirement capture to achieve this is detailed, separated by subsystem.

4.3.1 Configuration of transmission-under-test

Transmission-under-test should be mounted such that boundary conditions of the chain spans is representative of that in real-world use.

1. Fixed centre-centre distance between sprockets.

2. Presence of low-tension span on return path between sprockets.
3. Multiple configurations possible with/without idle sprockets (i.e. presence of rear derailleur or chain tensioner).

4.3.2 Loading of transmission-under-test

Loading of transmission-under-test must be controllable in live time and induce equivalent chain tensions to those found in real-world use, while driving the chain at typical speeds. Necessary requirements for loading are:

1. Wide torque range and precise control of torque in loading driving sprocket and braking the driven sprocket (driving/driven):
   (a) Up to 300Nm/100Nm instantaneous to capture extreme acceleration in track racing.
   (b) Up to 150Nm/50Nm continuous to capture extreme of steady state in track racing.
2. Application of a non-constant driving torque delivered at a frequency twice that of the rotational rate of the driving sprocket to mimic pedalling torque profile.
3. Accurate braking of test transmission based on real-world resistances and inertia.
4. Driving sprocket at up to 150 RPM ($\sim$16 rad/s); driven sprocket at up to 750 rpm ($\sim$80 rad/s), equivalent to 100km/h on $\sim$0.7m diameter wheels.

4.3.3 Measurement of loads

Torque and rotational speed must be measured at both transmission input and output.

1. Torque and speed should be measured to high accuracy with torque transducer.
2. Torque sensor should be appropriately rated for the expected loads.

The measurement devices should be protected from parasitic loads caused by high reaction forces from span tension in the TUT. This is necessary to ensure that the torque flange does not exceed its sheer load limit. The following should be included in the design:

1. Highly stiff structural pieces with negligible deformation under load.
2. Support bearings to isolate significant parasitic loads from sensitive measurement hardware. These should be oversized for their application to ensure there is negligible deformation under typical loads.

4.3.4 Data acquisition

Torque and speed data must be captured at high acquisition rate to effectively filter dynamic behaviours, and to specifically measure the influence of dynamics in test subjects.

4.4 Description of hardware in rig as built

The actual hardware used in this build represents existing equipment available within the laboratory and that available within the constraints of the budget. The rig as built is illustrated in Figure 4.1, showing the subsystems which are detailed in this this section.

The driving side is denoted 'Driveline A' and the driven side 'Driveline B', which is the nomenclature used in the rest of this thesis when referring to the dynamometer test rig.

4.4.1 Electric machines

Appropriately rated electric machines act as motor and brake for the driving and driven sides of the test transmission. Electric machines physically scale with rated torque so a larger machine is required for driving the cycling-specific transmission than in braking due to typical cycling gear ratios. The electric machines are summarised in Table 4.1 and shown in Figure 4.3.

Table 4.1: Parameters of electric machines used in dynamometer rig.

Electric machine parameter	**Driveline**	
	Driving side (A)	**Driven side (B)**
Manufacturer (model)	SEM (ASM 260 U)	Heidenhain (QSY190K)
Type	Asynchronous (induction)	Synchronous (PM)
Rated power / kW	24	12.2
Rated torque / Nm	153	39
Rated speed / RPM	1500	3000

4.4.2 Coupling assembly

Shafts on each Driveline are supported by the bearing blocks and affixed to the torque transducer flange with flexible bellows couplings, seen in Figure 4.4.

The lateral flexibility accounts for residual offset from the misalignment of shaft and torque flange. The couplings are very stiff in torsion. The torque flange is attached to the spindle of the electric machine with a rigid shrink-fit coupling. A laser shaft alignment tool is used to minimise lateral and angular offset in assembly, shown in Figure 4.5.

4.4.3 Measurement

Flange type torque transducers are installed inline between the bearings and the electric machines. The measuring body, housing the strain gauge assembly, is fixed in the shaft drive chain through

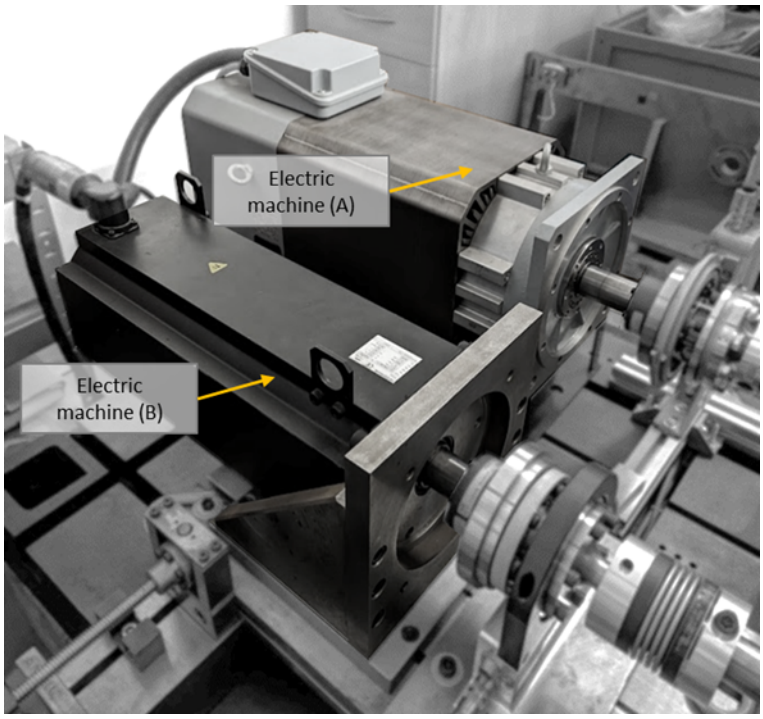

Figure 4.3: Electric machines for Driveline A and Driveline B.

rigid coupling flanges. The antenna is fixed to the base on Driveline B with appropriate shim to ensure concentricity. On Driveline A, the antenna is fixed to a vertical strut due to space constraints. The transducer models and key capabilities are summarised in Table 4.2, and images shown in Figure 4.4. The rated torque is conservative to ensure that overloading does not risk damage to the equipment.

Table 4.2: Details of torque transducers used in rig as built.

Torque transducer parameter	**Driveline**	
	Driving side (A)	**Driven side (B)**
Torque transducer series	HBM T10F	HBM T40B
Rated torque	500 Nm	200 Nm
Accuracy class	0.1	0.05

The torque transducers are installed according to manufacturer's guidelines.

4.4.4 Load isolation

The shaft is supported by two bearings to isolate the measurement equipment from parasitic loads induced by the transmission. The bearings are pressed onto the drive shaft and externally housed in a two split-block bearing housings, seen in Figure 4.6.

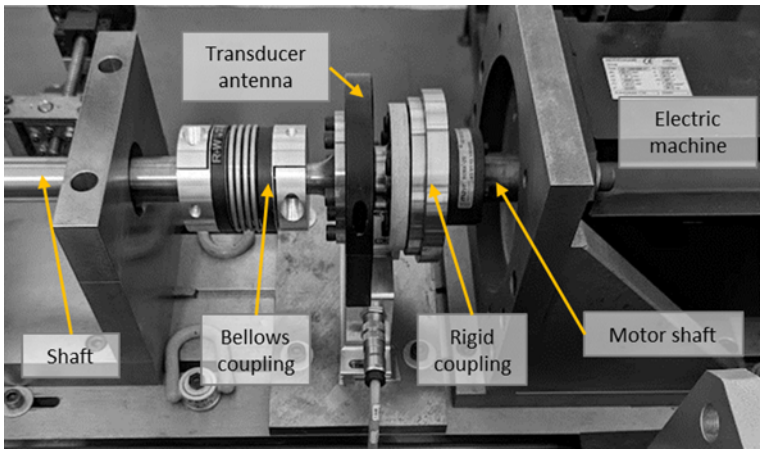

Figure 4.4: Attachment of flange type torque transducer between transmission shaft and motor shaft with bellows coupling and rigid coupling.

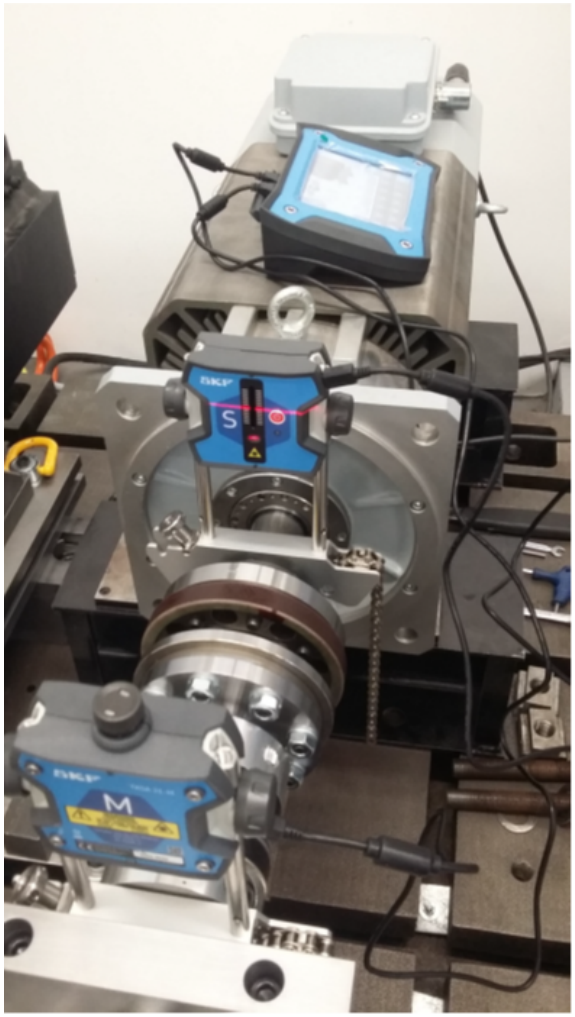

Figure 4.5: Alignment of shafts with SKF laser alignment tool [87].

Different bearings are selected for the front (transmission-side) and rear (machine-side) positions on either end of the shaft. Each sees different load due to the significant radial loads originating from the span tension from the test transmission which is cantilevered beyond the front of the

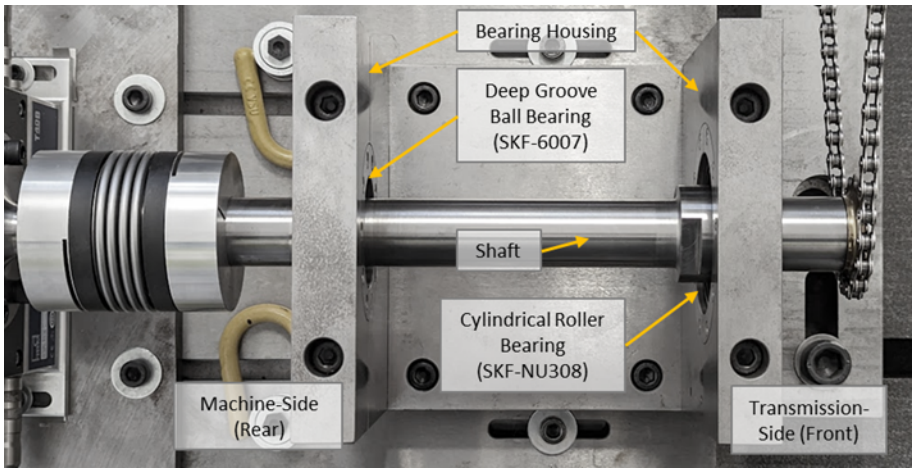

Figure 4.6: Bearing block (top view) showing SKF-6007 deep groove ball bearing supporting machine end (left of picture) and SKF-NU308 cylindrical roller bearing supporting transmission end (right of picture).

bearing block. The transmission end (front) is the 'high-load' end; hence, large cylindrical roller bearings are used here (SKF-NU308). These are significantly oversized for the application. With static load rating of 78 kN, they are approximately an order of magnitude above an extreme loading case from span tension. This design is intended to limit the dependence of bearing performance on radial load. Furthermore, the use of a cylindrical roller bearing and a deep groove ball bearing ensures that the shaft is sufficiently constrained axially.

On the machine end (rear), which is the 'low-load' end, physically smaller deep groove ball bearings are used (SKF-6007). Less extreme radial loads are experienced in this position and deep groove ball bearings provide the best option to minimise friction. Deep groove ball bearings also constrain the shaft axially. Schematics of both bearings can be seen in Figure 4.7 and their details summarised in Table 4.3.

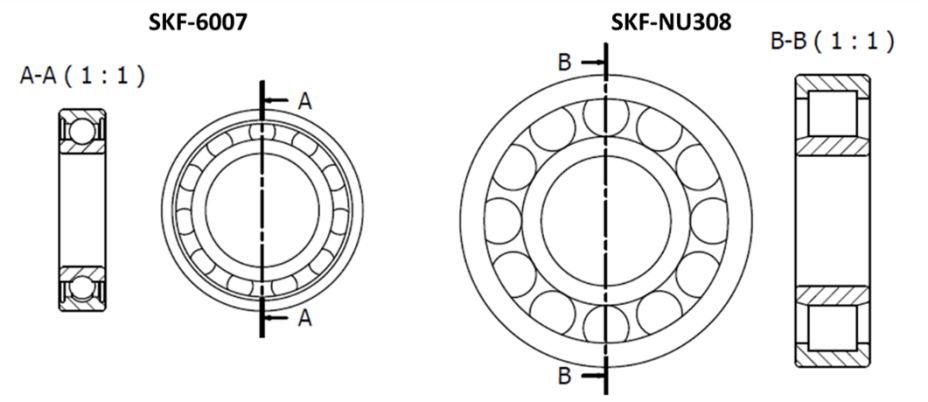

Figure 4.7: Bearing series on each driveline.

Table 4.3: Details of bearings used in rig as built.

Bearing parameter	Bearing position	
	Transmission end (front)	Machine end (rear)
Bearing type	Cylindrical roller	Deep groove ball
Bearing series	SKF-NU308	SKF-6007
Bore diameter / mm	40	35
Outside diameter / mm	90	62
Width / mm	23	14
Rated static load / kN	78	10.2

The bearings operate without seals to reduce frictional drag. Seals are not necessary as laboratory conditions are maintained and bearings are cleaned and relubricated regularly. Light oil is used as lubricant and regularly applied, reducing viscous drag as well as temperature and speed dependent viscous properties which can be expected from grease-based lubrication.

4.4.5 Mounting of transmission-under-test

A variety of transmission types must be tested with various sprocket bolt patterns standard to cycling or industry, or threaded connections. Solutions are chosen to maintain concentricity with minimal measurement during installation. The mounting options are designed to offer maximum flexibility with standard components and maintain the same shaft wherever possible. It is both time and cost saving to limit the changeover between tests, but importantly also ensures that parameters such as shaft alignment can be maintained between comparative tests.

On the driving shaft (Driveline A), the shaft has a ground surface finish over which a hub is fitted with a shrink-fit coupling (Figure 4.8). Several hubs are made to suit a variety of internal diameter and bolt patterns. A cycling chainring is attached to the appropriate hub with appropriate fixings.

The driven side (Driveline B) has attachments for rear sprockets of several designs. Two different shafts are made with attachments appropriate to two major types of fitting in bicycles:

1. Rear ‘fixed gear’ sprocket, with a threaded shaft-end for sprocket (1.37” x 24 tpi) and lock-ring (LH 1.29” x 24 tpi)
2. 11-Speed cassette sprockets, with a splined shaft-end for Shimano Hyper Glide (HG) technology and internal lockring thread

Both shafts are shown in Figure 4.9, with the fixed gear sprocket in use on the test rig. To test a transmission with a cassette, a rear derailleur is mounted to the face of the bearing housing block.

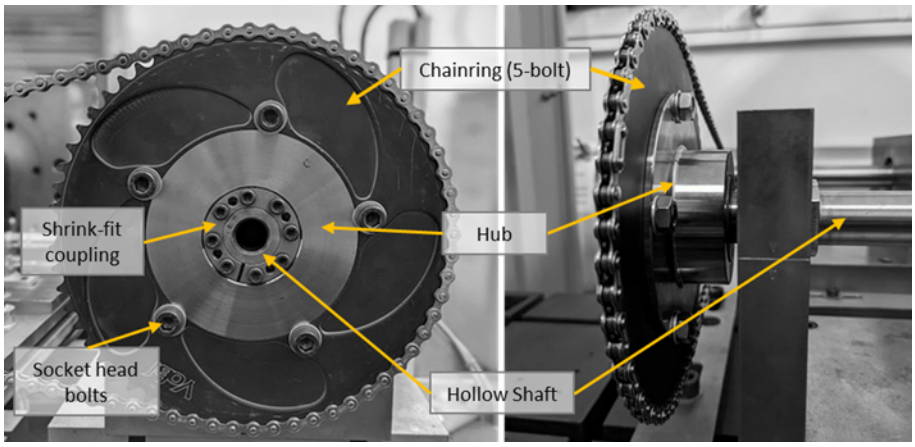

Figure 4.8: Chainring attachment with hub and shrink-fit coupling.

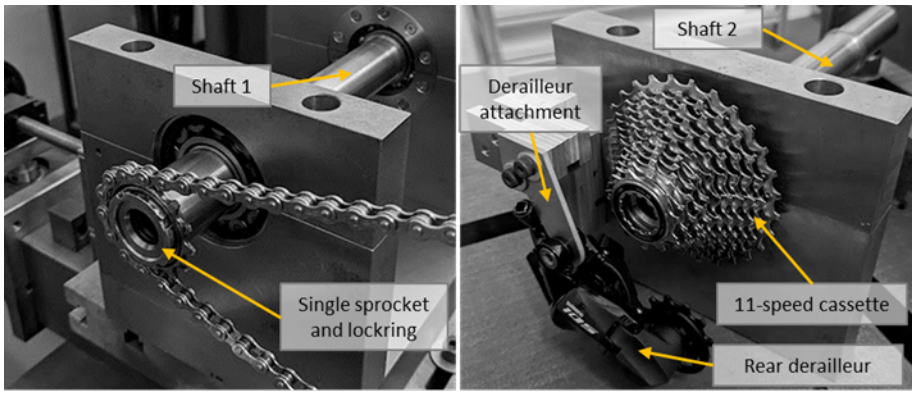

Figure 4.9: Driven side shaft with two shaft options: shaft 1 with thread-on sprocket attachment (with lock-ring thread) and shaft 2 with Shimano HG 11-speed cassette attachment.

4.4.6 Test transmission boundary condition control

To offer flexibility with test transmission boundary conditions, the entirety of Driveline B is built on a sub-bed which can move in a plane parallel to the main test bed, highlighted in Figure 4.10.

The sub-bed is adjusted using lead screws attached to the side of the bed and sub-bed, positioned at the front and rear. These adjust laterally and change the yaw of Driveline B. The axial adjustment of Driveline B is also possible to adjust in-plane alignment of the sprockets. Shaft centre distance can be adjusted to specified distance, or to achieve a specified pre-tension in the test transmission. The sprocket plane alignment is determined with a dial gauge indicator measured from a datum surface.

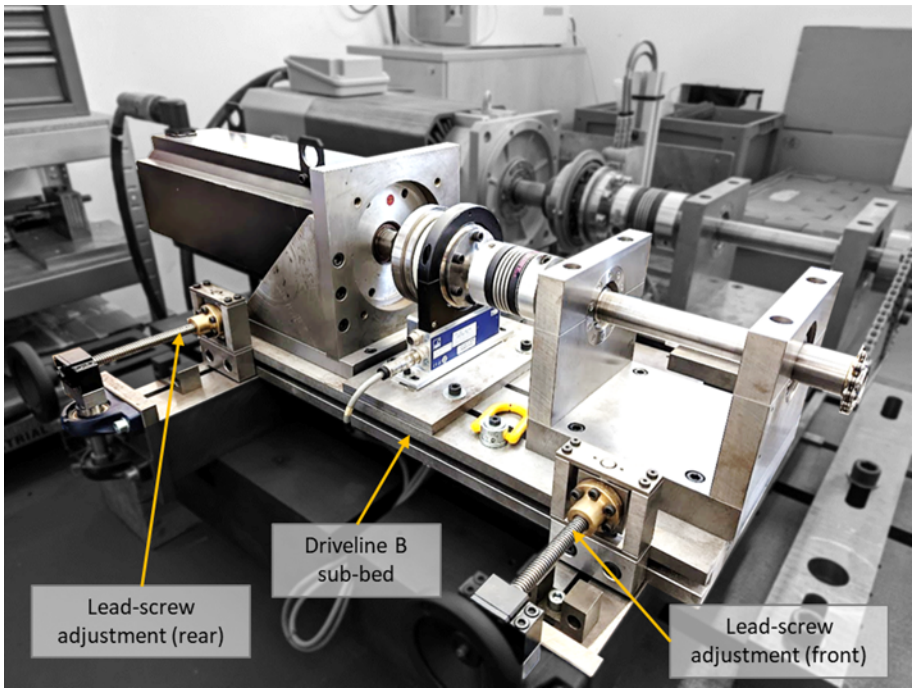

Figure 4.10: Driveline B sub-bed shown with adjustment lead-screws.

4.5 Control of electric machines

Electric machines are controlled via Variable Frequency Drives (VFDs) and real-time dSpace computing hardware such that position, speed and torque data may be used to define drive parameters. A schematic of the control interfaces is shown in Figure 4.11.

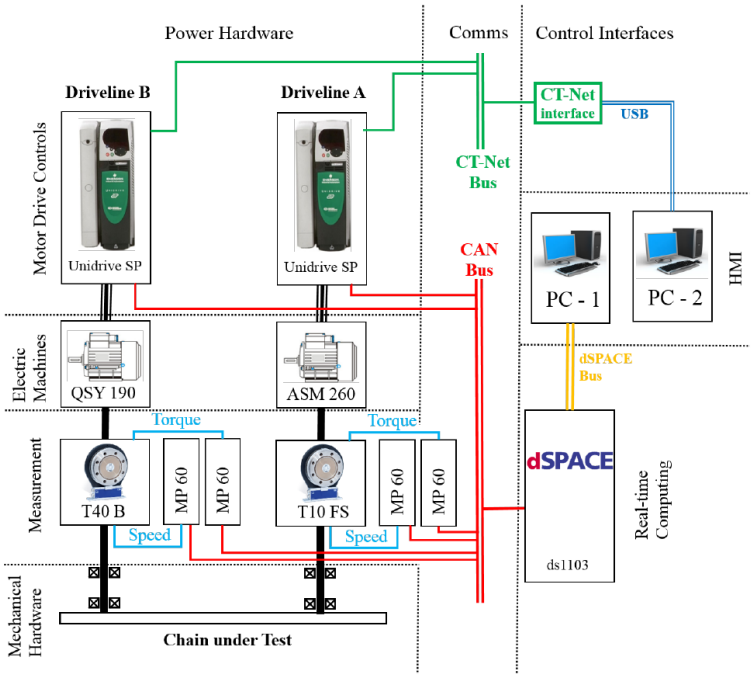

Figure 4.11: Schematic of control and computing interfaces with dynamometer rig hardware [87].

In typical testing, the electric machine on Driveline A acts as motor (drawing current from electrical supply) and that on Driveline B acts as generator. Generated power is recirculated, such that after the start-up power is delivered, the operation of the dynamometer rig draws power necessary to top up the losses from the circuitry, drives, machines and transmission. Previous testing solutions based on the four-square power testing principle (described in Section 2.3.1) recirculate power mechanically at the detriment of changing the conditions for transmission-under-test. The sophisticated power recirculation solution does not mechanically influence the transmission-under-test.

The drive is not limited to this driving/driven configuration, and the ability of both electric machines to operate in all four quadrants (motoring or generating, in positive and negative directions, Figure 4.12) offers significant flexibility. Further, the control systems allow both machines to be run in both 'torque-mode', where the machine delivers a specified torque, and 'speed-mode', where the machine delivers a specified speed, controlled by the relevant control mechanisms.

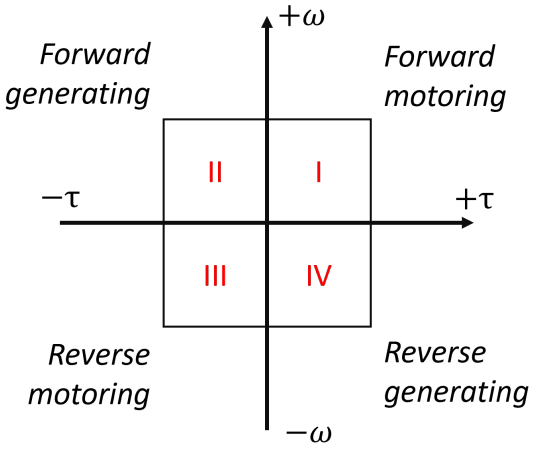

Figure 4.12: Four quadrants of electric machine operation (forward motoring, I: $+\tau, +\omega$; forward generating, II: $-\tau, +\omega$; reverse motoring, III: $-\tau, -\omega$; reverse generating, IV: $+\tau, -\omega$).

In torque-mode operation, a torque is demanded of the motor in the direction specified. This torque may drive the transmission (motoring) or resist the transmission (generating). A PID controller maintains the torque at the specified value. This may result in motoring, generating or dynamically changing between the two. In torque control, external resistance is necessary to limit a machine's speed since there is very little internal resistance. Safety trips and safe use practice ensure that personnel and equipment is protected from spin out and mechanical failure.

In speed-mode operation, a speed is demanded of the motor. A nested PID controller (within the torque/current loop) varies the applied torque (motoring) or resistive torque (generating) to main-

tain that speed. As in torque mode, an electric machine may dynamically swap between motoring and generating to achieve a steady speed. Due to the nested control loops there is increased latency with speed control.

With these fundamental workings of both electric machines, several applications are possible, detailed in the next section.

4.6 Novel capabilities of chain dynamometer test rig

The control mechanisms and hardware capability of the dynamometer allow for a number of novel capabilities which are summarised here.

4.6.1 Model of rider applied to driving motor

It is possible to apply a model of the pedalling torque of a cyclist to the driving electric machine on the new dynamometer. Pedalling torque is not constant, but varies with a frequency twice that of the crank rotation due to the riders preference for applying torque downwards. It is of interest in parametric testing because the tensions in the chain span may vary quite significantly due to this harmonic disruption, affecting the frictional interaction at chain links and disrupting or exciting dynamic behaviours which may be different when considering constant torque application only.

The crank movement travels through a phase of positive impulse (a cyclist's down stroke) and a negative impulse, illustrated in Figure 4.13. Minimising the magnitude of the negative impulse results in a more physiologically efficient the pedalling stroke [21]. Cyclists with more experience improve their minimum torque [28]. Pedalling changes with workload [41], and with rider fatigue [69].

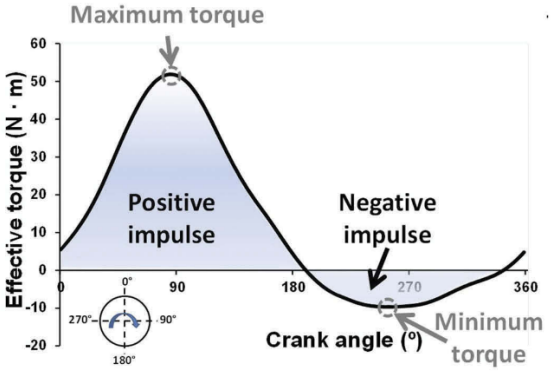

Figure 4.13: Effective torque from a single pedal stroke for full rotation crank [28].

A rider's torque profile can be applied by driving Driveline A in motoring torque mode with a real-time model updating the torque input as a function of rotational position. This model can be expressed using a series of sinusoids, meaning that a specific rider profile could be applied from data captured by a crank or pedal based power meter by expressing a measurement as a suitable number of sinusoids (via a Fourier transform).

Alternatively, a general expression for rider torque, τ, can be applied such as in Equation 4.1 which approximates the summed torque from two cranks at 180° separation.

$$\tau = \tau_{av}\left[1 + K\sin\left(2\theta\right)\right] \tag{4.1}$$

τ_{av} is mean torque and θ is the angular position of the shaft. Variable K represents the scaling of the torque variation relative to the average torque. The effect of varying K is illustrated in Figure 4.14.

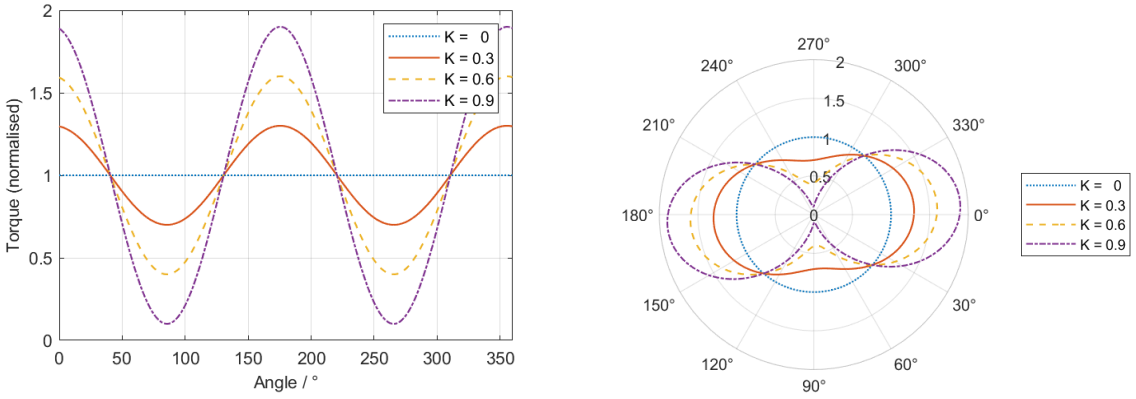

(a) Cartesian coordinates.

(b) Polar coordinates.

Figure 4.14: Effect of varying smoothness factor 'K' on delivered torque as function of crank angle for a full rotation in different coordinate systems.

With the same value for average torque, T_{av}, the energy expenditure is equivalent for an integer number of full sinusoids (half rotations of driving shaft). However, it can be seen that the variation in torque is quite significant, resulting in proportional changes in tension in the chain span and hence contact force between articulating chain links.

4.6.2 Inertial loading of resistive torque

Another capability offered by the control systems of the dynamometer rig as built is a model describing the braking on Driveline B to replicate real-world conditions. By operating Driveline B in 'torque-mode', the real-world resistance may be applied based on description of rolling resistance, aerodynamic forces and modelled inertia, such as Equation 4.2.

$$\tau_B = 0.5\rho C_d A_f \omega^2 {r_w}^3 + mg\mu r_w + \left(m{r_w}^2 + 2I_w\right)\alpha_w \tag{4.2}$$

Where variable description and typical values for constants are given in Table 4.4.

Table 4.4: Real-world resistive torque model parameters.

Model parameter	Description	Approx. value	Units
ρ	Air density	1.2	kgm^{-3}
C_d	Coefficient of drag (rider and bicycle)	0.3	-
A_f	Frontal area (rider and bicycle)	1	m^2
r_w	Wheel radius	0.35	m
m	Mass (rider and bicycle)	90	kg
g	Gravitational constant	9.81	$kgms^{-2}$
μ	Coefficient of rolling friction (tyre-ground)	0.002	-
I_w	Wheel 2nd moment of inertia	0.05	kgm^2
ω	Rotational speed (live – measured)	$\sim$	$rads^{-1}$
α	Rotational acceleration (live – calculated)	$\sim$	$rads^{-2}$

Real-time expressions for speed and acceleration of the shaft are used in this expression, which makes this more challenging to implement than the torque control based on position above. It is not just limited by the speed of signal, but the speed of computation (acceleration is not directly measured), and the error in the estimation of acceleration.

With implementation of this configuration, the effect of different inertias on transmission behaviours could be investigated. Inertia offers damping to accelerations, which may be caused by active acceleration from a rider or by dynamic effects in the transmission. The relative inertia in the driving and driven sides will affect how the accelerations in the transmission from dynamic effects is felt by the rider, or whether there are fluctuations in bicycle velocity.

4.6.3 Integrated electronic shifting

The hardware necessary for testing multi-speed transmission systems with rear derailleurs, typical in road cycling, is designed and built (shown in Section 4.4.5). This can be implemented in a low-technology solution by manually changing gear with cable actuated shifting during testing or between tests to ascertain performance of gears configurations in multi-speed transmissions.

Alternatively, gear shifting can be integrated into a duty cycle by exploiting modern electronic shifting systems into the control of the rig. A duty cycle may cover a number of torque and speed

test points, and also a selection of gears to submit a transmission to a more full test envelope. A standard test may be defined with a variable 'gear' parameter. Alternatively, in recreating a recorded sequence from cycling data the duty cycle could recreate conditions on the rig including gear shifting at defined points from the recording.

Gear selection might otherwise be modelled based on other parameters. As a rider modifies their gear to ensure that the pedal cadence is at an optimum value, the selected gear may be defined on the test rig to maintain rotational speed of the driving shaft within defined limits.

4.6.4 High fidelity rider torque profile and race simulations

Data captured from on-bicycle measuring equipment could be used to define loading conditions of transmission-under-test on the dynamometer test rig. A high-fidelity rider torque profile could be applied by the driving machine against loads created from recorded races. This allows detailed understanding of the performance of transmission during a race by recreating the conditions the transmission experiences in use.

Time-dependent performance of transmission and lubricant, points of dynamic interference between rider and transmission and the effect of fatigue may all be tested with ability to collect a significant quantity of data. Analysis could motivate changes to equipment design or race strategy.

4.7 Summary of design process

The general construction of the novel dynamometer test rig was successful. Hardware is installed for use; power electronics and drives are configured and the rig is able to run a range of duty cycles utilising some of its configurative capability. There is scope for further development in the torque-mode control of braking and in using real world data to create output from a rider digital twin.

The electric machines used are rated appropriately for steady state conditions in velodrome racing, including with non-zero pedalling smoothness. They are limited in delivering the extreme accelerations possible in track racing from a standing start. Further, the two electric machines are of two different varieties due to availability of appropriately rated motors: Driveline A has an alternating current asynchronous induction machine while Driveline B has a permanent magnet synchronous machine. There will be differences in the delivery of torque and speed control of each, as well as the machine losses (due to additional magnetising losses in the asynchronous machine).

The torque transducers are over-sized for typical torque measurements to allow an appropriate safety factor. This results in additional measurement uncertainty at low measured torque. The conservative selection is necessary as extreme overloading would risk plastic deformation of the strain gauges. The accuracy class of the transducers might be improved in future upgrades at some additional investment.

4.8 Conclusions

This chapter presents the design work to create a new style dynamometer test rig for high torque cycling applications, with novel elements to test high performance transmissions in high fidelity loading regimes (in particular those associated with elite track cycling). The design is successfully realised, with limitations of the rig as built identified.

Realising the capability of the test rig through design of test protocols, analysis of data, quantified uncertainty and examining the holistic performance of transmission at a system level is detailed in the remaining chapters.

4.9 Summary of Chapter 4

1. The basis of design for a new dynamometer test rig was a Transmitted Power Measurement dynamometer, following design principles from several examples in literature.
2. Specific design requirements for testing in conditions representative of elite track racing context were set out.
3. The rig as built was detailed. Several key details were addressed which are the subject of research later in the thesis, including:
   (a) The operation of electric machines as motor and brake and their associated control systems.
   (b) The requirement and implication of including support bearings to protect sensitive measurement equipment.
   (c) The measuring equipment itself, in its operation and quality of measurement.
   (d) The novel capability of the test rig and its application in current and future work.

Chapter 5

Isolating Test Efficiency: Parasitic Influences on Assessment of Transmission Performance

5.1 Introduction

The design aim for the dynamometer test rig was to develop a facility which reproduces operating conditions as expected on a racing track bicycle. The solution is a sophisticated hardware-in-the-loop system with actuators, measurement, and control hardware. The use of these complex electro-mechanical systems have potential to introduce parasitic influences (undesirable effects in addition to nominal loading) on the test conditions and measurement, which is addressed in this chapter.

The parasitic influence on the test subject can be described by its influence on loading conditions, and its influence on measurement. These are annotated in the test apparatus schematic shown in Figure 5.1. Parasitic influence on loading originates in the machine elements in the respective drivelines through frictional or inertial effects. Inertial effects can be minimised by testing at steady state set points or by mathematical compensation. For most tests the former option is taken. Steady state operation is subject to the performance of control loops surrounding the Variable Frequency Drives (VFDs) and electric machines. Without appropriate mitigation, parasitic influences on loading limit the repeatability of testing conditions for the transmission-under-test and introduce inertial loads to the test subject, to the detriment of specified real-world loading conditions the rig is designed to emulate.

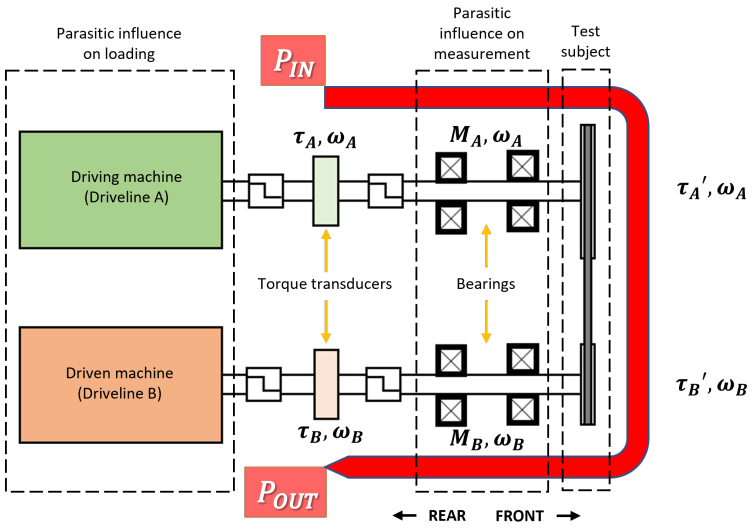

Figure 5.1: Power measurement loop on dynamometer test rig with hardware sources of parasitic influence on assessment of transmission performance annotated.

The presence of support bearings in the dynamometer introduces parasitic influence on the measurement, such that the torque at the sprocket on the driveline, τ', is not equivalent to the torque measured at the transducer, τ. This is illustrated in Figure 5.1. The difference between the measurements is equivalent to the bearing frictional moment, M. Bearing frictional moment may be minimised by appropriate hardware selection, and by maintaining favourable running conditions and lubrication. However, its influence cannot be mitigated to a point of being negligible since the energy consumed in the bearings is of a similar order of magnitude to that in the test subject. Hence, compensation is necessary to isolate the test losses from bearing losses in measurements.

This chapter discusses the parasitic influences on the loading conditions of the test subject and the measured power loss. Strategies employed to mitigate these influences are presented, and to compensate where mitigation is not sufficient. The impact of compensation methods on measurement uncertainty is considered in full in Chapter 6. The effect of higher frequency dynamics on measurement performance is examined in Chapter 7.

In this work, a system boundary is drawn around the measurement loop illustrated in Figure 5.1 and understanding the necessary compensation of parasitic influences within this power loop prioritised. This area addressing the effect of the support bearings makes up a significant portion of the following two chapters. Influences on the nominal loading conditions and measurement outside this system boundary are minimised through mitigation methods in test design which will be discussed, though this limits the functionality of the experimental test rig and will be an area for further work.

5.1.1 Structure of chapter

Sources of parasitic influence from hardware on the dynamic test rig introduced in Chapter 4 are discussed. Four sources of parasitic influence are highlighted:

1. Electric machines as driving motor and driven generator.
2. Misalignment in the shaft assemblies inducing spring forces in bellows couplings.
3. Influence of test sequencing and data processing on measurements from torque transducer.
4. Reducing and compensating bearing frictional moment.

To appropriately compensate the bearing frictional moment, loading conditions for the bearings are derived from span loads in transmission tests. Several strategies for bearing frictional moment compensation are discussed from the literature:

1. Applying models from literature introduced in Section 2.4.
2. Measuring speed-dependent frictional moment of bearings in situ, as used in previous dynamometer test rigs in the literature discussed in Section 2.3.3.

Benefits and weaknesses in these methods are discussed, and new test apparatus designed to determine frictional moment in equivalent test conditions to those on the dynamometer test rig. Results are presented alongside existing methods of bearing compensation to offer conclusions on their relative merits.

5.2 Mitigation of parasitic influences on loading and measurement

5.2.1 Control of electric machines

Energy is consumed in mechanical, electrical, and electromagnetic systems within electric machines on the dynamometer test rig. These are outside of the power measurement loop illustrated in Figure 5.1 and hence do not have direct influence on the test measurement. However, they impact the delivery of driving and resistive loads to the transmission and hence the repeatability of experimental test points. This might be mitigated by running equipment at thermal equilibrium in a controlled environment, though this is not practical with current testing methods.

The inertial influence of the machine elements in each driveline of the dynamometer are neglected in tests by running at steady state test points. The steady state operation is subject to the performance of Proportional-Integral-Derivative (PID) control loops surrounding the Variable Frequency Drives (VFDs) and electric machines. With improper tuning of the controllers' PID gains, several issues may be introduced which are illustrated in Figure 5.2:

1. Long settling time.
2. Constant steady state error.
3. Dynamic steady state error.

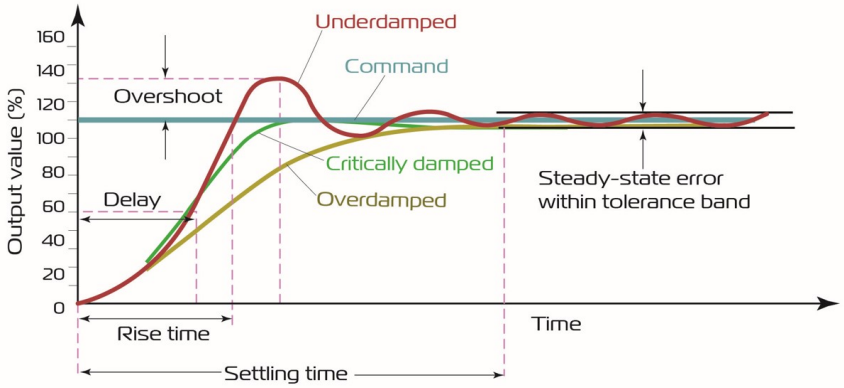

Figure 5.2: Under-damped and over-damped system control results in larger steady state error and longer settling time [13].

A long settling time causes practical issues for testing, where long data points must be considered to capture sufficient data at steady state, or risk including inertial effects. A constant steady state error presents issues of repeatability as discussed above. A dynamic steady state error is induced by motors rapidly changing operational quadrant (Figure 4.12) in an under-damped control system. This presents two problems:

1. Harmonic loads can be induced in the transmission.
2. High frequency direction changes to strain gauges inducing error in measurement (further discussed in Section 5.2.3).

The gains in controllers are defined with an 'autotune' programme on the VFD for each drive which optimises the speed control by accounting for the inertia in the system. In post processing, data is checked for steady state. Harmonic influences on captured data from motor dynamics is evaluated in Chapter 7.

5.2.2 Spring forces from bellows couplings

Strain gauges used to measure torque in the flange transducers on each driveline of the dynamometer do not distinguish between true torsion and bending or lateral loads due to parasitic influences. The presence of support bearings protects the torque flange from significant lateral loads due to high span tensions, though some parasitic loads remain due to the presence of the bellows coupling.

Torsionally stiff bellows couplings are capable of operating under up to 1 mm lateral offset, allowing some forgiveness in mechanical assembly. However, where there is deflection in the coupling to compensate for misalignment, illustrated in Figure 5.3, the resultant flexing of the bellows will provide a spring force against the shaft and torque flange. This results in some harmonic straining in the torque transducers as the shaft rotates.

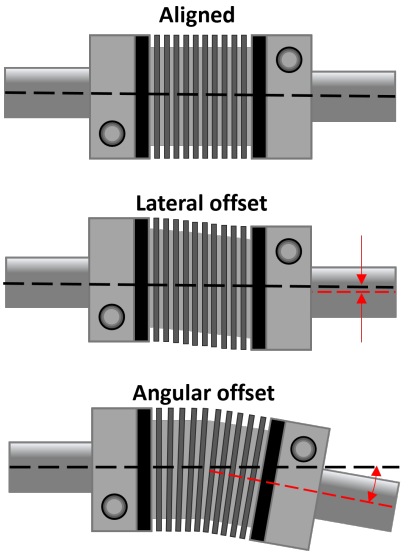

Figure 5.3: Possible misalignment in bellows coupling, resulting in parasitic load proportional to stiffness in direction of displacement.

Both lateral and angular offset is minimised using a laser alignment tool, shown in Figure 4.5, which is capable of measuring lateral offset to precision of 0.01mm. Residual offset is measured in orthogonal planes (vertical and horizontal), and total offset calculated. The product of the offset and the lateral spring stiffness of the coupling, quoted by the manufacturer, gives the parasitic influence of the coupling misalignment.

The torque flange has strain gauges spread evenly around the inside circumference of the hollow shaft. Lateral offset will cause increased reading on one side, and decreased reading on the opposite. To minimise the effect of any misalignment, the torque measurement is averaged over an time interval equivalent to an integer number of shaft rotations such that the result is an integral over a complete period of variation over a full rotation.

5.2.3 Torque measurement sensitivity to loading direction

Torque transducers are sensitive to the direction of applied torque. The linearity deviation of a torque measurement is the uncertainty associated with the deviation from a linear curve of the measured signal relative to the true value. When direction is reversed, the strain in the torque

flange is unloaded dissimilarly from how it was loaded. This results in a hysteresis effect, as seen in Figure 5.4, and causes reversibility errors.

To mitigate the effect this has on the torque measurement, electric machine loading and duty cycle design are biased to ensure loading is in constant direction.

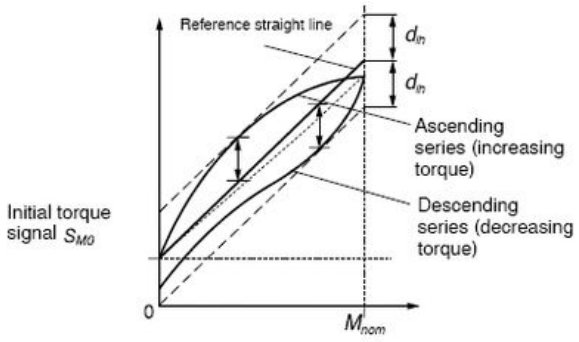

Figure 5.4: Linearity deviation of torque signal and hysteresis at reversal of load direction, resulting in two paths for increasing and decreasing measurement and zero error [31].

The design of the duty cycle also must be sensitive to this, in both the direction and quality of loading. Steps taken to improve quality of measurement by duty cycle design and post processing include:

1. Dynamic torque is minimised by limiting rate of acceleration.
2. Direction of loading is consistent for each drive, ensured at start-up by programming a pre-load at zero speed. Note this is positive motoring for the driving machine (Driveline A) and negative braking for the driven machine (Driveline B).
3. Zero compensation (tare) is determined by non-zero extrapolation to minimise impact of zero error hysteresis.
4. Data test points are pseudo-randomised for speed test values.
5. Torques are always measured at increasing loads for each speed test point.
6. Data averaged over integer rotations to remove dynamic changes.

5.3 Compensation of parasitic influence of bearings

5.3.1 Bearing frictional moment in determination of test efficiency

The efficiency of the system may be calculated as in Equation 5.1 by finding the ratio of output power (Driveline B) to input power (Driveline A) from measurements of torque and speed

illustrated in Figure 5.1.

$$\eta_{system} = \frac{P_{OUT}}{P_{IN}} = \frac{\tau_B \omega_B}{\tau_A \omega_A} \tag{5.1}$$

The efficiency of the transmission is different from the efficiency of the system since the torque at the sprockets, τ', is not equivalent to the measured torque at the transducer flange. Hence, transmission efficiency is described as in Equation 5.2.

$$\eta_{transmission} = \frac{P'_{OUT}}{P'_{IN}} = \frac{\tau'_B \omega_B}{\tau'_A \omega_A} \tag{5.2}$$

Where torque at driving sprocket, τ'_A , and driven sprocket, τ'_B, are defined as below.

$$\tau'_A = \tau_A - M_A \tag{5.3}$$

$$\tau'_B = \tau_B + M_B \tag{5.4}$$

Where M_A and M_B are the combined frictional moment of the bearings on Driveline A and B respectively.

The effect of bearing frictional moment is direct on inferring power efficiency of transmission. Both bearing pairs are identical types and similar in lubrication and environmental conditions, however they see quite different speeds due to typical test transmission gear ratios. Hence, each driveline must be compensated by substantially different values. In addition to compensating parasitic loss, the impact of this process on measurement uncertainty must also be assessed.

5.3.2 Compensation methods with dynamometer data

In the literature addressing chain dynamometer test rigs presented in Section 2.3.3, the parasitic influence of bearing frictional moment on test measurement is not frequently commented on. Where it is, compensation is made by determining speed-dependent losses of the bearings in situ with existing measurement hardware. The shaft or shafts on which measurements are made are turned at incremental speeds and frictional moment measured with the torque transducer. If testing is done at a single test speed, only losses at this speed need to be considered.

Bearing characterisation with this method is both cost- and time-efficient, though there are some weaknesses in this approach in high torque applications:

1. Unknown dependence of frictional moment on radial load.
2. Same (low) load is applied to both bearings simultaneously (the cantilevered radial load from chain spans results in a high-load front end and low-load rear end, discussed in Chapter 4).
3. Inherently high uncertainty by using high rated torque transducers for very small measurements.

4. Electric machines operate in different quadrants than in test-operation (Figure 4.12). This may change the torque measurement characteristics.

Further literature is presented in Section 2.4 which discusses analytical methods for determining bearing frictional moment. These offer a load- and speed-dependent solution for evaluating bearing frictional moment, and are explored in the next section.

5.4 Analytical modelling as compensation of bearing frictional moment

Several models in the literature which describe frictional moment in rolling element bearings are introduced in Section 2.4. The two most widely used are those developed by Harris [30] and SKF [71], where Harris' model builds on previous work from Palmgren [63]. Both models are used to estimate the frictional moment in the bearings of the specific types and conditions seen in the typical test envelope on the dynamometer test rig. Parameters for bearing types and lubrication types are described in each instance.

5.4.1 Loading and environmental conditions

The bearings on the chains dynamometer test rig operate at very low speed and low radial load relative to their rated parameters. Clean laboratory conditions are maintained and the raceways and rolling element bearings are lubricated with light oil which is regularly reapplied. This is quite different from typical industrial application, where conditions are much closer to the rated load and speed, with grease lubrication and packaging to protect the bearings from contaminants and minimise regularity of maintenance.

The loading state and lubrication, therefore, is at an extreme for the support bearings in the dynamometer test rig. Furthermore, each of the four bearings experience a unique combination of load and speed. Driveline A and Driveline B are low speed and high speed respectively in typical tests due to the large gear ratios tested in a cycling application. Furthermore, the 'front' bearings (transmission-side) are subjected to significantly more radial load than the 'rear' bearings (machine-side) from the high span tensions in the chain. This is the rationale for different bearing types used in transmission-side and machine-side on the shafts, explained in Section 4.4.4. The design also negates axial loads.

The radial loads on the bearings are calculated from combination of span tensions and shaft weight. Radial load from span tension, T, is induced by tensions in the top span, T_t, and bottom span,

T_b, of the transmission-under-test. Input torque, τ_1, acts at the chain pitch circle radius, r_1, in combination with any pretension in the system, T_{pre}.

$$T_t = \frac{\tau_1}{r_1} + T_{pre} \tag{5.5}$$

$$T_b = T_{pre} \tag{5.6}$$

The span tension acts at angle φ from the horizontal (Figure 5.5b), dependent on sprocket pitch radii and distance between centres, c.

$$\varphi = \sin^{-1}\left(\frac{r_1 - r_2}{c}\right) \tag{5.7}$$

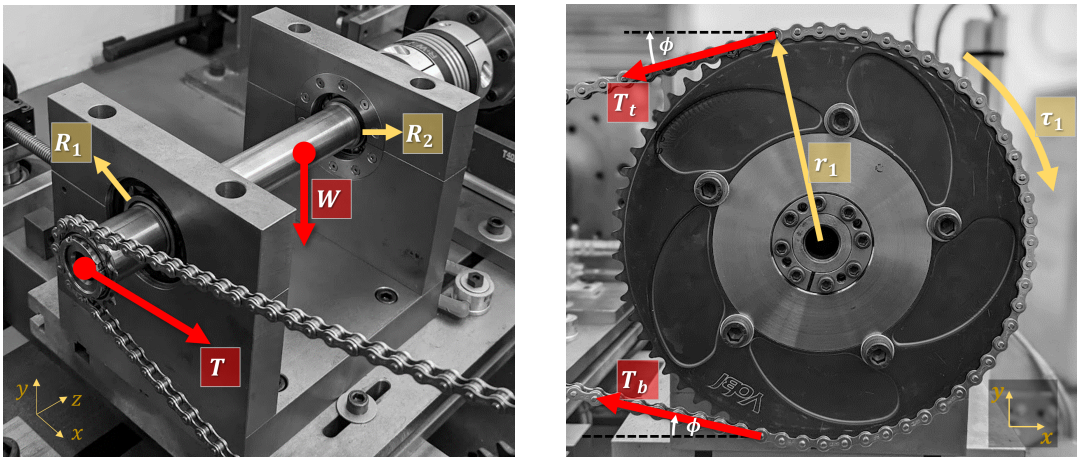

(a) Radial loads from weight and spans.

(b) Span loads induced by applied torque.

Figure 5.5: Resultant radial load on bearings from shaft weight, W, and combined span forces, T induced by applied torque.

Radial load from span tension can be described in x (parallel to the test bed) and y (against gravity) orthogonal directions:

$$T_{(x)} = (T_t - T_b)\sin\varphi \tag{5.8}$$

$$T_{(y)} = (T_t + T_b)\cos\varphi \tag{5.9}$$

This force on the shaft overhangs the bearings in the z direction and combines with the shaft weight in radial loading of the front and rear bearings. Force balance in the vertical plane (y) are shown in Figure 5.6a.

The vertical component of radial force on the bearings is calculated with by balancing moments. $R_{3(y)}$ is assumed to be zero.

$$R_{1(y)} = T_{(y)}\frac{(L_1 + L_2)}{L_2} + W\frac{(L_2 - L_3)}{L_2} \tag{5.10}$$

$$R_{2(y)} = T_{(y)}\frac{L_1 - WL_3}{L_2} - W\frac{L_3}{L_2} \tag{5.11}$$

In the horizontal plane, there is no contribution from shaft weight and bearing radial load is from chain span component only, shown in Figure 5.6b.

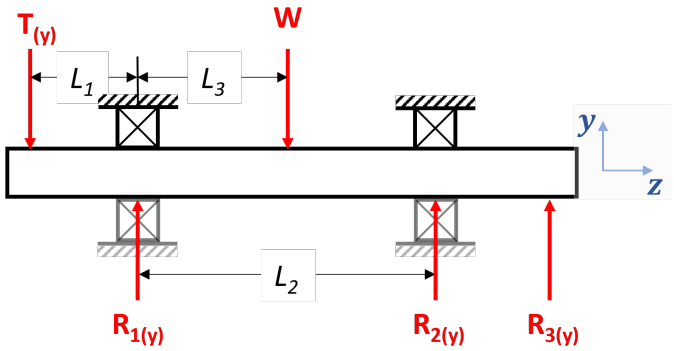

(a) Vertical plane (side view).

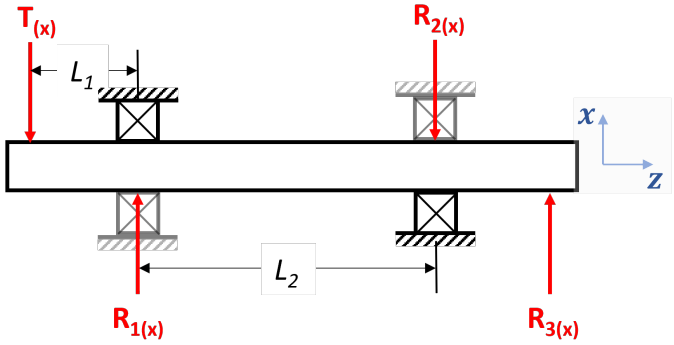

(b) Horizontal plane (top view).

Figure 5.6: Point loads on shaft from span load reaction in vertical and horizontal planes.

The horizontal component of radial force on the bearings is described in equations below. $R_{3(x)}$ is assumed to be zero.

$$R_{1(x)} = T_{(x)} \frac{(L_1 + L_2)}{L_2} \tag{5.12}$$

$$R_{2(x)} = T_{(x)} \frac{L_1}{L_2} \tag{5.13}$$

Total radial load is calculated by combining the orthogonal components for each bearing with Pythagoras:

$$R_1 = \sqrt{\left(\frac{T_{(x)}\,(L_1 + L_2)}{L_2}\right)^2 + \left(T_{(y)} \frac{(L_1 + L_2)}{L_2} + W \frac{(L_2 - L_3)}{L_2}\right)^2} \tag{5.14}$$

$$R_2 = \sqrt{\left(T_{(x)} \frac{L_1}{L_2}\right)^2 + \left(T_{(y)} \frac{L_1 - WL_3}{L_2} - W \frac{L_3}{L_2}\right)^2} \tag{5.15}$$

The geometric parameters of the bearing support in the dynamometer test rig are summarised in Table 5.1.

Table 5.1: Geometric parameters for calculation of bearing radial load.

Parameter	Description	Value	Units
L_1	Sprocket centre to bearing centre 1	60	*mm*
L_2	Bearing centre 1 to bearing centre 2	200	*mm*
L_3	Bearing centre 1 to mass centre	100	*mm*
W	Weight of shaft assembly	19.6	*N*

Where the gear ratio approaches 1:1, φ may be approximated as a small angle. When the torque-induced load dominates the contribution from shaft weight and the bottom span tension, equations for R_1 and R_2 reduce to:

$$R_1 = T\left(1 + \frac{L_1}{L_2}\right) \tag{5.16}$$

$$R_2 = T\frac{L_1}{L_2} \tag{5.17}$$

Applying geometric parameters from Table 5.1, bearing radial loads in the dynamometer test rig are approximately $R_1 = \ 1.3\ T$ and $R_2 = 0.3\ T$.

5.4.2 SKF model of frictional moment

As presented in the literature review, the SKF model for frictional moment is described by summing terms describing four independent sources of friction:

$$M = M_{rr} + M_{sl} + M_{seal} + M_{drag} \tag{5.18}$$

In the application on the test rig, there are no seals present on the bearings and there is no drag component since the bearings are not operating in an oil bath lubrication system. Hence, two terms reduce to zero $M_{seal} = M_{drag} = 0$ and the model simplifies to the terms describing rolling resistance and sliding friction:

$$M = M_{rr} + M_{sl} \tag{5.19}$$

Descriptions of terms in Equation 5.19 application are summarised in Table 5.2.

5.4.3 Harris model of frictional moment

The Harris model of bearing frictional moment is presented in full in Section 2.4. It is described by the sum of frictional moments due to applied load M_1, viscous friction M_v and end-flange friction M_f.

$$M = M_1 + M_v + M_f \tag{5.20}$$

Table 5.2: Variables for SKF model of bearing friction for front and rear bearings on chain dynamometer test rig.

Model parameter	Front bearing (SKF-NU308)	Rear bearing (SKF-6007)	Units
R_1	1.09×10^{-6}	4.1×10^{-7}	$\sim$
d_m	65	48.5	mm
d	40	35	mm
D	90	62	mm
K_Z	5.1	3.1	$\sim$
S_1	0.16	3.73×10^{-3}	$\sim$
S_2	0.0015	$\sim$	$\sim$
K_{rs}	6×10^{-8}		$\sim$
ν	23.31 [82]		$mm^2 s^{-1}$
F_a	0		N
μ_{bl}	0.12		$\sim$
μ_{EHL}	0		$\sim$

In the application on the dynamometer test rig, there is negligible axial load by design. Hence, the end flange term is eliminated $M_f = 0$ and the equation reduced:

$$M = M_1 + M_\nu \tag{5.21}$$

Descriptions of terms in Equation 5.21 are detailed in Chapter 2.4. Parameters associated with the bearings and conditions in the application are summarised in Table 5.3.

Table 5.3: Harris model parameters in dynamometer test rig application.

Model parameter	Front bearing (SKF-NU308)	Rear bearing (SKF-6007)	Units
z	$\sim$	0.004	$\sim$
y	$\sim$	0.55	$\sim$
F_s	$\sim$	$= F_r$	N
C_s	$\sim$	10,200	N
f_1	0.0004	$= z\left(\frac{F_s}{C_s}\right)^y$	$\sim$
f_0	0.6	0.7	$\sim$
d_m	65	48.5	mm
F_a	0		N
ν_0	23.31 [82]		$mm^2 s^{-1}$

5.4.4 Modelled results

The bearing frictional moment defined by SKF and Harris models is calculated for an operating envelope of driving torque and speed on the dynamometer test rig. Radial loads are calculated according to theory presented in Section 5.4.1. The frictional moment from front (SKF-NU308) and rear (SKF-6007) support bearings on the dynamometer test rig are displayed individually in Figure 5.7.

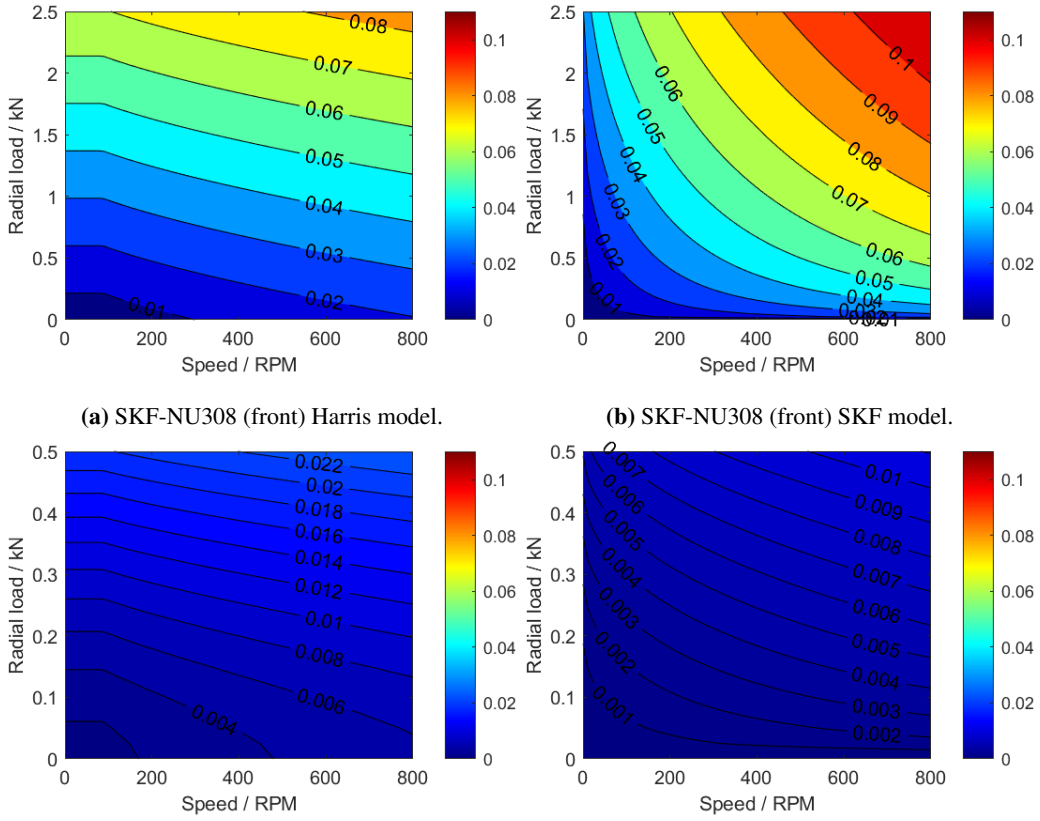

(a) SKF-NU308 (front) Harris model.

(b) SKF-NU308 (front) SKF model.

(c) SKF-6007 (rear) Harris model.

(d) SKF-6007 (rear) SKF model.

Figure 5.7: Modelled bearing frictional moment [Nm] as function of applied torque and speed.

Frictional moment is calculated with both models over a range of speed and radial load which is representative of typical use. The losses are significantly lower for the rear bearings due to reduced radial load, and favourable friction parameters as a ball bearing over a cylindrical roller bearing.

The SKF model predicts more significant frictional moment in the front bearings (SKF-NU308), particularly at high speed. The Harris model predicts small speed dependence. In the rear bearings (SKF-6007), frictional moment has similar dependence on speed and load across both models. The Harris model predicts roughly twice the frictional moment in this bearing than the SKF model.

5.5 Experimental assessment of bearing frictional moment

Literature addressing test apparatus previously developed to determine the radial load and rotational speed dependence of bearing frictional moment is summarised in Section 5.5. New test apparatus was built at the University of Bristol following existing design principles. Equivalent bearings to those in the dynamometer test rig were tested under equivalent loads, speeds, lubrication regime and in similar laboratory conditions. The validity of existing models for this application can be determined, or empirical results used directly to compensate parasitic losses in the bearings of the chain dynamometer test rig.

5.5.1 Design of experimental apparatus

Four bearings are arranged on a common shaft with inner and outer pairs housed separately in a whippletree assembly, illustrated in Figure 5.8. The outer bearing pair is housed in stiff bearing block, identical to those used in the chain dynamometer test rig. This is mounted on a raised test bed. The inner bearing pair is housed in floating carriage. Load is applied to the carriage vertically downwards via a threaded bar attached securely to the carriage.

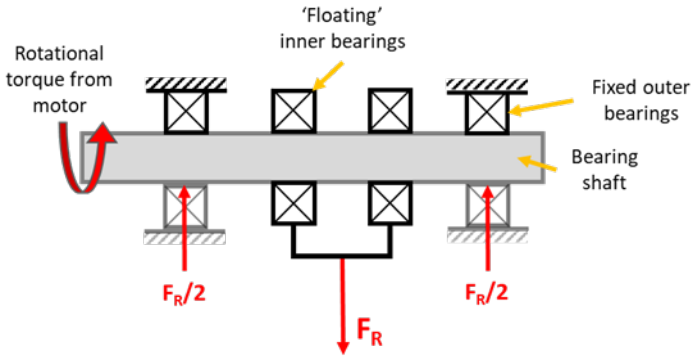

Figure 5.8: Load application to four test bearings, with F_R applied to inner bearings via floating carriage. With a stiff shaft (no bending), force reaction applies approximately $F_R/2$ to each bearing radially.

The vertical force on the carriage is applied via an assembly which is anchored to the base test bed, illustrated in Figure 5.9. With a stiff tension spring and turnbuckle in series, load is applied with sufficient incremental control to vary downwards force to the carriage. There is a load cell between the whippletree and load applicator assembly to accurately determine the applied load. All components have high stiffness and moment arms are minimised where practical to limit bending effects.

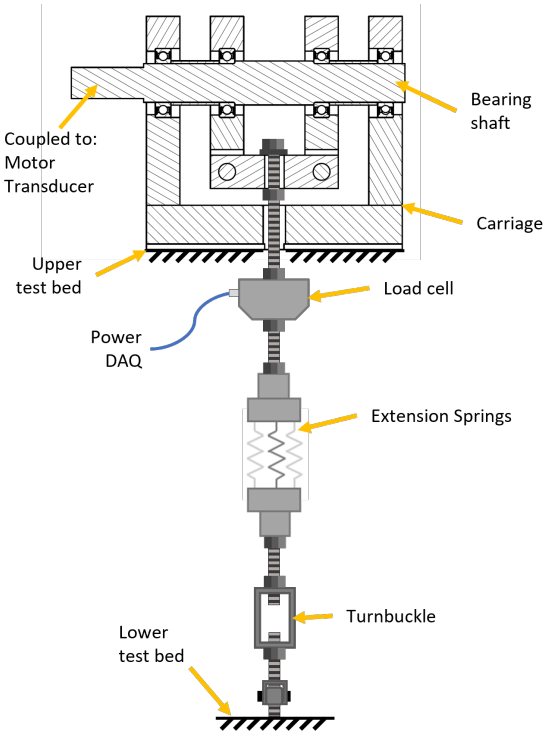

Figure 5.9: Schematic of load application to bearing carriage. The assembly connects the bearing carriage to the lower test bed.

The test rig as built is illustrated in Figure 5.10. The bearing shaft is turned by a servomotor at set speed points. With appropriate speed control to drive the shaft at constant speed, the torque overcome by the motor will be equal to the friction present in the system. A suitably rated pedestal type torque transducer is mounted between motor and bearings to measure frictional torque in the system, equal to the frictional moment in the four test bearings. Speed control to maintain steady state conditions discussed in Section 5.2.1 is more prevalent here due to the low rotational mass of this system. Parasitic mitigation discussed in Section 5.2 for the test rig is applied for bearing tests.

5.5.2 Design of experiments to isolate results for individual bearings

The frictional moment for applied radial load and speed must be determined for bearings individually since all four bearings on the dynamometer test rig experience a unique combination of speed and radial load. By design, there are four bearings-under-test on the rig apparatus and so the result for an individual bearing is inferred from the test measurement with some assumptions, discussed here.

Where four bearings of the same variety are tested together, it is assumed that each pair shares the applied load evenly and they incur equivalent losses. By testing four in parallel, this introduces

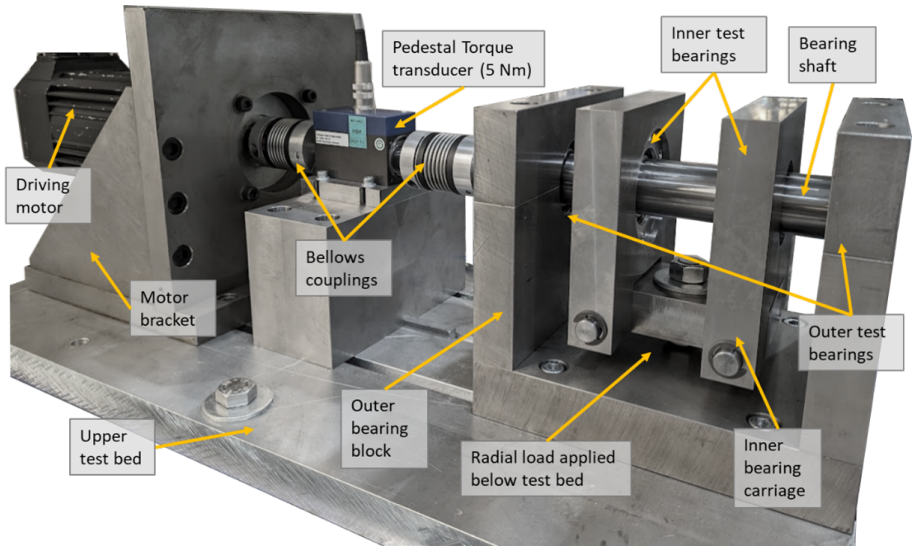

Figure 5.10: Photograph of upper test bed for bearing rig for determination of frictional moment as function of radial load and speed.

some randomness in manufacturing tolerances and serves to average the results. This type of test is possible for four deep groove ball bearings, and so the SKF-6007 bearings can be tested this way (Test-1).

Four cylindrical roller bearings cannot be tested in this way since the shaft is not axially constrained. Though no axial loads are induced, the bellows coupling has significant compliance in this direction. Dynamic excitation at a resonant point could cause inconsistencies in test results by flexing the strain gauges in the transducer, and risk damaging sensitive measurement equipment.

A secondary test – 'Test-2' – is designed where SKF-NU308 bearings are mounted as an inner pair in the carriage which is constrained axially with housing supports. An SKF-6007 outer pair is maintained. To infer results from the SKF-NU308 bearing pair, the results from the SKF-6007 tests must be used to appropriately isolate the frictional moment from the carriage pair. Shafts are manufactured for each test and are illustrated in Figure 5.11.

The rotational speed measurand is equivalent for all bearings since they share a common shaft. Inference of the load and frictional moment for individual bearings in Test-1 (4-off SKF-6007) is summarised in Table 5.4. The frictional moment is determined for the average loading and speed conditions across the four bearings. Radial load from weight upstream from load cell is added; masses as measured with a balance are summarised in Table 5.5. Carriage mass includes mass of the carriage, load cell and attachments.

The inner and outer bearings experience subtly different loads since the shaft weight is supported only by the outer bearings due to downward orientation of the applied load. There is therefore an

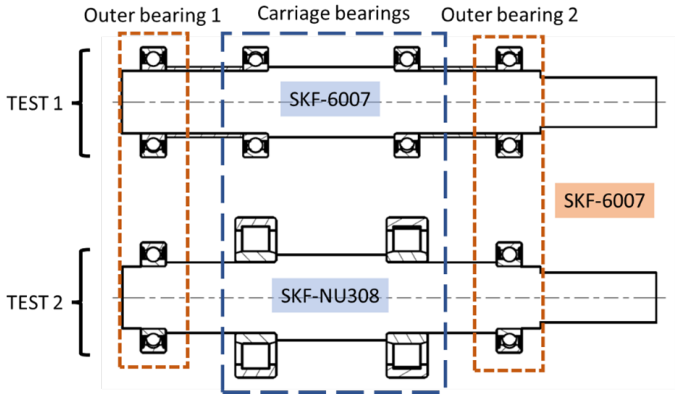

Figure 5.11: Bearing arrangement in two tests. Outer bearings are maintained in each test; inner bearings are different. Two test shafts are manufactured with appropriate fits for inner race and shoulder abutments. Shaft for Test-1 requires spacers between equivalent bearings.

error induced from using the average load across four bearings which is found to be negligibly small.

Table 5.4: Test-1 (4-off SKF-6007) relationship between measured parameters and those inferred for individual bearings.

Test-1 variables	Measurement	Inferred parameter for individual bearings
Radial load	F_{R1}	$F_{R_{1(av)}} = \frac{F_{R_1} + g\left(\frac{m_{shaft}}{2} + m_{carriage}\right)}{2}$
Frictional moment	M_1	$M_{1(av)} = \frac{M_1}{4}$

Table 5.5: Masses of hardware upstream of load cell measurement.

Upstream component	Mass / kg	
	Test-1	Test-2
Carriage ($m_{carriage}$)	10.201	8.365
Shaft (m_{shaft})	3.040	2.762

The individual frictional moment of each SKF-NU308 bearing in Test-2 is determined by combining results from Test-1 for the 'control' outer bearing pair with the results for total friction with the inner test pair of SKF-NU308 cylindrical roller bearings in Test-2. The relationship between the measured parameters and inferred results for individual bearings is summarised in Table 5.6.

In calculation for the frictional moment of the control bearings, $M_{2(outer)}$, the difference in load between outer bearings and the average case from Test-1 is accounted for by adjusting for the estimated load in the outer bearings, $F_{R_{2(outer)}}$.

Table 5.6: Test-2 (SKF-NU308 inner; SKF-6007 outer) relationship between measured parameters and those inferred for individual bearings, combining results of Test-1.

Test-2 variables	Measurement	Inferred parameter for individual bearings	
		Inner (test) bearing: SKF-NU308	Outer (control) bearing: SKF-6007
Radial load	F_{R_2}	$F_{R_{2(inner)}} = \frac{F_{R_2}+g\left(m_{carriage}\right)}{2}$	$F_{R_{2(outer)}} = \frac{F_{R_2}+g\left(m_{carriage}+m_{shaft}\right)}{2}$
Frictional moment	M_2	$M_{2(outer)} = \frac{F_{R_2}+g\left(m_{carriage}+m_{shaft}\right)}{2}$	$M_{2(outer)} = M_{1(av)}\left(F_{R_{2(outer)}}, \omega_2\right)$

5.5.3 Test results

Experimental results from Test-1 and Test-2 are illustrated in Figure 5.12. Total frictional moment is plotted across a map of speed and applied load. Parameters for individual bearings are defined from test data isolated according to equations in Tables 5.4 and 5.6 and inferred measurements of SKF-6007 bearings and SKF-NU308 bearings are illustrated in Figure 5.13.

5.6 Validity of bearing models

The validity of analytical models from the literature can be determined by comparing the modelled output to experimental results. Harris and SKF models are reproduced for the test envelope covered for the inferred results for individual bearings.

5.6.1 Rear bearing on dynamometer test rig (SKF-6007)

Modelled and experimental results for an individual SKF-6007 deep groove ball bearing are plotted in 5.14. The Harris model is compared with experimental data in Figure 5.14a, and the difference plotted in Figure 5.14b. The SKF model is compared with experimental data in Figure 5.14c, the difference plotted in Figure 5.14d.

As seen in Figure 5.14a, the Harris model predicts almost no friction at low load, and a significant dependence on radial load. Neither of these are corroborated by the experimental results; the model overstates the losses at high load and under predicts at low load (Figure 5.14b). The SKF modelled frictional moment is more closely aligned with experimental results, shown in Figure 5.14c. It predicts no losses at low load which is not corroborated by experimental results. It also suggests a reduction in friction for high load as speed increases. The experimental data suggests

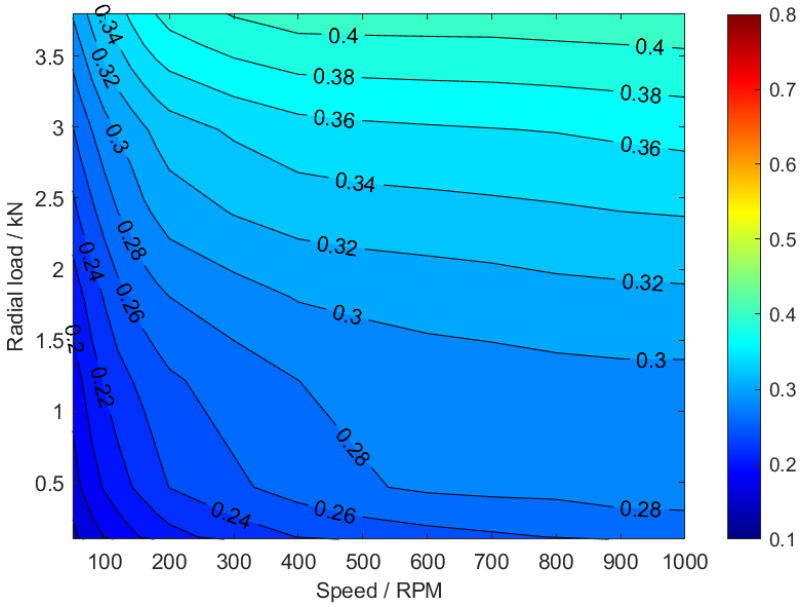

(a) Test-1 (4-off SKF-6007 deep groove ball bearings).

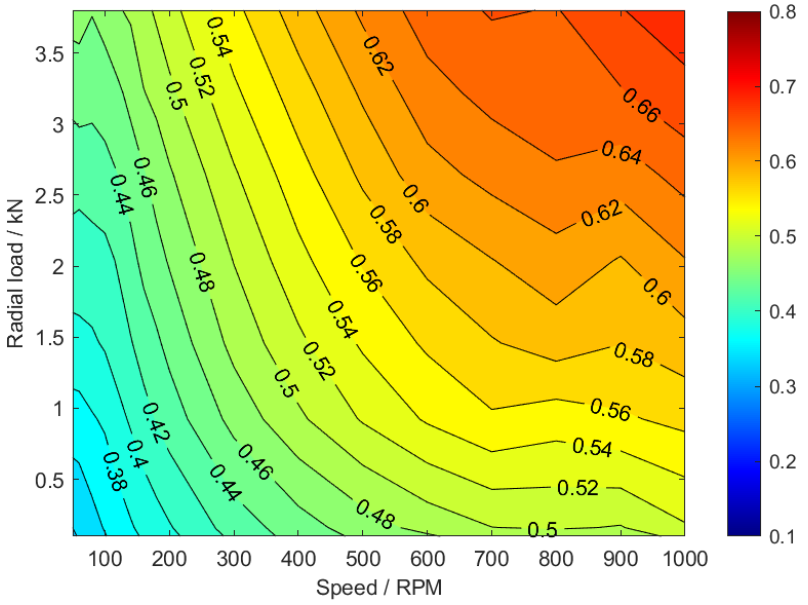

(b) Test-2 (2-off SKF-6007 deep groove ball bearings and 2-off SKF-NU308 cylindrical roller bearings).

Figure 5.12: Full test results showing combined frictional moment [Nm] from 4 test bearings against applied radial load to carriage and speed from servo motor.

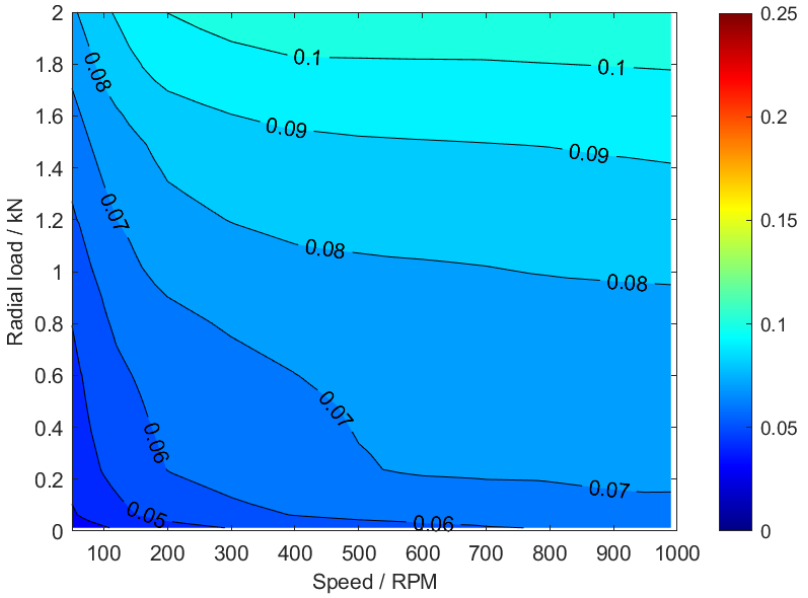

(a) Individual SKF-6007 deep groove ball bearing.

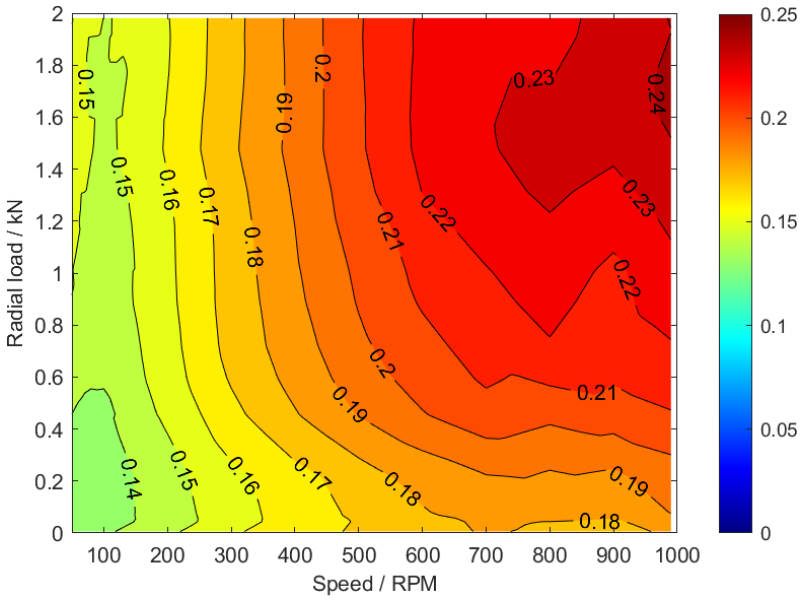

(b) Individual SKF-NU308 cylindrical roller bearing.

Figure 5.13: Results of frictional moment [Nm] for individual bearings from experimental results.

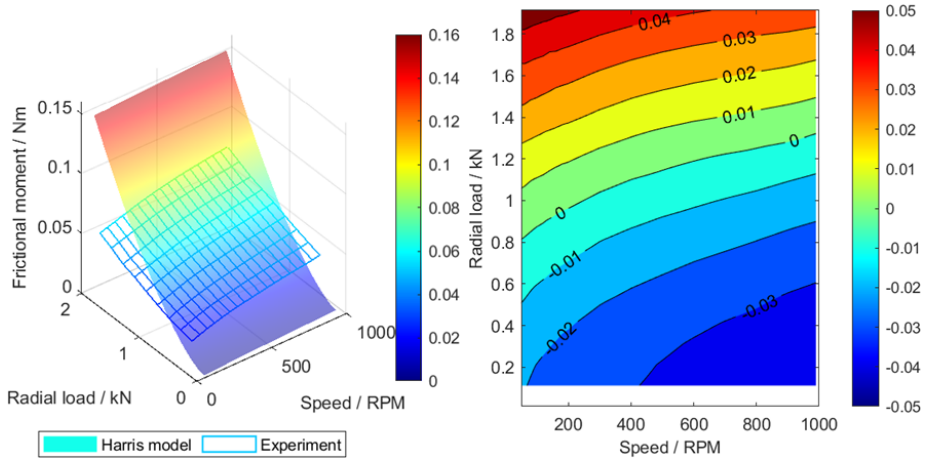

(a) Harris frictional moment [Nm] comparison.

(b) Harris-experiment difference [Nm].

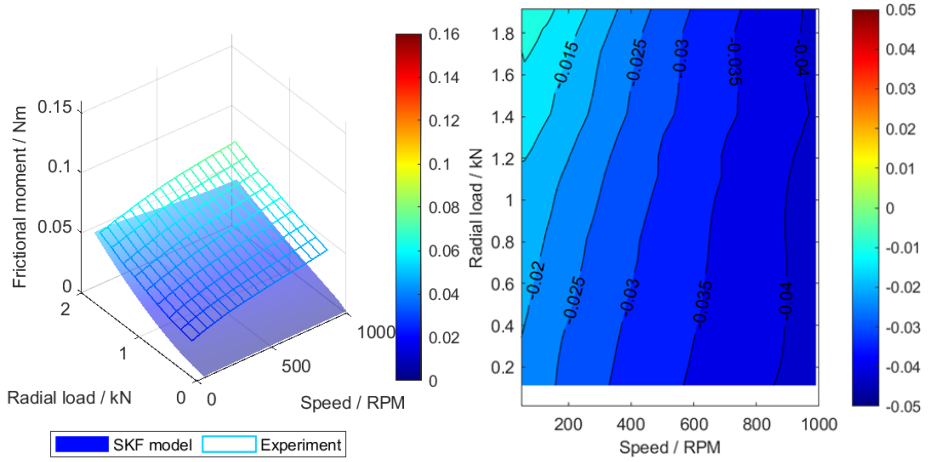

(c) SKF frictional moment [Nm] comparison.

(d) SKF-experiment difference [Nm].

Figure 5.14: Comparison of analytical models and experimental results for isolated SKF-6007 deep groove ball bearing.

maximum friction at maximum speed and load. The SKF model under-predicts across the test envelope (Figure 5.14d), with greatest difference at high speed.

The discrepancy between modelled results and experimental measurement can in part be explained by the extreme low area of the loading envelope the models are designed to predict. The modelled frictional moment across the rated loading envelope of the SKF-6007 bearings (up to 10.2 kN and 15,000 RPM) is plotted in Figure 5.15 for both the Harris model in Figure 5.15a and the SKF model in Figure 5.15b. The loading envelope covered in experimental tests is denoted by a red box in the Figures.

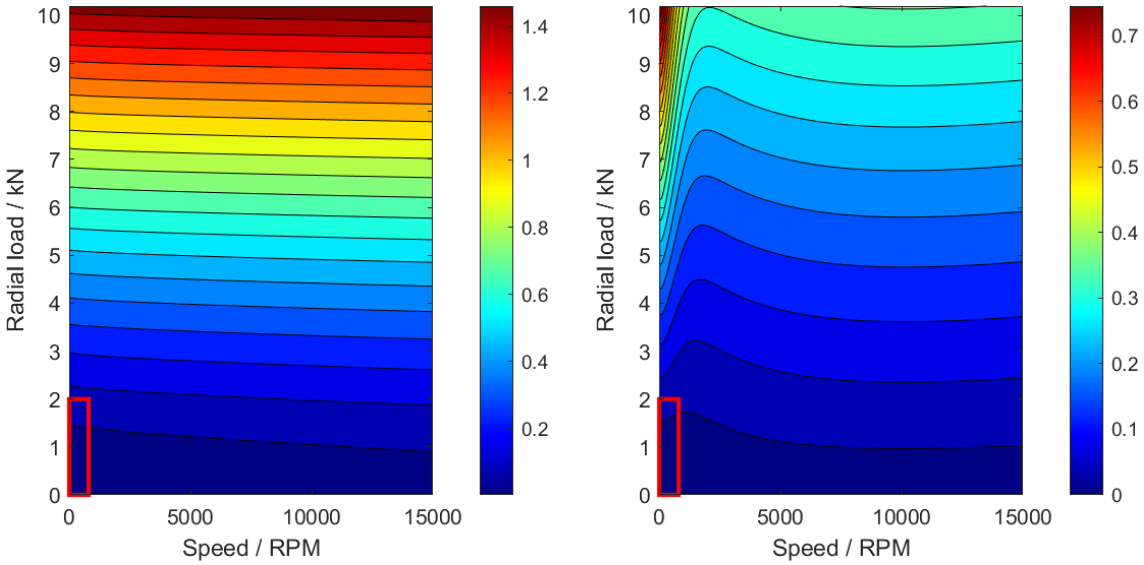

(a) Harris modelled frictional moment [Nm] for SKF-6007 operational range.

(b) SKF modelled frictional moment [Nm] for SKF-6007 operational range.

Figure 5.15: Frictional moment [Nm] modelled over operational range of SKF-6007. The tested envelope is shown with a red box.

5.6.2 Front bearing on dynamometer test rig (SKF-NU308)

Modelled results for an individual SKF-NU308 cylindrical roller bearing are plotted alongside experimental results in Figure 5.16. Frictional moment calculated using Harris is compared with experimental data in Figure 5.16a, and the difference plotted in Figure 5.16b. Frictional moment calculated with the SKF model is compared with experimental data in Figure 5.16c, the difference plotted in Figure 5.16d.

The Harris model predicts frictional losses much lower than the inferred results from experimental data, shown in Figures 5.16a and 5.16b. The SKF modelled results are illustrated alongside the experimental results in Figure 5.16c and under-predict similarly. The shape of the modelled surfaces is similar to one another and to the experimental data, showing highest frictional moment at maximum speed and radial load.

The difference between modelled cases and experimental results is more significant for the SKF-NU308 bearings. They are operating within a smaller band of their rated loading (78kN, 9000 RPM) even than the SKF-6007, illustrated in Figure 5.17. The validity of the models is stretched still further. In the SKF modelled moment there is a speed at which there is a trough in the frictional moment across all radial loads which is not captured in the low load results.

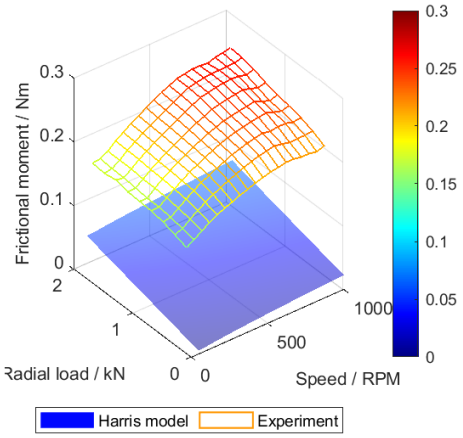

(a) Experimental and modelled (Harris) frictional moment.

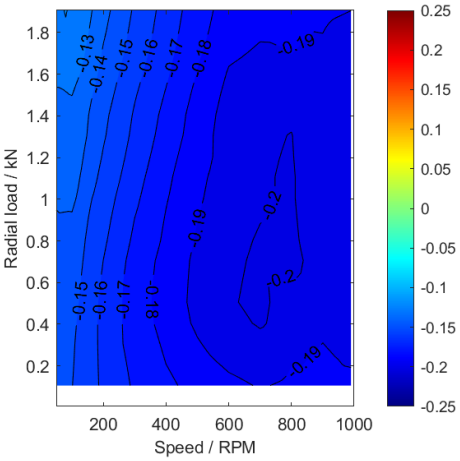

(b) Harris-experiment difference [Nm].

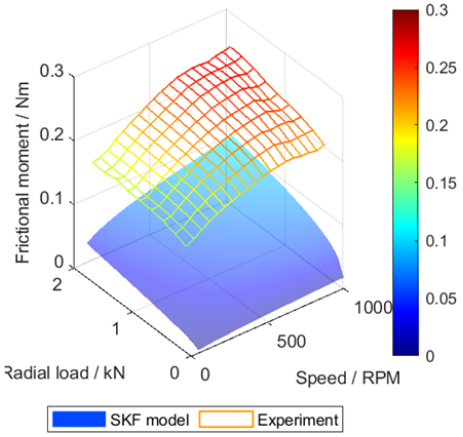

(c) Experimental and modelled (SKF) frictional moment.

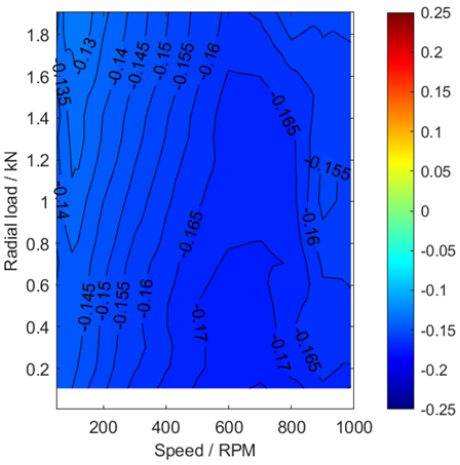

(d) SKF-experiment difference [Nm].

Figure 5.16: Comparison of analytical models and experimental results for isolated SKF-NU308 cylindrical roller bearing.

5.7 Applying empirical results to chain dynamometer test rig bearing friction compensation

Given the discrepancy between models and captured data, both in absolute terms and the trends with changing load and speed, they are not applicable without significant alterations. Alternatively, empirical data can be used directly to determine the frictional moment of the bearings on the chain dynamometer test rig to compensate in the chains test measurement.

The empirical results are now plotted as function of applied torque and speed for a typical gear ratio, Figure 5.18. Experimental data is interpolated (linear) and the radial load from torque calculated according to method detailed in Section 5.4.1.

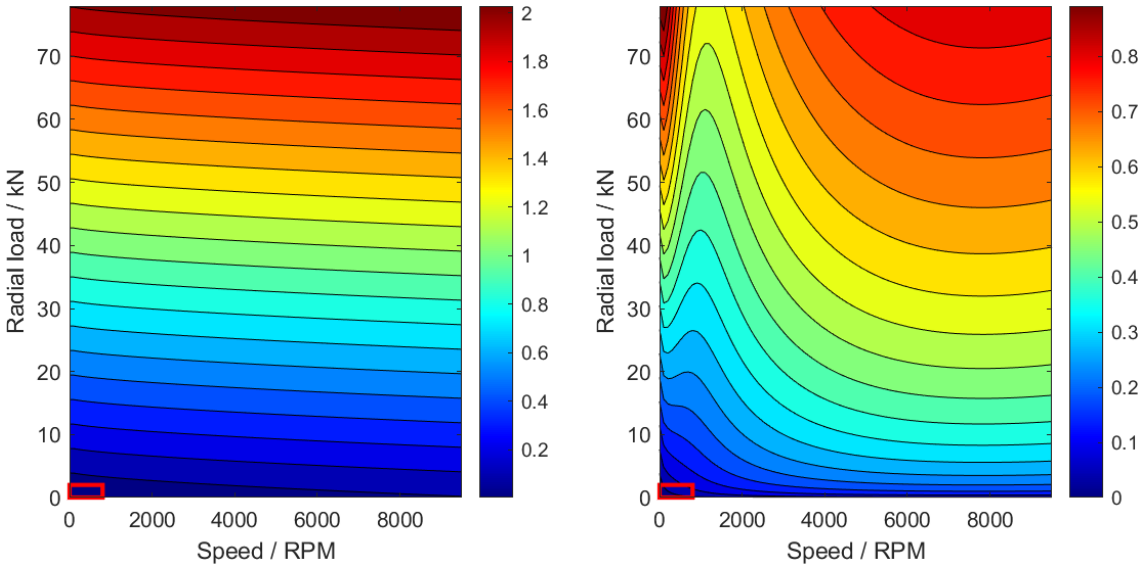

(a) Harris modelled frictional moment [Nm] for SKF-NU308 operational range.

(b) SKF modelled frictional moment [Nm] for SKF-NU308 operational range.

Figure 5.17: Frictional moment [Nm] modelled over operational range of SKF-NU308. The tested envelope is shown with a red box.

5.7.1 Effect of bearing compensation method on transmission loss results

Bearing friction in raw measurements from the dynamometer test rig can be compensated by analytical and empirical means. To illustrate the effect of different compensation methods, examples are given using a set of measured variables from the dynomometer test rig. These are shown in Figure 5.19.

Raw test results shown in Figure 5.19a show the total power losses between input measurement, τ_A and ω_A, and output measurement, τ_B and ω_B, including all four bearings and the transmission-under-test:

$$P_{loss,1} = \tau_A \omega_A - \tau_B \omega_B \tag{5.22}$$

Figures 5.19b, 5.19c and 5.19d illustrate the results from the transmission-under-test when the support bearing losses are compensated by different methods:

$$P_{loss,2} = \tau_A \omega_A - \tau_B \omega_B - P_{bearings,Empirical} \tag{5.23}$$

$$P_{loss,3} = \tau_A \omega_A - \tau_B \omega_B - P_{bearings,Harris} \tag{5.24}$$

$$P_{loss,4} = \tau_A \omega_A - \tau_B \omega_B - P_{bearings,SKF} \tag{5.25}$$

The results illustrate the choice in bearing compensation method significantly changes the results from transmission-under-test, and using models which under predict the power losses to the bearings mean that the contribution of transmission loss to the measured loss is overstated and the

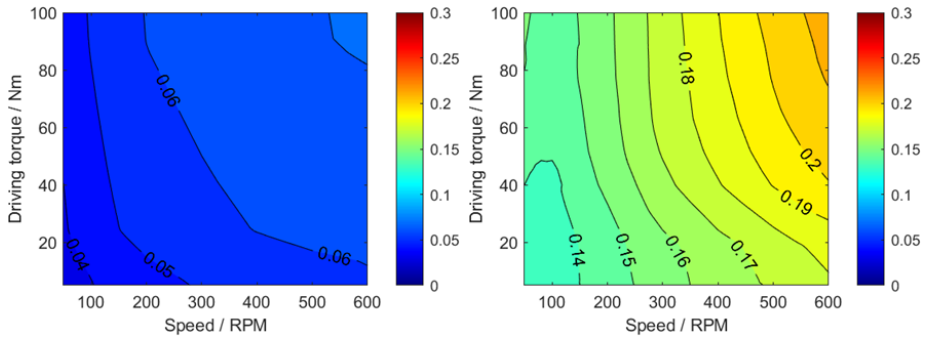

(a) SKF-6007 frictional moment.

(b) SKF-NU308 frictional moment.

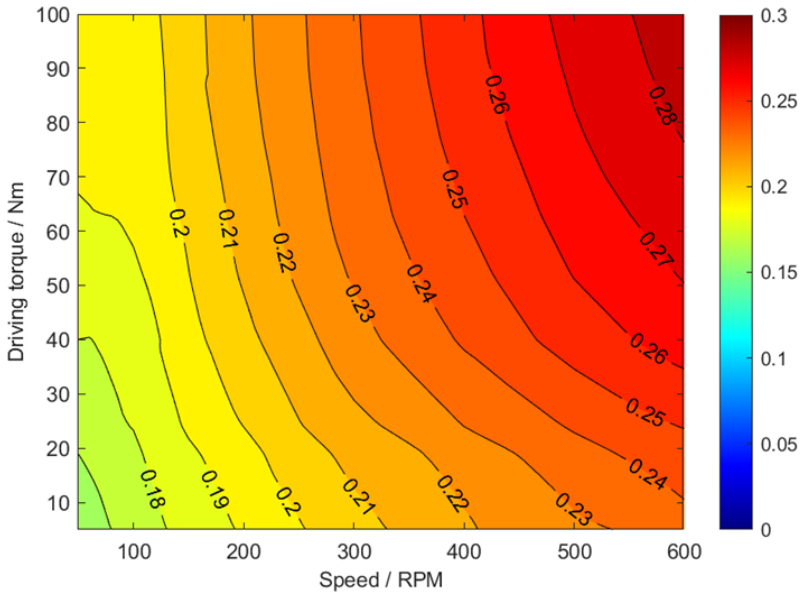

(c) combined frictional moment for both support bearings on shaft.

Figure 5.18: Frictional moment [Nm] of bearings as function of applied torque and speed on dynamometer test rig.

performance deemed to be worse. The difference is 7-11W across the tested envelope. Given the operating conditions are at extremes for the bearing models, the empirical data is judged to be much more representative of the conditions of the dynamometer test rig.

5.7.2 Limitations of empirical data as bearing friction compensation in dynamometer test data

There are some limitations of using empirical data for bearing frictional moment compensation which are now summarised, and form the basis of avenues for further work.

1. There are some minor differences between environmental conditions between the two experimental test rigs. A temperature difference changes the viscosity of lubricant.

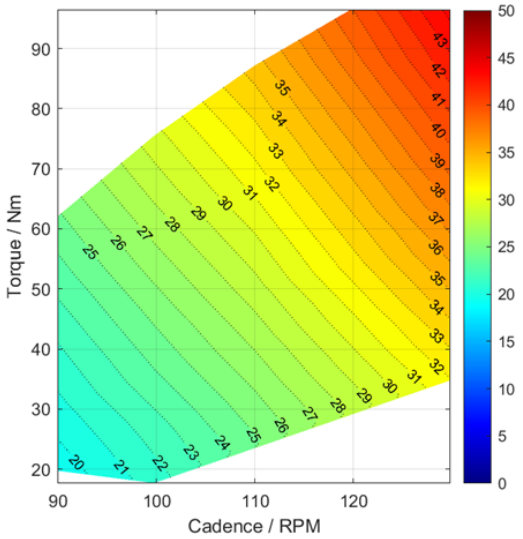

(a) No bearing-friction compensation (raw test results) [W].

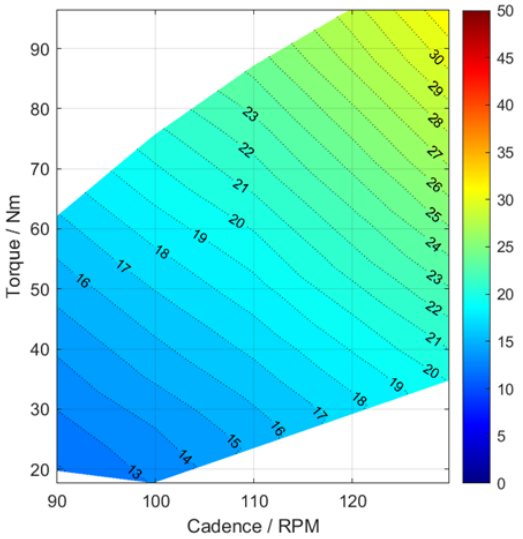

(b) Empirical compensation of bearing frictional power loss [W].

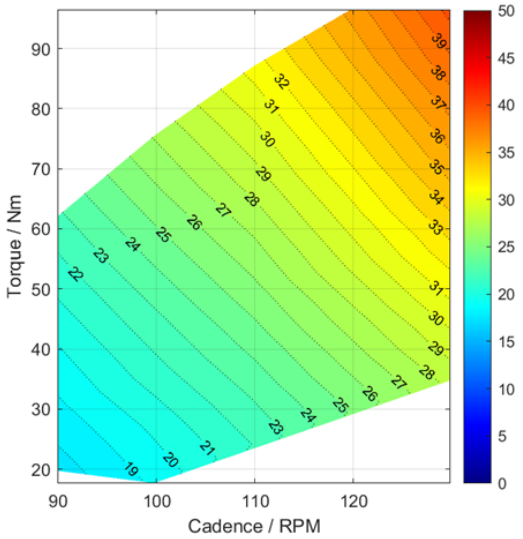

(c) Modelled (Harris) friction compensation of bearing frictional power loss [W].

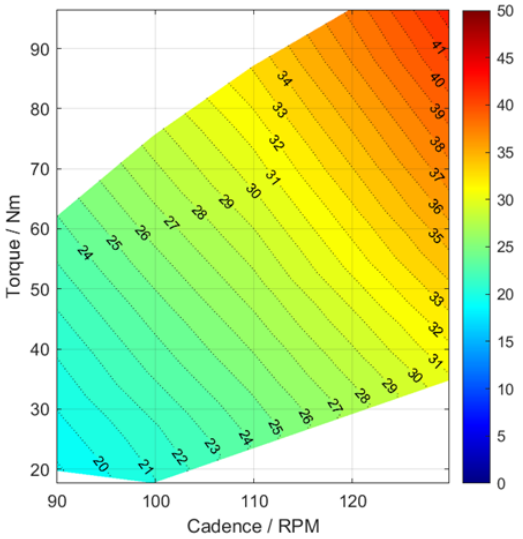

(d) Modelled (SKF) friction compensation of bearing frictional power loss [W].

Figure 5.19: Inferred transmission loss [W] on chain dynamometer test rig with different compensation methods for influence of frictional moment from bearings.

2. Bearings may exhibit trends across their lifetime that are not captured in independent tests. Level of use and loading should mitigate this.
3. The current requirement to use two sets of tests to infer test results for one bearing type (SKF-NU308) requires further validation and increases the measurement uncertainty.
4. Dynamic changes to radial load were not tested, which is of relevance in the context of cyclical torque profiles resulting in harmonic changes to span tension and hence radial load on bearings.

5.8 Conclusions and further work

The influence of parasitic effects on the measurement performance of the dynamometer test rig were discussed in this chapter. These included power losses from the test rig components in the measurement loop, effects resulting from control loop performance in driving and driven electric machines, and effects of geometric misalignment. Mitigation techniques were suggested for these effects and their suitability and performance were discussed.

The influence of electric motors and mechanical misalignments on nominal loading conditions were explored and mitigated through test design and data processing methods. Further work should be done to better mitigate and compensate these parasitic effects so that high-quality data could be captured in a shorter time frame, and inertial effects could be investigated to better understand transmission performance during accelerations, and with varying inertial loads.

The compensation of bearing frictional moment on the dynamometer test rig was identified as a significant source of error within the measurement loop. Where this is addressed in rotating experimental test rigs in the literature, the parasitic influence of bearing friction is usually considered as a speed-dependent effect. In high radial load applications such as the chain dynamometer a solution is required that also accounts for radial load.

An analytical solution was developed to determine the expected bearing frictional moment from applied radial load at given rotational speed using two commonplace models from the literature. It was shown that neither proposed model is appropriate for this application, and calls into question the wider validity of the models when conditions are quite different from typical industrial cases, such as light lubrication, low speed, and low radial load relative to static load rating of the SKF-NU308 and SKF-6007 bearings used in the dynamometer test rig.

There is no valid model describing the expected bearing frictional moment in a dynamometer rig with bearings under such conditions. A significant piece of further work would be to develop a new analytical description of frictional moment in bearings at the edge of their operating envelope,

which could then be used for the dynamometer test rig. Until this is successfully implemented and validated, this work demonstrates that a dynamometer test rig must always be built with a bearing characterisation rig alongside to have confidence in the quality of results in compensation of bearing friction. Sophisticated solutions might run both rigs in parallel to compensate in real time.

5.9 Summary of Chapter 5

This chapter has examined the parasitic influences on transmission tests on the dynamometer test rig introduced in Chapter 4. The mitigation and compensation of these influences has a direct effect on the uncertainty associated with measurement of transmission losses on the test rig, which is covered in Chapter 6. The salient points from this chapter are summarised below:

1. Parasitic influences on assessment of losses are introduced, with consideration of the electric machines, measurement quality and bearing frictional moment.
2. Influence of electric machines on loading, and measurement quality are minimised through appropriate control, test sequence design and post processing.
3. Bearing frictional moment is highlighted as a significant source of parasitic influence which cannot be mitigated, so must be compensated.
4. Several models exist in literature and are widely used, offering a solution to compensation of bearing friction. However, the operating conditions and loading cases are not typical of bearings in industry and it is not clear how relevant the models are to this case.
5. Partial validation of bearing models is possible in theory by testing the bearings in situ with the measurement equipment on the rig. However, this produces unreliable results due to the significant relative uncertainty associated with the zero tare on the torque transducers (measurement quality).
6. A new rig for measuring bearing frictional moment with changing radial load and shaft rotational speed is presented, and equivalence to the bearings on the chain dynamometer test rig shown.
7. Results show discrepancy with bearing models, opening up wider evaluation for validity of bearing model as further work. For compensation of losses in dynamometer test rig, empirical data is used.

Chapter 6

Uncertainty of Measurement on Dynamometer Test Rig

6.1 Introduction

Measurement uncertainty is introduced generally in Section 2.5, following the methodologies defined by the 'Guide to the Expression of Uncertainty in Measurement (GUM)' [6]. This chapter addresses the specific context of transmission tests on the dynamometer apparatus to determine the uncertainty of the inferred power consumption in a transmission-under-test over a full test envelope.

It is necessary and useful to quote the uncertainty of a measurand as the confidence with which a result can be claimed to be accurate highlights the benefits or detriments of particular measurement and loading cases in experimental apparatus.

The uncertainty of measured variables includes the random error caused by fluctuations in the measurement, uncertainty associated with equivalence of loading between different tests and uncertainty associated with modelled equivalence of loading. Practices detailed in Chapter 5 to mitigate and compensate for parasitic influences must first be followed before determining the uncertainty which is an estimate of what error remains.

On the dynamometer test rig, the performance metric which is evaluated (the measurand) is the power consumed in the transmission-under-test during operation, P_{loss}. The uncertainty of the measurand is a function of the uncertainty of measured variables which describe it: input and output torque, τ_A & τ_B, input and output rotational speed, ω_A & ω_B, and frictional moment of the bearings at input and output, M_A & M_B. The combined uncertainty is described by functional

relationship, f:

$$U_{P_{loss}} = f(u_{\tau_A}, u_{\omega_A}, u_{M_A}, u_{\tau_B}, u_{\omega_B}, u_{M_B}) \tag{6.1}$$

Approaches to evaluation of uncertainty are defined by Type A methods and Type B methods, introduced in Section 2.5. Several approaches are possible in each evaluation, and multiple methods are evaluated, and their validity addressed.

An estimate of uncertainty of measured variables may be calculated by considering the accuracy class of the torque transducers used to determine each measurement variable within function f. However, this approach is not recommended for detailed analysis of uncertainty since accuracy class is a representation of the absolute uncertainty of measurement at a nominal load. Nuances in application conditions are not considered.

Furthermore, determining the uncertainty is more involved than simply the error associated with each of the measurements above, since there is added complexity in the combination of results from two individual test rigs (since empirical data is used to compensate bearing frictional moment) and application of analytical models (for instance in estimation of radial load).

To accurately determine the estimate for the uncertainty of the measurand P_{loss}, the standard uncertainty from all input variables must first be estimated and then combined. These measured variables describe results from several different tests on two different test rigs (torque and speed measurement from dynamometer test results; bearing loss compensation is from bearing test results).

6.1.1 Structure of chapter

Equations for combined uncertainty of dynamometer measurand P_{loss} are introduced based on the description of power loss from the measured variables in tests. The following sections will seek to populate values for the uncertainty terms for each measured variable.

1. The uncertainty of raw measured variables captured in tests on both the chain dynamometer apparatus and bearing frictional moment test rig are introduced in Sections 6.3 and 6.4. These are evaluated by several methods and comment made on the validity of each.

2. Section 6.5 addresses the uncertainty of bearing loss compensation. This is divided into two sources: direct uncertainty of frictional measurement, and uncertainty of loading equivalence between environments on the chains dynamometer test rig and the bearing frictional moment test rig.

3. With all standard uncertainties defined, the combined standard uncertainty is calculated for transmission power loss in Section 6.6 across a typical test envelope of applied torque and speed.

6.2 Uncertainty of performance measurand from measured variables

The power consumed in the transmission may be calculated according to Equation 6.2.

$$P_{loss} = (\tau_A - M_A)\,\omega_A - (\tau_B + M_B)\,\omega_B \tag{6.2}$$

Terms for torque at transducer (τ_A), bearing compensation at driving sprocket (M_A), input rotational speed (ω_A), output torque at transducer (τ_B), bearing compensation at driven sprocket (M_B), and output rotational speed (ω_B) each have associated uncertainties. They are combined following methods defined in GUM [6] as in Equation 2.63, Section 2.5.

$$\begin{aligned} U^2_{P_{loss}} = &\frac{\partial P_{loss}}{\partial \tau_A}^2 u^2_{\tau_A} + \frac{\partial P_{loss}}{\partial \omega_A}^2 u^2_{\omega_A} + \frac{\partial P_{loss}}{\partial M_A}^2 u^2_{M_A} \\ &+ \frac{\partial P_{loss}}{\partial \tau_B}^2 u^2_{\tau_B} + \frac{\partial P_{loss}}{\partial \omega_B}^2 u^2_{\omega_B} + \frac{\partial P_{loss}}{\partial M_B}^2 u^2_{M_B} \end{aligned} \tag{6.3}$$

The partial derivatives describing the weighting factors are described below:

$$\frac{\partial P_{loss}}{\partial \tau_A} = \omega_A, \frac{\partial P_{loss}}{\partial \omega_A} = \tau_A - M_A, \frac{\partial P_{loss}}{\partial M_A} = -\omega_A$$

$$\frac{\partial P_{loss}}{\partial \tau_B} = -\omega_B, \frac{\partial P_{loss}}{\partial \omega_A} = -\tau_B - M_B, \frac{\partial P_{loss}}{\partial M_A} = -\omega_B$$

Total combined uncertainty of the measurand is described as below.

$$\begin{aligned} U_{P_{loss}} = \Big[&(\omega_A)^2 u^2_{\tau_A} + (\tau_A - M_A)^2 u^2_{\omega_A} + (-\omega_A)^2 u^2_{M_A} \\ &+ (-\omega_B)^2 u^2_{\tau_B} + (-\tau_B - M_B)^2 u^2_{\omega_B} + (-\omega_B)^2 u^2_{M_B} \Big]^{\frac{1}{2}} \end{aligned} \tag{6.4}$$

Uncertainties of torque u_τ, rotational speed u_ω, and bearing frictional moment u_M are addressed in the next sections, first by calculating the uncertainty of the raw measured variables in test data.

6.3 Uncertainties of raw measured variables on chain dynamometer

6.3.1 Rotational speed measurement

The uncertainty of measured rotational speed is evaluated by Type A uncertainty analysis through repeated observations of measured value at steady state operation during a test transmission duty cycle. Steady state conditions are captured by time-averaging for a complete rotation of the driving sprocket. To increase the number of observations to a statistically significant number, speed

values are normalised and captured for a the full range of applied torques so an uncertainty will be captured which represents an average across the whole test. There is no overlap between these data points. Histogram plots for Drivelines A and B are shown in Figure 6.1, each with a normal distribution overlayed. Illustrated data is from tests on a carbon belt (gearing: 60/21).

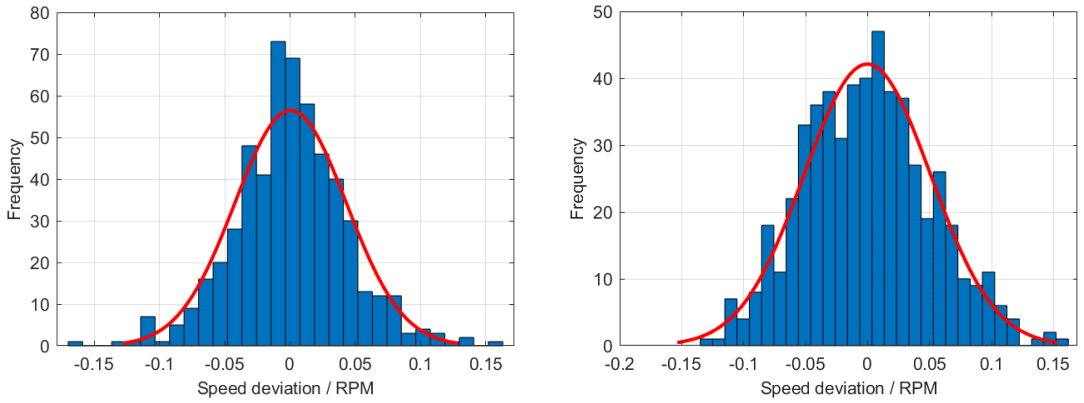

(a) Driveline A speed with fitted PDF ($\mu = 0.000$, $\sigma = 0.0427$).

(b) Driveline B speed with fitted PDF ($\mu = 0.000$, $\sigma = 0.0511$).

Figure 6.1: Histogram illustrating statistical spread of normalised speed data [RPM] from dynamometer test rig with Gaussian probability distribution fitted

6.3.2 Torque measurement

Torque is measured on both drivelines on the dynamometer test rig and its uncertainty may be estimated with the accuracy class and nominal torque rating of the transducers, or calculated by either Type A methods (directly from repeated empirical measurement), or Type B methods as introduced in Section 2.5.3. All three are calculated here and comment made on the agreement and validity of each.

Estimate of frictional moment uncertainty from transducer accuracy class

The torque transducer on driveline A is an HBM T10F (500Nm rated torque) with accuracy class of 0.1 (%). An estimate of absolute uncertainty of torque measurement is calculated:

$$\begin{aligned} U_{M_A(estimate)} &= 0.1\% \times 500Nm \\ &= 0.5Nm \end{aligned} \tag{6.5}$$

The torque transducer on driveline B is an HBM T40B (100Nm rated torque) with accuracy class of 0.05 (%). An estimate of absolute uncertainty of torque measurement is calculated:

$$\begin{aligned} U_{M_B(estimate)} &= 0.05\% \times 100Nm \\ &= 0.05Nm \end{aligned} \tag{6.6}$$

These estimates are compared with Type A and Type B methods of uncertainty characterisation, addressed in the next sections, in Table 6.4.

Direct assessment of test data (Type A)

Torque measurement may also be evaluated by Type A uncertainty analysis, through repeated observations of the normalised measured value relative to the average torque over a steady-state window as was done with speed data. Histogram plots for Driveline A and B are shown in Figure 6.2, each with a normal distribution overlayed. Each data point is time averaged over a full rotation of Driveline A to remove dynamic effects, ensuring no overlap between these windows.

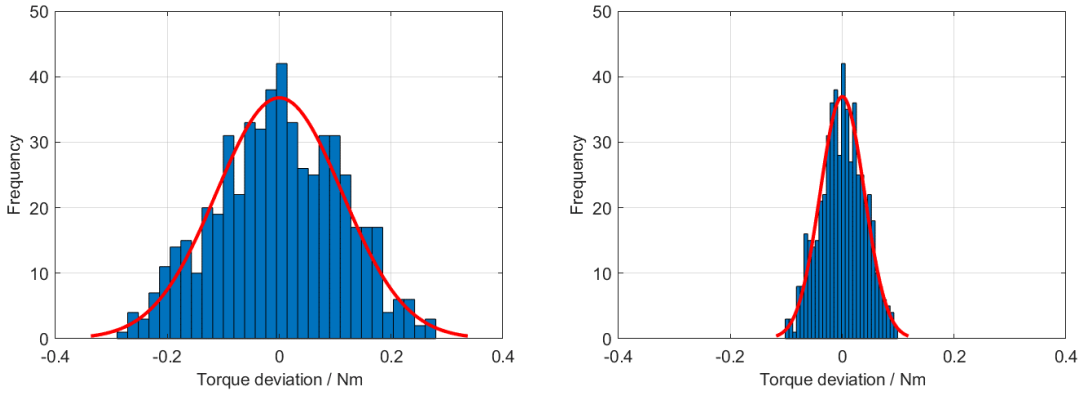

(a) Driveline A torque with fitted PDF ($\mu = 0.000$, $\sigma = 0.112$).

(b) Driveline B torque with fitted PDF ($\mu = 0.000$, $\sigma = 0.0394$).

Figure 6.2: Histogram illustrating statistical spread of normalised torque data [Nm] from dynamometer test rig with Gaussian probability distribution fitted

Analytical description (Type B)

The uncertainty of torque measurement for each driveline (A and B) on the chain dynamometer test rig is calculated according to the Type B uncertainty calculation described in the literature [83], introduced in Section 2.5.3. The general conditions in the dynamometer application are summarised in Table 6.1, while the torque transducer nominal properties from the data sheets are summarised in Table 6.2.

Data from Tables 6.1 and 6.2 is applied to the descriptions of uncertainty detailed in Table 2.9, Section 2.5.3. The combined uncertainty is calculated according to Equation 2.65. Calculated uncertainties are summarised in Table 6.3.

Table 6.1: Conditions in chain dynamometer measurement during typical test duty cycle.

Parameter	Description	Value		Unit
		T10F (A)	T40B (B)	
M_{appl}	Maximum torque in application	105	30	Nm
M_{nom}	Nominal rated torque of transducer	500	100	Nm
ΔT	Temperature range in application	1	1	K
$\frac{L_{para}}{L_{para,ref}}$	Total max parasitic load/limit load	1.23	9.80	%

Table 6.2: Properties of T10F and T40B transducers from manufacturer data sheets [33, 34].

Property	Symbol	Value		Reference
		T10F (A)	T40B (B)	
Sensitivity tolerance	d_C	0.1%	0.1%	M_{max}
Linearity incl. hysteresis	d_{lh}	0.1%	0.03%	M_{nom}
Temperature effect on zero signal	TK_0	0.05%	0.05%	M_{nom}
Temperature effect on the sensitivity	TK_C	0.1%	0.05%	M_{max}
Standard deviation of repeatability	σ_{rel}	0.03%	0.03%	ΔM
Allowable load limits	d_{para}	1%	0.6%	M_{nom}

Table 6.3: Contribution to uncertainty of torque measurement for each transducer on chain dynamometer from various sources, combined in quadrature sum. Calculated from equations detailed in Table 2.9

Uncertainty source	Symbol	Value / Nm	
		T10F (A)	T40B (B)
Sensitivity tolerance	U_C	0.0606	0.0173
Linearity incl. hysteresis	U_{lh}	0.0606	0.0052
Temperature effect on zero signal	U_{TK0}	0.0144	0.0029
Temperature effect on the sensitivity	U_{TKC}	0.0061	0.0009
Standard deviation of repeatability	$U_{b\prime}$	0.0315	0.0090
Allowable load limits	U_{para}	0.0354	0.0340
Total uncertainty	U_{total}	**0.0992**	**0.0396**

6.3.3 Summary of chain test measurement uncertainties

The derived measurement uncertainties for torque and speed on each torque transducer on driving and driven drivelines are summarised in Table 6.4. Type A and B approaches for the particular use case in the dynamometer test rig illustrate better uncertainty than the conservative estimate based

on quoted accuracy class in rated measurement range. The two more exact methods also show very good agreement. Type B method is used in calculations of combined uncertainty.

Table 6.4: Summary of calculated uncertainties of chains rig measurement variables.

Driveline	Measured variable	Uncertainty derivation			Units
		Estimate	Calculated (Type A)	Calculated (Type B)	
A	Torque	0.5	0.1123	0.0992	Nm
	Speed	$\sim$	0.00448	$\sim$	$rads^{-1}$
B	Torque	0.05	0.0394	0.0396	Nm
	Speed	$\sim$	0.00535	$\sim$	$rads^{-1}$

6.4 Uncertainties of raw measurements on bearing frictional moment test rig

The bearing test rig introduced in Chapter 5 is used to assess the load and speed dependence of bearing frictional moment, so that it may be accurately compensated in transmission tests on the chain dynamometer test rig. With empirical data used to directly compensate, there must be consideration of the uncertainty of this measurement which stems from the direct measurements in bearing tests: torque, rotational speed, and radial load.

The interaction between the electric machine control systems and the low inertial mass in the bearing test apparatus results in data distributed with more outliers and hence longer 'tails'. The resulting distribution is described better by a 't-Location scale', a scaled Gaussian distribution. The standard deviation of experimental data is inferred from this in place of a normal distribution used previously.

6.4.1 Rotational speed measurement

Uncertainty of speed measurement in the bearing rig is evaluated by Type A analysis, through repeated observations of measured value relative to the average torque over a steady-state window. Histogram plots for Test-1 and Test-2 are shown in Figure 6.3, each with a distribution overlayed. A 't-Location Scale' distribution is fitted. As before, each data point is time averaged over a full rotation of the shaft to remove dynamic effects, ensuring no overlap between these windows.

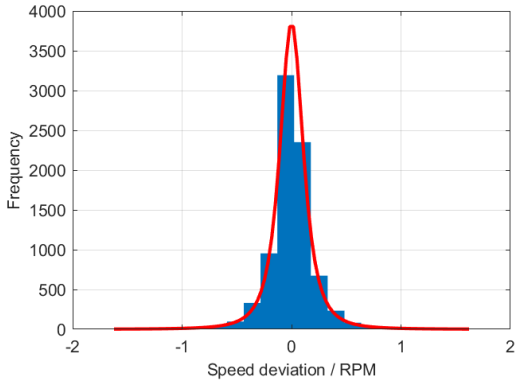

(a) Test-1 speed with fitted PDF ($\mu = 0.000$, $\sigma = 0.115$).

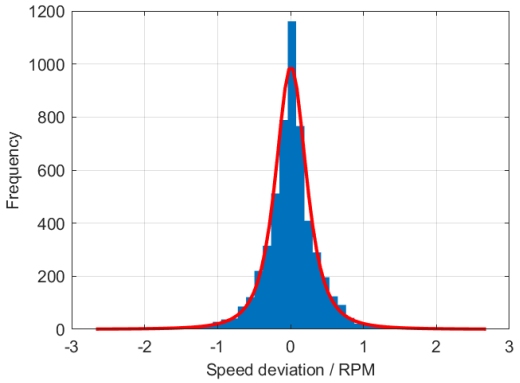

(b) Test-2 speed with fitted PDF ($\mu = 0.000$, $\sigma = 0.224$).

Figure 6.3: Histogram illustrating statistical spread of normalised speed data [RPM] from bearing test rig with t-Location Scale probability distribution fitted.

6.4.2 Frictional moment measurement

Estimate of frictional moment uncertainty from transducer accuracy class

The torque transducer used was an HBM T21WN (5Nm) with accuracy class of 0.2 (%). An estimate of absolute uncertainty of torque measurement is calculated:

$$\begin{aligned} U_{M(estimate)} &= 0.2\% \times 5Nm \\ &= 0.01Nm \end{aligned} \tag{6.7}$$

This is compared with Type A and Type B methods of uncertainty characterisation, addressed in the next sections, in Table 6.11.

Direct assessment of test data (Type A)

Uncertainty of torque measurement in the bearing rig is evaluated by Type A analysis, through repeated observations of measured value relative to the average torque over a steady-state window. Since data is used from two tests to cover both bearing types (described in Chapter 5), the spread of speed data is considered for each test. Histogram plots for Test-1 and Test-2 are shown in Figure 6.4, each with a distribution overlayed. The distribution chosen is a 't-Location Scale' distribution, a scaled normal distribution which suits data with heavier tails (more outliers) than a standard normal distribution. As before, each data point is time averaged over a full rotation of the shaft to remove dynamic effects, ensuring no overlap between these windows.

The standard deviation of a fitted distribution is a measure of the uncertainty of frictional moment measurement.

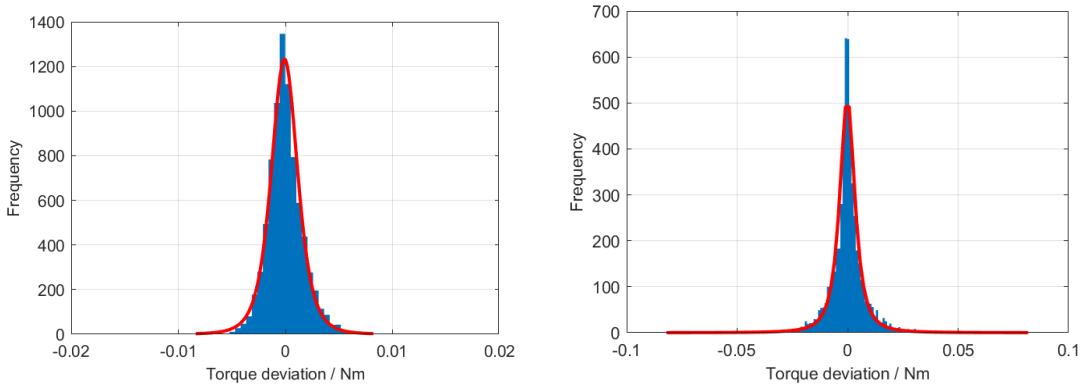

(a) Test-1 frictional moment with fitted PDF ($\mu = 0.000$, $\sigma = 0.00127$).

(b) Test-2 frictional moment with fitted PDF ($\mu = 0.000$, $\sigma = 0.00372$).

Figure 6.4: Histogram illustrating statistical spread of normalised moment data [Nm] from bearing test rig with t Location Scale probability distribution fitted.

Analytical description (Type B)

The uncertainty of frictional moment measurement in the bearing tests is calculated according to the same Type B uncertainty calculation as used in Section 6.3.2. The general conditions in the application are summarised in Table 6.5, while the torque transducer nominal properties from the data sheet is summarised in Table 6.6.

Table 6.5: Conditions in bearing torque measurement application.

Parameter	Description	Value		Unit
		Test-1	Test-2	
M_{max}	Maximum torque in application	1	0.5	Nm
M_{nom}	Nominal rated torque of transducer	5	5	Nm
ΔT	Temperature range in application	1	1	K
$\frac{L_{para}}{L_{para,ref}}$	Total max parasitic load/limit load	42.6	42.6	%

Table 6.6: Properties of T21WN transducer from manufacturer data sheet [35].

Property	Symbol	Value T21WN	Reference
Sensitivity tolerance	d_C	0.2%	M_{nom}
Linearity incl. hysteresis	d_{lh}	0.1%	M_{nom}
Temperature effect on zero signal	TK_0	0.2%	$\frac{M_{nom}}{10K}$
Temperature effect on the sensitivity	TK_C	0.1%	$\frac{M_{nom}}{10K}$
Standard deviation of repeatability	σ_{rel}	0.05%	M_{nom}
Allowable load limits	d_{para}	1%	M_{nom}

Data from Tables 6.5 and 6.6 is applied to the descriptions of uncertainty detailed in Section 2.5.3. Calculated uncertainties are summarised in Table 6.7.

Table 6.7: Uncertainty of bearing torque measurement from various sources and combined.

Uncertainty source	Symbol	Value / Nm	
		Test-1	Test-2
Sensitivity tolerance	U_C	0.0012	0.0012
Linearity incl. hysteresis	U_{lh}	0.0029	0.0029
Temperature effect on zero signal	U_{TK0}	0.0006	0.0006
Temperature effect on the sensitivity	U_{TKC}	0.0001	0.0001
Standard deviation of repeatability	U_{bt}	0.0005	0.0005
Allowable load limits	U_{para}	0.0123	0.0123
Total uncertainty	U_{total}	**0.0127**	**0.0127**

6.4.3 Load measurement

Literature from the load cell manufacturer suggests that a Type A approach to uncertainty analysis is not appropriate for the type of load cell used and Type B uncertainty evaluation should be employed [32].

Estimate of load uncertainty from load cell accuracy class

The load cell is an HBM U10M (5kN) with accuracy class of 0.02 (%). An estimate of absolute uncertainty is calculated:

$$\begin{aligned} U_{F(estimate)} &= 0.02\% \times 5000N \\ &= 1N \end{aligned} \tag{6.8}$$

Analytical description (Type B)

The uncertainty of load measurement in the bearing test is calculated according to the Type B uncertainty calculation [32] introduced in Section 2.5.4. General conditions of the application are summarised in Table 6.8, while the load cell's nominal properties from its data sheet are summarised in Table 6.9.

Data from Tables 6.8 and 6.9 is applied to the descriptions of uncertainty in Table 2.11 in Section 2.5.4. They are combined by quadrature sum as in Equation 2.66.

The experiments to determine load dependence of frictional moment were conducted as a series of discrete tests as detailed in Section 5.5. Since the radial load is maintained for each test, there

Table 6.8: Conditions in application.

Parameter	Description	Value	Unit
F_{appl}	Maximum load in application	4.5	kN
F_{nom}	Full range of load cell	5	kN
ΔT	Temperature range in application	1	K

Table 6.9: Properties of U10M load cell from manufacturer data sheet [36].

Property	Symbol	Value U10M	Reference
Tolerance of rated output	d_C	0.1%	F_{appl}
Linearity deviation	d_{lin}	0.02%	F_{nom}
Hysteresis	$v_{0.4}$	0.02%	F_{nom}
TCSpan	TC_S	0.015%	$\frac{F_{appl}}{10K}$
TCZero	TC_0	0.015%	$\frac{F_{nom}}{10K}$
Creep	d_{cr}	0.02%	F_{appl}

Table 6.10: Uncertainty of load cell force measurement from various sources and combined in quadrature sum.

Uncertainty	Symbol	Value / N
Tolerance of rated output	Δ_{dC}	4.5
Linearity deviation	Δ_{dlin}	1
Hysteresis	Δ_{hys}	1
TCSpan	Δ_{TKC}	0.34
TCZero	Δ_{TK0}	0.38
Creep	Δ_{cr}	0.9
Total uncertainty	U_{ges}	**4.83**

is a spread of associated uncertainties since the maximum load in application (F_{appl}) changes. The uncertainty changing with applied load is shown in Figure 6.5. The interpolated uncertainty between tested values is used is in further propagation of load uncertainty.

6.4.4 Summary of bearing rig

Torque measurements are determined by estimate with accuracy class of measurement devices, and involved Type A and Type B uncertainty evaluation. The calculated standard uncertainties of measured variables in the bearing characterisation tests are summarised in Table 6.11.

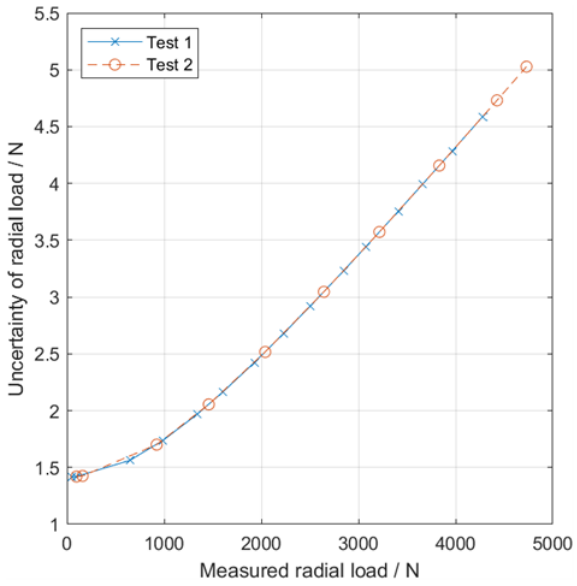

Figure 6.5: Uncertainty of load as function of applied radial load in discrete tests. Uncertainty is calculated using Type B method described.

There is difference in uncertainty of torque measurement between Test-1 and Test-2 due to different range of frictional moment measured. The estimation by Type B evaluation is used in combined uncertainties as the more conservative estimate which accounts for the specific loading conditions.

Table 6.11: Summary of calculated uncertainties for bearing characterisation measurands.

Test	Measured variable	Uncertainty estimate (accuracy class)	Test uncertainty (Type A)	Test uncertainty (Type B)	Units
1	Torque	0.01	0.0013	0.0127	Nm
	Radial load	1	$\sim$	1.4 - 5	N
	Speed	$\sim$	0.0120	$\sim$	$rads^{-1}$
2	Torque	0.01	0.0037	0.0127	Nm
	Radial load	1	$\sim$	1.4 - 5	N
	Speed	$\sim$	0.0235	$\sim$	$rads^{-1}$

6.5 Uncertainty of bearing compensation in chains test

Described in Chapter 5, empirical data describing the frictional moment of bearings as a function of rotational speed and applied radial load is used to compensate for bearing influence in chain dynamometer tests. This data has associated uncertainty which is calculated in this section. The uncertainty of compensated bearing loss, U_M, is defined from two different sources:

1. $U_{M(bearing)}$ – direct uncertainty of frictional moment measurement in individual bearings, inferred from measured frictional moment across all test bearings.
2. $U_{M(\omega,F_R)}$ – indirect uncertainty of inferred frictional moment in bearings, from equivalence in loading conditions between bearing test rig and chain dynamometer.

These values of uncertainty are combined in quadrature to describe the combined uncertainty of compensated bearing loss.

$$U_M = \sqrt{U_{M(bearing)}{}^2 + U_{M(\omega,F_R)}{}^2} \tag{6.9}$$

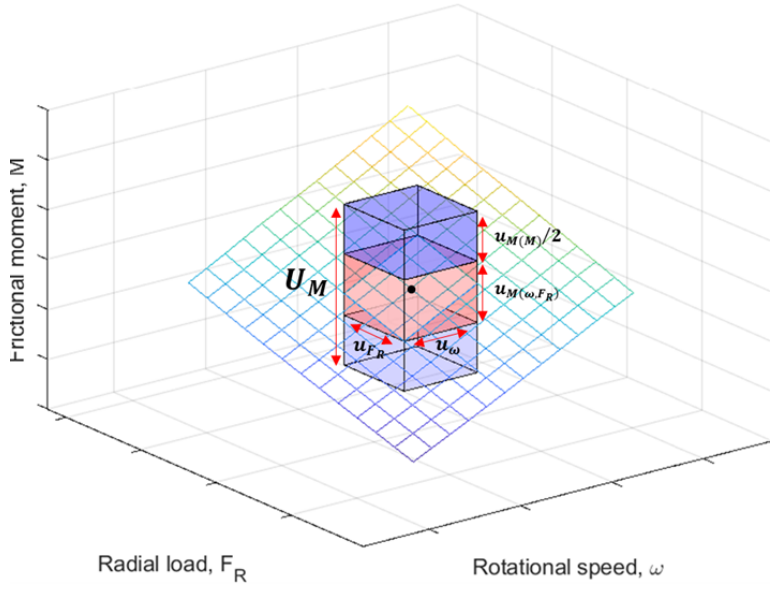

Figure 6.6: Graphical representation of combined uncertainty of frictional measurement and loading equivalence between test apparatus.

The combined sources of uncertainty are illustrated graphically in Figure 6.6, where a surface is plotted describing frictional moment as a function of radial load and rotational speed. For applied radial load and speed, the corresponding point on the surface describes the expected frictional moment. The uncertainty of applied radial load and uncertainty of rotational speed define a patch on the surface with maximum and minimum values of frictional moment, defining the uncertainty of moment due to equivalence (drawn by the red cuboid). Additional direct uncertainty of the bearing frictional moment measurement is shown as blue boxes extending above and below the extremes of the frictional moment surface. The overall height of the combined boxes represents the statistical variation in frictional moment from variance in three independent measurements.

Uncertainty of characterised frictional moment, $U_{M(bearing)}$, is equivalent to the uncertainty associated with the measurement of frictional moment in the original tests when isolated for an individual bearing. The derived uncertainty is directly applied.

Uncertainty of loading equivalence, $U_{M(\omega,F_R)}$, is characterised by first deriving the complete uncertainty of the dependent parameters and propagating this to the frictional moment by considering how changes in parameters ω and F_R due to uncertainties affect the expected value of $M(\omega,F_R)$ for an interpolated surface derived from experimental data.

In the context of the bearings on the dynamometer test rig, there are four individual uncertainties to characterise to evaluate the impact each has on the combined uncertainty. Each bearing is denoted 'front' or 'rear' and 'A' or 'B' according to Figure 6.7

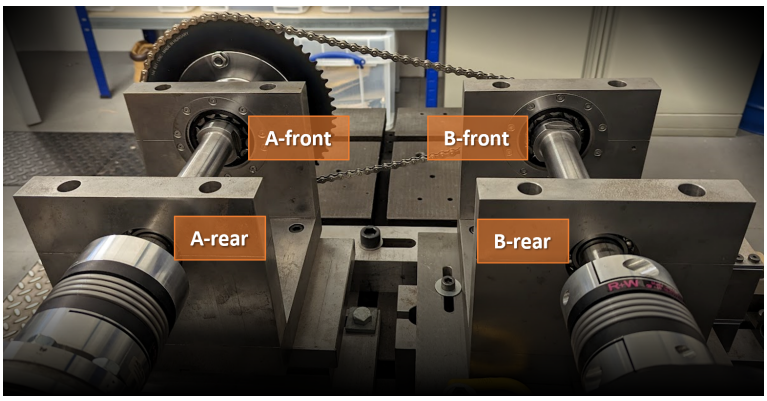

Figure 6.7: Denotation of bearings in chain test. Driving side are 'A', driven side 'B'; transmission-side is 'front' and measurement-side is 'rear'.

For each bearing, the propagation of uncertainties contributing to uncertainty of bearing frictional moment compensation is summarised in Figure 6.8 . The uncertainties are described in Table 6.12.

6.5.1 Uncertainty of radial load equivalence

The radial load is applied to bearings on the bearing characterisation rig through the spring assembly and induced in bearings on the dynamometer by the torque-induced chain span tension. There is uncertainty in equating these cases from inferred radial load in both instances, which are introduced in turn.

$U_{F_R(test)}$ – Radial load uncertainty in bearing tests

Uncertainty of inferred load on individual bearings in bearing characterisation tests is primarily from the uncertainty of the load cell measurement, which is a function of the maximum load in application (derived in Section 6.4.3). There is also consideration of the uncertainty associated

Table 6.12: Contributions to total uncertainty of bearing frictional moment compensation, U_M.

Uncertainty	Section	Description	Units
u_{τ_A}	6.3.2	Standard uncertainty of torque measurement (driveline A)	Nm
$u_{M_A(est)}$	6.5.1	Standard uncertainty estimate (conservative) of bearing compensation frictional moment	Nm
$U_{F_R(\tau)}$	6.5.1	Combined uncertainty of radial load calculated from applied torque	N
u_{F_R}	6.4.3	Standard uncertainty of radial load from load cell measurement	N
$U_{F_R(test)}$	6.5.1	Combined uncertainty of radial load from load cell measurement and additional influences	N
$U_{F_R(bearing)}$	6.5.1	Combined uncertainty of radial load acting on individual bearing	N
U_{F_R}	6.5.1	Total combined uncertainty of radial load equivalence	N
$u_{\omega(chains)}$	6.3.1	Standard uncertainty of rotational speed on chains test	$rads^{-1}$
$u_{\omega(bearing)}$	6.4.1	Standard uncertainty of rotational speed on bearing test	$rads^{-1}$
U_ω	6.5.2	Combined uncertainty of rotational speed equivalence	$rads^{-1}$
$U_{M(\omega,F_R)}$	6.5.3	Total combined uncertainty of frictional moment from radial load and rotational speed equivalence	Nm
$u_{M(test)}$	6.4.2	Standard uncertainty of frictional moment measurement on bearing test	Nm
$u_{M(bearing)}$	6.5.3	Standard uncertainty of frictional moment of individual bearing in bearing test	Nm
U_M	6.5.3	Total combined uncertainty of frictional moment for bearing compensation	Nm

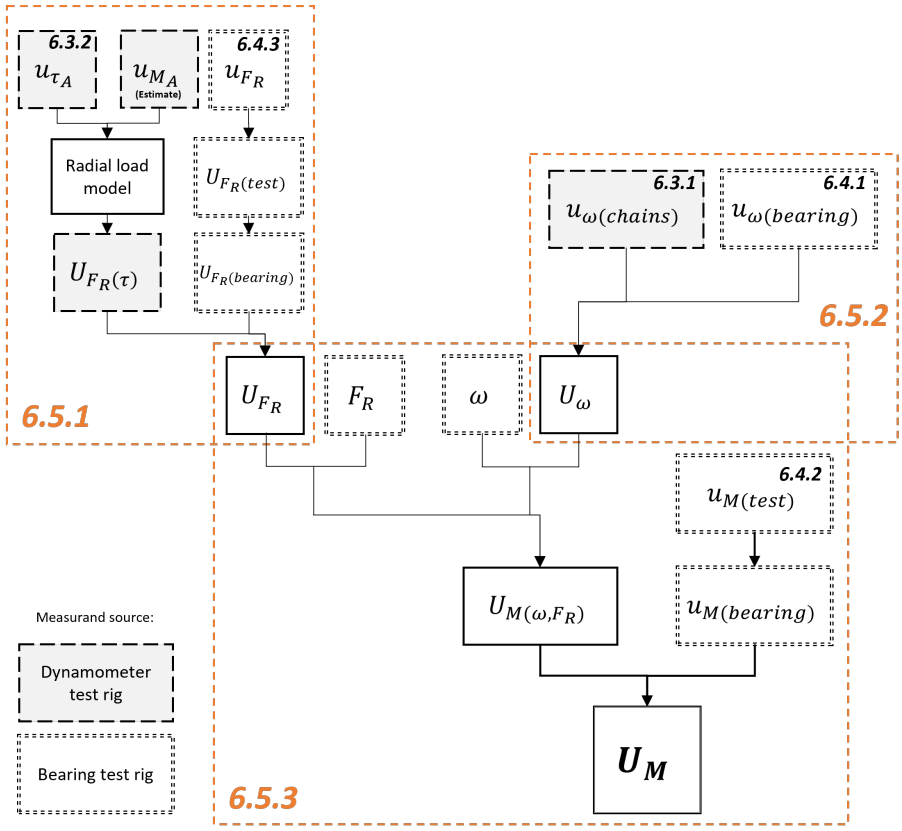

Figure 6.8: Propagation of uncertainty in bearing frictional moment compensation on dynamometer test rig transmission results.

with the additional weight on the bearings from mass upstream of the load cell. Furthermore, the value of measured load is 'tared' by subtracting the reading from the load cell when no load is applied; this introduces an additional uncertainty contribution from the zero measurement which is determined from the Type B analysis in Section 6.4.3. All parameters used to calculate radial load and associated error distributions are summarised in Table 6.13.

The combined standard uncertainty is expressed in Equation 6.10, which is the quadrature sum of standard uncertainties for parameters described in Table 6.13. Where the error is expressed as a uniform distribution, a standard uncertainty is defined by applying a coverage factor of 0.58 to approximate a value for normal standard deviation.

$$U_{F_R(test)} = \sqrt{\left(0.58 \cdot u_{W(carriage\ )}\right)^2 + \left(0.58 \cdot u_{W(shaft)}\ \right)^2 + {u_{F_R(0)}}^2 + {u_{F_R}}^2} \tag{6.10}$$

The uncertainty of load measured in bearing test is dependent on applied load during test. The load seen by the bearing, and hence the absolute uncertainty, is half of the total:

$$U_{F_R(bearing)} = \frac{U_{F_R(test)}}{2} \tag{6.11}$$

The calculated uncertainty of radial load on individual bearings across a torque-speed test envelope is illustrated in Figure 6.9. Uncertainty is higher for the front bearing than the rear due to higher

Table 6.13: Parameters in radial load calculation and associated error distributions.

Variable	Distribution (parameters)	Parameter 1	Parameter 2	Source of value/error
Carriage + Load cell mass	Uniform (min, max)	8.578 kg	8.778 kg	Laboratory balance
Shaft mass	Uniform (min, max)	2.662 kg	2.862 kg	Laboratory balance
Load cell measurement (Type B)	Normal (μ, σ)	various	various	Type B load measurement
Zero tare	Normal (μ, σ)	0	1.4162 N	Type B load measurement

radial loads. It also has a more significant dependence on torque. The uncertainty does not change with speed in either case.

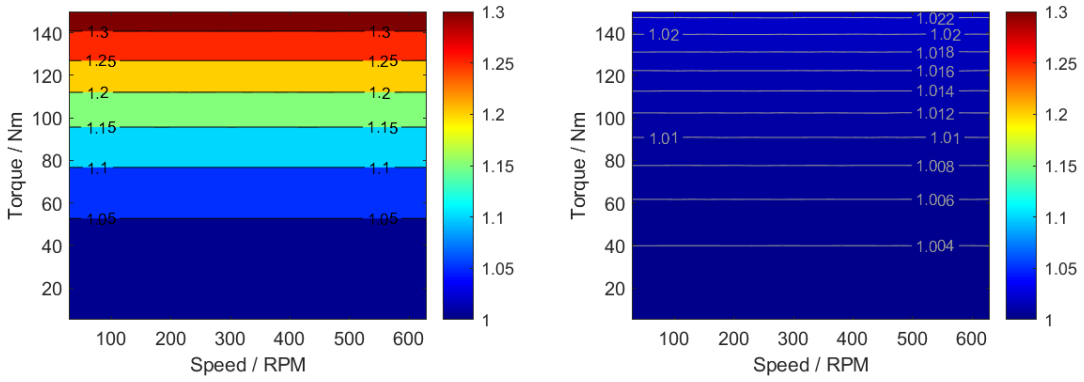

(a) $U_{F_R(bearing)}$ (Front) / [N]

(b) $U_{F_R(bearing)}$ (Rear) [N]

Figure 6.9: Absolute uncertainty [N] of inferred radial load on individual bearing as function of applied torque and speed for typical test configuration.

$U_{F_R(\tau)}$ – Radial load uncertainty in model

The radial load experienced by support bearings in the dynamometer test rig is calculated from the lever effect of the cantilevered load from the applied torque inducing tension in the chain span. The full calculation is detailed in Section 5.4.1. In deriving the radial load, there is uncertainty in applying various measurements involved in the calculation. The parameters and associated distributions are summarised in Table 6.14. Where uncertainties are unknown (such as the uncertainty of bearing compensation, since this is yet to be calculated), conservative estimates are included.

Table 6.14: Variables in radial load calculation and associated error distributions.

Variable	Distribution (parameters)	Parameter 1	Parameter 2	Source of value/error
Measured torque	Normal (μ, σ)	Various	0.105 Nm	Torque flange
Bearing compensation estimate	Normal (μ, σ)	Calculated	20%	Estimate (conservative)
Pretension	Normal (μ, σ)	2 N	0.5 N	Modelled
Shaft weight	Normal (μ, σ)	19.6 N	0.5 N	Modelled
Sprocket-bearing distance (L_1)	Normal (μ, σ)	60 mm	1 mm	Measured
Location of shaft mass centre (L_3)	Normal (μ, σ)	100 mm	1 mm	Modelled
Sprocket teeth	Uniform (min, max)	12	18	Tested range

The distributions are combined by running a Monte Carlo analysis, as described in Section 2.5.2. Randomised values for each variable are distributed according to the specified probability density functions described in Table 6.14. At each nominal test point with defined speed and torque, the analysis is run 1000 times and the distribution of radial load recorded. The histogram of data at an example nominal set point is shown in Figure 6.10, with a fitted normal distribution plotted. There is more absolute uncertainty in the front bearing radial load due to the larger forces.

The standard deviation of the fitted normal distribution shown in Figure 6.10 is equivalent to the combined standard uncertainty for the calculated radial load on bearings in the dynamometer test rig. The combined standard uncertainty across the entire test envelope is calculated and plotted in Figure 6.11. There is a clear dependence of uncertainty of applied radial load with increasing torque, and slightly higher uncertainty in the front bearing than the rear.

U_{F_R} – Combined uncertainty on bearing load

For a nominal range of speed and torque the radial load uncertainty is calculated by combining the uncertainty from radial load measured in bearing tests with the uncertainty from calculation of induced load from torque in on the dynamometer test rig as in Table 6.15.

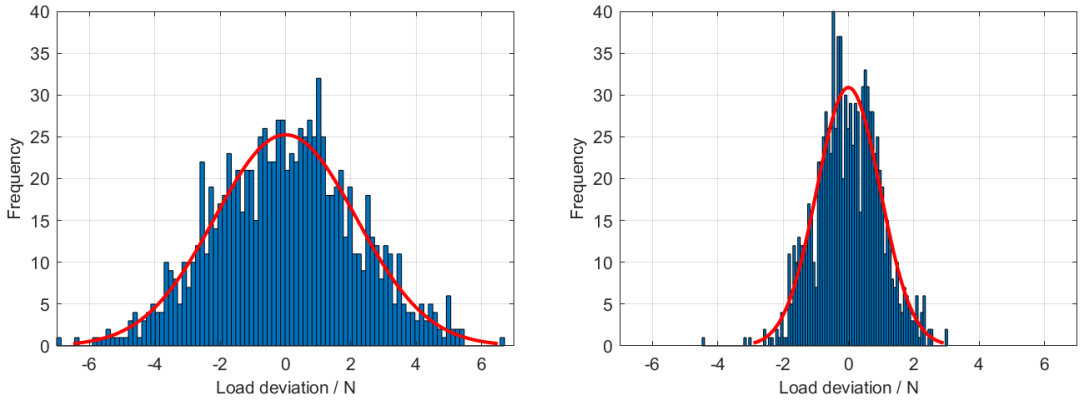

(a) Front position bearing.

(b) Rear position bearing.

Figure 6.10: Histogram showing radial load deviation from Monte Carlo simulation ($N = 1000$) at $20Nm$ and $11 rads^{-1}$ nominal inputs for front and rear bearings. Normal distribution is fitted and shown. Standard deviation represents the uncertainty at this test point.

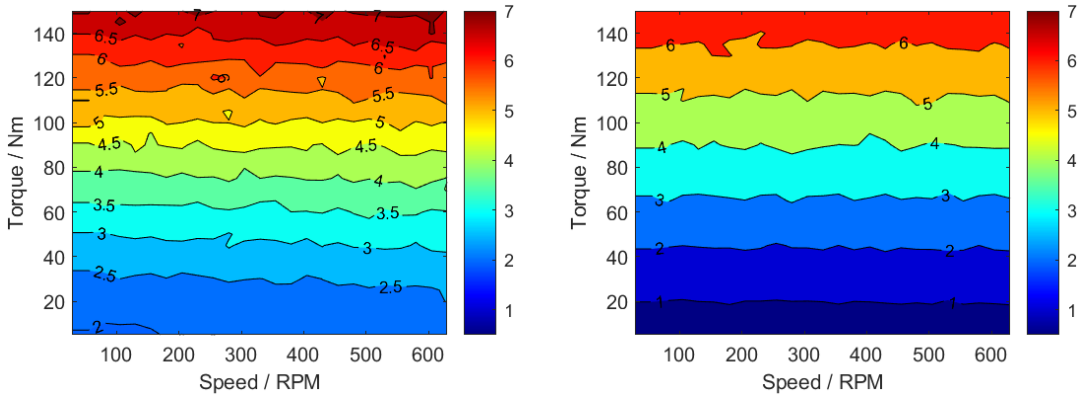

(a) $U_{F_R(\tau)}$ (front) $[N]$

(b) $U_{F_R(\tau)}$ (rear) $[N]$

Figure 6.11: Absolute combined uncertainty of calculated radial load in bearings [N] on dynamometer test rig across speed/torque envelope from model parameters distributed according to Table 6.14.

Table 6.15: Descriptions for U_{F_R} for front and rear bearings on Drivelines A and B on dynamometer rig.

Driveline	$U_{F_R}/N =$	
	Front bearing	**Rear bearing**
A	$\sqrt{U_{F_R(\tau)_{A-front}}^2 + U_{F_R(bearing)_{front}}^2}$	$\sqrt{U_{F_R(\tau)_{A-rear}}^2 + U_{F_R(bearing)_{rear}}^2}$
B	$\sqrt{U_{F_R(\tau)_{B-front}}^2 + U_{F_R(bearing)_{front}}^2}$	$\sqrt{U_{F_R(\tau)_{B-rear}}^2 + U_{F_R(bearing)_{rear}}^2}$

The combined uncertainty of bearing load is calculated across the test envelope and illustrated in Figure 6.12. The uncertainty of measured radial load is small and the uncertainty of dynamometer

radial load from applied torque dominates, hence the resultant combined uncertainty has changed little from the uncertainty from torque only, illustrated in Figure 6.11.

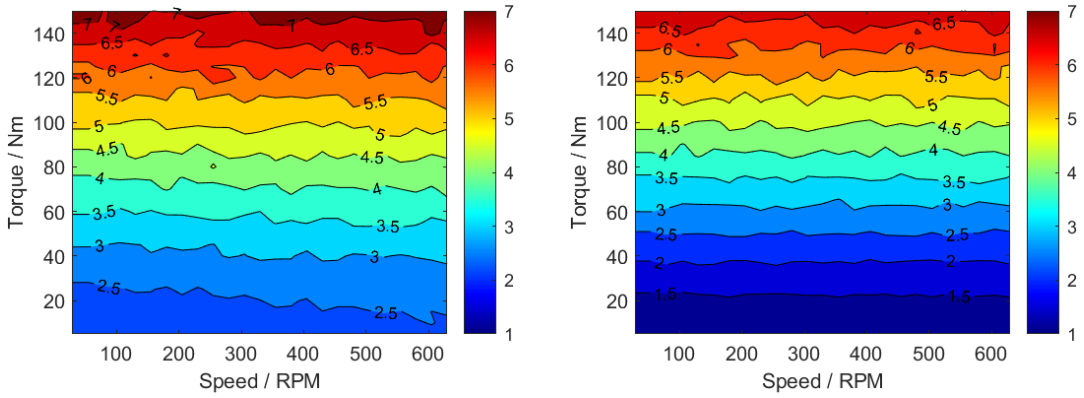

(a) U_{F_R} (front) $[N]$ **(b)** U_{F_R} (rear) $[N]$

Figure 6.12: Combined standard uncertainty of radial load [N] from combination of load measurement uncertainty and modelled radial load uncertainty for front and rear bearings on each driveline.

6.5.2 Uncertainty of rotational speed equivalence

The combined uncertainty of rotational speed equivalence between tests on the bearing and chains test rigs is the quadrature sum of uncertainty of individual measurements for each bearing in the chains rig. The uncertainty of rotational speed of each test rig as determined by Type A methods (Sections 6.3.1 and 6.4.1) is not dependent on speed or load since it is aggregate normalised data from a duty cycle with changing parameters. Their constant values are summarised in Table 6.16.

Table 6.16: Descriptions and calculated values of U_ω for front and rear bearings on Drivelines A and B on dynamometer rig.

Driveline	$U_\omega / rads^{-1}$	
	Front bearing	**Rear bearing**
A	$\sqrt{{u_{\omega_A}}^2 + {u_{\omega_2}}^2} = 0.2280$	$\sqrt{{u_{\omega_A}}^2 + {u_{\omega_1}}^2} = 0.1226$
B	$\sqrt{{u_{\omega_B}}^2 + {u_{\omega_2}}^2} = 0.2297$	$\sqrt{{u_{\omega_B}}^2 + {u_{\omega_1}}^2} = 0.1257$

6.5.3 Uncertainty of compensated frictional moment

$U_{M(\omega,F_R)}$ – From combined speed and load uncertainty

The uncertainty of equivalence in radial load, U_{F_R}, and equivalence in rotational speed, U_ω, between the chains and bearing tests were derived in the previous section. The resultant uncertainty of frictional moment from their combined uncertainties, $U_{M(\omega,F_R)}$, is evaluated now with consider-

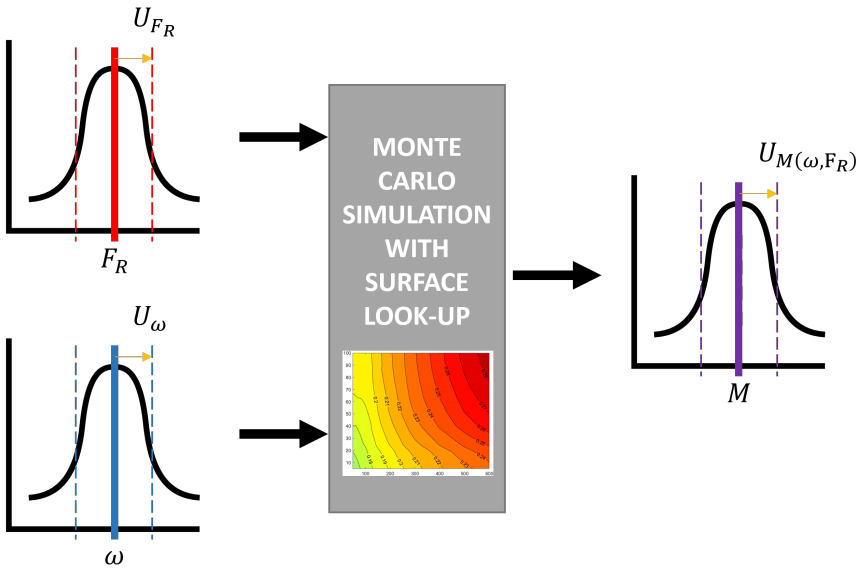

Figure 6.13: Combined effect on frictional moment uncertainty of radial load and speed equivalence between test rigs evaluated by Monte Carlo analysis using data from interpolated empirical results. Simulation is run 1000 times for each load and speed data point.

ation of the dependency of frictional moment on both the radial load and rotational speed across the test envelope. The uncertainty of bearing load uncertainty, Table 6.12, and rotational speed uncertainty, Table 6.16, define a 'patch' on the speed-load surface of frictional moment, Figure 5.18. The spread of values of frictional moment within this 'patch' determine the resultant uncertainty from equivalence. This process is illustrated in Figure 6.13.

A Monte Carlo simulation is used to derive a distribution based on normally distributed values of radial load and speed defined by nominal inputs and their calculated uncertainties. Rotational speed ω and radial load F_R with associated uncertainties U_ω and U_{Fr} are fed into the bearing radial load results to produce a spread of frictional moments for each test point. The model is run 1000 times, with each randomised pairing producing a unique value of bearing friction. The spread of this data is used to derive an uncertainty of the bearing friction. The resultant histograms from the Monte Carlo analysis are shown in Figure 6.14. Simulated data of frictional moment shows greater spread in the front bearing than the rear bearing.

Normal distributions are fitted to all nominal torque and speed inputs, and the standard deviation of each distribution is a measure of the uncertainty at that input. The uncertainty across the test envelope is shown in Figure 6.15. There is no discernible general trend, with low values of uncertainty across the test envelope for the front and rear bearing positions.

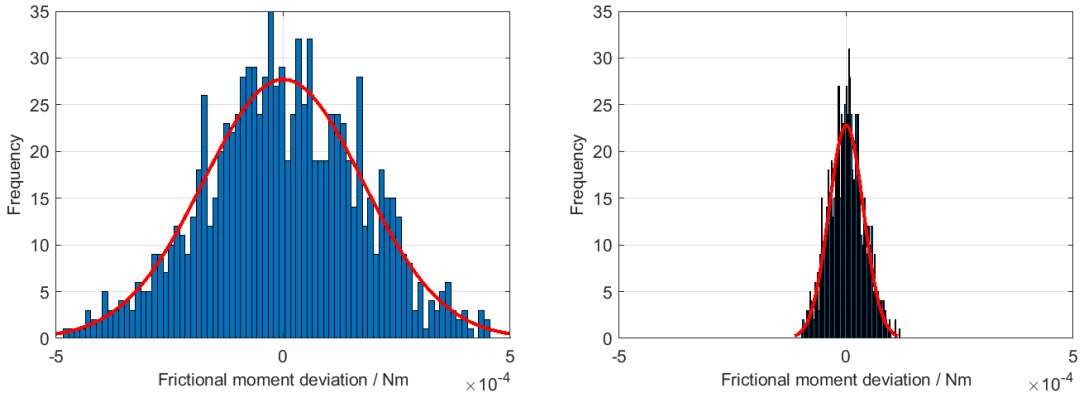

(a) Front position bearing.

(b) Rear position bearing.

Figure 6.14: Frictional moment histogram for N=1000, shown at 20Nm nominal input torque and 105 RPM nominal input speed. Normal distribution is fitted and shown.

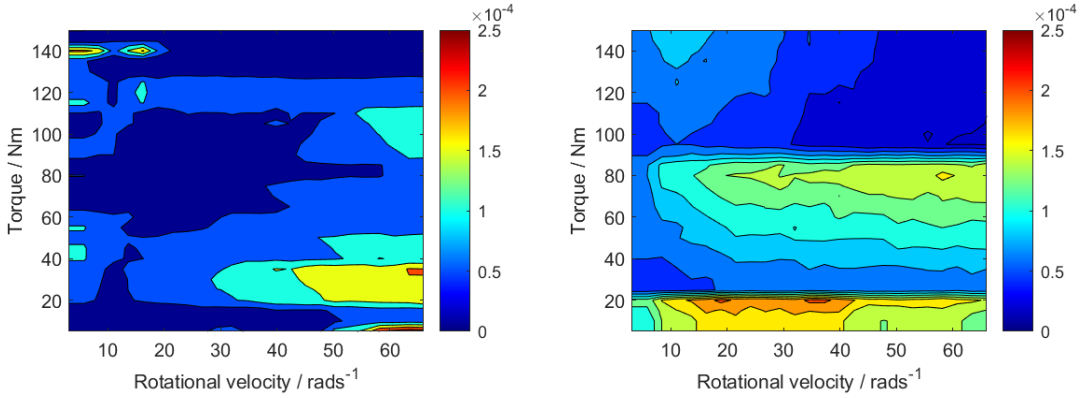

(a) $U_{M(\omega,F_R)}$ (front) $[Nm]$

(b) $U_{M(\omega,F_R)}$ (rear) $[Nm]$

Figure 6.15: Frictional moment uncertainty [Nm] as function of speed and torque for combined effect of equating speed and loading between conditions on bearing and chains test rigs (shown for Driveline A). Contour labels are removed for clarity.

$U_{M(bearing)}$ – From bearing test measurement of frictional moment

The uncertainty of frictional moment in individual bearings is calculated from the uncertainty of measurement in the tests conducted on the bearing rig, detailed in Section 5.5. The calculation of uncertainty is related to the calculation of inferred individual frictional moment of a single bearing. In Test-1, the friction on an individual SKF-6007 bearing is calculated in Table 5.4 and uncertainty calculated in Equation 6.12.

$$U_{M_{rear}} = \frac{U_{M_1}}{4} \tag{6.12}$$

The calculation for frictional moment in SKF-NU308 bearings in test-2 detailed in Section 5.5 is shown in Table 5.6. Since Test-1 data is used to isolate the SKF-NU308 bearings, uncertainty is a function of uncertainty of the rear bearing. It is calculated in Equation 6.13.

$$U_{M_{front}} = \sqrt{\left(\frac{U_{M_2}}{2}\right)^2 + {U_{M_{rear}}}^2} \tag{6.13}$$

The absolute results are summarised in Table 6.17.

Table 6.17: Uncertainty of measured frictional moment.

Uncertainty source	**Frictional moment uncertainty /** Nm	
	Front bearing (Test-2)	**Rear bearing (Test-1)**
Test	0.0127	0.0127
Individual bearing	0.00318	0.00710

U_M – Combined uncertainty on frictional moment

The uncertainty of speed and load equivalence, $U_{M(\omega,Fr)}$, and uncertainty of frictional moment measurement $U_{M(bearing)}$, are summed in quadrature to express the combined uncertainty of frictional moment, U_M. Equations for each bearing are shown in Table 6.18.

Table 6.18: Descriptions of U_M for front and rear bearings on Drivelines A and B on dynamometer rig.

Driveline	U_M/Nm	
	Front bearing	**Rear bearing**
A	$\sqrt{{U_{M(\omega,Fr)_{A-front}}}^2 + {U_{m_{front}}}^2}$	$\sqrt{{U_{M(\omega,Fr)_{B-front}}}^2 + {U_{m_{rear}}}^2}$
B	$\sqrt{{U_{M(\omega,Fr)_{A-rear}}}^2 + {U_{m_{(fr)}}}^2}$	$\sqrt{{U_{M(\omega,Fr)_{A-rear}}}^2 + {U_{m_{rear}}}^2}$

The results for Driveline A front and rear bearings are illustrated across the test envelope in Figure 6.16. The scale of each contour plot demonstrates the very small fluctuations in uncertainty of frictional moment across the test envelope, showing that the uncertainty of frictional moment measurement, $U_{M(bearing)}$, dominates in both front and rear positions.

6.5.4 Combined uncertainty on each driveline

The final step in determining uncertainty of frictional moment compensation, the uncertainty of frictional moment compensation for front and rear bearings are combined to express a total uncertainty for each driveline. The uncertainty of compensated frictional moment and uncertainty of compensated frictional power are calculated.

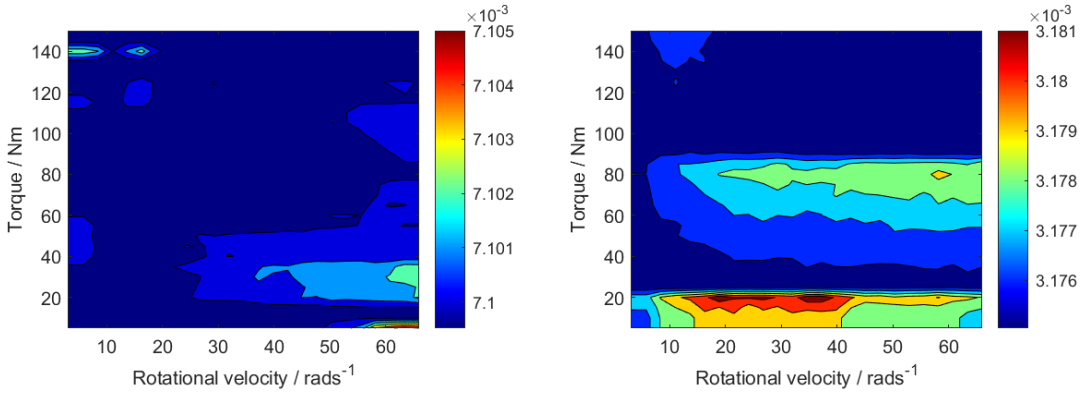

(a) U_M (front) $[Nm]$ **(b)** U_M (rear) $[Nm]$

Figure 6.16: Frictional moment uncertainty [Nm] as function of speed and torque for bearings on driving shaft (Driveline A). Contour labels are removed for clarity.

U_{M_A}, U_{M_B} – Compensated frictional moment

The quadrature sum of uncertainties of front and rear bearings on each driveline give the combined uncertainty of bearing frictional moment on each shaft over the test envelope.

$$\begin{aligned} U_{M_A} &= \sqrt{{U_{M_{A-front}}}^2 + {U_{M_{A-rear}}}^2} \\ U_{M_B} &= \sqrt{{U_{M_{B-front}}}^2 + {U_{M_{B-rear}}}^2} \end{aligned} \tag{6.14}$$

The combined uncertainty for Driveline A and Driveline B bearing frictional moment compensation is illustrated for the test envelope in Figure 6.17.

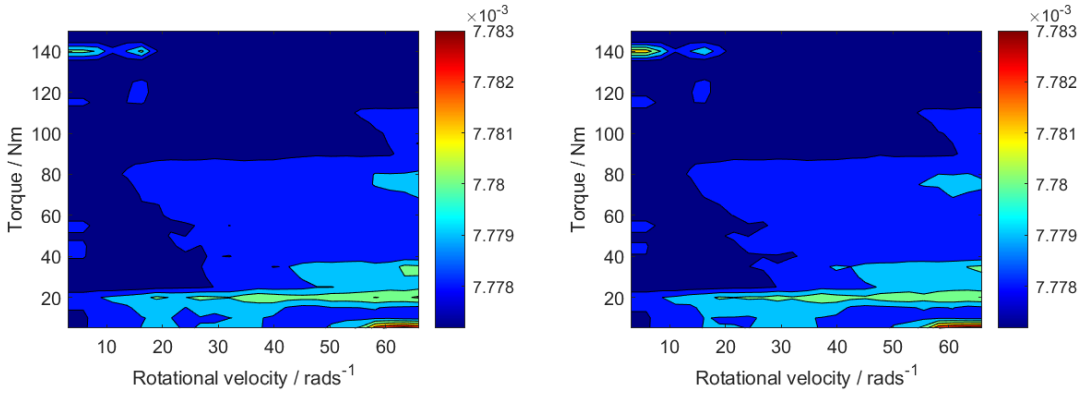

(a) U_M (Driveline-A) $[Nm]$ **(b)** U_M (Driveline-B) $[Nm]$

Figure 6.17: Frictional moment uncertainty U_{M_A} & U_{M_B} [Nm] as function of speed and torque for combined bearings on each driveline of dynamometer test rig.

The relative influence of each source of uncertainty which is introduced in previous sections is illustrated for both drivelines in the pie chart in Figure 6.18.

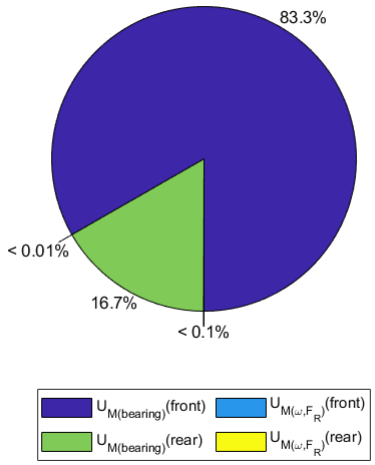

Figure 6.18: Breakdown of uncertainty of bearing frictional moment on individual driveline (U_M) for nominal test point ($20Nm$, $11rads^{-1}$). Contribution from uncertainty of equivalence is negligible for front ($< 0.01\%$) and rear ($< 0.1\%$) bearings.

As already discussed, the contribution from uncertainty of loading equivalence is negligible for both front and rear bearings. The uncertainties in radial load, U_{F_R}, and rotational speed U_ω, are not negligible, but the effect they make on the frictional moment is not significant.

The uncertainty of the frictional moment compensation is dominated by measurement of frictional moment of the front bearing, accounting for 83.3% of the uncertainty on each driveline. The front bearing has larger direct frictional moment uncertainty, $U_{M(bearing)}$, due to using data from two tests, and hence twice the uncertainty. It also has larger frictional moment, and so the absolute contribution is more significant.

$U_{P(bearing)_A}, U_{P(bearing)_B}$ – Compensated consumed power

The uncertainty of power consumed in the bearings is calculated by applying Equation 2.63 to the description of $P_{loss(bearings)}$:

$$\begin{aligned} P_{loss(bearings)_A} &= M_A \omega_A \\ P_{loss(bearings)_B} &= M_B \omega_B \end{aligned} \tag{6.15}$$

Absolute uncertainty is described as below.

$$\begin{aligned} U_{P(bearing)_A} &= \sqrt{M_A^2 U_{\omega_A}^2 + \omega_A^2 U_{M_A}^2} \\ U_{P(bearing)_B} &= \sqrt{M_B^2 U_{\omega_B}^2 + \omega_B^2 U_{M_B}^2} \end{aligned} \tag{6.16}$$

The power uncertainty is calculated across the test envelope and illustrated in Figure 6.19, separated by driveline. There is no discernible trend with torque, which is due to the dominating influence of the uncertainty of frictional moment measurement $U_{M(bearings)}$, which is an absolute value of torque across the test envelope. When multiplied by rotational speed to calculate power, the dependence of power uncertainty is in speed only. The only difference between Drivelines A and B are in subtle effects now shown to have a negligible influence.

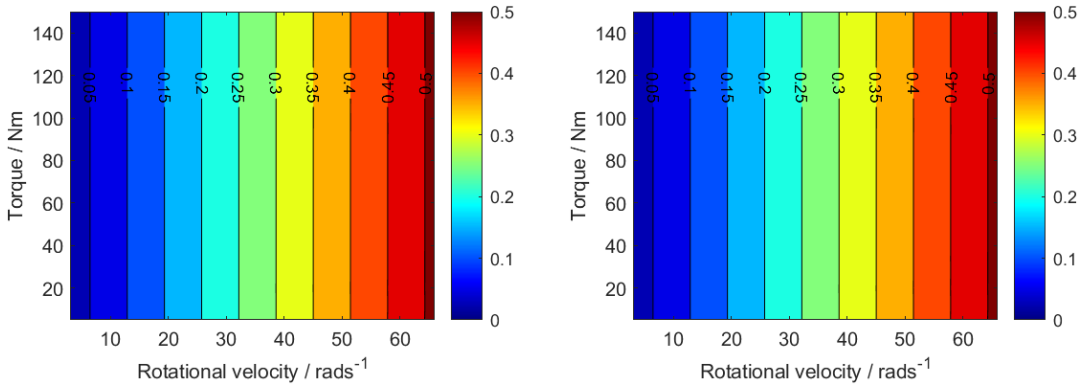

(a) $U_{P(bearing)}$ (Driveline-A) $[W]$

(b) $U_{P(bearing)}$ (Driveline-B) $[W]$

Figure 6.19: Power uncertainty $U_{P_{bearing}}$ [W] as function of speed and torque for combined bearings.

6.6 Uncertainty of transmission power loss chains test

The uncertainty of the bearing compensation is now derived and must be combined with the uncertainty of measurements in the dynamometer transmission tests. The uncertainty of transmission efficiency and transmission power loss are considered separately.

6.6.1 Combined standard uncertainty of power loss

The combined standard uncertainty of power loss is calculated from the sources of uncertainty derived in this chapter and the measured variables they are describing, shown in Figure 6.20.

Measured variables and derived uncertainties are combined as in Equation 6.4, and results illustrated for a range of input torque and rotational speed based on nominal gear ratio of 3:1. This is illustrated in Figure 6.21. As previously, uncertainty of transmission power loss has dependence on the applied speed.

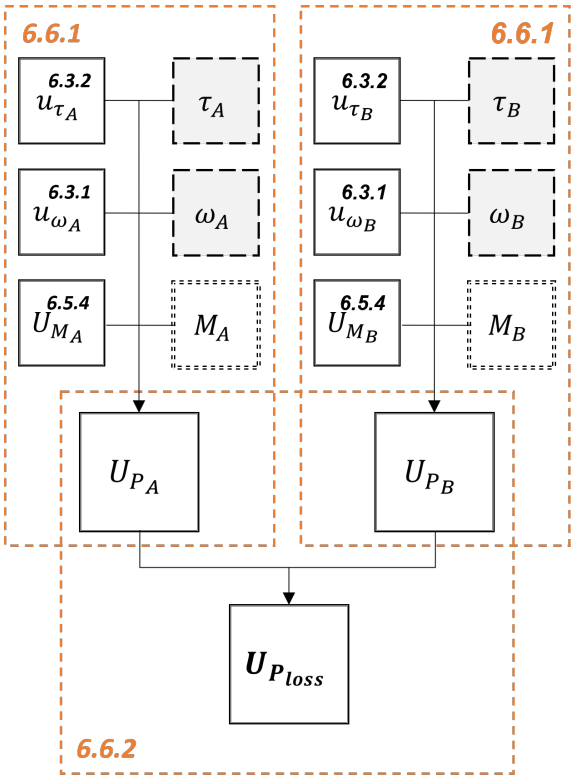

Figure 6.20: Propagation of uncertainty in determination of power loss on dynamometer test rig.

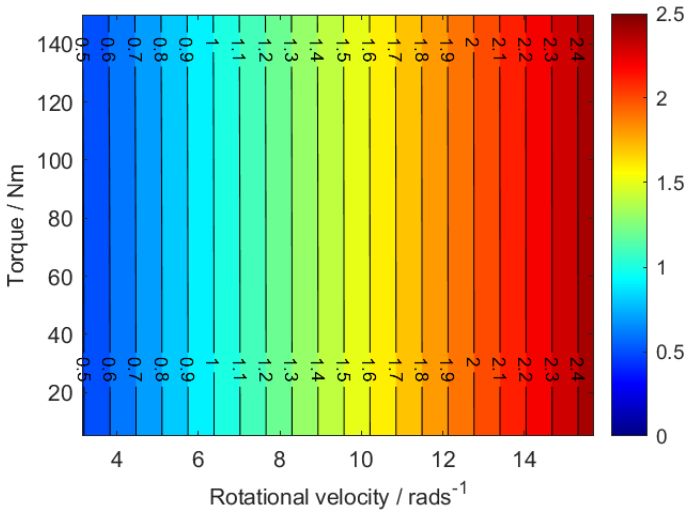

Figure 6.21: Uncertainty of transmission power loss $U_{P_{loss}}$ [W] as function of applied driving torque and speed.

6.6.2 Relative contribution to uncertainty

The relative contribution of uncertainties to the overall uncertainty of power loss is demonstrated here to illustrate the origin of the uncertainty, and which should be targeted for improvement to effectively improve overall uncertainty. A pie chart is plotted in Figure 6.22 for several nominal

gearing options, which changes the relative torque and speed, affecting absolute uncertainty and the relative source contributions.

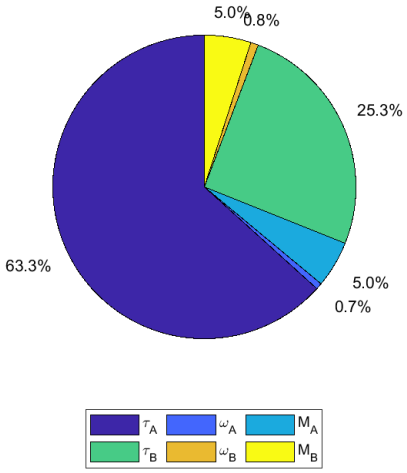

(a) 1:1 gearing, $U_{P_{loss}} = 1.2W$.

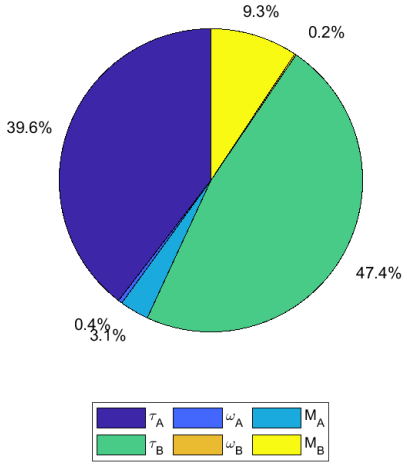

(b) 3:1 gearing, $U_{P_{loss}} = 1.7W$.

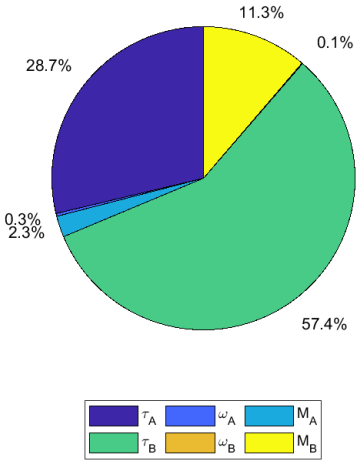

(c) 5:1 gearing, $U_{P_{loss}} = 2.5W$.

Figure 6.22: Contribution to combined uncertainty of power loss $U_{P_{loss}}$ for different gear ratios at set test point ($\omega_A = 11 rads^{-1}, \tau_A = 25Nm, P_A = 275W$).

Figure 6.22 shows that the uncertainty of transmission power loss is influenced overwhelmingly by the uncertainty of the torque measurements, accounting for 80-84% in the examples shown. For higher gearing, the influence of uncertainty on Driveline B increases since its scaling increases with rotational speed. Uncertainty of frictional moment compensation of the bearings is next biggest contribution, at 8.2-12.6% in illustrated examples in Figure 6.22. This is more significant at higher speed, and increased at equivalent test points for increased gearing. Uncertainty of speed measurement is more significant than that from bearing compensation at low speeds, though small at high speeds.

6.7 Reducing uncertainty & quoting uncertainty

6.7.1 Repeat measurements

Reliability of results can be increased by running independent repeat experiments. The conditions of the transmission-under-test are randomised by refitting the test chain between experiments so any subtle variation in the alignment and pretension can be averaged out across tests. Furthermore, the measuring equipment is re-zeroed and electric machines restarted after a period of cooling down. There are practical challenges of running repeat experimental which are truly independent of one another, since the same equipment must be used in the same environmental conditions, operated by the same electrical supply, so experiments are independent insofar as is reasonably practical with present equipment.

Where n independent repeats are made of a test the uncertainty is reduced by a factor $\frac{1}{\sqrt{n}}$, from the description of the standard deviation of independent estimations of the same measurement according to the Central Limit Theorem. The experimental results detailed in Chapter 8 are determined with 5 independent tests, thus reducing the uncertainty by a factor of $\frac{1}{\sqrt{5}} = 0.447$. The uncertainty of power loss measurand is illustrated across the test envelope in Figure 6.23.

6.7.2 Quoting a single measurand value

For tests across a test envelope with variety of applied torque and speed, a surface contour plot as used in the latter part of this chapter is an effective method to graphically display results. The associated combined standard uncertainties may be displayed on an equivalent surface, as is demonstrated.

When quoting individual results and corresponding uncertainties, the GUM literature recommends stipulating the confidence interval which that uncertainty covers [6].

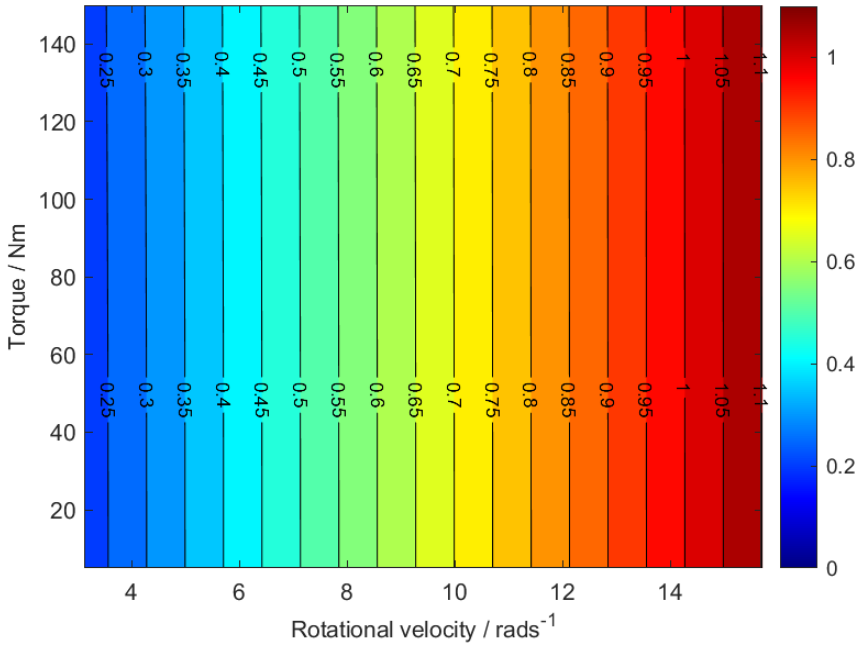

Figure 6.23: Uncertainty of transmission power loss $U_{P_{loss}}$ [W] as function of applied driving torque and speed for 5 independent repeats.

If using an expanded uncertainty, where $U_c = k \cdot u_c$, the coverage factor k is used to ensure that the confidence interval is sufficient for the application. In safety applications there may be need for this to be 99% coverage, or even higher. The coverage factors and associated confidence intervals are shown in Table 2.7 in Section 2.5.

If using an expanded uncertainty which conforms with a standard for the particular industry, then the GUM suggests a result may be quoted as '$value \pm expanded\ uncertainty$'. With confidence in the repeatability of experiments through repeated observation during extended testing experience on the dynamometer apparatus, an expanded uncertainty is used with a coverage factor of 1. Hence, the an individual result is quoted as below.

$$value \pm u_c\ (68\%) \tag{6.17}$$

6.7.3 Side-by-side comparison

Tests are often conducted to determine how transmission 'α' compares to transmission 'β', which may be a standard datum or have particular differences which are the focus of the test (e.g. same chain with different gear sizes). When such tests are conducted, they should be repeated in such a sequence that the average environmental or time-dependent conditions are similar for both (α-β-β-α-α-β etc). Conducting tests side-by-side also can ensure that the handling and set-up of the transmissions under test are equivalent since they are being done at the same time by the same person.

In instances of direct comparison, it is possible to calculate the confidence with which one can claim that there is reduced power losses in transmission α when compared with transmission β based on the measured data and calculated uncertainty. With two nominal results at equivalent loading conditions, there are two associated mean values for power loss (μ_α and μ_β) and two associated standard deviations for this result (σ_α and σ_β), equivalent to the standard uncertainties of the measurand described by μ. Assuming this represents a normal distribution, the statistical probability that $\alpha < \beta$ is an expression of its confidence. This can be calculated as the cumulative distribution function for the standard normal distribution, shown below.

The normal probability density function (PDF) is described as in Equation 6.18.

$$f(x) = \frac{1}{\sqrt{2\pi}} e^{-\frac{1}{2}\left(\frac{x-\mu}{\sigma}\right)^2} \tag{6.18}$$

The cumulative distribution function for the standard normal distribution ($\mu = 0,\ \sigma = 1$) is a description of the proportion of a distribution between negative infinity and a set point, x.

$$\begin{aligned} F(x) &= \int_{-\infty}^{x} \frac{1}{\sqrt{2\pi}} e^{-\frac{1}{2}\left(\frac{t-0}{1}\right)^2}\, dt \\ &= \frac{1}{\sqrt{2\pi}} \int_{-\infty}^{x} e^{-\frac{t^2}{2}}\, dt \end{aligned} \tag{6.19}$$

For numerical calculation it is possible to perform a Taylor series expansion to approximate the integral, where the first four terms of the expansion are described:

$$\begin{aligned} F(x) &\approx \frac{1}{2} + \frac{1}{\sqrt{2\pi}} \sum_{k=0}^{n} \frac{(-1)^k x^{(2k+1)}}{2^k k!\,(2k+1)} \\ &\approx \frac{1}{2} + \frac{1}{\sqrt{2\pi}} \left(x - \frac{1}{6}x^3 + \frac{1}{40}x^5 - \frac{1}{336}x^7 \right) \end{aligned} \tag{6.20}$$

To determine the confidence with which one result is smaller than another, the two variables are considered as normally distributed with means μ_α and μ_β and standard deviations σ_α and σ_β:

$$\alpha \sim N\left(\mu_\alpha, \sigma_\alpha^2\right) \tag{6.21}$$

$$\beta \sim N\left(\mu_\beta, \sigma_\beta^2\right) \tag{6.22}$$

The confidence in α being smaller than β is can be written as a probability:

$$P(\alpha < \beta) = P(\alpha - \beta < 0) \tag{6.23}$$

A new normal distribution, γ, is defined $\gamma = \alpha - \beta$, such that γ is normally distributed with mean and standard deviation below:

$$\gamma \sim N\left(\mu_\alpha - \mu_\beta, \sigma_\alpha^2 + \sigma_\beta^2\right) \tag{6.24}$$

The proportion of γ that is less than zero represents the confidence with which it can be said a variable from distribution α is smaller than a variable from distribution β. Φ is the cumulative distribution function for the standard normal distribution.

$$P(\gamma > 0) = 1 - \Phi\left(\frac{\mu_\alpha - \mu_\beta}{\sqrt{\sigma_\alpha^2 + \sigma_\beta^2}}\right) \tag{6.25}$$

When $\sigma_\alpha = \sigma_\beta = \sigma$

$$P(\gamma > 0) = 1 - \Phi\left(\frac{\mu_\alpha - \mu_\beta}{\sqrt{2}\,\sigma}\right) \tag{6.26}$$

A numerical example is illustrated. Two results α and β have mean and uncertainty as summarised in Table 6.19.

Table 6.19: Mean and standard deviation of example results, α and β.

Transmission result	Mean μ	Std deviation σ
α	40	1.5
β	42	1.5

The result suggests that transmission α performs better than transmission β. The confidence with which this claim can be made is calculated as below.

$$\begin{aligned} x &= \frac{\mu_\alpha - \mu_\beta}{\sqrt{2}\,\sigma} \\ &= \frac{40 - 42}{\sqrt{2} \cdot 1.5} \\ &= -0.943 \end{aligned} \tag{6.27}$$

$$\begin{aligned} \Phi(x) &\approx \frac{1}{2} + \frac{1}{\sqrt{2\pi}}\left(x - \frac{1}{6}x^3 + \frac{1}{40}x^5 - \frac{1}{336}x^7\right) \\ &= 0.173 \end{aligned} \tag{6.28}$$

$$\begin{aligned} P(D > 0) &= 1 - \Phi(x) \\ &= 1 - 0.173 \\ &= 0.827 \end{aligned} \tag{6.29}$$

In this example, the confidence with which it can be claimed that the power loss measurand β is greater than α is 83%.

6.8 Conclusions and further work

Determining the uncertainty of inferred power losses based on measurements on the dynamometer test rig is an involved process, combining measurements from several tests across multiple test rigs

as well as static determination of masses and lengths for use in corrections or equivalence models. The outcome of this study is an estimate of the uncertainty associated with the measurand, which allows for contextualised results.

The uncertainty of transmission power loss across a test envelope changes as a function of rotational speed, with very little variation with torque. At low applied speed, the absolute uncertainty is lower than at high speeds. The speed dependency of power loss uncertainty is due to the overwhelming impact of the torque uncertainty relative to the speed uncertainty in calculating power loss. A large absolute torque uncertainty is scaled as speed scales much more significantly.

Areas where uncertainty may be improved are highlighted by the quantified contribution to the numerical uncertainty, illustrated in Figure 6.22. It is clear, for instance, that the uncertainty of the bearing compensation is small when compared with that of the measurement of torque on the dynamometer test rig. The most obvious improvement is to upgrade the torque transducers such that a higher accuracy class is used.

While limiting the functionality of the rig, it may also be of note to use transducers of smaller nominal torque rating and test at reduced power inputs for tests which emphasise improved uncertainty, although this moves the test rig away from its primary purpose of creating representative conditions. A less conservative trade-off may be possible with more bespoke equipment.

Quoting uncertainty in the context of side-by-side comparisons provides a confidence level to binary results in comparative tests. It is a simple expression of the confidence in a result which might be effectively communicated alongside results to encapsulate all contributions to uncertainty of measurement.

Further improvements to uncertainty can be explored by considering data fusion. Speed measurement, for example, is made independently by two different technologies on each driveline: both the torque transducer and the encoder on the electric machine. Through an appropriate estimation scheme, each value (with associated uncertainty) can be used to shrink the overall uncertainty.

6.9 Summary of Chapter 6

Standard uncertainty of measured variables was calculated for both dynamometer test rig and bearing characterisation rig. Where Type B methods are available, these are calculated alongside Type A methods and comment has been made on their validity and hence preference.

The combined uncertainty of bearing compensation in transmission tests on dynamometer test rig is calculated through combining the uncertainties of measurands and other static measurements made in to infer the equivalence of physical loading between test rigs.

The combined standard uncertainty of results from the dynamometer test rig is then determined from the pre-calculated factors and shown as function of applied torque and speed.

Comment is made on how to use these results, which will be demonstrated in full in the next chapter where select results from the dynamometer test rig are presented.

Chapter 7

Isolating and Measuring Vibration Performance of Test Transmission on Dynamometer Test Rig

7.1 Introduction

The experimental design and set-up of transmissions-under-test on the dynamometer test rig is intended to maximise the fidelity of rig conditions compared with those expected in-use. The benefit of accurately recreating loading and boundary conditions for transmission-under-test is that behaviours induced, and subsequently observed and measured, can be directly related to behaviours which manifest in use.

Vibration has previously been introduced as a significant factor of performance alongside wear characteristics and power efficiency. Dynamic behaviours in the transmission are a source of vibration and noise which affect performance in transmission systems. Depending on the use, high levels of vibration may directly detract from performance or may accelerate wear or induce further losses, reducing efficiency. In the context of bicycle racing, particularly in indoor velodromes, vibration from the transmission may be the most significant source of vibration in the bicycle-cyclist system and interacts directly with the cyclist's torque input.

From interaction of polygonal action and resonant modes in span vibration, dynamic interaction of the chain and driving sprocket is inevitable in roller chains. Other transmission types may mitigate this. With testing on the dynamometer test rig, the relative impact of various parameters on the vibration can be observed. Previous research at the University of Bristol described in Section

2.3.4 used high speed camera technology to observe dynamic effects on the dynamometer test rig, including resonant frequencies in the span [1].

An earlier experimental test rig by Turnbull [80, 22] measured the effect of dynamics on sprocket accelerations on a dual-sprocket drive operating at constant speed. Polygonal action had a measurable influence on sprocket accelerations. Though resonance was observed, it was not measured in accelerations. Acceleration was examined in time and frequency domain to identify the peaks coinciding with tooth frequency of the transmission.

The acceleration of sprockets on the dynamometer test rig at the University of Bristol is readily measured since torque is captured to determine the input and output power measurands. Torque is related to angular acceleration according to Newton's Second Law, where the constant of proportionality is defined by inertia, J.

$$\tau = J\alpha \tag{7.1}$$

Torque data is captured at 1kHz, approximately an order of magnitude higher than the chain tooth frequency. It is therefore possible to examine the effect of the transmission dynamics on the torque measurement and develop a performance metric from the level of vibration in the system.

However, the transmission dynamics do not occur in isolation: there are many other sources of harmonic excitation or systematic noise which might be of influence. When purely observing the transmission to ascertain its dynamic response to measured loading, it is difficult to determine to what extent the system dynamics might influence the transmission dynamics.

A study of the transmission dynamics therefore must start with the external influences on test transmission dynamics from the system. This may highlight opportunity for mitigation through replacement of mechanical components or adjusting electro-mechanical control of the dynamometer. More fundamentally, appreciating the dynamic influence on driving and braking torque of the test transmission will offer validation for the nominal loading conditions the rig is designed to induce.

This chapter introduces a new method of measuring dynamics by taking advantage of high frequency data acquisition and considering the fluctuations in measured speed and torque. The benefit of this technique is that subtle systemic influences can be explored alongside the influence from the transmission and relative impact of all effects analysed. By filtering the measured signals of systemic influence, the dynamics of the transmission are isolated and can serve as an assessment of the smoothness of a particular transmission and help build a holistic picture of its performance.

7.1.1 Structure of chapter

The dynamics inherent to chain and belt drive transmission systems are detailed, and then theoretical systematic dynamics in the dynamometer test rig are introduced in this context, showing the frequency range where dynamic interaction may occur.

Methods for analysing the vibration in data captured from the dynamometer test apparatus are developed, with initial focus on identifying, commenting on and filtering the parasitic influences in different measured variables captured. Example test data will be analysed to demonstrate where theoretical frequencies manifest and in which measurement. By identifying parasitic influence with some certainty, it can be filtered from the data in effort to isolate the chain dynamics. With chain dynamics isolated, the magnitude and frequency are compared across different transmission parameters.

7.2 Transmission dynamics

7.2.1 Excitation from polygonal action

Sources of vibration in chain drive transmissions are introduced in Section 1.3.3. The most likely physical effect to influence torque and speed is polygonal action: where the changing wrap of the chain around the sprockets causes fluctuations in torque radius, illustrated in Figure 7.1. This is already shown to impact sprocket rotational speed and span tension in an ideal modelled environment, addressed in Section 3.3. The fluctuation of torque or speed is a regular, high-frequency source of excitation in the transmission system.

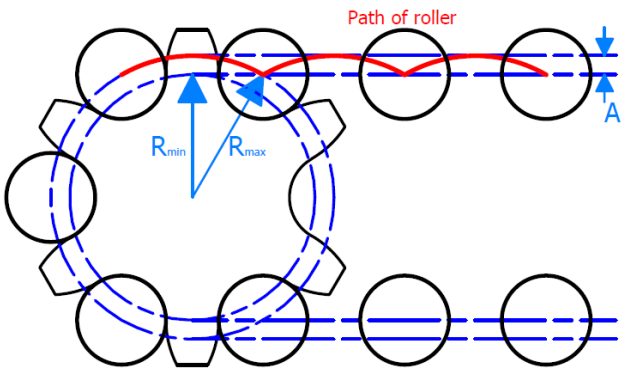

Figure 7.1: Polygonal action in chain leaving a sprocket, resulting in changing torque radius and transverse movement in the chain span.

Polygonal action acts at both ends of the transmission's high tension top span. Only when the tangent between pitch circles of two equal sized sprockets is an integer number of pitches is polygonal

action in phase; more commonly they are out of phase. The effect of polygonal action therefore will have some dependence on the length of this tangent from the centre distance between sprockets. With typical gear ratios in cycling, the contribution to polygonal action from the driving sprocket (chainring) is much smaller than from the driven sprocket (rear sprocket).

Alongside the polygonal action, the impact force from chain-sprocket meshing also occurs at the same frequency. The frequency of both is expressed in Equation 7.2.

$$f_{PG} = N_1 \frac{\omega_1}{2\pi} \tag{7.2}$$

The amplitude of variation in torque radius is calculated by finding the difference between minimum and maximum pitch circle radius of the driven sprocket on which the roller sits.

$$A = R_{max} - R_{min} = p \sin\left(\frac{\pi}{N_i}\right) \tag{7.3}$$

The speed ratio of two sprockets on a drive can be expressed as the tooth ratio in Equation 7.4. The fluctuations in torque radius at frequency f_{PG} and amplitude A result in a torque ratio between driving and driven sprockets in Equation 7.5

$$\frac{\omega_2}{\omega_1} = \frac{N_1}{N_2} \tag{7.4}$$

$$\frac{\tau_1}{\tau_2} = \frac{R_1 + A_1 \left|\sin\left(f_{PG}\left(t+\phi_1\right)\pi\right)\right|}{R_2 + A_2 \left|\sin\left(f_{PG}\left(t+\phi_2\right)\right)\pi\right|} \tag{7.5}$$

Where ϕ is the phase angle of the sprocket. The torque ratio relative to speed ratio is plotted in Figure 7.2 for an example drive demonstrating the combining effect of polygonal action at each span end when they are is in phase (even number of chain half links in the span), and out of phase (odd number of half chain links in the span).

7.2.2 Resonant frequencies

Previous studies were introduced in Section 2.3.4 which considered resonance in chain span. The high tension span of a chain may be likened to a heavy string, where tension and mass parameters dictate the frequency at which one wavelength matches the span length and it will produce different modes of vibration, illustrated in Figure 7.3.

When excitation frequency from sources discussed above align with resonant frequency in the chain span, mode one vibration is expected to be induced, increasing the amplitude of vibration beyond the previously demonstrated effect from polygonal action alone. Deflection may lead to higher tension in the span due to axial stretch and further articulation. Energy is lost to friction, hysteretic effects and aerodynamics resulting from these effects. Furthermore, the increased tension in the span will affect the resistance to driving torque.

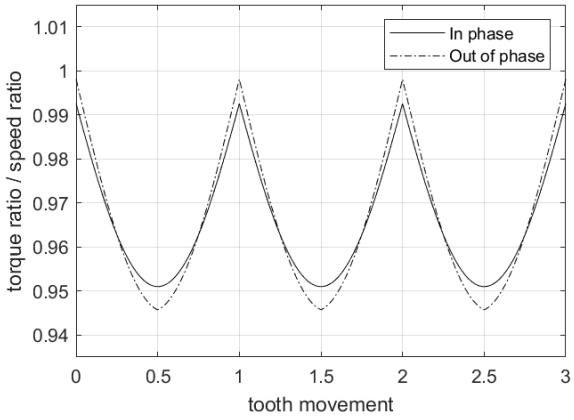

Figure 7.2: Torque gear ratio changing during tooth movement due to polygonal action at driving and driven sprockets [42T/14T]. Polygonal action is in phase when there are an even number of half-links in the tight span, and out-of-phase for odd number of half-links.

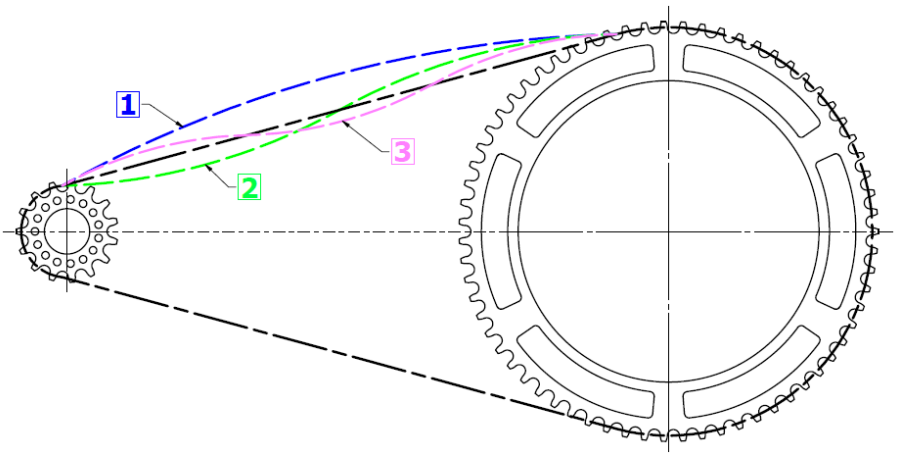

Figure 7.3: Three modes of vibration in the tight span of a chain drive transmission.

The increased tension peaks twice during mode one resonance: once at maximum amplitude and once at minimum amplitude. Hence, the tension will fluctuate at twice the frequency of excitation at resonance, as will the observed torque on the sprockets.

7.3 Sources of harmonic system dynamics

In the dynamometer test rig the mechanical and electro-mechanical systems may cause harmonic disruption to the driving or braking torque on the transmission. Where sources of harmonic disruption are mechanical fault or over-acting control systems in the drive, they may be identified and rectified. Alternatively, they may be inherent in the system and should be identified to demonstrate the subtleties in recreating a ‘representative’ load.

The parasitic influences on dynamics are from three sources: component assembly, electric machines and rolling element bearings. Effects from misalignment in assembly from concentricity will appear at frequencies associated with the rotational speed of the shaft featuring such problems. In the case of effects from electric machines and bearings, the possible frequencies are more involved to compute and discussed in detail.

7.3.1 Electric machine dynamic behaviours

In a dynamic system, torque output of the electric machines is continuously updated via Proportional-Integral-Derivative (PID) feedback control loops. The gains on these should be appropriate to ensure that the error between measured and demanded torque or speed is minimised. The rate at which the torque is delivered is dependent on the topology of the electric machine's rotor and stator, dictated by its pole pairs, the number of rotor bars, and number of winding plots in the stator.

Current and speed control are dictated by the Variable Frequency Drive (VFD). The sinusoidal current is delivered by Pulse Width Modulation (PWM) with associated switching frequency. The resultant sinusoidal frequency is directly related to the rotational frequency of the rotor. The switching frequency of the drive will limit the steepness of the pulse ramp, though this is too fast to impact the measured data (multiples of kHz).

Speed or torque control is also influenced by the style of motor. As introduced in Chapter 4, the dynamometer test rig as built features an asynchronous wound field induction electric machine on Driveline-A, and a synchronous permanent magnet electric machine on Driveline-B. Their topological parameters are summarised in Table 7.1.

Table 7.1: Physical parameters associated with electric machines used in dynamometer rig.

Parameter	Symbol	Driveline-A	Driveline-B
Motor type	$\sim$	Asynchronous	Synchronous
Poles	P	4	8
Electric Current	$\sim$	3 $\sim$ AC (PWM)	3 $\sim$ AC (PWM)
Stator winding slots	N_{SWS}	72	36
Rotor bars	N_{RB}	64	52

A synchronous machine as used on Driveline-B is so-called since the rotating magnetic field of the rotor is synchronous with the magnetic field induced in the stator, $\omega_{sync} = \omega$. For the asynchronous machine on Driveline-A, these are not synchronised and there are two electrical frequencies asso-

ciated with its operation due to the effect of 'slip' [10]. The synchronous speed related to the line frequency from the VFD describes the speed of the magnetic fields in the stator. The mechanical rotation speed of the rotor can never match this when there is work being done at non-zero speed, and there is a 'slip speed' between the two speeds, described as:

$$\omega_{slip} = \omega_{sync} - \omega \tag{7.6}$$

Slip, S, is expressed as the ratio:

$$S = \frac{\omega_{slip}}{\omega_{sync}} = \frac{\omega_{sync} - \omega}{\omega_{sync}} \tag{7.7}$$

When the electric machine is motoring, S is between 0 and 1. As an initial estimate, slip is assumed to be 5% [10]. However, slip is expected to change as a function of torque and speed during operation.

In both electric machines, there are a number of frequencies expected from electro-mechanical interactions between the rotor and stator in the electric machine from parameters shown in Table 7.1. The frequencies and equations are summarised in Table 7.2.

Table 7.2: Expected frequencies at example test point (Speed A: 99.82 RPM; Speed B: 429.97 RPM; slip ratio, S estimated to be 0.05).

Harmonic event	Equation		Frequency / Hz	
	A	B	A	B
Shaft rotation	$f_\omega = \frac{\omega}{60}$		1.66	7.17
Synchronous speed	$f_{sync} = \frac{f_\omega}{1-S}$	$f_{sync} = f_\omega$	1.75	7.17
Line frequency (stator)	$f_L = \frac{f_{sync}P}{2}$		3.50	28.66
Electrical frequency (rotor)	$f_r = sf_L$	$\sim$	0.18	$\sim$
Winding slot pass	$f_{WSPF} = N_{SWS} \times f_\omega$		119.78	257.98
Rotor bar pass	$f_{RBPF} = N_{RB} \times f_\omega$		106.47	372.64

7.3.2 Bearing dynamic behaviours

The four support bearings on the dynamometer test rig feature numerous rotating elements under loading conditions unique to each bearing. There will be imperfections in the roundness of the rotating parts due to manufacturing tolerances, defects or wear which might induce harmonic disturbances in the contact or friction of the rotating elements. These are not expected to be significant unless there is a defect present, which cause harmonic fluctuations in the delivery of rotational speed or torque between the electric machine and transmission [30]. Each shaft has two different bearing sets in the bearing block. The parameters of each is summarised in Table 7.3.

Table 7.3: Physical parameters associated with bearings used on each driveline on dynamometer rig.

Bearing designation		SKF-NU308	SKF-6007
Bearing type		Cylindrical roller	Deep groove ball
Number of rolling elements	$Z/\#$	12	11
Rolling element diameter	D/mm	14	7.94
Pitch diameter	d_m/mm	66	48.5
Contact angle	$\alpha/^\circ$	0	≈ 0

There are several harmonic events which occur in the rotation of a rolling element bearing, dependent on the relative size of the rolling elements and the contact angle. These are summarised in Table 7.4. All calculations assume no-slip conditions.

Table 7.4: Harmonic frequencies associated with rolling element bearings.

Frequency	**Equation**
Rotational speed of cage	$f_c = \frac{1}{2}\left(1 - \frac{D}{d_m}\cos\alpha\right)$
Rotational speed of inner ring (relative to cage)	$f_{ci} = \frac{1}{2}\left(1 + \frac{D}{d_m}\cos\alpha\right)$
Rolling element pass outer raceway	$f_{bpor} = Zf_c$
Rolling element pass inner raceway	$f_{bpir} = Zf_{ci}$
Rotation of rolling element about its own axis	$f_R = \frac{d_m}{2D}\left[1 - \left(\frac{D}{d_m}\cos\alpha\right)^2\right]$

Frequencies of defects in the rolling elements and bearing raceways are shown in Table 7.5, related to the harmonic sources described in Table 7.4. The frequency of a rolling element defect is twice its rotational frequency, f_R, since a defect interacts with both inner and outer raceway during rotation. Values for the defect frequencies are quoted at an example test point which is illustrated in the following section. Each driveline operates at different speed, with two different bearings situated on each. Hence, four frequencies are possible at each defect frequency.

Table 7.5: Defect frequencies per shaft revolution for bearing types.

Defect type	**Defect frequency**	**Driveline-A bearings frequencies / Hz**		**Driveline-B bearings frequencies / Hz**	
		SKF-NU308	**SKF-6007**	**SKF-NU308**	**SKF-6007**
Outer Race	f_{pbor}	7.40	7.65	31.89	32.96
Inner Race	f_{bpir}	12.56	10.65	54.10	45.86
Rolling element	$2 \cdot f_R$	6.89	10.43	29.67	44.93
Cage	f_c	0.62	0.70	2.65	3.01

Bearing frequencies described so far use nominal values for bearing components at no load, and may differ subtly in use. There may be some discrepancy and load-dependent deformation present, sourcing from the loads in use and those induced from the interference fits of the raceways on shaft or external housing. Furthermore, bearings require some friction to induce rolling and at low load and can slip up to this point. Directional radial load will increase friction in the rolling elements supporting the load and reduce the rolling friction in elements on the opposite side.

The effect of tolerances, slip and deformation on expected bearing fault frequencies in use is not trivial and some discrepancy from predicted frequencies might occur.

7.3.3 Summary of harmonic system influences

When parasitic and transmission frequencies align, there is potential for interaction which takes the transmission further from representative loading, inducing additional vibration which may affect performance characterisation. The frequency range of all nominal dynamic system influences discussed in this section are plotted in Figure 7.4. The range of transmission frequencies associated with typical tooth-count in the driving sprocket for 1/2 inch pitch cycling chain is shown alongside.

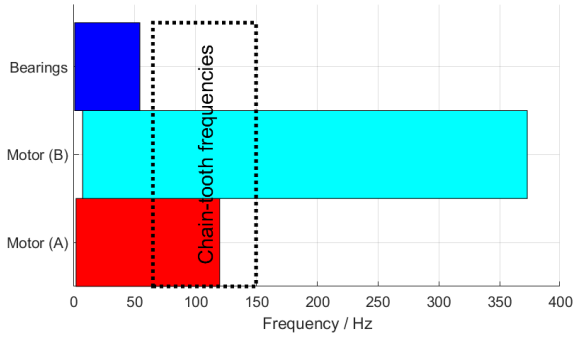

Figure 7.4: Frequencies of theoretical parasitic influences and theoretical chain dynamics [Hz].

All frequencies fall approximately within the same order of magnitude as the chain-tooth frequencies. The bearing frequencies fall below the range expected for the chain-tooth frequency, though influences from electric machines on Driveline-A and B ranges over the transmission influence. Sub-harmonics and harmonics of these base frequencies may manifest physically. The alignment of likely dynamic influence illustrates the need for isolation of transmission effects as there is scope for interaction.

By identifying system influences and isolating transmission influences on measured data, the system influences may be assessed as validation of proper function in the test rig and condition monitoring of the mechanical components. Where parasitic influences can be separated from trans-

mission dynamics, the influence of the transmission on measured variables can also be assessed to determine parametric effects on transmission dynamic interaction.

7.4 Assessing dynamic behaviours in dynamometer rig data

The dynamometer test rig captures data with torque transducers at input and output from the transmission-under-test. The transducers used are limited to 1000 samples per second, which are capable of measuring fluctuations at up to 500 Hz according to the Nyquist theorem.

7.4.1 Choice of channel

The data routinely captured from the dynamometer test rig is the rotational speed and torque at input and output of the transmission including bearings. In testing a transmission, the measurements are not independent since they are mechanically linked via the transmission. However, if the source of different dynamics can be identified it can be possible to highlight where certain dynamic changes to measurement have travelled via the transmission, and what have not.

When relating the dynamometer rig to the rider and bicycle, the influence of transmission dynamics on input torque and speed is equivalent to the feedback to the cyclist via the cranks and pedals. The effect of transmission on the output torque and speed has implications for the rotation of the rear wheel.

7.4.2 Analysis of measured variables

Measured variables on the dynamometer test rig are captured at discrete time intervals, and a time-dependent signal is recorded for the duration of a test duty cycle. An example of raw signals from Driveline-A are illustrated in Figure 7.5.

The raw data displays a combination of chain transmission dynamics, system influence and signal noise. It is useful to decompose the measured data and identify the influence of the system harmonic influence, which can be done in the frequency domain. With a Fourier Transform, any time-dependent signal can be expressed as a summed series of sinusoids of unique frequency, magnitude, and phase, illustrated in Figure 7.6.

In the frequency domain, the significant influences on sinusoidal variation can be identified by the highest amplitude peaks and non-harmonic noise is filtered quite easily. Furthermore, identification of the frequency and magnitude of the most influential frequencies allows comparison with expected frequencies in the system, such as those discussed in Section 7.3, to match measured signal with the source of this influence.

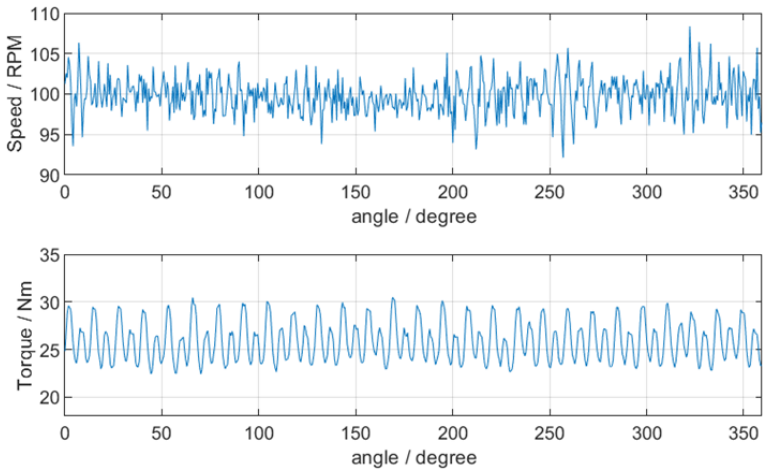

Figure 7.5: Time domain signal during single rotation of driving sprocket for measured variables on Driveline-A.

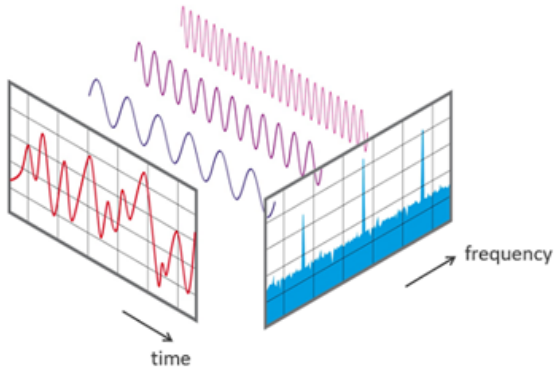

Figure 7.6: Time-domain signals can be expressed as sum of sinusoids which can be identified in the frequency domain [62].

To analyse a discrete time domain signal, a Discrete Fourier Transform (DFT) is used. The most typical algorithm is that of a Fast Fourier Transform (FFT), a computationally efficient and widely used type of DFT.

7.4.3 Fast Fourier Transform (FFT)

An FFT function [56] is used to calculate the Fast Fourier transform, expressed in 7.8.

$$X(k) = \sum_{n=0}^{N-1} x(n)\, e^{-i\left(\frac{2\pi}{n}\right)nk} \quad for\ k = 0, 1, \ldots, n-1 \tag{7.8}$$

The range of frequencies for which sinusoids may exist is defined as half of the sample frequency in the time domain, according to Nyquist theorem. The output frequency domain signal, X, is the same length as the input time domain signal but is symmetric due to repeated combinations of discrete data points. The two-sided frequency spectrum is given as:

$$P_2 = \left| \frac{X(k)}{N} \right| \tag{7.9}$$

The magnitude is split between the two sides of the spectrum, so when expressing the magnitude as function of frequency the data from the two sides must be summed. This is achieved by considering the first half of the two-sided spectrum and doubling for all but the first and last discrete points.

The resultant single-sided amplitude spectrum is the amplitude for constituent sinusoids in the original signal which falls into the bin corresponding to that point in the frequency range, from 0 to F_s (sample frequency of the original time domain data).

The number of 'bins', and therefore the precision to which the data may be displayed, is dictated by the number of samples in time signal.

7.4.4 Pre-processing data for FFT

To maximise the quality and clarity of the frequency domain signal, several steps are taken in performing FFT on the time-domain signal.

Firstly, the length of the time-domain window is defined by the largest possible integer number of known lowest frequency harmonic events. This maximises the length of the signal, while ensuring that the chance of significant discontinuities in the data is reduced. In the case of analysing the data from the dynamometer rig, this means integer rotations of the shafts.

Secondly, to limit the effect of remaining minor discontinuities in the data, a windowing function is applied. A Hanning function is chosen, also known as a Cosine Bell, which is expressed for signal length N and discrete points n.

$$w(n) = \frac{1}{2} - \frac{1}{2}\cos\left(\frac{2\pi n}{N-1}\right) \quad 0 \geq n \geq N-1 \tag{7.10}$$

The windowed signal is the term-wise product of time-domain data and Hanning function w, seen in Figure 7.7.

Finally, as a method of interpolation of the frequency domain data, the time signal is zero padded before the Fourier transform is applied. A series of data points with zero value are added to the end of the signal. This increases the number of bins used in the Fast Fourier Transform and decouples the frequency resolution from the length of the time domain signal. This specifically increases the resolution at which data is separated by frequencies, reducing the bandwidth for each bin where amplitude data is displayed in each frequency point. Resolution frequency is defined by the sample frequency and signal length according to Equation 7.11.

$$F_{res} = \frac{F_s}{L} \tag{7.11}$$

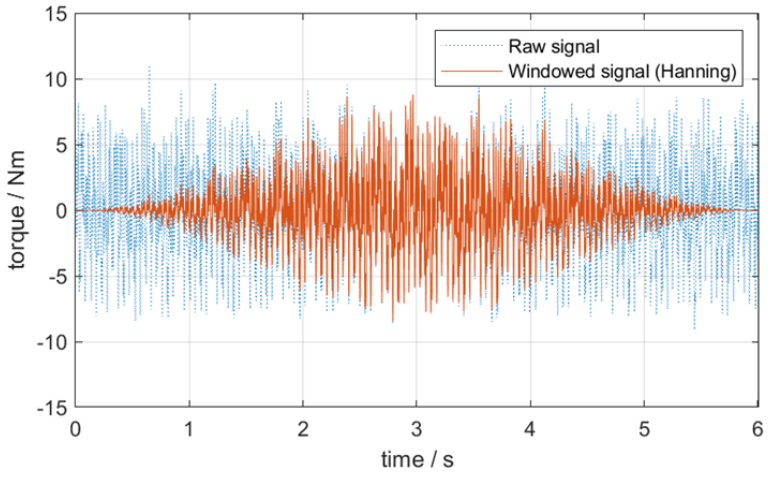

Figure 7.7: Time signal with a Hanning function.

The target precision is 0.1 Hz (such that the frequency bins are $x \pm 0.05Hz$) and with data captured at 1000 Hz, the length of time signal is increased to $L = 10,000$ with zero padding.

Alternative or further pre-processing is possible, such as sampling overlapping windows to ensure that any windowing function applied (Hanning function in this instance) does not artificially attenuate longer period harmonics. Since the sample window is designed to include many full rotations, and this is the lowest frequency harmonic expected, the risk is already mitigated.

7.5 Identifying dynamics with Fast Fourier Transform

The measured signals can be examined for dynamics from transmission and from parasitic influences. The quality of applied load can be assessed and parasitic dynamics used for condition monitoring of rig components over time.

7.5.1 Dynamics in measured rotational speed

Raw torque signals recorded on the test rig are expressed in the frequency domain by performing an FFT following the processing methods described in Section 7.4. FFTs of measured speed on Drivelines A and B are illustrated in Figure 7.8. Each peak is labelled with the corresponding theoretical frequency introduced in Section 7.3.

The rotational speed FFT for Driveline-A, Figure 7.8a, shows significant peaks associated with the winding slot frequency pass, f_{WSPF-A} and its second harmonic. The rotor bar pass frequency, f_{RBPF-A} is also present, and the rotational frequency, $f_{\omega-A}$.

Peaks associated with the line frequency of Driveline-A, f_{line-A}, are identified by improving on the initial guess of slip. With $S = 3.61\%$ in the example shown, a frequency in the data aligns with

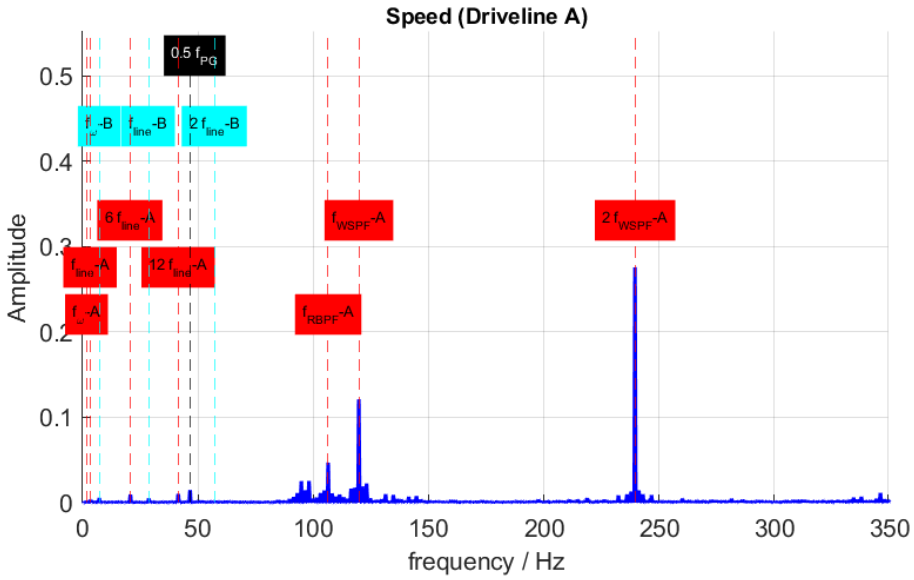

(a) Speed FFT (Driveline-A).

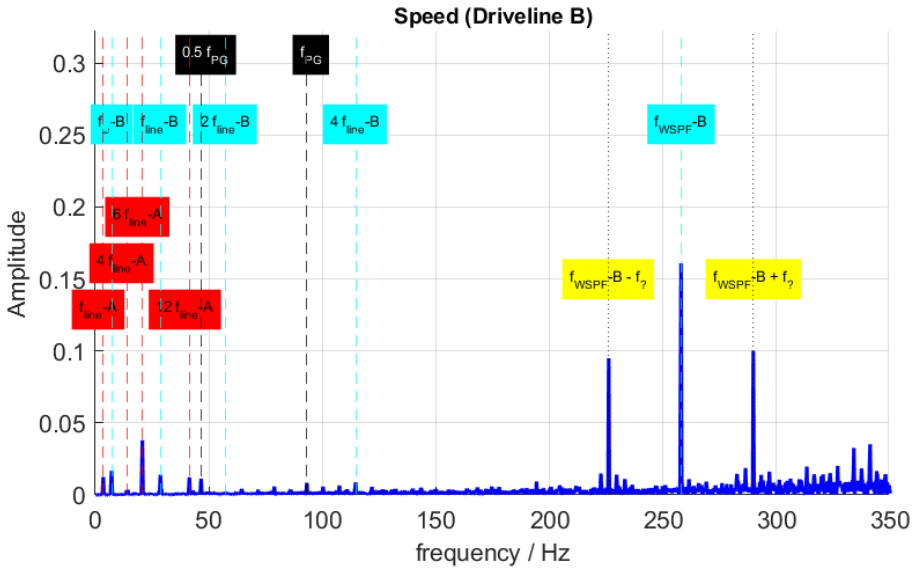

(b) Speed FFT (Driveline-B).

Figure 7.8: Annotated peaks in frequency domain speed data using FFT.

f_{line-A} with a number of harmonics. The most significant peaks are at its 6th and 12th harmonics, which are thought to be associated with the number of poles (4) and number of phases (3) and a reflection of how many torque-transferring interactions there are on the rotor circumference.

There is also some interaction via the transmission evident in the speed data on Driveline-A in Figure 7.8a. A frequency aligned with the sub-harmonic of chain-tooth frequency is seen, alongside the rotational frequency and line frequency of Driveline-B.

Many of the same frequencies are evident in the speed data of Driveline-B in Figure 7.8b. Line frequencies of Driveline-A and its harmonics are seen again, and some interaction from the chain frequencies with the primary chain-tooth frequency and its sub-harmonic.

The direct interaction from the synchronous motor on Driveline-B is more evident. Its rotation frequency, $f_{\omega-B}$, and line frequency, f_{line-B}, and harmonics are present. The winding slot pass frequency, f_{WSPF}, is the largest peak in the data, with significant side bands at $\pm 31.82Hz$. Side bands occur due to the carrier wave's amplitude modulating at a lower frequency. The origin of the modulation frequency is not clear, and changes seemingly randomly between test points.

7.5.2 Dynamics in measured torque

Where the speed data does not show much influence of the chain dynamic frequencies, the torque data does. FFTs of measured torque on Drivelines A and B are illustrated in Figure 7.9.

Both drivelines measure very similar peaks and when scaled relative to the peak size they look identical. The scaling demonstrates much larger peaks in the data from Driveline-A as the torque is higher by a factor equivalent to the gear ratio (56:13). The most significant peaks correspond to frequencies associated with the mechanical action of the chain meshing and the line frequency of torque delivery from Driveline-A.

The chain tooth frequency, sub-harmonics and harmonics are seen, with the most significant peak at the primary frequency and its sub-harmonic. The peaks corresponding to harmonics of the line frequency of Driveline-A machine, f_{line-A}, are a similar order of magnitude, particularly its 6^{th} and 12^{th} harmonic. The 12^{th} harmonic is a similar frequency to the sub-harmonic of chain frequency.

There are sidebands around the second harmonic of chain-tooth frequency corresponding with 6^{th} and 12^{th} harmonics of Driveline-A line frequency. This suggests some interaction between the chain dynamics and torque application from the induction machine, which is of some significance as it is evidence that the transmission dynamics are affecting the delivery of torque upstream. This has implications for the realism of the torque profile when recreating that from a cyclist.

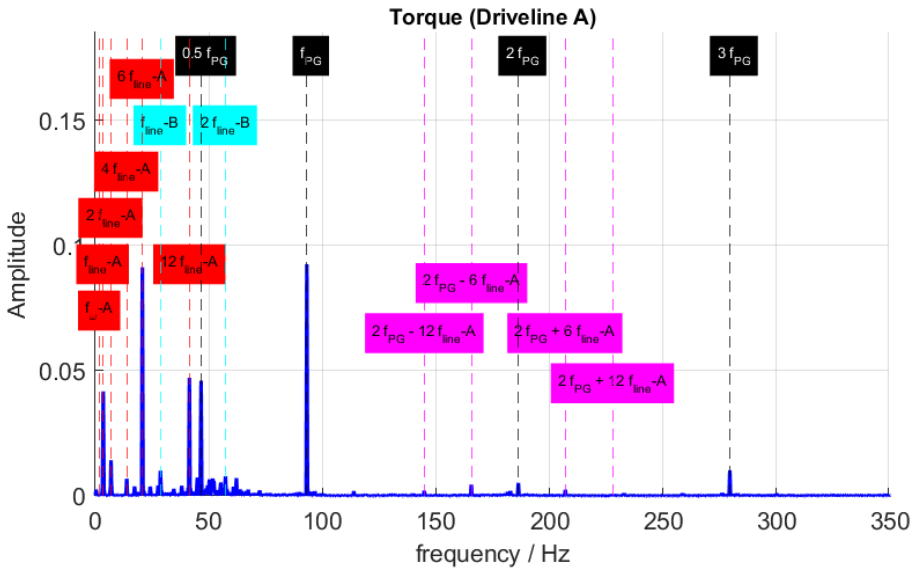

(a) Torque FFT (Driveline-A).

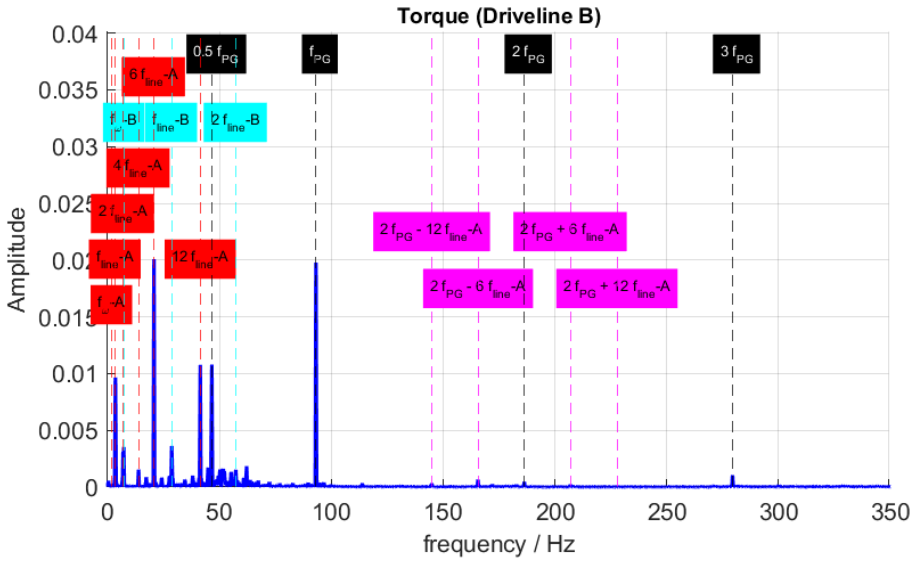

(b) Torque FFT (Driveline-B).

Figure 7.9: Annotated peaks in frequency domain torque data using FFT.

There is frequency associated with the rotation of Driveline-B in the torque data from that shaft; the B line frequency and its second harmonic are present on both drivelines.

7.5.3 Summary of observed dynamics

All frequencies observed in the example data from measured variables on each driveline illustrated in Figures 7.9 and 7.8 are summarised in Table 7.6. There is good agreement between theoretical frequencies calculated in Section 7.3 and those observed in data.

7.6 Filtering systemic influence to isolate transmission behaviour

Analysis of the parasitic influences on measured variables allows for the quality of motor control of torque and speed to be assessed, insofar as where it may impact the measurements and reveal the condition of the system components. The effect of the transmission is clear in frequency domain data, but in a similar order of magnitude to several parasitic events.

To isolate the transmission dynamics from the parasitic influence, targeted filtering is applied to the time trace for the measured data. To achieve this, a series of band stop filters are applied at frequencies where a peak matches a parasitic frequency predicted in the theory.

The band-stop filter used is an in-built MATLAB function [55] with inputs of time-domain signal, and the normalised stop band frequency range. Since frequencies associated with transmission and system influences are in similar orders of magnitude, and theoretical and observed frequencies match closely, a narrow bandwidth is used to ensure filtering is precise ($\pm 0.1 Hz$). The filter uses a minimum order filter with a stop band attenuation of $60 dB$. An individual stop-band filter is applied at a time, so a series of filters are used to remove all identified dynamic influences sequentially.

Filtering in this way removes specific frequencies from the data, but not necessarily their effect. There may still be dynamics present due to an interaction which is not removed when the interacting frequencies are removed.

7.6.1 Filtered rotational speed data

The system frequencies in rotational speed data from the dynamometer test rig identified in Figure 7.8 are filtered to isolate the dynamic influence of the transmission-under-test. The filtered signals are plotted in Figure 7.10. The filter's effect on both the frequency domain and time-domain signal is seen in both drivelines.

Table 7.6: Dynamic frequencies observed in test data and corresponding likely theoretical source.

	Frequency Origin	Symbol	Theoretical freq / Hz	Observed freq / Hz	Error / %	Measured presence
	Tooth frequency	f_{PG}	93.163	93.155	-0.008	ω_A, ω_B, τ_A, τ_B
	Shaft A rotation	$f_{\omega-A}$	1.66	1.68	+0.99	ω_A
	Line frequency A +harmonics	f_{line-A}	3.444	3.450	+0.198	ω_A, ω_B, τ_A, τ_B
	Rotor Bar Pass Frequency A	f_{RBPF}	106.47	106.46	-0.00	ω_A
	Winding Slot Pass Frequency A + harmonics	f_{WSPF-A}	119.78	119.77	-0.01	ω_A
	Shaft B Rotation	$f_{\omega-B}$	7.17	7.20	+0.47	ω_A, ω_B, τ_B
	Line frequency B +harmonics	f_{line-B}	28.66	28.68	+0.07	ω_A, ω_B, τ_A, τ_B
	Winding Slot Frequency Pass B	f_{WSPF-B}	257.98	257.96	-0.00	ω_B
	Tooth and line frequency interaction	$2f_{PG}$ $\pm 6/12 f_{line-A}$	207.03	207.01	-0.00	τ_A, τ_B
	Unknown sidebands on WSPF-B	f_{WSPF-B} $\pm f_?$	$\sim$	± 31.82	$\sim$	ω_B

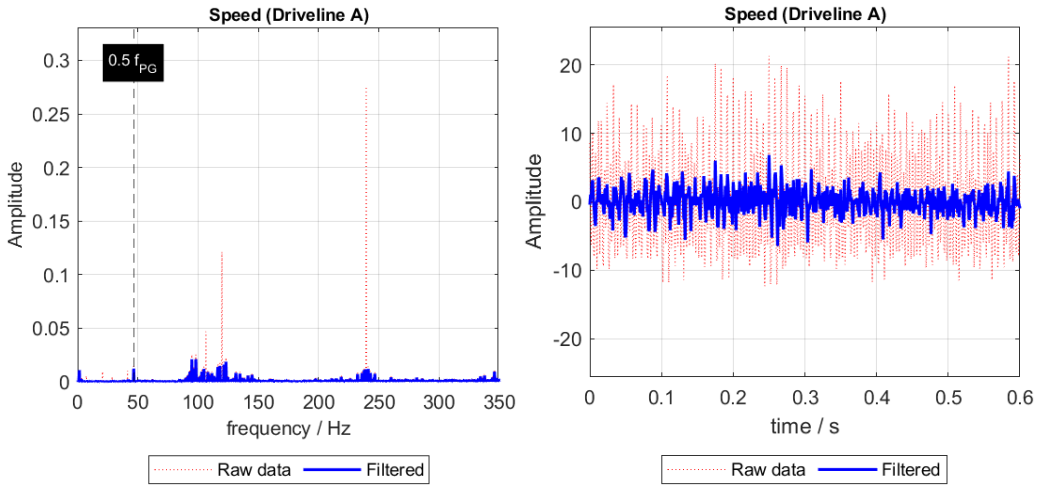

(a) Filtered speed FFT (Driveline-A).

(b) Filtered speed time-domain (Driveline-A).

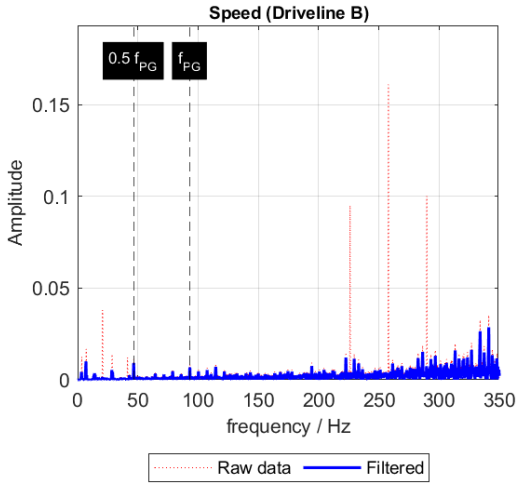

(c) Filtered speed FFT (Driveline-B).

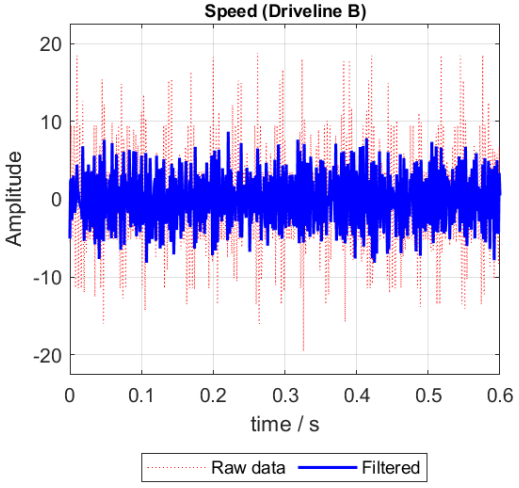

(d) Filtered speed time-domain (Driveline-B).

Figure 7.10: The effect of targeted band-stop filter of system harmonic influence on rotational speed data in time- and frequency-domain.

The effect of the filters on the time domain signals is to remove some extreme amplitudes, and fluctuations in Driveline-A which have a positive bias. The remaining influence of the transmission, annotated, is not significant relative to the noise remaining in the signal. High frequency noise is particularly significant on Driveline-B.

7.6.2 Filtered torque data

Torque data offers more scope for measuring isolated dynamics of the transmission-under-test since the peaks due to transmission are among the most significant in the data presented. The effect of the sequential band stop filters is illustrated in Figure 7.11 on measurement from Driveline-A and B.

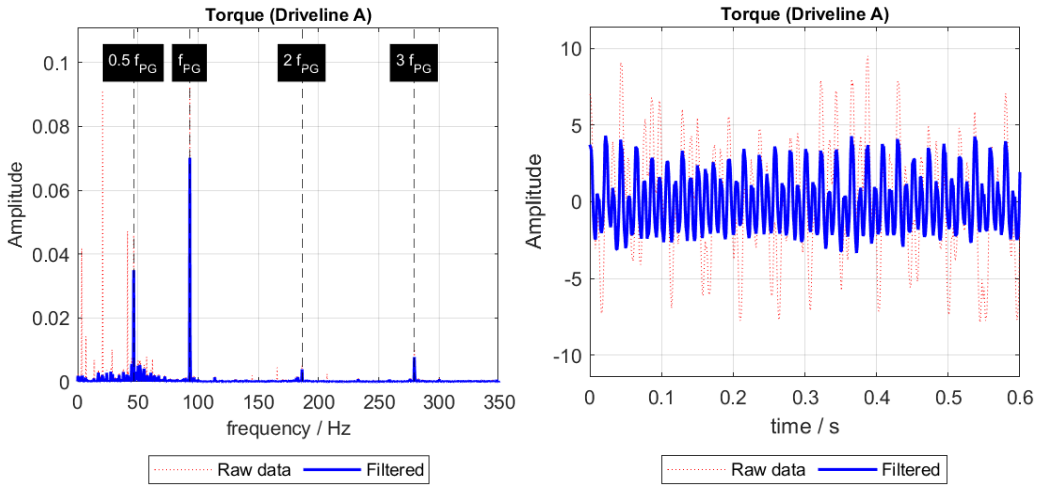

(a) Filtered Torque FFT (Driveline-A).

(b) Filtered Torque time-domain (Driveline-A).

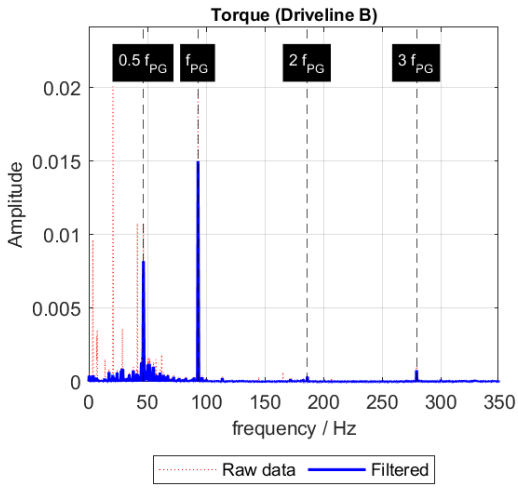

(c) Filtered Torque FFT (Driveline-B).

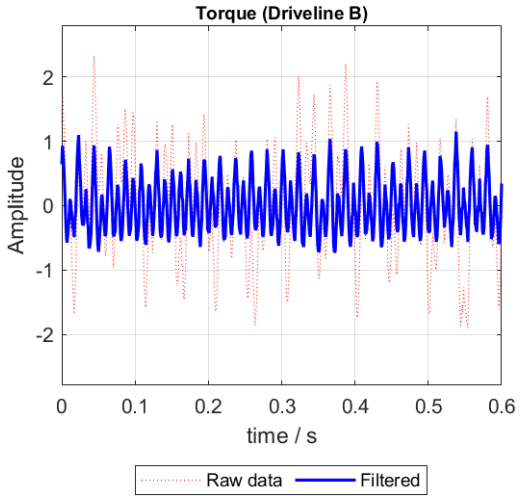

(d) Filtered Torque time-domain (Driveline-B).

Figure 7.11: The effect of targeted band-stop filter of system harmonic influence on torque data in time- and frequency-domain.

In both Driveline-A and B, the filtered effects remove dynamics of sporadically large amplitudes. Clearly defined from the noise which is left, there are peaks associated with chain frequency in both cases. The remaining fluctuations in the time-domain signals are overwhelmingly caused by a combination of 0.5 sub-harmonic and primary frequency of the chain-tooth frequency.

7.6.3 Measurement of isolated test dynamics

Having filtered the systemic influences measured in data, the remaining torque fluctuation can be distilled into a pair of metrics to estimate the impact of transmission dynamics: firstly, the frequency of the primary transmission frequency and secondly, the amplitude of combined fluctuations on the measured variable with parasitic influences filtered.

The primary frequency of chain-tooth interaction can be read from the filtered torque data shown in Figure 7.11. To consider the influence of the remaining transmission dynamics on measured torque, the fluctuations in the filtered time-domain signal are considered and a variable defined to express the fluctuations in torque: τ_{fluc}. This is expressed by calculating the root mean square of the torque signal as in Equation 7.12.

$$\tau_{fluc} = \sqrt{\frac{1}{N}\sum_{i=1}^{N}\left(\tau_i - \tau_{av}\right)^2} \tag{7.12}$$

This is plotted on top of the time domain signal of a full rotation of a driving sprocket in Figure 7.12.

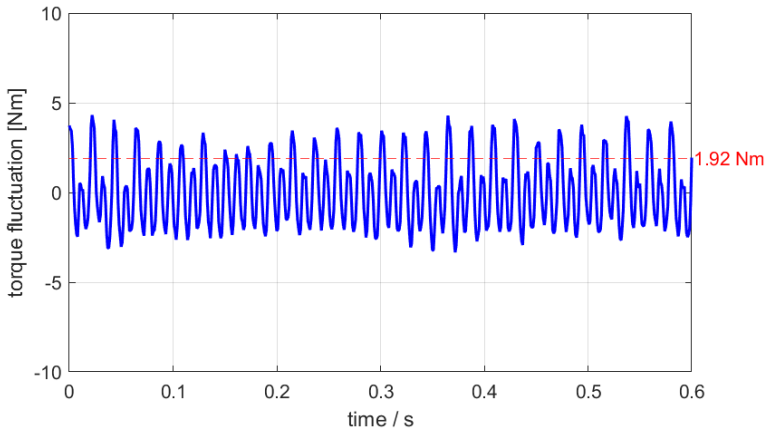

Figure 7.12: τ_A time domain signal with torque fluctuation annotated.

7.7 Parametric influence on transmission dynamics

Having isolated the transmission dynamics in an example test of a half-inch pitch bicycle chain, the measured polygonal action can be compared with alternative transmission parameters. Several parameters are expected to influence the polygonal action in both frequency and magnitude of torque fluctuations.

7.7.1 Transmission type

Several transmission types are tested where fundamentally different polygonal effects are expected. In bush roller chains of different pitches, the same diameter sprockets have different number of teeth and therefore changed chain frequency and magnitude of torque fluctuations. Furthermore, an inverted tooth chain (ITC) is designed to offer smooth operation, and so the polygonal action is expected to be far reduced. Finally, a toothed carbon belt is also examined. Parameters of test transmissions are summarised in Table 7.7.

Table 7.7: Parameters of transmissions in transmission type comparison.

Transmission type	**Pitch**	**Speed** / RPM	**Torque** / Nm	N_1/N_2 / **teeth**	f_{PG} / Hz	τ_{fluc} / Nm
Bush roller chain	1/2"	99.8	25.9	56/13	93.15	1.92
Bush roller chain	3/8"	100.0	30.0	76/17	126.63	0.75
Carbon belt	11mm	99.8	30.1	60/21	99.73	0.39
Inverted Tooth Chain	3/8"	100.0	28.2	57/19	93.50	1.02

The torque data measured on the Driveline-A is plotted for each case in the time and frequency domain in Figure 7.13. The frequency of the primary peak for polygonal action changes as well as the magnitude. These results are summarised in the final two columns of Table 7.7.

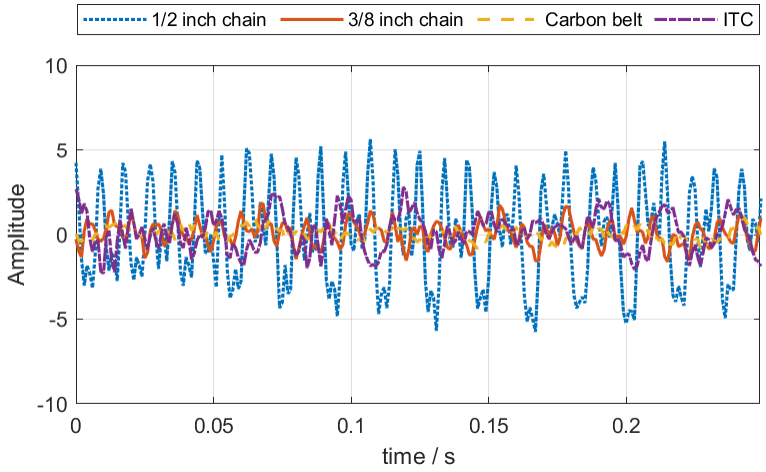

(a) Filtered torque signal in time domain.

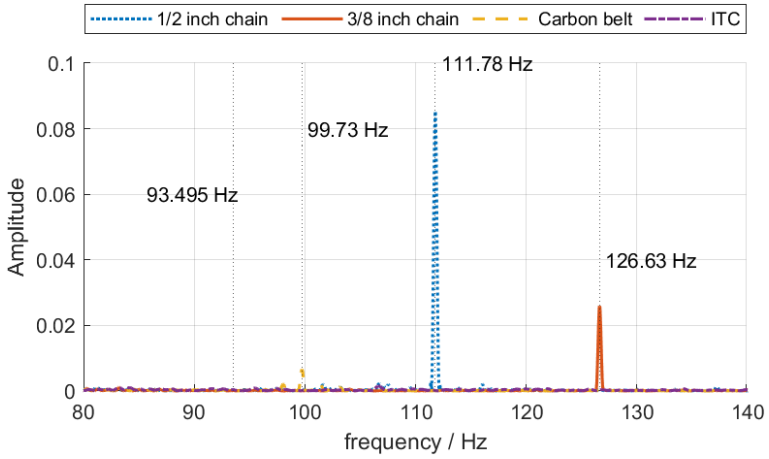

(b) FFT of torque signal.

Figure 7.13: Time and frequency domain torque data with different transmission types plotted.

These results show that between similar bush-roller chains, smaller pitch results in higher transmission frequency and smaller torque fluctuation in similar gear size and loading conditions. The half-inch pitch roller chain has a significant secondary peak at half chain frequency; the equivalent peak in the smaller pitch chain is much smaller.

The ITC has no discernible peak from transmission frequency since there is no polygonal action. However, the dynamic fluctuations in the torque data are not eliminated: in fact, there is greater fluctuation than the small pitch roller chain. The ITC is heavy and dynamics not directly associated with transmission meshing frequency may originate from dynamic movement in the bottom span.

There is a transmission frequency associated with the toothed carbon belt. The peak is small and overall fluctuations in the time-domain data lowest of all test cases. In part, this may be due to a low mass, pre-tensioned system as well as minimal polygonal action.

7.7.2 Resonance

In tests on the dynamometer rig the chain span can be observed entering harmonic resonance with particular speed and torque inputs. Resonance is achieved where excitation frequency of the top span (from polygonal action) aligns with the resonant frequency of the span. The excitation frequency is a function of speed, while resonant frequency in the span is a function of torque which changes the span tension.

A test point is selected with equivalent excitation frequency and torque is changed to find a test point both in- and out-of-resonance at equivalent speed. Two cases where in the first no resonance is observed, and then resonance is observed, are summarised in Table 7.8 and illustrated in time and frequency domains in Figure 7.14.

Table 7.8: Parameters of transmissions in on/off resonance comparison.

Resonance observed	**Speed / RPM**	**Torque / Nm**	N_1/N_2 **/ teeth**	f_{PG} **/ Hz**	τ_{fluc} **/ Nm**
Yes	69.9	65.3	56/13	65.21	3.62
No	69.9	88.3	56/13	65.21	2.95

The torque fluctuation in the time domain signal is more significant in the case with observed resonance. In the FFT, the primary peak of chain-tooth frequency, f_{PG}, is similar in both cases though there is a substantially larger peak at its second harmonic. Mode 1 resonance is expected to increase tension in the span at a frequency twice the excitation frequency since extension above

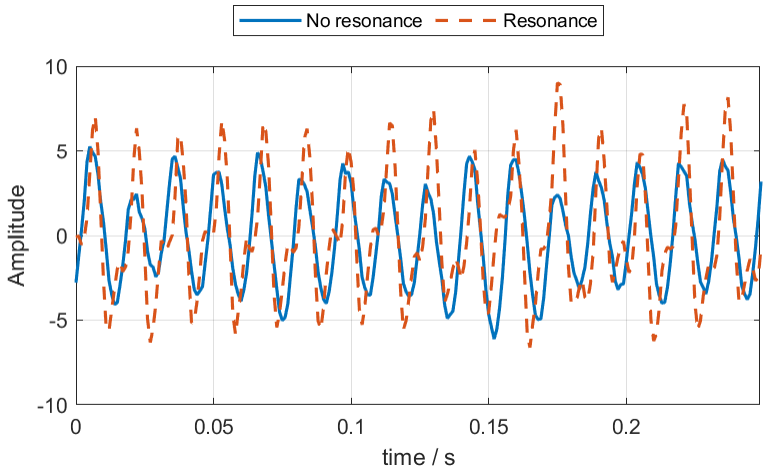

(a) Filtered torque signal in time domain.

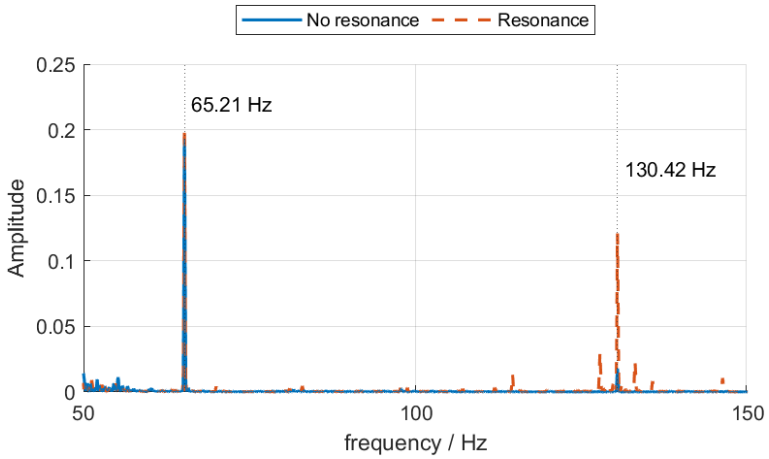

(b) FFT of torque signal.

Figure 7.14: Time and frequency domain torque data with resonance and no resonance (same speed, different torque).

and below the tangential line between sprockets results in high tension, with a minima at the centre point. This effect is observed in this measurement.

7.7.3 Transmission torque and speed

Comparisons made so far have considered single steady state loading points, though parameters discussed will change with applied torque and speed of transmission-under-test on the dynamometer. The polygonal frequency and dynamic fluctuations of the torque data for the tested transmission may be determined across a whole test duty cycle to appreciate how changing set points impact them. Figure 7.15 shows the frequency of the primary chain-tooth frequency in measured data across an example test envelope on the dynamometer rig (1/2 inch pitch chain, gearing: 56/13).

Linear interpolation is employed to create the continuous heat map across the tested envelope. As expected, this changes with speed only and corroborates Equation 7.2.

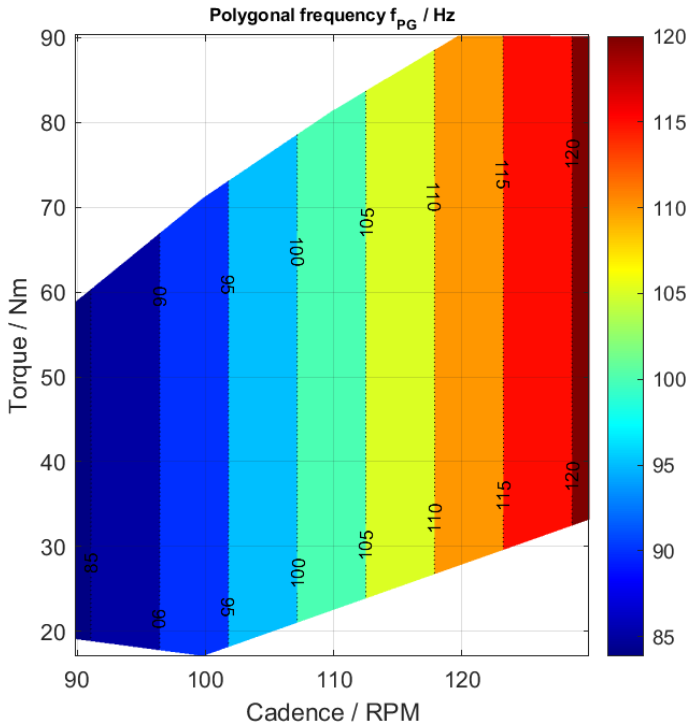

Figure 7.15: Measured polygonal frequency from fluctuations in torque data across test envelope.

The dynamic fluctuation of torque is evaluated using Equation 7.12 at each steady state point across the test range. The results of these are plotted as a heat map in Figure 7.16; again, linear interpolation is used.

The torque fluctuations illustrated in Figure 7.16 show areas where increased amplitude transmission dynamics exist in the measured torque. Generally, the oscillations increase with applied torque though there are several peaks, most notably at $120RPM$ / $50Nm$. This is a suspected area of resonance in the chain data, which may be corroborated by checking the second chain-tooth frequency harmonic. The amplitude of this peak, relative to the peak associated with the primary chain-tooth frequency, is calculated at all set test points and plotted in Figure 7.17.

Figures 7.16 and 7.17 appear to demonstrate a 'ridge' of higher fluctuation due to resonance. The location of resonance is shown to trend with increasing torque and speed, which is expected since resonant frequency increases with span tension and excitation frequency increases with rotational speed; where they align there is resonance in the data. The absolute magnitude of fluctuations also increases for resonant points at higher torque.

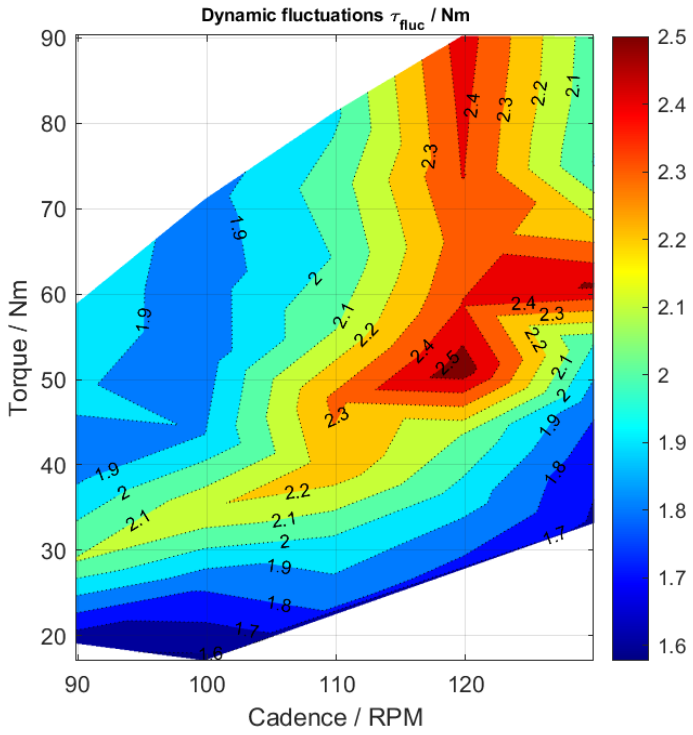

Figure 7.16: Absolute torque fluctuation [Nm] across steady state loading test points across test envelope (with linear interpolation).

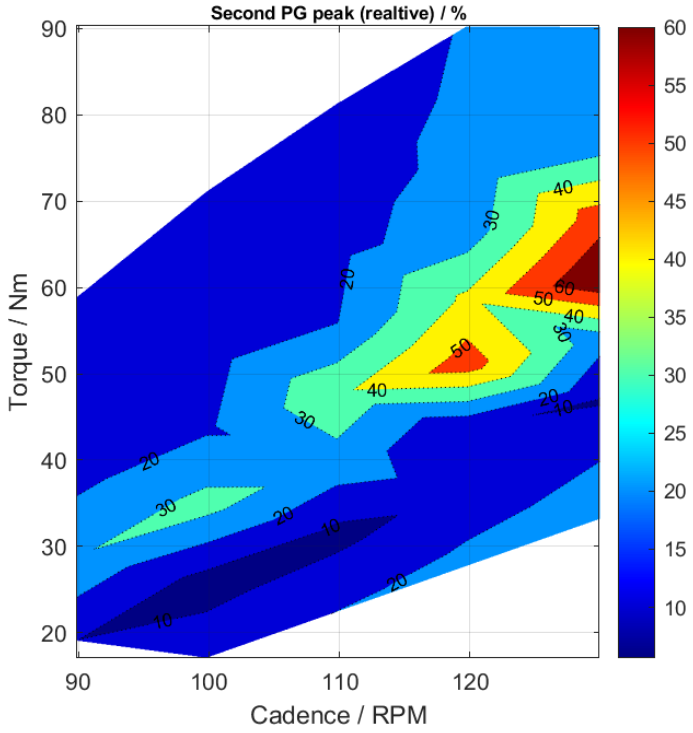

Figure 7.17: Relative amplitude of peak at $2f_{PG}$ [%] across test envelope (with linear interpolation.

7.8 Conclusions and further work

The dynamometer test rig is capable of revealing and measuring dynamic behaviours in transmissions under test, as well as the interaction between dynamics in transmission and electric machines and the systematic influence on measurements. The methods presented in this chapter expand the capability of the test apparatus to characterise performance of a transmission-under-test by detailing its dynamic response across a test envelope, encapsulating torque fluctuations due to polygonal action and areas of top span resonance.

Through analysis of speed and torque data in the frequency domain, via a Fast Fourier Transform, sources of dynamic fluctuation of measurement can be matched by linking the measured frequency to that which is expected from various sources. The Winding Slot Pass Frequency (WSPF) of the electric machines is significant in the speed data on each driveline respectively, as well as frequencies associated with the line frequency of torque delivery from the induction motor on Driveline-A.

By detecting and diagnosing frequencies seen in the FFT data, test data can be used for effective condition monitoring where the likely source of dynamics through potential faults is identifiable from the base frequency and any presence of harmonics.

While system influence is present in current data, it can be identified and filtered effectively to isolate the transmission impact on dynamics measured in the torque data especially. Assessing the dynamic influence of transmission offers a direct measure of polygonal action and other dynamic effects. Polygonal action is shown to be reduced for bush-roller chain by reducing pitch for equivalent gear size.

Alternative transmission types to bush roller chain show reduced or negligible effect from a polygonal or meshing frequency. Other dynamics exist in the system which become more significant, such as interaction in the slack span from inertial forces in heavy chains. The pretension and low inertial mass of the carbon belt resulted in the smoothest torque data of those tested.

Resonance in chain spans is observed in tests and is evident in test data from increased transverse vibration and a significant second harmonic of polygonal action. Points of resonance can be found from measured data across a test envelope by identifying this effect, aligning with the areas of increased dynamics.

Considering the measured vibration as a performance characteristic for transmission when used on bicycles, anecdotally it is clear that a cyclist prefers smoother action. The test data is captured on the driving shaft and so fluctuations in torque are expected to be felt by the rider via the cranks

and pedals. Further work directly measuring vibration at different points on a bicycle and rider would complete the picture to understand where induced vibrations manifest and where they are dampened. It may be possible to achieve this with appropriately placed accelerometers on a rider and bicycle in use.

Further studies on the effect of transmission vibration on the rider themselves during cycling would also be pertinent to understand whether variation in frequency and amplitude has significant physiological effects which might motivate future choices in transmission.

7.9 Summary of Chapter 7

1. Vibration was introduced as a key part of holistic performance; in the context of elite bicycle racing, vibration in the transmission translates to the muscles and may cause additional fatigue.
2. To appreciate the dynamic behaviours of the transmission, the theoretical contributors to parasitic vibration of the dynamometer test rig were summarised from the electric machines and bearings on each driveline.
3. These were compared with the expected transmission dynamics and shown to be in similar frequency orders of magnitude.
4. Using Fast Fourier Transforms of data captured on the dynamometer test rig (originally introduced in Chapter 4), the frequencies in test data were matched to theoretical influences to understand the parasitic influence, and areas for improvement identified.
5. The transmission dynamics were isolated by filtering the parasitic influence. This allowed specific measurement of its influence on time domain data.
6. Parametric dependence of dynamic behaviours were shown with various test data. Changing pitch in bush-roller chain or using different technologies such as inverted tooth chain or carbon belt demonstrated reduced dynamics in measured data.

Chapter 8

Parametric Results from Dynamometer Test Rig

8.1 Introduction

This chapter is a culmination of the developed methods for performance characterisation for chain drive transmissions detailed in Chapters 5, 6 and 7 to demonstrate the application of novel testing methods and data analysis to performance characterisation with the Transmitted Power Measurement chain dynamometer test rig introduced in Chapter 4.

Transmission tests are conducted in representative conditions for the in-use case of elite level bicycle track racing at constant speed test points. The sequence of test points is designed to mitigate parasitic influence where possible as discussed in Chapter 5. The contribution of support bearings to the measured power loss is compensated with empirical data derived from experimental test results from separate bearing characterisation test apparatus.

The absolute value of confidence in results is quoted as the uncertainty of the test measurand, as introduced in Chapter 6. Where two results are compared, the binary comparison has its own uncertainty as derived in Section 6.7.3.

The dynamic response of transmission at steady-state test points is illustrated with analysis presented in Chapter 7, where parasitic influence on the dynamic response is filtered and the remaining dynamics occurring at frequencies related to the chain meshing frequency of the transmission illustrate the dynamic response from the transmission.

The three areas of analysis demonstrate a holistic and evidenced evaluation of performance in samples. Results from a novel loading configuration on the dynamometer test rig are illustrated,

and a comparison of bush roller chains of different designs. The capability of the dynamometer test rig, detailed in Chapter 4 and analysis in the subsequent chapters allow for this characterisation of a transmission-under-test.

8.1.1 Structure of chapter

The chapter serves to illustrate experimental data from the dynamometer test rig to characterise performance of transmissions under test.

1. Test protocol is outlined.
2. Techniques for data analysis are outlined for each performance measure:
   (a) Calculation of power loss measurand in transmission-under-test.
   (b) Determination of uncertainty of measurand.
   (c) Torque fluctuation from transmission.
3. Results from the dynamometer are presented to illustrate comparisons between:
   (a) Different loading conditions (constant and sinusoidal torque cases).
   (b) Different bush roller chain designs.

8.2 Test protocol

A standard duty cycle was developed for transmissions under test to record measurement variables at steady-state test points. The points are defined as driving torque and speed on Driveline-A based on typical inputs of cadence and power by elite cyclists in ranges summarised below:

- Speed of Driveline-A: 90-130 *RPM* (9.4 - 13.6 $rads^{-1}$).
- Power input Driveline-A: 200-1200 W.

Power and speed combinations are neglected where they are not possible in steady state conditions with typical gearing for chosen cadences based on a cubic relationship between cadence and power when aerodynamics dominate the source of drag. The test points are shown in Table 8.1, highlighted in green.

Time windows at each test point are defined by a required number of rotations of Driveline-A, such that the test points at faster speed are shorter duration. For each speed, the duty cycle steps through the tested torques. The speed sequence is quasi-random. A typical duty cycle sequence is illustrated in Figure 8.1.

The test sequence is conducted 5 times with systematic error in configuration setup limited by remeasuring centre distance and alignment between each test.

Table 8.1: Applied torque [Nm] for defined cadence and input power input.

		Cadence / Speed A				
		90 RPM	**100 RPM**	**110 RPM**	**120 RPM**	**130 RPM**
Power A	**200 W**	**21.2**	**19.1**	17.4	15.9	14.7
	300 W	**31.8**	**28.6**	**26.0**	23.9	22.0
	400 W	**42.4**	**38.2**	**34.7**	**31.8**	29.4
	500 W	**53.1**	**47.7**	**43.4**	**39.8**	**36.7**
	600 W	**63.7**	**57.3**	**52.1**	**47.7**	**44.1**
	700 W	74.3	**66.8**	**60.8**	**55.7**	**51.4**
	800 W	84.9	**76.4**	**69.4**	**63.7**	**58.8**
	900 W	95.5	85.9	**78.1**	**71.6**	**66.1**
	1,000 W	106.1	95.5	**86.8**	**79.6**	**73.5**
	1,100 W	116.7	105.0	95.5	**87.5**	**80.8**
	1,200 W	127.3	114.6	104.2	**95.5**	**88.1**

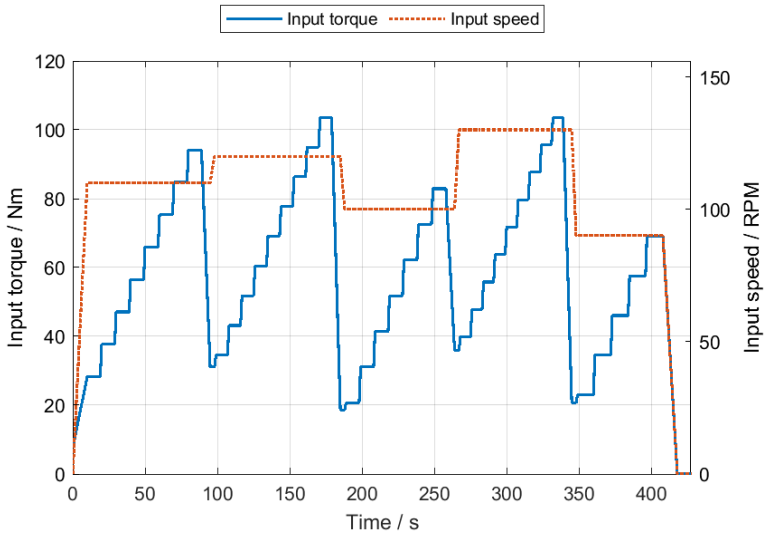

Figure 8.1: Duty Cycle test points defined by torque and speed of driving input.

8.3 Data analysis

8.3.1 Transmission power loss

The primary measurand in tests on the dynamometer test rig are the power losses in transmission-under-test at each test point in the duty cycle, calculated in Equation 8.1.

$$P_{loss} = \left(\overline{\tau}_A - \overline{M}_A\right)\ \overline{\omega}_A - \left(\overline{\tau}_B + \overline{M}_B\right)\ \overline{\omega}_B \tag{8.1}$$

Where measurement variables recorded by the torque transducers on Driveline-A and B are time-averaged over the defined integer number of rotations:

- $\overline{\tau}_A, \overline{\tau}_B$ – time-averaged torque measurement of transmission input and output $[Nm]$.

- $\overline{\omega}_A, \overline{\omega}_B$ – time-averaged speed measurement of transmission input and output [$rads^{-1}$].

The compensations for bearing frictional moment, $\overline{M}_A$ and $\overline{M}_B$, are determined by interpolation of empirical data which is detailed in Chapter 5. The function, f, describing dependence of frictional moment on radial load and rotational speed is illustrated in Figure 5.18c. Radial load is calculated from the reaction of torque at the radius of the driving sprocket in both instances. This limits the error from discrepancy between measured torque and torque at the sprocket since bearing frictional moment is lower on Driveline-A. The look-up value for bearing frictional moments are described as:

$$\begin{aligned} \overline{M}_A &= f\ (\overline{\tau}_A, \overline{\omega}_A) \\ M_B &= f\ (\overline{\tau}_A, \overline{\omega}_B) \end{aligned} \tag{8.2}$$

8.3.2 Uncertainty of measurand

The uncertainty of the power loss measurand is calculated as is derived in Chapter 6 and restated in Equation 8.3. Values of uncertainty of measured variables are summarised in Table 8.2.

$$\begin{aligned} U_{P_{loss}} = \Big[&(\overline{\omega}_A)^2 u_{\tau_A}^2 + \left(\overline{\tau}_A - \overline{M}_A\right)^2 u_{\omega_A}^2 + (-\overline{\omega}_A)^2 U_{M_A}^2 \\ &+ (-\overline{\omega}_B)^2 u_{\tau_B}^2 + \left(-\overline{\tau}_B - \overline{M}_B\right)^2 u_{\omega_B}^2 + (-\overline{\omega}_B)^2 U_{M_B}^2 \Big]^{\frac{1}{2}} \end{aligned} \tag{8.3}$$

Table 8.2: Absolute uncertainty of measured variables and bearing frictional moment in dynamometer tests.

Uncertainty	Value	Units
u_{τ_A}	0.0992	Nm
u_{ω_A}	0.00448	$rads^{-1}$
U_{M_A}	0.00778	Nm
u_{τ_B}	0.0396	Nm
u_{ω_B}	0.00535	$rads^{-1}$
U_{M_B}	0.00778	Nm

8.3.3 Dynamic torque fluctuations

Torque fluctuations from dynamic events in the transmission are extracted from data with post processing methods detailed in Chapter 7. The torque measurement is filtered of system influence as described in Chapter 7 and remaining torque fluctuation is described by root mean square of the fluctuations about mean torque at each test point as done in Section 7.6.3. The fluctuations

in torque on Driveline-A are treated as an equivalent measure to the mechanical feedback of the transmission to the cyclist via the crank and pedals. For each individual test point the torque fluctuation is described by Equation 8.4.

$$\tau_{A_{fluc}} = \sqrt{\frac{1}{N}\sum_{i=1}^{N}\left(\tau_{A,i} - \overline{\tau}_A\right)^2} \tag{8.4}$$

8.4 Results of transmission performance

8.4.1 Effect of non-constant torque profile

In cycling transmission applications, torque varies during rotation of the driving sprocket due to the preference of a rider to apply force downwards on the pedals and there exist 'dead spots' of reduced torque when the crank is vertical. As introduced in Section 4.6.1, the capability of the dynamometer test rig allows for torque to be defined as a function of the live angular position of the shaft and a sinusoidal torque profile is applied to approximate a rider pedalling. The applied torque is defined as a function of median torque τ_{av} in Equation 8.5.

$$\tau_A = \tau_{av}\left[1 + K\sin\left(2\theta_A\right)\right] \tag{8.5}$$

θ_A is angular position of Driveline-A, smoothness-factor K is zero for constant torque and 0.5 for sinusoidal torque. The results from equivalent transmission systems are compared for constant torque and sinusoidal torque.

Transmission power losses

Figures 8.2a and 8.2b show that power losses increase with driving torque and speed. This is in good agreement with the literature in both analytical and experimental studies. Losses are higher in the case of sinusoidal loading torque. The difference between the cases ranges between 1.9W and 3.6W, illustrated in Figure 8.2c.

The uncertainty for each of the power loss measurands over the test envelope are illustrated in Figure 8.3. They are very similar which is to be expected since the driving parameters are identical but for the angular position-varying torque profile during revolution of Driveline-A. A more complete assessment of comparative uncertainty can be made using the technique described in Section 6.7.3, where the confidence of a binary claim of one set-up outperforming the other over the test envelope can be made. This is calculated across the test envelope and illustrated in Figure 8.3c. Across the test envelope, the confidence of the power loss being greater in the sinusoidal torque profile tests is between 86% and 94%.

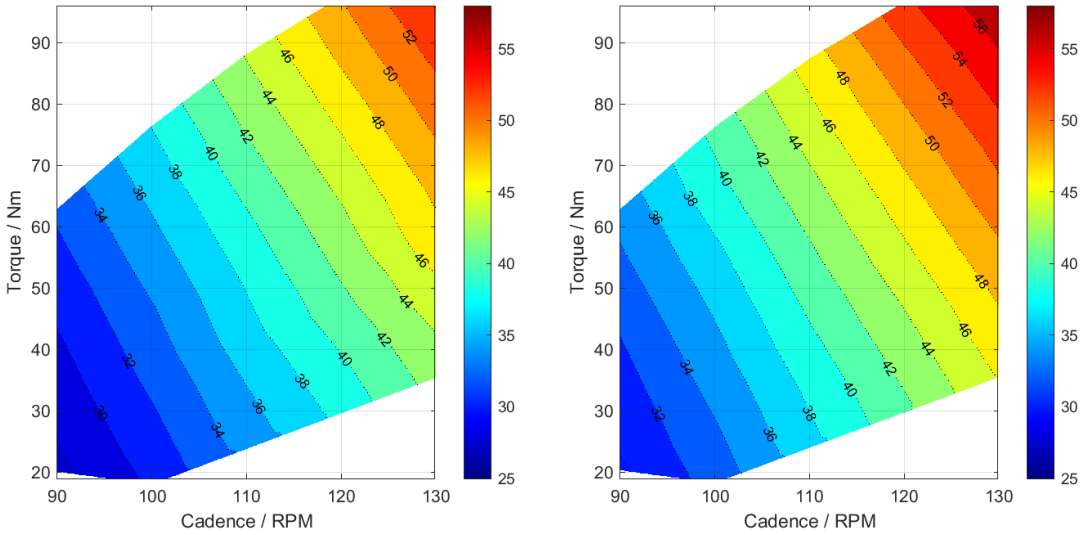

(a) Constant torque power loss [W].

(b) Sinusoidal torque power loss [W].

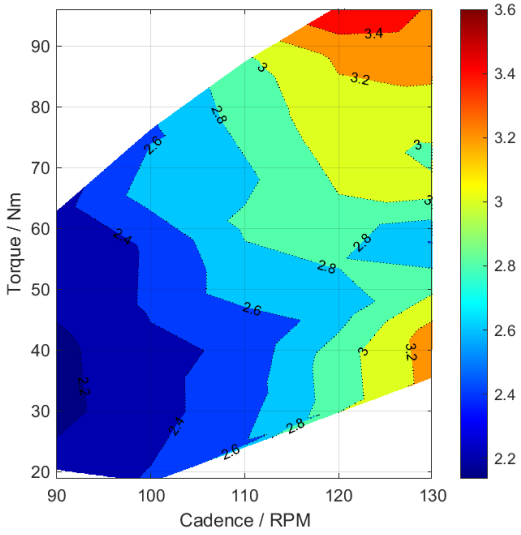

(c) Power loss difference [W].

Figure 8.2: Power loss [W] measurand in tests of identical equipment with constant and sinusoidal driving torque.

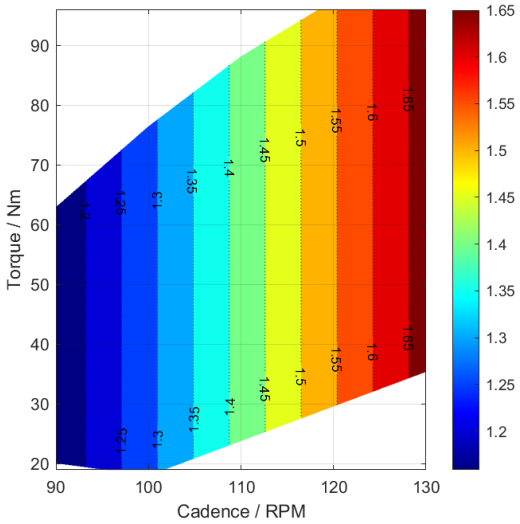

(a) Absolute uncertainty [W] of measurand (constant torque).

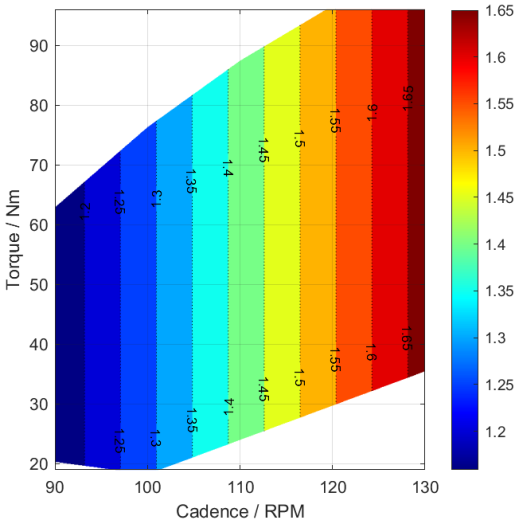

(b) Absolute uncertainty [W] of measurand (sinusoidal torque).

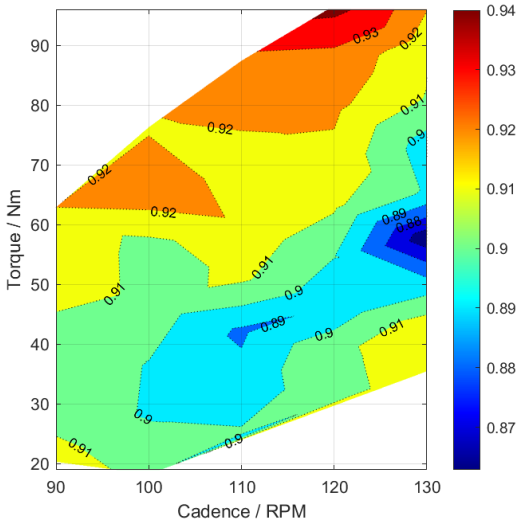

(c) Confidence of higher losses in sinusoidal data across test envelope.

Figure 8.3: Uncertainties of power loss measurand in individual tests for constant and non-constant torque with same equipment and speed parameters.

Dynamic fluctuations

Results for dynamic fluctuations from two test cases for different torque inputs are presented in Figure 8.4, based on analysis described in Section 7.6.

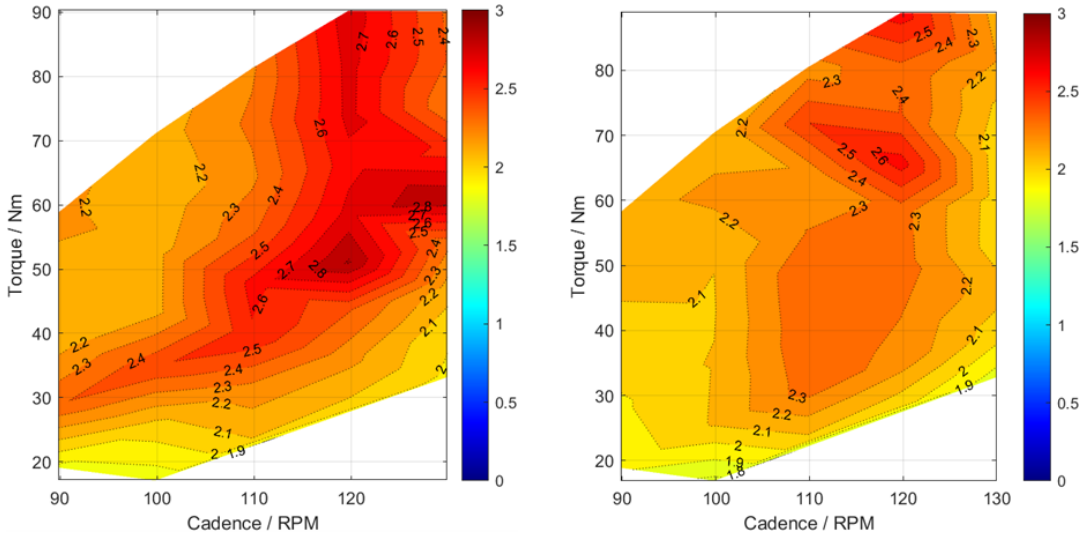

(a) Dynamic fluctuations [Nm] in driving torque (Constant torque input).

(b) Dynamic fluctuations [Nm] in driving torque (sinusoidal torque input).

Figure 8.4: Dynamic fluctuations from transmission in driving torque [Nm].

Between the two cases, similar values of torque fluctuation are observed across the test envelope between 1.8 Nm and 2.8 Nm. The peaks of dynamic activity have previously been identified as excitation frequency from polygonal action aligning with an area of resonance in the chain top span. This peak appears in different locations between the two cases. Seen in Figure 8.4a, the dynamic peak for constant torque is at approximately 120 RPM, 50Nm. A similar peak in Figure 8.4b is at 120 RPM, 65 Nm.

The peak in the sinusoidal torque dynamics is less pronounced that that in constant torque data, likely due to partial resonance during a test window as the tension in the span changes. The change of location is likely an artefact of the discrete test points and is a subject of further investigation. There may be some non-linearity to the resonance where the chain response is different depending on whether the tension is increasing or decreasing, which will skew the location of the resonance.

8.4.2 Pitch-dependent performance

Transmission power losses

The transmission power losses for two similar configurations are compared where a different pitch bush-roller chain is used. The power losses across a test envelope are illustrated in Figure 8.5. The

two plots illustrated in Figure 8.5a and 8.5b are similar in trend and value; the difference is -0.6 - +1.2 W and illustrated in Figure 8.5c.

The difference between the power losses of the two pitch chains is quite small. It appears that the 3/8 inch pitch transmission performs favourably at lower torques across the speed range of the envelope, while performing relatively unfavourably at high torque. However, the differences fall within the uncertainties of the individual tests which are illustrated in Figure 8.6a and 8.6b. In a binary comparison, the confidence that the losses in the 1/2-inch pitch tests than the 3/8-inch pitch tests are illustrated in Figure 8.6c. The confidence that 1/2-inch pitch transmission outperforms the 3/8-inch pitch transmission is between 40% and 60% across most of the test envelope, suggesting the uncertainty is too great to have confidence in claiming that one chain is better than the other.

Dynamic fluctuations

Where there is little difference in power losses in the two bush roller chain pitches considered, there is a clear difference in the dynamic fluctuations seen in data as introduced in Chapter 7. Results for dynamic fluctuations from test cases are presented in Figure 8.7.

The reduced pitch has a significant reduction in dynamic fluctuations. Where there is a peak within the results in the 1/2-inch pitch chain at $120RPM$ / $60Nm$, illustrating an area of resonance in the high-tension chain span, there is no such point single point in the results map for smaller pitch.

8.5 Conclusions and further work

This chapter demonstrated options for performance characterisation on the dynamometer test rig by examining data collected in a standard test sequence. The duty cycle used encapsulates steady state conditions for track cycling on fixed gear bicycles, covering cyclist power input from 200-1200W and cadence between 90 and 130 RPM.

The primary measurand from the experiment was power losses in the transmission-under-test. It was calculated with measured torque and rotational speed of input and output shafts, and empirical data of bearing frictional moment compensation. This was from the secondary bearing friction characterisation test rig, described in Chapter 5.

Results for several test transmissions illustrate the dependency of transmission power losses on both applied speed and torque. Losses increase with both parameters in the range 28-56 W in the chains tested, representing power transmission efficiency of 85.5-96.4 %.

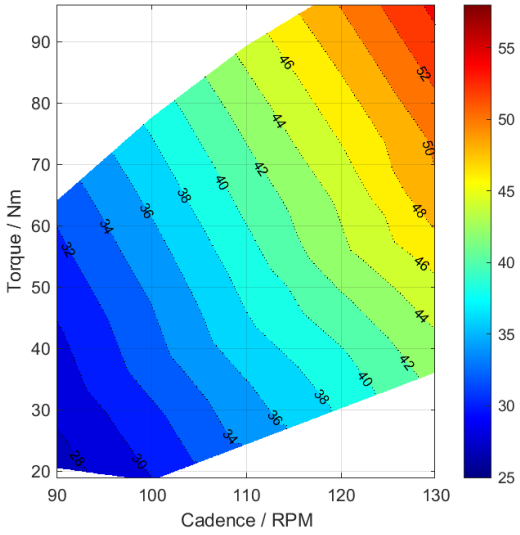

(a) Power loss [W] for 1/2-inch pitch bush-roller chain.

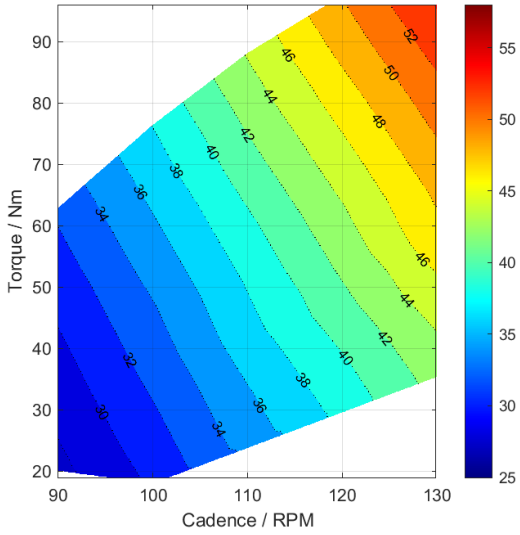

(b) Power loss [W] for 3/8-inch pitch bush-roller chain.

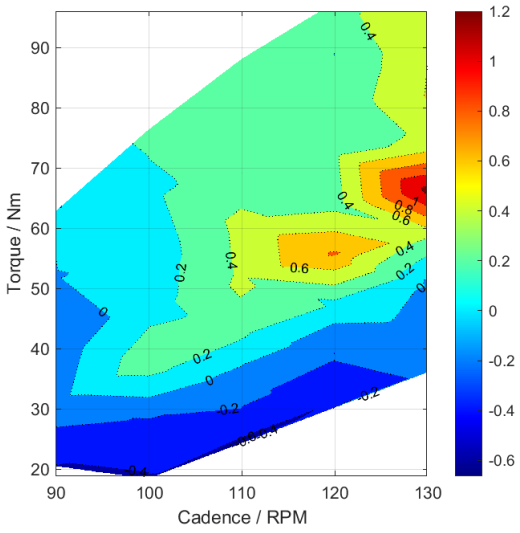

(c) Power loss difference [W]

Figure 8.5: Power loss [W] measurand chains of different pitch.

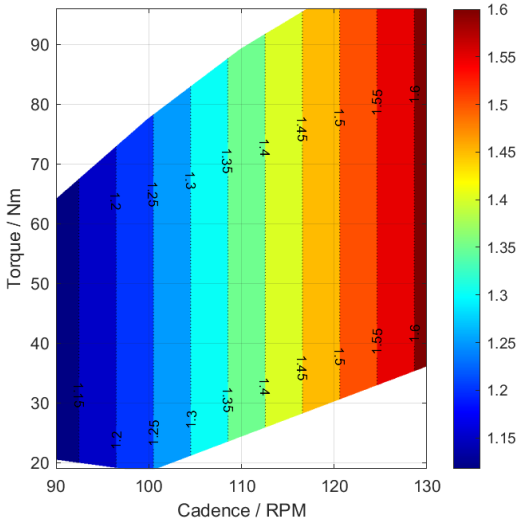

(a) Absolute uncertainty [W] for 1/2 inch pitch chain tests.

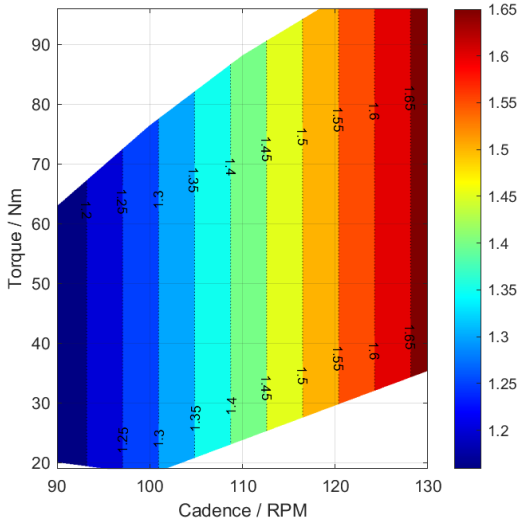

(b) Absolute uncertainty [W] for 3/8 inch pitch chain tests.

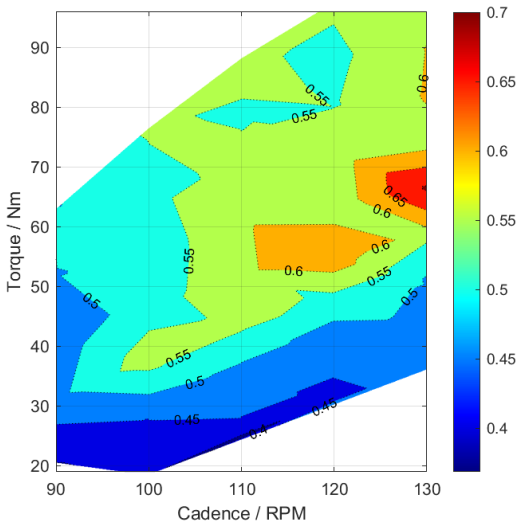

(c) Confidence that there is greater loss from a 3/8-inch pitch than 1/2-inch pitch based on calculated uncertainties.

Figure 8.6: Uncertainties of power loss measurand in individual tests for 1/2-inch pitch and 3/8-inch pitch with equivalent driving loads, and confidence in binary comparison.

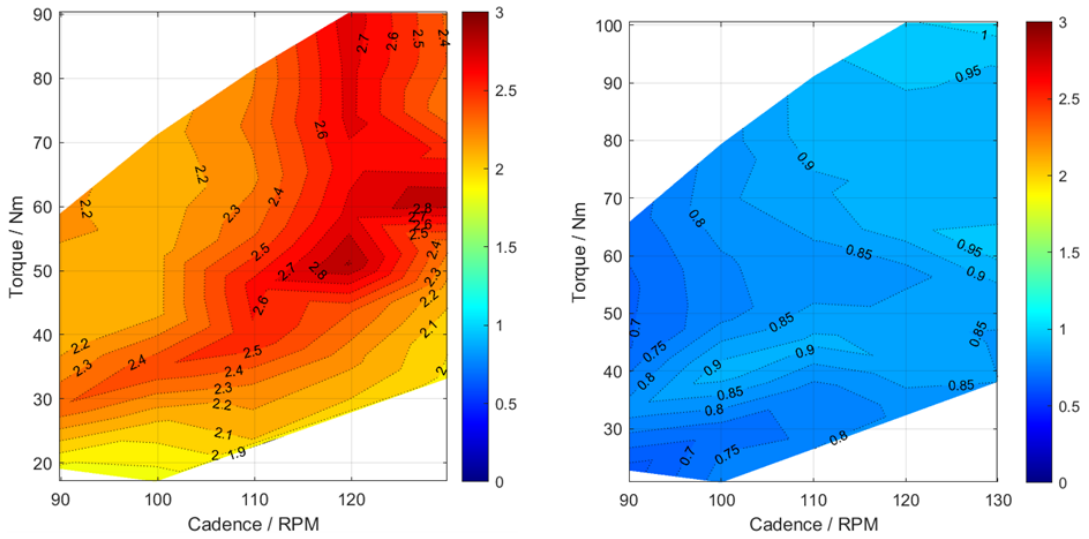

(a) 1/2-inch pitch chain.

(b) 3/8-inch pitch chain

Figure 8.7: Dynamic fluctuations from transmission in driving torque [Nm].

Changes to additional test parameters novel to this test rig impact the measured power losses. The effect of sinusoidal torque profile is to increase the losses in a transmission for the same time-averaged torque input. In the example shown, the difference is 2.2-3.6 W greater losses across the test envelope. This result suggests that the torque profile from a pedalling cyclist is an important parameter to include in representative tests.

The effect of different torque profiles on the measurand demonstrates that factors influencing the profile of delivered torque in cycling should be considered in parametric testing of transmission. The literature suggests a smaller amplitude torque sinusoid is a more physiological efficient pedalling stroke [21] which is improved with a cyclist's experience [28]. Pedalling torque profile also changes with workload [41], suggesting that it should be defined as a function of input torque, and rider fatigue [69]. All tests of varying sinusoidal torque input corroborate the illustrated phenomenon that losses increase with greater amplitude torque variation.

A small difference is seen in power loss results from example chains of different pitch sizes, and one chain is not favourable across the whole tested range of torque and speed test points in the comparison shown.

The uncertainty of the experimental measurand is quoted alongside results, as derived in Chapter 6. Where comparisons are made between similar tests to isolate the effect of specific parametric changes, the binary uncertainty confidence interval is calculated across the test envelope. With this tool, it is demonstrated that there is high confidence that a sinusoidal torque profile induces more loss than a constant torque profile at 86% - 94% confidence across the test envelope. In contrast,

the confidence in difference between the examples shown for chains of different pitches is low and does not exceed the previously defined minimum confidence interval of 68.27% ($k_p = 1$).

While the primary measurand is not appreciably different between the chains of different pitch sizes in similar configurations, there is significant difference in the vibration signature on the driving torque from the tested transmissions. Analysis introduced in Chapter 7 is applied and shows significantly smaller chain vibration from polygonal action from the 3/8-inch chain when compared with the 1/2-inch chain across the test envelope. Furthermore, the presence of a peak denoting higher dynamic response due to top-span resonance is present in the 1/2-inch pitch results at 120 RPM and 50 Nm; there is no discernible peak across the test envelope of the 3/8-inch pitch chain.

Characterisation of the torque dynamics for the constant and sinusoidal torque shows that resonance is impacted by the changing torque profile. This is also observed during experiment where the top span of a chain is seen coming in and out of resonance at a constant speed test point. The effect seems to be a less pronounced peak, which is expected since there is no longer a test point entirely at resonance, but several neighbouring test points partially at resonance. The resonance also changes location. The most significant peak also is at a slightly different torque for the same speed, suggesting that discrete test points do not necessarily coincide with the resonance exactly. A test sequence with more test points would be beneficial to fully understand this.

8.6 Summary of Chapter 8

This chapter collated the experimental and analytical techniques developed for tests on the chain dynamometer test rig and illustrated some example results.

1. The duty cycle developed for time-efficient testing of transmission was detailed, demonstrating a range of driving torques and rotational speeds.
2. The methods for performance characterisation and uncertainty assessment developed in previous chapters were reintroduced:
   (a) Calculation of primary measurand: transmission power loss.
   (b) Assessment of uncertainty of measurand.
   (c) Dynamic fluctuations at steady state loading points.
3. Test results were illustrated for some example tests, demonstrating differences between performance of:
   (a) A transmission loaded with sinusoidal varying torque profile.
   (b) A transmission with different pitch bush roller chain.

THIS PAGE IS INTENTIONALLY LEFT BLANK.

Chapter 9

Whole Duty Cycle Modelling of Chain Transmission Efficiency: Case Study of Elite Bicycle Racing

9.1 Introduction

Literature and test results presented in this work demonstrate that transmission efficiency is dependent on several factors:

- Applied torque.
- Rotational speed.
- Torque profile.
- Gear selection.
- Planar alignment.
- Lubrication.

In a variety of contexts where chain drives are used as transmission, some or all these parameters can change in use. To understand the performance of a transmission, there must be appreciation of its contextual application. In applications where parameters affecting performance change in limited and specific ways, average conditions may be considered to derive a single performance metric. An example is cycling in indoor track races. In velodrome track racing, a narrow band of parameters will define most of a race: the gear ratio does not change; many races include a single acceleration phase followed by steady power riding; and there are no course profile or environmental changes (only in alternating between a straight and a corner). As a result, quoting a

single transmission efficiency at a representative steady state point is a reasonable approximation for a particular race.

Other transmission use cases see much more variation in their duty cycle during operation. In the most complex examples, analysis of the whole life of the transmission is necessary to accurately assess its aggregate performance. One such extreme is in bicycle road racing.

Bicycle road races have much more complex duty cycles than track cycling. They feature varying inclines (an example is shown in Figure 9.1), environmental conditions, rider power output and gear selection. Hence, efficiency can vary quite dramatically. There is limited use in considering an instantaneous efficiency as a measure of transmission performance across a whole race since inaccuracies are introduced and efficiency does not change linearly with all parameters on which it depends. Furthermore, the transmission efficiency as a performance metric does not appreciate trade-offs such as mass of gears versus efficiency. A more accurate method is to derive a performance metric of net energy consumed for specified rider, equipment and race course.

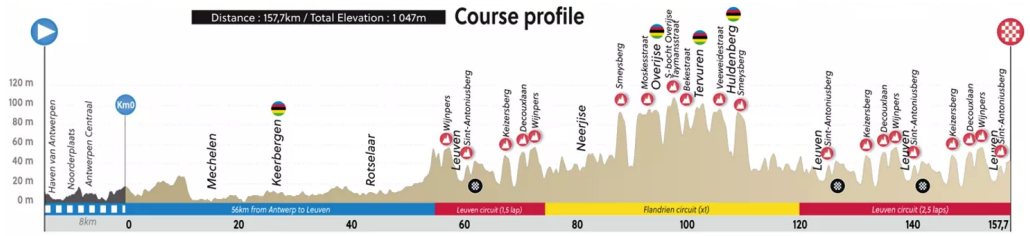

Figure 9.1: Course profile of UCI 2021 Road World Championships, Antwerp-Leuven [81].

To determine the net energy consumed in a race, the transmission power loss may be estimated (from empirical data or validated models) for a large number of discrete points in a racecourse, and the product of power lost and time to completion in each discrete segment equates to the energy cost. The sum of the energy expenditure in each segment determines the overall energy expenditure on overcoming transmission frictions.

Using such a technique, a whole-life-cycle consideration of performance can be applied to compare the net effect of equipment choices or design changes to transmission. An analysis which is capable of defining the net energy cost of equipment may also be used to calculate time to completion for races. With enough sophistication, equipment choices (linked with transmission and otherwise), physiological input from rider and even race tactics could be modelled to determine an optimal strategy for a given race.

A method of evaluating whole race performance is presented in this chapter, and illustrated with the application of analytical models describing the power balance in cycling and the transmission

efficiency.. The modelling methods may be employed with alternative analytical descriptions of physical behaviours or applying empirical data.

9.1.1 Structure of chapter

The chapter content is structured as below:

1. A racecourse profile is defined with discrete segments of a road route with fixed distance, gradient and direction. This is demonstrated from adapting Global Positioning Satellite (GPS) data.
2. A power model for road cycling is introduced to calculate velocity for given power input and other physical parameters. The power model may take analytically or empirically derived parametric inputs. It is combined with an analytical description of transmission efficiency from literature.
3. Whole-life-cycle performance measures are presented which consider the riding equipment, physiological input and course profile in the success of the case stated. Further applications of the modelling are presented.
4. Finally, discussion of the modelling techniques introduced highlight improvements and further uses by including modelled or empirical data from various sources.

9.2 Course profile defined by discrete elements

A course profile is built by combining discrete elements of defined distance with known gradient. Additional parameters are defined which vary during a bicycle race, such as the wind speed and wind direction relative to the forward velocity of the bicycle and rider. Furthermore, varying physiological parameters for efficient energy or tactical gain are considered, such as a rider's preferred cadence, gear shifting, or variation to power input. With small segments, the parameters are varied regularly and parameters are quasi-dynamic.

GPS data describing a route can be collected by recording a cycled route, or by using mapping software. An example case is taken from a mapped route of a road race from the UCI 2021 Road World Championships in Flanders, Belgium.

9.2.1 Approximation of real-world course profile

A real-world course profile is described by a series of GPS data points which describe location on the surface of the Earth through triangulation of three parameters: angle of latitude, angle of longitude and elevation above sea level. Table 9.1 shows data for the initial points in a course.

Table 9.1: Triangulation points for first 5 discrete points in race course.

Point	Latitude, ϕ / $^\circ$	Longitude, λ / $^\circ$	Elevation, Δz / m
1	51.16455	4.39777	14
2	51.16439	4.39789	13
3	51.16413	4.39814	12
4	51.16358	4.39843	11
5	51.16345	4.39845	11
6	...	...	...

Each point with defined latitude, longitude and elevation represents the start and end of a discretised straight-line segment; when combined in series, they compose a close approximation for the whole cycled route. The straight-line distance travelled in each segment, d, can be approximated as in Equation 9.1. This describes the shortest path between two points on a sphere and is known as the Haversine distance. There is error of up to 0.334% when using this for distance on the Earth [52] since the Earth is not spherical, though for small distances the error will be negligibly small. Approximating the Earth as a sphere with radius $r = 6.365 \times 10^6 m$, distance d_{xy} is calculated as below.

$$d_{xy,i} = 2r\sin^{-1}\left(\sqrt{\sin^2\left(\frac{\varphi_i - \varphi_{i-1}}{2}\right) + \cos\varphi_{i-1}\cdot\cos\varphi_i\cdot\sin^2\left(\frac{\lambda_i - \lambda_{i-1}}{2}\right)}\right) \tag{9.1}$$

Further parameters for each segment are calculated from d_{xy}. The total distance travelled, d_{xyz}, and gradient, $m_{\%}$, of each segment is calculated as in Equations 9.2 and 9.3 from change in elevation above sea level, Δz.

$$d_{xyz,i} = \sqrt{d_{xy,i}^2 + \Delta z_i^2} \tag{9.2}$$

$$m_{\%,i} = \frac{rise}{run} = \frac{\Delta z_i}{d_{xy,i}} \cdot 100\% \tag{9.3}$$

The direction of the velocity vector during each segment may be described as an orientation relative to north, θ. The bearing during a segment is calculated by creating a spherical triangle with the two points and the north pole as in Equation 9.4.

$$\theta_i = \frac{180}{\pi}\tan^{-1}\left[\frac{\sin(\lambda_i - \lambda_{i-1})\cos(\varphi_i)}{\cos(\varphi_{i-1})\sin(\varphi_i) - \sin(\varphi_{i-1})\cos(\varphi_i)\cos(\lambda_i - \lambda_{i-1})}\right] \tag{9.4}$$

The calculated course profile parameters are summarised for each segment in Table 9.2.

An example sequence of segments from GPS data is illustrated in Figure 9.2, with route derived from the UCI 2021 Road World Championship in Flanders, specifically the senior road races held

Table 9.2: Parameters of first five segments in course profile.

Segment	d_{xy}/m	$\Delta z/m$	d_{xyz}/m	$m_{\%}/\%$	θ / °
1	0.7	0	0.7	0.0	90.0
2	49.7	0	49.7	0.0	330.6
3	7.1	0	7.1	0.0	242.0
4	6.5	0	6.5	0.0	239.1
5	91.3	-1	91.3	-1.1	149.8
6	...	...	...	...	...

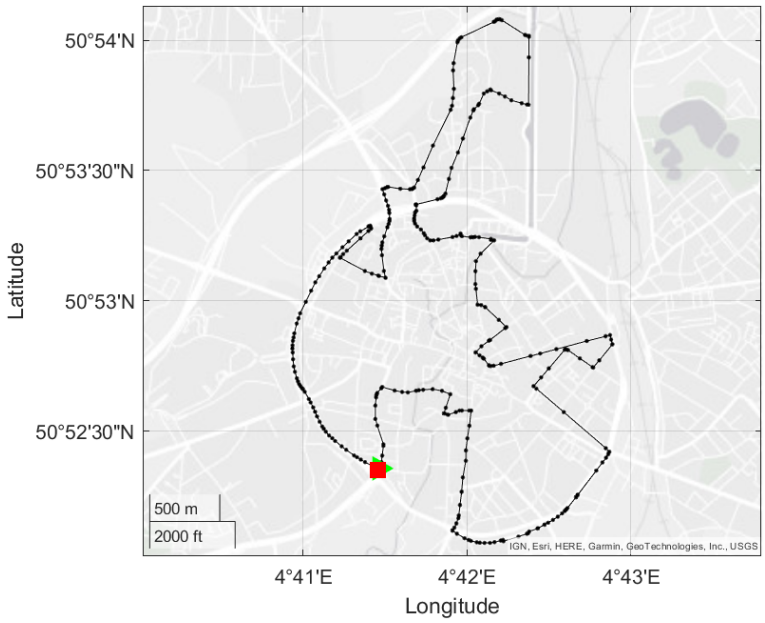

(a) Longitude and Latitude data points plotted over street map.

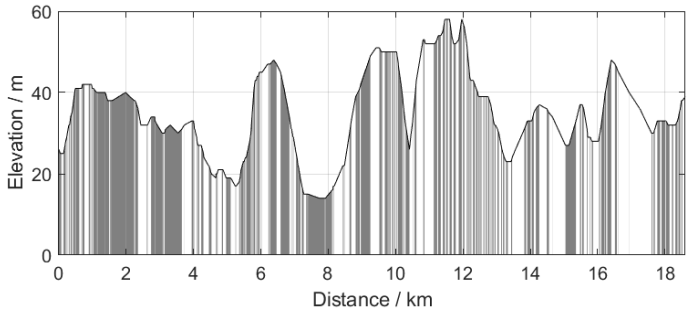

(b) Elevation profile against distance, alternately shaded segments.

Figure 9.2: 18km section of mapped route for application to model based on the road race from Road World Championships 2021 in Flanders. Segments for modelling are shown.

September 24th-26th 2021. The route is created using online mapping software and downloaded as a GPS file (.GPX format).

Since the GPS route is defined as a series of points, the segments are already described as the route between these points. There is scope for interpolation where they are not sufficiently regular, though this must create new nodes to be of value.

9.3 Modelling efficiency within power model

9.3.1 Analytical model for road cycling power

To model variation of transmission efficiency in a race, simulation of typical power input and race profile is necessary since efficiency depends on power and gear selection, themselves having multivariant dependencies. The power required to overcome resistance during cycling may be described by Equation 9.5 [54].

$$P_{in} = \frac{P_{AD} + P_{RR} + P_{PE} + P_{KE}}{\eta} \tag{9.5}$$

Where P_{AD} is power to overcome aerodynamic drag, P_{RR} is power to overcome rolling resistance of the tyres, P_{PE} is power to overcome changes in potential energy (from climbing gradient), P_{KE} is power to overcome changes in kinetic energy and η is transmission efficiency. Expanding each expression, P_{in} is described as in Equation 9.6.

$$\begin{aligned} P_{in} = \Big[& \frac{1}{2}\rho \left(C_D A + F_W\right) V_\mu^2 V_G + V_G C_{RR} mg \\ & + V_G mg sin\left(\tan^{-1}\left(G_R\right)\right) + \frac{1}{2} m \frac{V_{G,f}^2 - V_{G,i}^2}{t_f - t_i} \Big] / \ \eta \end{aligned} \tag{9.6}$$

This can be rewritten in the form of a cubic to solve for final velocity of bicycle relative to the ground in segment i, $V_{G,f} = V_{G,i}$, derived in Appendix A.

$$a{V_{G,i}}^3 + b{V_{G,i}}^2 + cV_{G,i} + d = 0 \tag{9.7}$$

Coefficients a to d are described in Equations 9.8 - 9.11, where new variables are defined from constants in each source of drag, defined in Appendix A.

$$a = \frac{{P_{AD}}'}{8} + {P_{KE}}' \tag{9.8}$$

$$b = {P_{AD}}' \left(\frac{3}{8} V_{G,i-1} - \frac{V_W'}{2}\right) + {P_{KE}}' V_{G,i-1} \tag{9.9}$$

$$c = {P_{AD}}' \left(\frac{3}{8} V_{G,i-1}^2 - V_{G,i-1} {V_W}' + \frac{1}{2} {V_W}'^2\right) + \frac{{P_{RR}}'}{2} + \frac{{P_{PE}}'}{2} - {P_{KE}}' V_{G,i-1}^2 \tag{9.10}$$

$$\begin{aligned} d = & {P_{AD}}' \left(\frac{1}{8} V_{G,i-1}^3 - \frac{1}{2} V_{G,i-1}^2 {V_W}' + \frac{1}{2} V_{G,i-1} {V_W}'^2\right) \\ & + \frac{V_{G,i-1} {P_{RR}}'}{2} + \frac{V_{G,i-1} {P_{PE}}'}{2} - {P_{KE}}' V_{G,i-1}^3 - \eta P_{in} \end{aligned} \tag{9.11}$$

Transmission efficiency, η, is described in Section 9.3.2.

9.3.2 Efficiency in power model

The efficiency term in power modelling might be derived from empirical data which captures all considered dependencies in this power model. Alternatively, an analytical description of efficiency might be used, which is explored here.

Kidd described a model for frictional losses in a bicycle derailleur drive in their thesis [42], described in Section 2.2.3. A similar model of transmission efficiency is developed independently by extending the frictional loss models of Lodge [48], also introduced in Section 2.2.3 and used in Chapter 3. This model considered a dual-sprocket system without auxiliary gears, so additional loss mechanisms must be considered beyond those in the original application of a dual-sprocket system.

In a derailleur transmission system with two auxiliary sprockets, the chain will articulate more and hence there is added sliding friction. Furthermore, there is additional loss from the bearings in the auxiliary sprockets, illustrated in Figure 9.3.

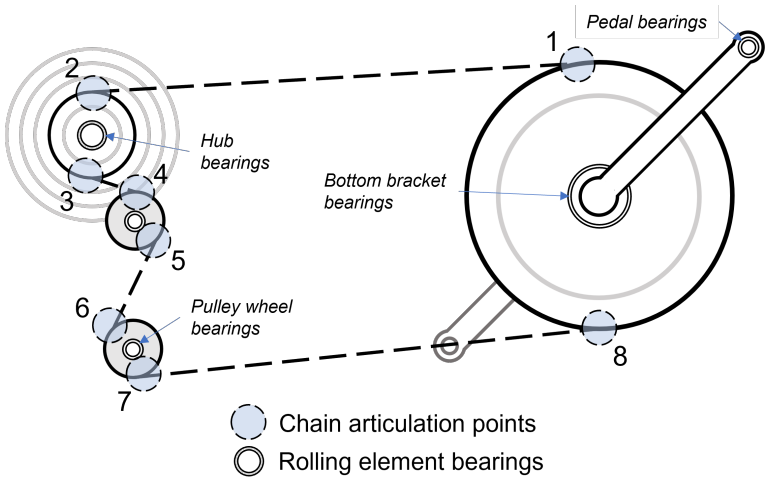

Figure 9.3: Source of rolling and sliding friction in derailleur transmission.

Frictional loss at chain articulations is proportional to the tension between links during articulation, which is assumed to be equal to an approximation of the span tension. In the upper span, tension is predominantly caused by torque applied at the crank. In the lower span, the derailleur system works to engage the chain with the selected sprocket and hold the bottom span in tension through a sprung arm, illustrated in Figure 9.4.

Tension in the bottom span is higher than in a dual sprocket slack span and also varies with selected gear. The tension is calculated with a geometric model which solves the derailleur angle for given chain lengths by maintaining tangential spans. The angle of rotation and spring rate of the torsional spring in the derailleur arm provides the tension force.

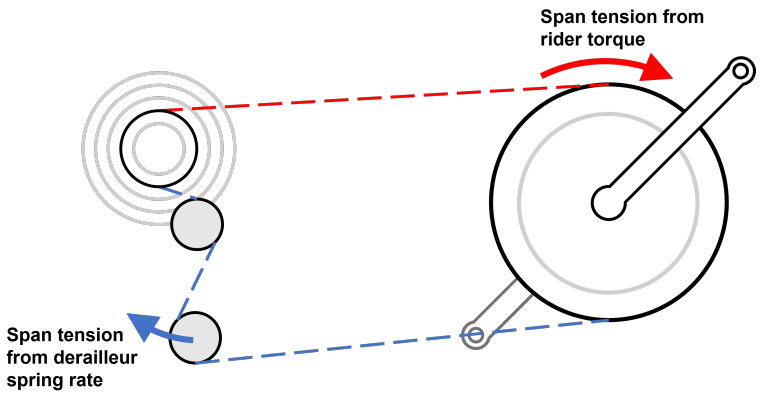

Figure 9.4: Source of span tension for top and bottom chain spans.

Work done against friction at each chain articulation point is a function of tension, geometric and sliding friction parameters [48, 47]. Transmission efficiency is defined as in Equation 9.12.

$$\eta = \frac{\left(P_{in} - \frac{N_s \omega_s}{2\pi} \sum_{i=1}^{8} W_i\right)}{P_{in}} \tag{9.12}$$

where W is the work done against friction in each of 8 articulating links (entry and exit to each sprocket), ω_s is the rotational frequency of the chainring (s^{-1}) and N_s is number of teeth in the chainring.

The efficiency is dependent on selected gear due to both changing articulation angle and tension in the bottom span from derailleur angle. To model efficiency for a range of gear ratios available in a derailleur drive, gear ratios available are defined as a sequence with combinations typical of a road bicycle, summarised in Table 9.3. To simplify analysis, overlapping gear ratios are neglected.

Modelled efficiency is calculated for the range of gear ratios across various torque inputs and illustrated as a contour plot in Figure 9.5. The vertical dividing line represents the shift in the front derailleur, hence the step change in efficiency values.

The efficiency is shown to change by up to 3%-pts across the range of torque and gearing shown, demonstrating the potential differences which may be seen during a varied course profile. This expression for efficiency may be applied within the power model to determine its effect.

9.4 Application of models

The models for velocity and efficiency described over the previous sections may be combined to calculate the expected velocity across the example road race based on changing power demands. To determine the velocity for each segment, the power model described in Section 9.3.1 is solved for given input power with parameters defined according to equipment used by a virtual rider.

Table 9.3: Sequential gear ratios with corresponding combination of chainring and sprocket. Travel is estimated assuming 700mm diameter rear wheel (including tyre).

	Gear no.	Driving sprocket / # teeth	Driven sprocket / # teeth	Gear ratio / N_1/N_2	Travel per crank rev / m
Small chainring	1	39	28	1.39	3.06
	2	39	24	1.63	3.57
	3	39	21	1.86	4.08
	4	39	19	2.05	4.51
	5	39	17	2.29	5.05
	6	39	16	2.44	5.36
	7	39	15	2.60	5.72
Big chainring	8	53	19	2.79	6.13
	9	53	17	3.12	6.86
	10	53	16	3.31	7.28
	11	53	15	3.53	7.77
	12	53	14	3.79	8.33
	13	53	13	4.08	8.97
	14	53	12	4.42	9.71
	15	53	11	4.82	10.60

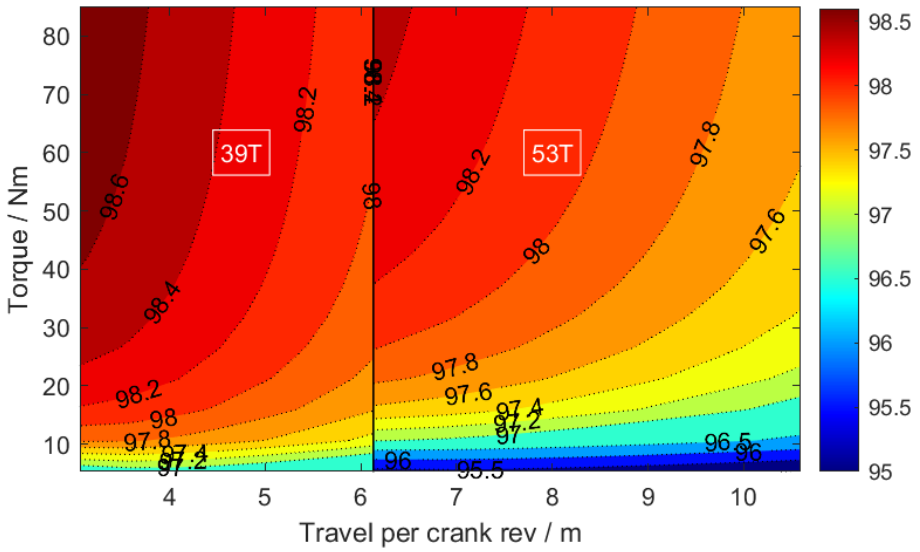

Figure 9.5: Power efficiency [%] contour map for varying rider torque and gear ratios as summarised in Table 9.3.

The model follows the flow diagram illustrated in Figure 9.6. Several iterative loops exist since the velocity is dependent on efficiency, itself dependent on gear. Gear is selected based on suitable cadence, which is itself a function of velocity.

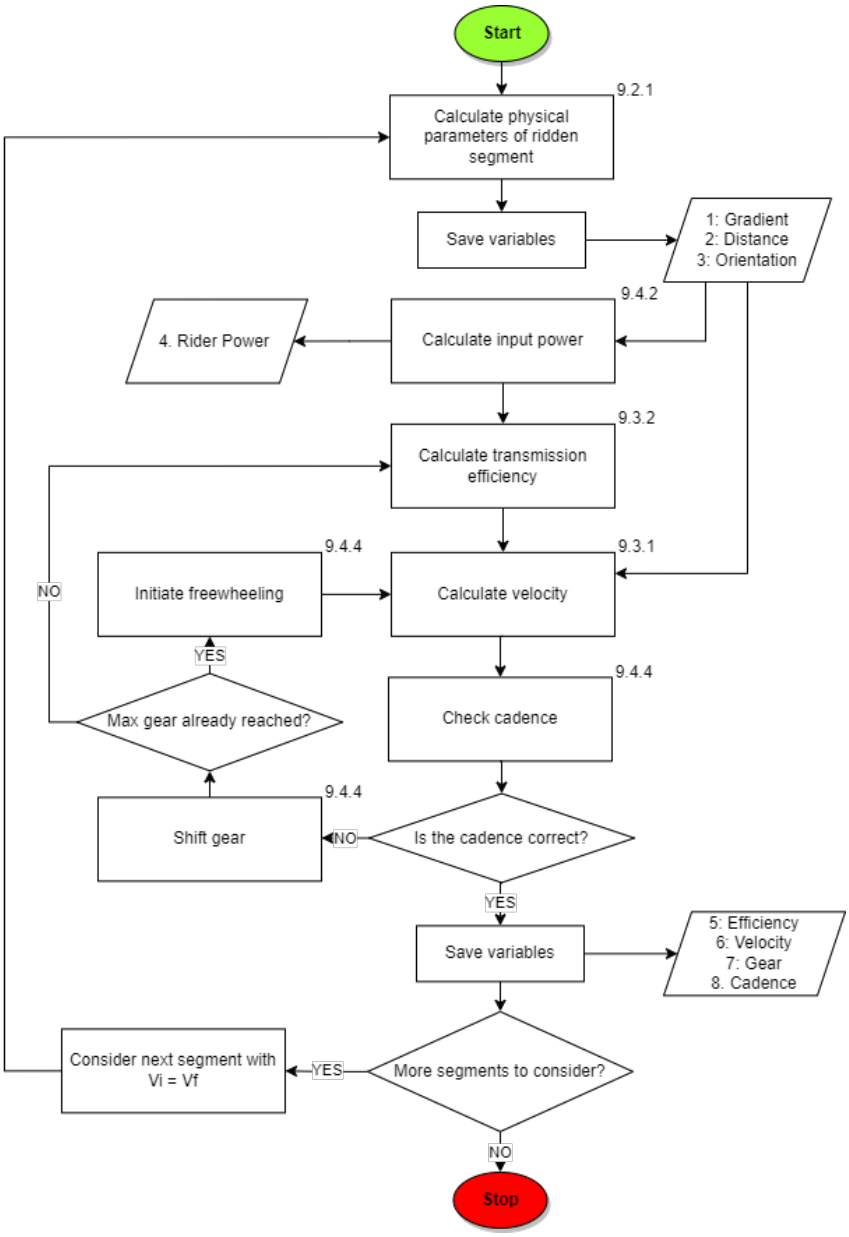

Figure 9.6: Model flow diagram.

9.4.1 Rider power curve

For road races which may last several hours, a rider is likely to vary their physiological effort according to a number of factors. Changes to input power can be incorporated into the model by defining it according to one or more parameters. A varying power curve is presented here which changes with gradient, based on variation about an expected power input. The selected curve for this model is linear with constant $k_P = 2.5$.

$$P_{in} = P_{av}\,(1 + k_P G_R) \tag{9.13}$$

A power curve shown varies linearly with gradient, though could as easily be described as a function of distance, or another parameter based on race strategy.

9.4.2 Gear selection to maintain cadence

With velocity calculated for given power input, the cadence of the rider (equivalent to the rotational speed of pedals, n_1) is determined according to Equation 9.14, based on the bicycle velocity, V, transmission gear ratio, $\frac{N_1}{N_2}$, and radius of the rear wheel, R_W.

$$n_1 = V \frac{30}{\pi} \frac{N_1}{N_2} \frac{1}{R_W} \tag{9.14}$$

Initially, this is calculated with gear ratio used in the previous segment (or an initial guess for the first segment), from the selection of gears detailed in Table 9.3. Cadence may be calculated and then compared with an acceptable range (which may be different depending on the rider or conditions). The gear is shifted if the cadence falls outside this range to ensure that an appropriate cadence is found for given bicycle velocity.

When the maximum gear ratio is reached and the velocity increases above maximum cadence, the rider is defined as 'freewheeling' during this segment. When minimum gear ratio is reached and velocity decreases below the minimum cadence, the cadence is allowed to stray downwards.

When the gear is shifted, the efficiency calculation has new parameters and so the model recalculates the new expected velocity. In the efficiency equation, the gear ratio changes but also applied torque changes with cadence for given input power, according to Equation 9.15.

$$\tau = \frac{P_{in}}{n_1 \frac{\pi}{30}} \tag{9.15}$$

Since the velocity is itself dependent on gear ratio, the model changes by one gear at a time to find the closest gear which satisfies the conditions. Gears are assumed to shift instantaneously with no disruption to rider input torque.

9.4.3 Limitations of current implementation

The model has some limitations:

1. Braking is not considered, and so there will be some error in racecourses where braking is necessary for safety, for instance in steep descents featuring tight corners.
2. A rider changing body position is not considered, such as standing up out the saddle. This occurs at low cadence and allows a rider to output high torque, for instance in steep hill-climbing sections of a course. The pedalling style, torque, frontal area will all change. The error from not having this is small since the frontal area affects aerodynamic drag which is less significant at low speeds.

3. Much more significant changes to torque output and drag losses from sprinting is also not considered. Cyclists stand up out the saddle in large gear ratios and transmit large peak power during sprints which is not considered in this analysis.
4. Changing aerodynamic drag from interaction between riders is not included in this analysis, where riders in a group experience reduced drag when compared with riding solo.

9.5 Model outputs for example racecourse

As way of example, the model outputs for a virtual rider are calculated for the Flanders racecourse described. This rider has input parameters summarised in Table 9.4, based on estimates described in literature [86].

Table 9.4: Parameters describing inputs associated with virtual rider.

Parameter	Value	Units
Mass, m	60	kg
C_dA	0.25	m^2
Average power	250	W
Cadence, n	90±10	RPM

The power input, fluctuating with gradient as described in the previous section, is plotted over the race distance in the first graph on Figure 9.7. Power input is fluctuating significantly in the steeper sections of the racecourse in the latter half. The segments with zero power input correspond to the steep descents.

Gear selection, corresponding to Table 9.3, across the race distance is illustrated in the second graph in Figure 9.7. Low gear ratios are successfully used for steep inclines and the highest gear ratios when the virtual rider is descending. Gear 'zero' denotes the freewheeling segments. It can be seen in the third graph of Figure 9.7 that the gear selection successfully ensures the cadence remains in the range defined for the virtual rider: between 80 and 100 rpm.

The modelled velocity across the race distance is shown in the fourth graph of Figure 9.7. The average velocity over the race distance is calculated by determining the total time taken over the total distance: 38.17 km/h. As a simple form of validation it is worth noting that this is within typical range for a race of this type in professional road racing. Furthermore, the minimum and maximum speeds are within expected limits. The latter stages of the course, which see steeper uphill and downhill sections, show modelled velocity has much greater minima and maxima respectively, as is expected.

Finally, the efficiency as modelled with changing parameters between segments, such as torque and gear, is illustrated in the fifth graph of Figure 9.7. This shows quite significant variation between 96.8 % - 98.8%.

9.6 Whole-race performance measures

9.6.1 Time to completion

The time to complete a racecourse is found by summing the modelled time to complete all n segments from distance covered and average velocity in each segment, described in Equation 9.16.

$$T = \sum_{i=1}^{n} \frac{2d_i}{V_i + V_{i-1}} \tag{9.16}$$

This may be used in assessing the modelled differences to race standing by using different equipment, race strategy or other. In the modelled example, time to completion is 3h 18m 10.8s.

9.6.2 Whole-course efficiency

The transmission efficiency with defined gear and torque input is used in this analysis; a more particular version of transmission efficiency can be determined to describe its performance with the particular inputs of the duty cycle used. To determine this, the ratio of energy lost to the transmission and total energy supplied to the pedals is found.

$$\eta_{holistic} = \frac{\int P_{in} - P_{lost}\ dt}{\int P_{in}\ dt} = \frac{\sum_{i=1}^{n} \eta_i \cdot P_{in,i} \cdot t_i}{\sum_{i=1}^{n} P_{in,i} \cdot t_i} \tag{9.17}$$

In the modelled example, the holistic efficiency for the virtual rider on this racecourse is 97.88%.

9.6.3 Whole-course efficiency across multiple racecourses

General trends can be demonstrated by repeating this analysis across multiple racecourses with varying parameters. The most significant parameter in course profile affecting overall efficiency is elevation gain per unit distance. The key parameter in the rider is their average power input during a race (often dependent on race type, higher power seen in time trial races). Holistic efficiency changing with these parameters is illustrated in Figure 9.8.

9.7 Applications for model

The modelling strategy demonstrated can be applied to various contexts to calculate holistic measures of performance for specific inputs. The benefit of using this analysis above applying the

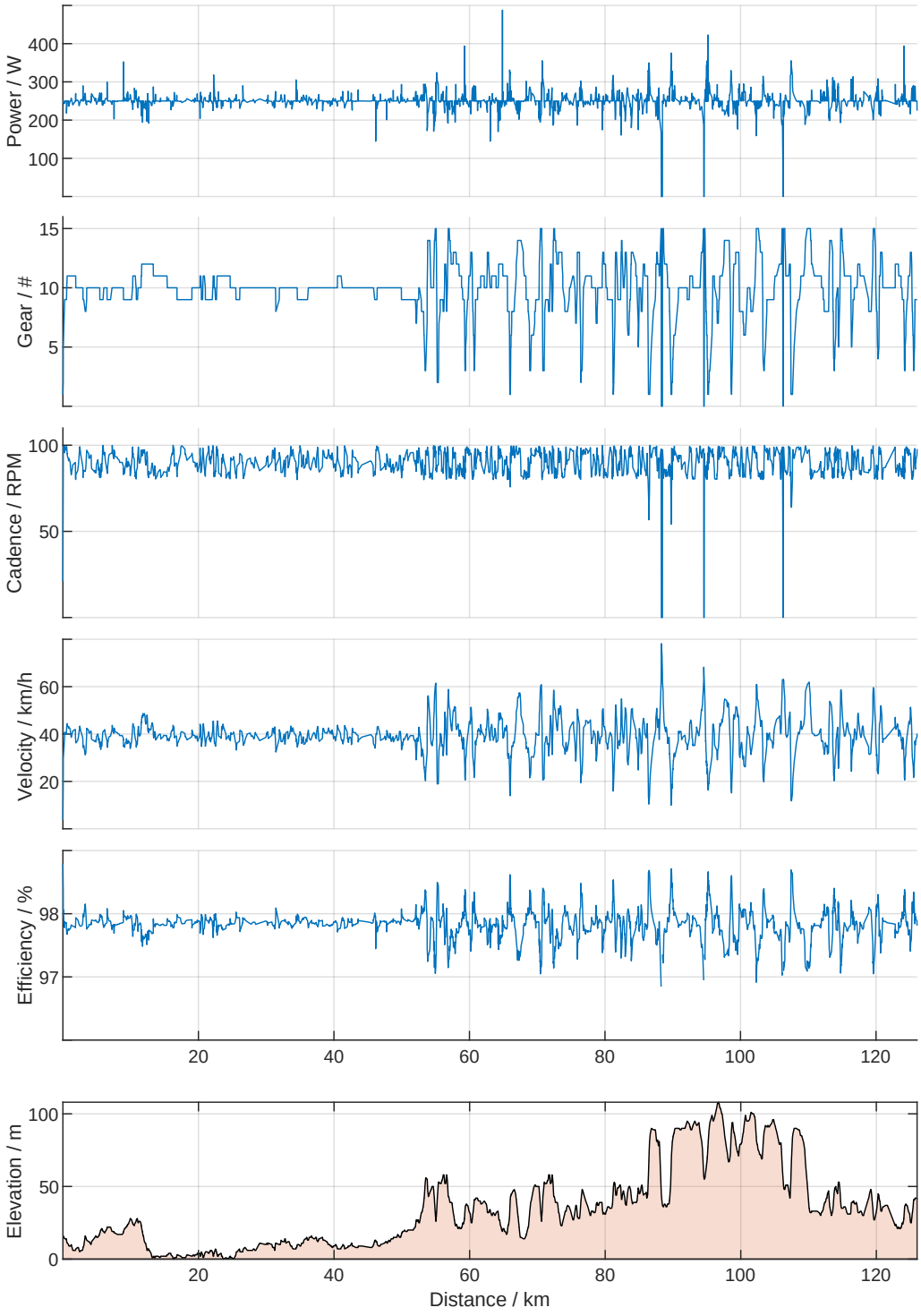

Figure 9.7: Varying modelled parameters over race distance. From top: input power [W], gear selected (corresponding to Table 9.3), cycling cadence [RPM], velocity [km/h], and transmission efficiency [%]. Finally, course elevation is also illustrated.

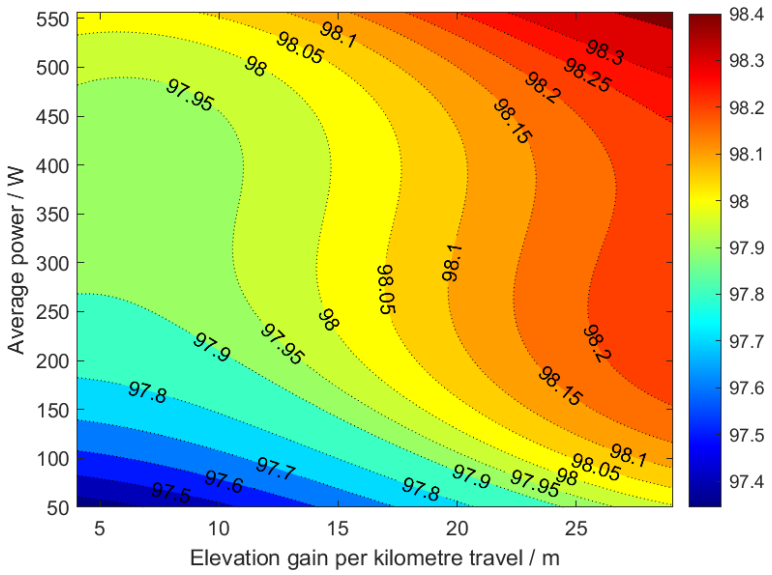

Figure 9.8: Contour map of example transmission power efficiency [%] as function of average power during a race and its elevation profile.

power model as described in previous literature is that the transmission is modelled within it, such that modelling may consider the effects of transmission changes on race outcomes, and secondary effects of other parameters on transmission efficiency.

9.7.1 Rider parameters

Several parameters particular to a rider can be specified in this model. Changing power input has been demonstrated and may be further explored. The preferred pedalling cadence and how responsively a rider changes gear will affect the transmission efficiency and hence impact the model, too. Furthermore, the impact of a rider's mass and body position (affecting frontal area) can be determined over a varying course profile.

9.7.2 Environmental factors

The impact of environmental factors such as wind speed and wind direction can be determined in expected completion time for a race. Having calculated the direction of travel for each segment, the relative direction and speed of the wind can be used to factor the additional or reduced aerodynamic drag and its secondary effects on gear selection, and transmission efficiency.

Furthermore, changes to air density based on air temperature or elevation (both of which may change dramatically during a mountainous road race) can be included to improve the realism of the model.

9.7.3 Equipment choices

An estimate for the holistic effect of equipment choice is perhaps the most useful application for this model. This could be a fundamental change such as the choice of a road or time trial bicycle with associated changes to all parameters including aerodynamics, mass, and physiological output from different riding position.

Changes to equipment within the transmission may also be explored. The choice of sprockets in the chainrings and cassette, for instance, may be optimised or the impact of secondary upgrades to the drive determined. Where there are trade-offs, such as use of equipment which reduce losses but increase mass, the net effect can be determined.

9.8 Conclusions and further work

The application of a cycling power model to complex duty cycles seen in road racing offers more complete appreciation of the typical loading and boundary conditions for the transmission in use, by considering the choice of gear based on fundamental rider motivations. Previously, the efficiency could be quoted for nominal conditions only which comes with potentially significant error since the course profile, rider, equipment and environmental conditions directly and indirectly affect the conditions seen by the transmission.

Through developing a model which factors in gear selection in multi-speed transmission types, it is shown that key parameters affecting the expected efficiency over a race distance for identical transmission types is the hill climbing expected during the race and the average input power from a rider. Secondary parameters such as mass and aerodynamic drag of rider also subtly impact the transmission performance. Where simplified models apply a single efficiency term which does not appreciate race type or rider expected rider power input, there may be some error which will be more pronounced for more extreme conditions.

Further to showing the dependencies of efficiency, the power model with variable transmission efficiency term can be used to predict race outcomes based on the value of input parameters which affect the transmission. Environmental, rider and equipment parameters can be changed to determine the net effect on race outcome. In the context of transmission, this allows for comparisons of drive changes which have some trade-offs, such as the enlargement of gears offering better efficiency for increased mass and frontal area.

The study described in this chapter was completed independently of the body of work by Dahmen et al. at the University of Konstantz which considered applications of mathematical power models

to road cycling [19], calibration of cycling power models with on-bicycle telemetry data [18], and optimisation of pacing strategies with use of power cycling models [17]. Further work should be completed to consider the application of varying transmission efficiency addressed in this chapter to Dahmen's work, which is itself an extension of Martin et al., [54] on which power modelling is based in this chapter.

Following the work set out in this chapter, further research is required to validate several proposed models since they extrapolate the scenarios considered in literature, even where validated previously. A validated model of transmission efficiency for derailleur drives would be a significant contribution to the field. This is possible to achieve with the test equipment described in Chapter 4 and so is a logical next step for the research at this institution or with a dynamometer test rig based on its design.

Whole duty cycle modelling shown here may be applied to chain drive transmissions in different contexts with similar descriptions of primary and secondary influences on loads in the transmission. Measures of whole-duty cycle performance are eminently applicable to any context.

9.9 Summary of Chapter 9

A modelling strategy has been developed for applying a description of transmission efficiency with multiple dependencies to the complex duty cycle of a bicycle road race.

A power model for road cycling was introduced which formed the basis of modelling parameters, including transmission efficiency, for a whole race. The power model may take analytically or empirically derived parametric inputs. For the sake of illustrating the effect of variable transmission efficiency during a race, it was described by an established analytical description of transmission efficiency.

All models were combined to demonstrate the changing parameters of a virtual rider during a road race. Results were shown.

Holistic performance measures were presented which consider the riding equipment, physiological input and course profile in the success of the case stated. Further applications of the modelling were presented.

Finally, discussion of the modelling technique highlighted further work to improve and utilise this work with potential to input modelled or captured data from various sources.

THIS PAGE IS INTENTIONALLY LEFT BLANK.

Chapter 10

Summary of Thesis

10.1 Thesis overview

Chapter 1 introduced chain drives as transmission systems and their performance metrics. Links were made between three strands of performance - wear, efficiency and vibration - and the importance of each being related to the context of the transmission use-case. The case for holistic consideration of performance was demonstrated as these factors are connected. Vibration increases friction, and friction is the cause of both wear and reduction in power efficiency. The aims of the research were stated and expanded in research methodology, and the thesis structure was set out.

Chapter 2 evaluated the literature relevant to this project. The four themes covered were analytical approaches and experimental methods to determine chain transmission performance, methods to determine frictional performance of rolling element bearings, and finally literature pertaining to the characterisation of measurement uncertainty in experimental apparatus.

Chapter 3 appraised two common designs of chain dynamometer apparatus with qualitative and quantitative comparisons. Analytical models from the literature were adapted and used to compare the kinematic movement and link forces between the two cases based on differences in loading and boundary conditions. The varying centre distance and double tight span of Frictional Power Measurement dynamometer had influence on the modelled results when compared with the Transmitted Power Measurement dynamometer. Discontinuities in span tension and shaft rotational speed resulted from the changing centre distance, and tension distribution around the sprocket was quite different. The uncertainty of measurand on each test apparatus was also calculated and shown to be improved in the FPM since power losses are inferred from two measurements in this instance, and four measurements for the TPM.

Chapter 4 introduced a new dynamometer test rig at the University of Bristol with loading capability for elite track cycling applications. Hardware of the rig-as-built was described and its novel testing configurations discussed. The sophisticated power management and control systems allowed for controlling torque input and resistance according to high fidelity models, and high resolution and accuracy measurement of input and output power to a transmission system. The following four chapters were based on studies on this apparatus.

Chapter 5 described parasitic influence on the measured variables and chain loading conditions on the chain dynamometer. The design and assembly of hardware, speed control of electric machines and test sequencing necessary to mitigate these influences was evaluated. Compensation methods for the influence of bearing friction on assessment of transmission performance was a particular focus, and models from the literature were found to be inappropriate for the environmental and loading conditions of support bearings in the dynamometer test rig. The design of a secondary bearing test rig was described and its empirical data was used to compensate power loss data in results for transmission tests on the dynamometer test rig.

Chapter 6 addressed calculation of the combined uncertainty of the power loss measurand in transmission tests on the dynamometer test rig. The uncertainty of empirical bearing compensation from the tests described in Chapter 5 was computationally significant though had a small effect on overall uncertainty of transmission test measurand. The uncertainty of torque measurements by transducers was found to dominate overall uncertainty, which was shown to be a function of applied torque and rotational speed.

Chapter 7 evaluated the high frequency system influences on measured variables, and the measured dynamics from the transmission-under-test on the dynamometer test rig. A method for filtering parasitic influence on measured data was presented, and the remaining influence of transmission dynamics was evaluated. A new performance metric was introduced which captured the torque fluctuations in data at steady state test points. Where excitation frequency from polygonal action aligned with a resonant frequency in the high tension span, mode one resonant behaviours were observed in tests and seen in measured data with increased torque fluctuation in time-domain data and a significant peak in the frequency spectrum corresponding to the second harmonic of chain-tooth frequency.

Chapter 8 presented the experimental protocols developed for standard duty cycle tests on the dynamometer test rig. The test sequence and torque/speed inputs were illustrated for a steady state duty cycle to cover loading conditions typical in elite track cycling. Experimental results of several test transmissions are presented to characterise its performance which are a culmination of

work in the previous three chapters. Power loss and vibration results are illustrated across tested torques and speeds, with quoted uncertainty of efficiency shown across the same envelope. Areas of resonance in the test envelope are seen in the vibration data, the location and magnitude of which changes with chain type and torque loading type. Vibration was shown to be reduced for smaller pitch roller chain. Power losses were shown to increase where transmission was driven with a sinusoidal torque profile compared with constant application.

Chapter 9 presented an analytical approach to calculating whole-duty-cycle transmission efficiency performance. A case study of elite road cycling is used as an example chain drive application with varying parameters known to affect transmission efficiency (e.g. sprocket selection, span tension). The models presented allow for holistic consideration of how hardware changes affect race outcome of an elite bicycle race.

10.2 Conclusions

10.2.1 Loading state and boundary conditions for high-accuracy performance characterisation of chain transmission

A central requirement for high-accuracy performance characterisation was shown to be testing in conditions representative of in-use loading and boundary states. The design of various test apparatus in the literature was detailed in Chapter 2, where loading and boundary conditions were often simplified to promote practical, cost effective, and accelerated testing solutions.

Two test apparatus were compared in Chapter 3, which represent two common testing solutions. The Friction Power Measurement (FPM) dynamometer has been commonly used in the bicycle transmission industry for validation of components and lubricants, while the Transmitted Power Measurement (TPM) dynamometer is more common in academic investigations of transmission performance for a variety of applications. The FPM dynamometer induced tension in chain spans independently from the driving torque, so that losses could be directly measured and hardware was scaled for the power losses and not the equivalent full power transmitted. Using analytical models, the variable centre distance and double tight span was shown to change both the kinematic movement of the chain and the tension in the links, when compared with a case more similar to both real-world and a TPM style dynamometer where driving torque induces high tension in a single chain span.

Changes to the source of chain tension had implications for the measured losses and inferred power efficiency of the drive. The primary source of this difference was from the implication

of a neglected slack span in the FPM case. The slack span tension increases with chain mass and so this error would increase for tests of a heavier chain. Furthermore, vibration and dynamic effects are a function of harmonic variation in link tension and transverse movement, which were demonstrated to be different between the two cases from the changing boundary condition of varying centre distance.

The design of a new TPM dynamometer for testing in high fidelity conditions for track cycling applications was introduced in Chapter 4 . Its capable power electronics and sophisticated control of both driving and braking mechanics solved shortcomings of previous dynamometers in the literature and allowed for novel testing capabilities to promote representative loading and creating conditions for whole-life-cycle testing.

The parasitic influence of the mechanical system in the dynamometer test rig bore relevance in maintaining representative conditions and improving quality of measurement, discussed in Chapter 5. Many influences were mitigated in system design such as removal of gearboxes and use of high-stiffness hardware. Further effects from hysteresis in torque transducers and dynamic influences were mitigated through proper test sequencing and post processing of measured variables. Hardware configuration and control were shown to affect the application of nominal loading conditions, and such parasitic influences must be mitigated to ensure that the boundary and loading conditions in tests are those which are intended.

High frequency influences on loading and measurement were examined in Chapter 7. The analysis presented was primarily intended to measure the transmission influence on measured variables, also serving as a check of the system influence on the test transmission. Under- or over-damped control would be seen in significant accelerations in the torque data. Influence from mechanical defect or misalignment would also be measured. There was confidence that these effects were not significant although there was evidence of some interaction between line frequency of the torque delivery to the driving sprocket and the frequency of polygonal action in the transmission. Mitigation of this is a subject of further work.

10.2.2 Compensation of support bearing frictional moment in rotating test apparatus

Support bearings are necessary in the assembly of rotating test equipment to isolate the torsional measurement in the strain gauges of torque transducers from high radial loads induced by chain span tension. The bearings in the dynamometer test rig are selected based on their load-dependent performance, detailed in Chapter 4.

The presence of bearings introduces additional friction within the measurement loop on the dynamometer test rig. Frictional losses in rolling element bearings are approximately one order of magnitude lower than those in the test transmission, and a similar order of magnitude to the uncertainty of torque measurement in the dynamometer test rig. To minimise uncertainty of the transmission power loss measurand, frictional power losses to support bearings must be minimised and accurately compensated, addressed in Chapter 5.

Several compensation methods are available. Analytical approaches from literature did not corroborate results from tests described in this thesis, undertaken in conditions representative of those in the dynamometer test rig. The use of empirical data was demonstrated to compensate parasitic influence of bearing losses, such that the measurand of power loss in the transmission-under-test is calculated from data collected on two experimental test rigs.

10.2.3 Uncertainty of measurand from uncertainties in measured variables and parasitic compensation

The uncertainty of the power loss measurand on the dynamometer test rig was described in Chapter 6. The uncertainty of measured variables from bearing characterisation tests on the secondary test apparatus were included in the calculation. Overall uncertainty of the test measurand on the chain dynamometer, $P_{loss} \pm U_{P_{loss}}$, was dominated by the torque measurement on input and output torques, with small contribution from the uncertainty of speed measurement and uncertainty of bearing frictional moment compensation. The bearing compensation uncertainty was itself dominated by the torque transducer frictional moment measurement on the bearing test rig. The relative contribution from each driveline depended on the gear ratio in the transmission-under-test, as the absolute uncertainty of the measurand changed with measured torque.

The uncertainty of equivalence between bearing performance on the different test rigs was calculated at some length. In the context shown, it was demonstrated to have little consequence on the propagation of uncertainty as the effect was small compared with the uncertainty contribution from the measurement of frictional moment. With improved torque measurement or higher load/speed dependency of bearing frictional moment, the uncertainty of equivalence would become more significant. In alternative applications this may be the case.

Commonly, tests on the dynamometer were conducted to compare two similar transmissions with a single changed parameter, for instance testing a chain with two different lubrication choices. The measurands from these tests were directly compared to judge whether one result suggested a measurable improvement in performance. The uncertainty of such a binary comparison was calcu-

lated to determine the confidence with which one transmission outperforms another at equivalent loading points.

10.2.4 Novel parametric results

The presented methods for measuring torque fluctuations in transmission from the captured test data, detailed in Chapter 7, was a new data analysis technique to determine the effect of polygonal action on the driving torque. In the literature, accelerometers are used similarly, though the use of torque transducers for direct measurement of chain vibration and its torsional effect is not known and is shown to be effective. Furthermore, the influence of resonance in the chain span was not previously measured and is shown to be evident in measured variables in both its effect on time-domain fluctuations and in increases to a specific peak in the frequency-domain spectrum. It is shown that there is not necessarily a requirement to develop separate test apparatus or use separate instrumentation for studying vibration from chain dynamics.

The novel loading capability of the dynamometer test rig described in this thesis produced novel results in characterisation of chain transmission performance related to the driving torque profile. Loading capability of defining applied torque as a function of rotational position, introduced in Chapter 4, was used to mimic a sinusoidal torque input from a cyclist. Results from tests of these compared with tests are constant torque are illustrated in Chapter 8. An increase in sinusoidal amplitude at a frequency twice the rotational frequency of the drive increased the power loss in tests on equivalent equipment. The absolute increase was higher for test points at increased torque and speed. Furthermore, the dynamic impact of chain dynamics changed for increased sinusoidal torque.

This suggests:

1. Performance of constant loading is not equivalent to torque-varying loading, with implications for testing in representative conditions.
2. There is some interaction between the cyclist torque profile and the dynamics induced in the chain span.
3. A cyclist with ‘smoother’ torque profile (which is known to be physiologically efficient), will benefit from reduced losses in the chain transmission.

10.3 Research impact: Olympic Games Tokyo 2020

The test apparatus and testing methodologies described and developed in this thesis were used to validate a novel track bicycle chain by Renold PLC for British Cycling between 2018 and 2020.

A reduced pitch chain was developed with validation from the dynamometer test rig, in its power efficiency and consideration of the vibration signature to develop technologies which would reduce negative impact on the cyclist while maintaining favourable power losses in track cycling conditions.

Results from experiments at the University of Bristol aided selection of chain technology, lubrication, preparation, and favourable gear ratios. The new Renold transmission was part of a package of new technologies used in track cycling events by athletes representing Great Britain and Northern Ireland at Tokyo Olympics 2020 (postponed to 2021). Team GB won seven Olympic medals in the velodrome, including three golds, making them the most successful track cycling team in the competition.

Test protocols developed in this research continue to be used for chain drives being developed for future elite bicycle races, including the Paris Olympics in 2024.

10.4 Recommendations for further research

10.4.1 Further work to extend dynamometer capability

1. To validate analytical models for chain transmission power loss from the literature with experimental results on dynamometer test rig. Research could initially focus on the different modelled phenomena in the literature, and which factors can be examined. Specific hardware could be used to amplify certain effects, such as roller-tooth sliding from significant difference between sprocket and chain pitch. More configurations can be tested to develop or validate a new analytical description of dual-sprocket transmissions and those with auxiliary sprockets.

2. Development of an FPM dynamometer test rig to complement the TPM dynamometer. Measurement of link tension, shaft speed and frictional losses can be done to expand on analytical descriptions developed in this thesis. Developing new methods of dynamic link tension measurements would be of interest in collecting more data to further investigate the implication of new loading methods on the chain tension in TPM and FPM dynamometers.

3. The effect of chain dynamics and vibration on measured power losses requires further testing, and continued analysis, of the parameters affecting vibration. The interaction between driving torque and chain dynamics needs to be explored further, including an explanation of the relationship between machine and chain dynamics.

4. Analytical models which predict resonant frequency of chain spans can be validated against resonance identified across the torque-speed envelope in tests by new methods.

10.4.2 Experimental investigations in real-world applications of chain drives

1. Investigate vibration from transmission dynamics in in-use cases, for instance on industrial machinery or on a push bicycle during riding to compare with dynamometer results.
2. Further to the above, a multi-disciplinary investigation into the bio-mechanical response of a cyclist to vibration from transmission and physiological implications would be of significant interest to fully understand the benefit of smoother operation in transmissions.
3. Where whole-life-cycle analysis is conducted for road cycling, the analysis would be strengthened with experimental validation of performance metrics and parameters used in modelling rider power outputs. The model can also be applied with improved and validated models of transmission efficiency, which can be validated with results from the dynamometer test rig.
4. Further development for whole-life-cycle analytical approaches and application to alternative cycling and industrial contexts.

10.4.3 Experimental work on bearings

1. Validation of isolation method for individual bearings from four-bearing test arrangement will strengthen current method.
2. Collect further experimental data to consider influence of parameters affecting bearing frictional moment. Performance under different lubrication, wear state, and presence of defects could be tested for example.
3. Test bearing friction under changing radial load as is the case in sinusoidal testing on the dynamometer test rig.
4. Development of bearing frictional moment model for typical chain dynamometer conditions (light lubrication, low load and speed relative to rated). New empirical data could motivate changes to models from the literature for bearings operating at low end of their rated loading conditions.
5. Development of new experimental solution for bearing friction compensation to work in parallel with the dynamometer test rig, where bearings between test apparatus are run under same loading conditions in same environmental conditions throughout their working life.

References

[1] B. Alexander, R. Peterson, W. Bouette, W. Miller, and S. C. Burgess. An Investigation into the Effects of Vibration on Bicycle Chain Transmissions. 2017.

[2] G. H. Beaho. Webinar: Torque Measurement Uncertainty 101, 2016. URL `https://www.hbm.com/fr/5781/torque-measurement-uncertainty-101/`.

[3] A. Becker, D. Meffert, and B. Sauer. Friction and Wear Investigations on Single Chain Joints. *Forschung im Ingenieurwesen/Engineering Research*, 83(1):53–63, 3 2019.

[4] F. Berto, R. Shepherd, and R. Henry. *The Dancing Chain: History and Development of the Derailleur Bicycle*. Van der Plas Publications, San Francisco, first edition, 2000.

[5] R. C. Binder. *Mechanics of the Roller Chain Drive*. Prentice-Hall, Inc., Englewood Cliffs, New Jersey, 1956.

[6] BIPM, IEC, IFCC, ILAC, ISO, IUPAC, IUPAP, and OIML. Evaluation of measurement data — Guide to the expression of uncertainty in measurement. Joint Committee for Guides in Metrology, JCGM 100:2008.

[7] O. Blomstedt. Measurement and Control System for a Bearing Test Rig. Master's thesis, Aalto University, Helsinki, 11 2017.

[8] S. C. Burgess. Improving Cycling Performance with Large Sprockets. *Sports Engineering*, 1:107–113, 1998.

[9] S. C. Burgess, T. Pyper, and C. S. Ling. A Linear Actuated Chain Test Rig Capable of Accelerated Test Speeds and Continuous Wear Measurements. *Proceedings of the Institution of Mechanical Engineers, Part C: Journal of Mechanical Engineering Science*, 227(5):1047–1055, 2013.

[10] S. J. Chapman. *Electric Machinery Fundamentals*. The McGraw-Hill Companies, Inc, third edition, 1999.

[11] C. K. Chen and F. Freudenstein. Toward a More Exact Kinematics of Roller Chain Drives. *Journal of Mechanisms, Transmissions, and Automation in Design*, 110:269–275, 9 1988.

[12] W. Coenen and H. Peeken. Wirkungsgrad von Rollenkettengetrieben unter besonderer Berucksichtingung des Schmierungszustandes. (German) [Efficiency of roller chain drives with particular consideration of the lubrication condition]. *Antriebstechnik*, 24(11):56–61, 1985.

[13] D. Collins. How to Address Overshoot in Servo Control, 10 2017. URL `https://www.motioncontroltips.com/how-to-address-overshoot-in-servo-control/`.

[14] J. C. Conwell and G. E. Johnson. Experimental Investigation of Link Tension and Roller-Sprocket Impact in Roller Chain Drives. *Mechanism and Machine Theory*, 31(4):533–544, 1995.

[15] J. C. Conwell and G. E. Johnson. Design, Construction and Instrumentation of a Machine to Measure Tension and Impact Forces in Roller Chain Drives. *Mech. Mach. Theory*, 31(4): 525–531, 1996.

[16] M. G. Cox and B. R. L. Siebert. The Use of a Monte Carlo Method for Evaluating Uncertainty and Expanded Uncertainty. *Metrologia*, 43(4), 8 2006.

[17] T. Dahmen. Optimization of Pacing Strategies for Cycling Time Trials Using a Smooth 6-Parameter Endurance Model. In *Pre-Olympic Congress on Sports Science and Computer Science in Sport*, Liverpool, 7 2012. IACSS Press.

[18] T. Dahmen and D. Saupe. Calibration of a Power-Speed-Model for Road Cycling Using Real Power and Height Data. *International Journal of Computer Science and Sport*, 10(2):18–36, 2011.

[19] T. Dahmen, S. Wolf, and D. Saupe. Applications of Mathematical Models of Road Cycling. In I. Troch and F. Breitenecker, editors, *IFAC Proceedings Volumes*, pages 804–809, Vienna, 2 2012.

[20] G. J. M. Dupoyet. Transmission Chain [Patent], 5 1981.

[21] L. M. Edwards, S. A. Jobson, S. R. George, S. H. Day, and A. M. Nevill. Whole-Body Efficiency is Negatively Correlated with Minimum Torque Per Duty Cycle in Trained Cyclists. *Journal of Sports Sciences*, 27(4):319–325, 2 2009.

[22] J. N. Fawcett and S. W. Nicol. Vibration of a Roller Chain Drive Operating at Constant Speed and Load. *Proc Instn Mech Engrs*, 194:97–101, 1980.

[23] C. Fretz. Dripping With Speed: Inexpensive Drivetrain Efficiency is All About Lube. *Velo*, pages 62–64, 3 2013.

[24] Friction Facts. Chain Testing: Full Tension Test Method, 2012. URL https://www.ceramicspeed.com/en/cycling/support/technology/test-data-reports/full-tension-test-method.

[25] N. Fuglede. *Kinematics and Dynamics of Roller Chain Drives*. PhD thesis, Technical University of Denmark, Kongens Lyngby, 2014.

[26] N. Fuglede and J. J. Thomsen. Kinematic and Dynamic Modeling and Approximate Analysis of a Roller Chain Drive. *Journal of Sound and Vibration*, 2016.

[27] N. Fuglede and J. J. Thomsen. Kinematics of Roller Chain Drives - Exact and Approximate Analysis. *Mechanism and Machine Theory*, 100:17–32, 6 2016.

[28] J. García-López, S. Díez-Leal, A. Ogueta-Alday, J. Larrazabal, and J. A. Rodríguez-Marroyo. Differences in Pedalling Technique Between Road Cyclists of Different Competitive Levels. *Journal of Sports Sciences*, 34(17):1619–1626, 9 2016.

[29] I. Geonea, N. Dumitru, and I. Dumitru. Experimental and Theoretical Study of Friction Torque from Radial Ball Bearings. In *IOP Conference Series: Materials Science and Engineering*, volume 252. Institute of Physics Publishing, 10 2017.

[30] T. A. Harris. *Rolling Bearing Analysis*. Wiley-Interscience, fourth edition, 2001.

[31] HBM. Terms and Expressions for Specifying Torque Transducers. URL https://www.hbkworld.com/en/knowledge/resource-center/articles/tips-and-tricks-terms-and-expressions-for-specifying-torque-transducers-glossary.

[32] HBM. Measurement Uncertainty of Force Measurements, 2019. URL https://www.hbm.com/en/9995/uncertainty-of-force-measurements/.

[33] HBM. T10F Torque Flange [Data sheet], 2021. URL https://www.hbm.com/en/2379/t10f-torque-meter-with-an-extremely-short-design.

[34] HBM. T40B Torque Flange [Data sheet], 2021. URL https://www.hbm.com/en/3004/t40b-universal-torque-transducer-for-test-benches.

[35] HBM. T21WN Torque Meter [Data sheet], 2022. URL https://www.hbm.com/en/7343/t21wn-torque-meter-with-cylindrical-shaft-stubs.

[36] HBM. U10M Load Cell [Data sheet], 2022. URL https://www.hbm.com/en/2410/u10-ultra-precision-load-cell-the-reliable-choice.

[37] N. E. Hollingworth. A Four-Square Chain Wear Rig. *Tribology International*, 20(1):3–9, 2 1987.

[38] N. E. Hollingworth and D. A. Hills. Forces in a Heavy-Duty Drive Chain During Articulation. *Proc Instn Mech Engrs*, 200:367–374, 1986.

[39] N. E. Hollingworth and D. A. Hills. Theoretical Efficiency of a Cranked Link Chain Drive. *Proc Insn Mech Engrs*, 200(C5):375–377, 1986.

[40] M. S. Kan. *Multi-Sensor Condition Monitoring of Bearings Using Support Vector Machines*. PhD thesis, Queensland University of Technology, Brisbane, 2017.

[41] S. A. Kautz, M. E. Feltner, E. F. Coyle, and A. M. Baylor. The Pedaling Technique of Elite Endurance Cyclists: Changes with Increasing Workload at Constant Cadence. *International Journal of Sport Biomechanics*, 7(1):29–53, 8 2016.

[42] M. D. Kidd. *Bicycle Chain Efficiency*. PhD thesis, Heriot-Watt University, Edinburgh, 5 2000.

[43] M. D. Kidd, N. E. Loch, , and R. L. Reuben. Bicycle chain efficiency. *The Engineering of Sport*, pages 217–220, 1996.

[44] K. Kozlov, V. Belogusev, A. Egorov, and N. Syutov. Development of Method to Evaluate Friction Losses of Chain Drives. In *17th International Scientific Conference Engineering for Rural Development*, volume 17, pages 930–936. Latvia University of Agriculture, 2018.

[45] C. Kyle and F. Berto. The Mechanical Efficiency of Bicycle derailleur and Hub-Gear Transmissions. *Human Power*, 52:3–11, 2001.

[46] G. Lanaspeze, B. Guilbert, L. Manin, and F. Ville. Preliminary Modelling of Power Losses in Roller Chain Drive: Application to Single Speed Cycling. *Mechanics and Industry*, 23: 217–226, 2022.

[47] C. J. Lodge. *Theoretical and experimental studies of the mechanical behaviour of roller chains*. PhD thesis, University of Bristol, 2002.

[48] C. J. Lodge and S. C. Burgess. A Model of the Tension and Transmission Efficiency of a Bush Roller Chain. *J Mechanical Engineering Science*, 216(Part C):385–394, 2002.

[49] G. D. Mack. Tests of the Efficiency of the Bicycle. *Transactions of the ASME*, 18:1067–1075, 5 1897.

[50] S. Mahalingam. Transverse Vibrations of Power Transmission Chains. *British Journal of Applied Physics*, 8:145–148, 1957.

[51] S. Mahalingam. Polygonal Action in Chain Drives. *Journal of the Franklin Institute*, 1958.

[52] H. Mahmoud and N. Akkari. Shortest Path Calculation: A Comparative Study for Location-Based Recommender System. In *Proceedings - 2016 World Symposium on Computer Applications and Research, WSCAR 2016*, pages 1–5. Institute of Electrical and Electronics Engineers Inc., 12 2016.

[53] K. M. Marshek. On the Analyses of Sprocket Load Distribution. *Mechanism and Machine Theory*, 14:135–139, 1979.

[54] J. C. Martin, D. L. Milliken, J. E. Cobb, K. I. Mcfadden, and A. R. Coggan. Validation of a Mathematical Model for Road Cycling Power. *Journal of Applied Biomechanics*, 14(3): 276–291, 1998.

[55] MathWorks. Bandstop-filter signals, . URL `https://uk.mathworks.com/help/signal/ref/bandstop.html`.

[56] MathWorks. Fast Fourier transform, . URL `https://uk.mathworks.com/help/matlab/ref/fft.html`.

[57] D. Meffert, M. Oehler, and B. Sauer. Precise Friction Measurement in Drive Chains Using a Chain Joint Tribometer. *Tribology Online*, 16(3):151–158, 2021.

[58] M. R. Naji. *On Timing Belt and Roller Chain Load Distributions*. PhD thesis, University of Houston, 1981.

[59] M. R. Naji and K. M. Marshek. Analysis of Sprocket Load Distribution. *Mechanism and Machine Theory*, 18(5):349–356, 1983.

[60] M. R. Naji and K. M. Marshek. Experimental Determination of the Roller Chain Load Distribution. *Journal of Mechanisms, Transmissions, and Automation in Design*, 105:331–338, 9 1983.

[61] M. R. Naji and K. M. Marshek. The Effects of the Pitch Difference on the Load Distribution of a Roller Chain Drive. *Mechanism and Machine Theory*, 1989.

[62] NTI Audio. Fast Fourier Transformation FFT - Basics. URL https://www.nti-audio.com/en/support/know-how/fast-fourier-transform-fft.

[63] A. Palmgren. *Ball and Roller Bearing Engineering*. SKF Industries, Philadelphia, 1945.

[64] H. Peeken and W. Coenen. Influence of Oil Viscosity and Various Additives on the Wear of Roller Chains. *Wear*, 108(4):303–321, 1985.

[65] T. Pyper. *Development of an Accelerated and Automated Wear Testing Technology for Transmission Chains*. PhD thesis, University of Bristol, 12 2008.

[66] H. Renold. Improvements in Driving Chains [Patent], 3 1880.

[67] M. O. Ross and K. M. Marshek. Four-Square Sprocket Test Machine. *Mechanism and Machine Theory*, 17(5):321–326, 1982.

[68] M. O. Ross and K. M. Marshek. Machine for Testing Chain and Sprocket Type Drive Systems, 1983.

[69] D. J. Sanderson and A. Black. The Effect of Prolonged Cycling on Pedal Forces. *Journal of Sports Sciences*, 21(3):191–199, 3 2003.

[70] D. Sappok and B. Sauer. Wear measurement on chain joint components using a roundness instrument. *Periodica Polytechnica Mechanical Engineering*, 59(2):51–59, 2015.

[71] SKF. The SKF model for calculating the frictional moment. Technical report, 2018. URL https://www.skf.com/binaries/pub12/Images/0901d1968065e9e7-The-SKF-model-for-calculating-the-frictional-moment_tcm_12-299767.pdf.

[72] J. Slater. Improvements in Toothed Chains for Working Toothed or Chain Wheels [Patent], 10 1864.

[73] J. B. Spicer. Effects of the Nonlinear Elastic Behavior of Bicycle Chain on Transmission Efficiency. *Journal of Applied Mechanics, Transactions ASME*, 80(2), 2013.

[74] J. B. Spicer, C. J. K. Richardson, M. J. Ehrlich, and J. R. Bernstein. On the Efficiency of Bicycle Chain Drives. *Human Power*, 50:3–9, 2000.

[75] J. B. Spicer, C. J. K. Richardson, M. J. Ehrlich, J. R. Bernstein, M. Fukuda, and M. Terada. Effects of Frictional Loss on Bicycle Chain Drive Efficiency. *Journal of Mechanical Design, Transactions of the ASME*, 123(4):598–605, 2001.

[76] R. Stephenson, D. Glennie, J. N. Fawcett, and J. M. Hale. A Method of Measuring the Dynamic Loads in High-Speed Timing Chains. *Proc Instn Mech Engrs*, 214(Part D):217–226, 2000.

[77] I. Troedsson and L. Vedmar. A Method to Determine the Static Load Distribution in a Chain Drive. *Journal of Mechanical Design*, 121:402–408, 9 1999.

[78] I. Troedsson and L. Vedmar. A Method to Determine the Dynamic Load Distribution in a Chain Drive. *Proc Instn Mech Engrs*, 215(C):569–579, 2000.

[79] M. Tu. Validation and Modeling of Power Losses of NJ 406 Cylindrical Roller Bearings. Master's thesis, KTH Industrial Engineering and Management Machine Design, Stockholm, 9 2016.

[80] S. R. Turnbull. *The Dynamic Behaviour of Roller Chain Drives*. PhD thesis, University of Newcastle upon Tyne, 6 1974.

[81] UCI. Races Flanders 2021, 2021. URL `https://www.flanders2021.com/en/races`.

[82] WD-40 Company. *3-IN-ONE® Multi-Purpose Oil [Data sheet]*, 2020. URL `https://files.wd40.com/pdf/sds/3inone/3-in-one-multi-purpose-oil-w-telescoping-spout.pdf`.

[83] G. Wegener and J. Andrae. Measurement Uncertainty of Torque Measurements with Rotating Torque Transducers in Power Test Stands. *Measurement: Journal of the International Measurement Confederation*, 40(7-8):803–810, 2007.

[84] G. Wegener, W. Nold, J. Andrae, and K. Molitor. Measurement Uncertainty of Rotating Torque Transducers when Used in Partial Load Ranges. In *Metrology for a Sustainable Development*, Rio de Janeiro, 9 2006.

[85] D. G. Wilson. Transmission Efficiencies. *Human Power*, 48:20–22, 1999.

[86] D. G. Wilson and T. Schmidt. *Bicycling Science*. MIT Press, third edition, 2020.

[87] R. Wragge-Morley. Dynamic Rig Design and Development [Internal Report]. 12 2017.

[88] R. Wragge-Morley, J. Yon, R. Lock, B. Alexander, and S. Burgess. A Novel Pendulum Test for Measuring Roller Chain Efficiency. *Measurement Science and Technology*, 29(7), 5 2018.

[89] L. X. Xu, Y. H. Yang, Z. Y. Chang, and J. P. Liu. Modal Analysis on Transverse Vibration of Axially Moving Roller Chain Coupled with Lumped Mass. *J. Cent. South Univ. Technol*, 18, 2011.

[90] S. Yadav and H. Elgeti. Bearing testing methods and strategies [White Paper]. Technical report, Elgeti Engineering, 2019. URL `https://www.elgeti-engineering.com/about-us/articles/`.

[91] S. P. Zhang and T. O. Tak. Efficiency Estimation of Roller Chain Power Transmission System. *Applied Sciences (Switzerland)*, 10(21):1–13, 11 2020.

The webpages given for online references were valid at the time of submission of this thesis.

Appendix A

Re-arranging cycling power model to solve for velocity

Martin et al. 1998 [54] describe cycling input power, P_{in}, as the sum of sources of drag power loss divided by transmission efficiency, Equation A.1.

$$P_{in} = \frac{P_{AD} + P_{RR} + P_{PE} + P_{KE}}{\eta} \tag{A.1}$$

All terms are expanded in Equation A.2.

$$\begin{aligned} P_{in} = \Big[& \frac{1}{2}\rho \left(C_D A + F_W\right) V_\mu^2 V_G + V_G C_{RR} m_r g \\ & + V_G m_r g sin\left(\tan^{-1}\left(G_R\right)\right) + \frac{1}{2} m \frac{V_{Gf}^2 - V_{Gi}^2}{t_f - t_i} \Big] / \ \eta \end{aligned} \tag{A.2}$$

In the literature, input power is solved for known parameters and measured velocities: average bicycle velocity relative to the ground during cycling segment, V_G, velocity relative to air, V_μ, and initial and final velocity during cycling segment, V_{Gi} and V_{Gf}. To solve all velocities in sequential segments at known input power, the equation is rearranged to form a cubic in a single velocity.

For segment i, the ground velocity of the bicycle at the end of the segment, $V_{G,i}$ is to be calculated. The initial ground velocity is assumed to be known for the segment, either because it represents an acceleration from zero velocity (for the first segment) or that the initial velocity is the calculated final velocity for a previous segment. It is described by $V_{G,i-1}$. For calculation of drag forces other than changes in kinetic energy, the ground velocity is approximated to be constant during a segment, calculated as below:

$$V_{G(av),i} = \frac{V_{G,i-1} + V_{G,i}}{2} \tag{A.3}$$

The relative air velocity for each segment, $V_{\mu,i}$, is defined in terms of bicycle velocity as below.

$$V_{\mu,i} = V_{G,i} - V_{WG}\cos(\alpha_i) \tag{A.4}$$

Where V_{WG} is the air velocity relative to the ground, and α_i is the angle of wind direction relative to the forward velocity of the bicycle and rider. Note that when there is no air velocity relative to the ground (windless conditions), air velocity relative to the rider reduces to ground velocity of the rider.

Power due to aerodynamic drag is rewritten with new expressions of ground and air velocities:

$$P_{AD,i} = \frac{1}{2}\rho\left(C_D A + F_W\right)\left[V_{G,i} - V_{WG}\cos(\alpha)\right]^2 \frac{V_{G,i-1} + V_{G,i}}{2} \tag{A.5}$$

Two velocity-independent parameters are defined for clarity:

$$P_{AD}{}' = \frac{1}{2}\rho\left(C_D A + F_W\right) \tag{A.6}$$

$$V_W{}' = V_{WG}\cos(\alpha) \tag{A.7}$$

Combining the above equations, P_{AD} is expressed as a cubic of final ground velocity in segment i, where all other parameters are defined.

$$\begin{aligned} P_{AD} = {} & V_{G,i}^3\left[\frac{P'_{AD}}{8}\right] + V_{G,i}^2\left[P'_{AD}\left(\frac{3}{8}V_{G,i-1} - \frac{V'_W}{2}\right)\right] \\ & + V_{G,i}\left[P'_{AD}\left(\frac{3}{8}V_{G,i-1}^2 - V_{G,i-1}V'_W + \frac{1}{2}{V'_W}^2\right)\right] \\ & + P'_{AD}\left(\frac{1}{8}V_{G,i-1}^3 - \frac{1}{2}V_{G,i-1}^2 V'_W + \frac{1}{2}V_{G,i-1}{V'_W}^2\right) \end{aligned} \tag{A.8}$$

Similar rearrangements of rolling resistance drag and power losses in potential energy change are completed below. They are defined with new expression of ground velocity:

$$P_{RR} = \frac{V_{G,i} + V_{G,i-1}}{2} C_{RR} mg \tag{A.9}$$

$$P_{PE} = \frac{V_{G,i} + V_{G,i-1}}{2} mg\sin\left(\tan^{-1}\left(G_{R,i}\right)\right) \tag{A.10}$$

Velocity-independent variables are again defined for clarity:

$$P_{RR}{}' = C_{RR} mg \tag{A.11}$$

$$P_{PE}{}' = mg\sin\left(\tan^{-1}\left(G_{R,i}\right)\right) \tag{A.12}$$

Power in rolling resistance and potential energy is expressed as linear function of final segment velocity:

$$P_{RR} = V_{G,i}\left(\frac{P_{RR}{}'}{2}\right) + V_{G,i-1}\left(\frac{P_{RR}{}'}{2}\right) \tag{A.13}$$

$$P_{PE} = V_{G,i}\left(\frac{P_{PE}{}'}{2}\right) + V_{G,i-1}\left(\frac{P_{PE}{}'}{2}\right) \tag{A.14}$$

Power due to change in kinetic energy is described by start and end velocities, as well as the time over which this change in kinetic energy happens, Δt_i. Since it is to be solved for speed, Δt_i is rewritten in terms of average velocity, where d_i is the distance travelled during the segment.

$$\Delta t_i = \frac{d_i}{V_{G(av)}} = \frac{2d_i}{V_{G,i} + V_{G,i-1}} \tag{A.15}$$

P_{KE} may be written in terms of the velocities only:

$$\begin{aligned} P_{KE} &= \frac{1}{2}m\frac{\left(V_{G,i}^2 - V_{G,i-1}^2\right)\left(V_{G,i} + V_{G,i-1}\right)}{2d_i} \\ &= \frac{1}{2}m\frac{V_{G,i}^3 + V_{G,i}^2 V_{G,i-1} - V_{G,i-1}^2 V_{G,i} - V_{G,i-1}^3}{2d_i} \end{aligned} \tag{A.16}$$

By defining the non-velocity dependent parameters as $P_{KE}{}' = \frac{m}{4d}$, the power consumed in changes to kinetic energy is described as a cubic in terms of velocity at the end of a segment, $V_{G,i}$.

$$P_{KE} = V_{G,i}^3\left(P'_{KE}\right) + V_{G,i}^2\left(P'_{KE}V_{G,i-1}\right) + V_{G,i}\left(-P'_{KE}V_{G,i-1}^2\right) + \left(-P'_{KE}V_{G,i-1}^3\right) \tag{A.17}$$

By combining Equations A.8, A.13, A.14 and A.17 with Equation A.1, the power balance is written as a cubic expression with a single unknown velocity variable, final velocity $V_{G,i}$, to be solved by numerical methods for each segment with all other parameters defined.

$$a{V_{G,i}}^3 + b{V_{G,i}}^2 + cV_{G,i} + d = 0 \tag{A.18}$$

Where coefficients are described in Equations A.19 - A.22.

$$a = \frac{P_{AD}{}'}{8} + P_{KE}{}' \tag{A.19}$$

$$b = P_{AD}{}'\left(\frac{3}{8}V_{G,i-1} - \frac{V'_W}{2}\right) + P_{KE}{}'V_{G,i-1} \tag{A.20}$$

$$c = P_{AD}{}'\left(\frac{3}{8}V_{G,i-1}^2 - V_{G,i-1}V_W{}' + \frac{1}{2}{V_W}'^2\right) + \frac{P_{RR}{}'}{2} + \frac{P_{PE}{}'}{2} - P_{KE}{}'V_{G,i-1}^2 \tag{A.21}$$

$$\begin{aligned} d =& P_{AD}{}'\left(\frac{1}{8}V_{G,i-1}^3 - \frac{1}{2}V_{G,i-1}^2 V_W{}' + \frac{1}{2}V_{G,i-1}{V_W}'^2\right) \\ &+ \frac{V_{G,i-1}P_{RR}{}'}{2} + \frac{V_{G,i-1}P_{PE}{}'}{2} - P_{KE}{}'V_{G,i-1}^3 - \eta P_{in} \end{aligned} \tag{A.22}$$

THIS PAGE IS INTENTIONALLY LEFT BLANK.

Appendix B

Publication 1

A study was conducted by the author and written up as an abstract to present at the Science and Cycling conference in Nice, France in June 2020. The analysis in the paper was developed further and is the basis for modelling work in Chapter 9. Due to cancellation of the event, only the abstract exists and was included in a special issue of the Journal of Cycling and Science. It is reproduced on the following page.

THIS PAGE IS INTENTIONALLY LEFT BLANK.

Journal of Science & Cycling
Breakthroughs in Cycling & Triathlon Sciences

OPEN ACCESS

Abstract

Sprocket Size Optimization for Derailleur Racing Bicycles

G. C. Barnaby, J. Yon, and S. C. Burgess

Department of Mechanical Engineering, Queen's Building, University Walk, University of Bristol, Bristol BS8 ITR, UK.

* Correspondence: George C. Barnaby. gb14385@bristol.ac.uk

Received: 30 May 2020; Accepted: 30 June 2020; Published: 30 December 2020

1. Abstract

The traditional design goal for sprocket size on racing bicycles is for it to be minimized for a given gear ratio. However, optimum sprocket size is actually a trade-off: larger sprockets have the advantage of producing lower transmission losses whilst small sprockets have the advantages of lower mass, inertia and frontal area. This study analyses this trade-off to determine if there are advantages in increasing sprocket sizes for a given gear ratio.

Two methods of enlarging gears in a derailleur racing bicycle, while maintaining gear ratio for the rider, are addressed: (i) to increase the size of pulley wheels and (ii) to increase the size of all gears. Efficiency improvements from these two cases arise from different mechanisms and come at different detriment to mass and frontal area. Models for chain articulation efficiency and overall power required for constant velocity cycling are presented and used to show the effect of increased sprocket size on overall performance.

In the scenarios presented, increased pulley wheels can reduce overall losses by up to 0.7W, representing 0.3% overall power reduction compared with a benchmark case. This is modest compared with a benefit of up to 3.3W, representing 0.6% overall power reduction, when all sprockets are increased. This difference is particularly pronounced for heavier, more powerful riders when riding minimal gradient courses at maximum effort. For some riders and racing scenarios, increased gear size can result in an increase in the power required of up to 0.4W, representing 0.1% increase in power required.

For elite cyclists and triathletes searching for marginal reductions in power losses, using larger sprocket sizes sometimes has clear benefits but it depends on rider physiology and race profile. Choosing larger gears also has the advantage of increased smoothness of pedal action by reducing polygonal action in the top span of the chain. Further, reduced wear will lead to better longevity in components and longer optimal performance of the transmission.

THIS PAGE IS INTENTIONALLY LEFT BLANK.

Appendix C

Publication 2

A second study conducted by the author and presented at the Science and Cycling conference in Leuven, Belguim in September 2021 was later published in a special issue of the Journal of Cycling and Science. The paper aligns with work completed in Chapter 9 and is reproduced in the following pages.

THIS PAGE IS INTENTIONALLY LEFT BLANK.

Journal of Science & Cycling
Breakthroughs in Cycling & Triathlon Sciences

OPEN ACCESS

Article

Mapping whole-event drive losses: the impact of race profile and rider input on transmission efficiency in cycling

George C Barnaby*, Stuart Burgess and Jason Yon

Department of Mechanical Engineering, Queen's Building, University of Bristol. BS8 1TR. UK

* Correspondence: (GB) george.barnaby@bristol.ac.uk

Received: 17 May 2021; Accepted: 26 June 2021; Published: 30 November 2021

Abstract: Several studies have considered the factors influencing transmission efficiency in a bicycle. These conclude that the effective radius of sprockets engaged with the chain and the torque and cadence of the cyclist influence the frictional losses associated with transmission between rider and rear wheel. These parameters may vary significantly during a bicycle race since a rider modifies their gear, power, and cadence to maximise physiological efficiency for optimum bicycle velocity. Furthermore, gearing selection and power input varies between riders, riding group and course profile. However, power models used to estimate race outcomes tend to simplify efficiency to a single, arbitrary factor, describing losses which scale linearly with input power regardless of expected regime. This study extends existing analytical descriptions of transmission losses to the context of a road bicycle with front and rear derailleurs. The calculated efficiency is considered within a cycling model to judge different regimes under which the chain will typically operate and maps overall performance during an event. Efficiency may vary significantly under certain loading regimes shown. In the context of highly trained cyclists these differences result in small changes which are symmetrical about a mean value. This study shows there is limited error in assuming constant efficiency for certain race types, though the efficiency value itself is dependent on several factors affecting the average loading regime. Elevation profile of the racecourse and average power input from the rider are key parameters affecting average efficiency. More massive riders racing at high average power input will experience higher efficiency, while efficiency is higher across all riders racing courses with increased elevation gain.

Keywords: transmission; efficiency; model; losses; bicycle; derailleur.

1. Introduction

In cycling, the use of analytical models to describe the balance of input power at the crank and output power at the tyre-road interface allows the engineer to identify areas for improvement in rider technique or equipment design. One such example is described in equation (1), based on an analytical model from Martin et al, 1998.

$$P_{in} = V(F_a + F_r + F_g)/\eta, \qquad \text{Eq. (1)}$$

where P_{in} is the input power of the rider; F_a, F_r and F_g are the resistive forces associated with aerodynamic drag, rolling resistance between tyre and road, and gravitational resistance; V is the bicycle velocity; and η is the transmission efficiency.

In deriving this model, and commonly in literature, transmission efficiency is assumed to be a constant value such that losses scale linearly with power input, and often an arbitrary estimate. Later studies, however, demonstrate that the same chain in a derailleur transmission system has measured efficiency in the range 80.9 – 98.6% (Spicer et al., 2001). The changing factors causing this range in efficiency are

input power, rotational speed, and gear configuration, which may also vary greatly during a bicycle race: gear shifts and non-consistent physiological output from the rider are common consequences of varying road-race profiles.

There is a gap in published literature for a holistic consideration of the efficiency to study these dependencies in the context of different racecourses and riders, which may be useful in determining the error in assuming constant efficiency and providing recommendations for what efficiency estimate to use for riders and engineers based on course and rider profile.

This study seeks to investigate the variability of transmission efficiency in expected regimes and defines the key factors influencing the transmission efficiency in usable terms, such that riders and engineers might be better informed in their use of an estimated efficiency in future modelling.

2. Frictional loss model

The authors are unaware of a comprehensive model of frictional losses in a bicycle derailleur drive in literature, and so have derived an analytical approach. This is an extension of the work of Lodge & Burgess, 2001, as is used in Barnaby et al., 2020.

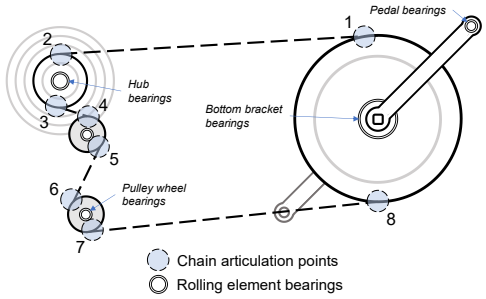

Figure 1. Sources of friction in a bicycle transmission, including rolling element bearings and points of chain articulation (numbered).

To determine the relative contribution of different sources of friction, analysis from Lodge & Burgess is used in conjunction with the geometry and spring rate of the rear derailleur to predict low-tension span tension. An industrial model of bearing losses is used to estimate friction in bearings (SKF, n.d.).

The relative losses of each of the sources of friction, shown in Figure 1, is summarised in Table 1. There is significant contribution to losses of the high-tension span articulations (71%), a smaller contribution from low-tension span articulations (26%), and a near-negligible contribution from rolling element bearings (3%). Friction in rolling element bearings is henceforth neglected in this analysis.

Table 1. Power losses are approximated for different sources of friction in the drive (300W / 90rpm)

	Power loss [W]	% of total
High-tension span [1]	5.5	71
Low-tension span [2]	2.0	26
Rolling element bearings	0.2	3
Total	7.7	100

[1] Chain articulations 1-2; [2] chain articulations 3-8.

Transmission efficiency is defined as in equation (2):

$$\eta = \left(P_{in} - N_s \omega_s \sum_{i=1}^{8} W_i\right)/P_{in}, \quad \text{Eq. (2)}$$

where W is the work done against friction in each of 8 articulating links (entry and exit to each sprocket), ω_s is the rotational frequency of the chainring (s^{-1}) and N_s is number of teeth in the chainring. Work done against friction is a function of chain geometry, articulation angle and chain tension, all of which may be calculated based on specific equipment and rider input. A further dependency is on coefficient of sliding friction within the chain links, which can be accurately determined experimentally using techniques such as those proposed by Wragge-Morley et al., 2017. The calculation for work done against friction is included in Appendix I.

2.1 Transmission efficiency variation

The variation of transmission efficiency is examined over a range of cycling torque inputs and riding gears, shown in Figure 2. The low, hill climbing gears offer higher efficiency due to the reduced articulation angle. Positive correlation between input

torque at the crank and efficiency is due to the relative reduction of significance of the low-tension span losses, which are independent of torque input. At low torque the torque-independent losses in the low-tension span, tensioned by the derailleur arm, are relatively more significant and so transmission efficiency changes rapidly as a function of torque.

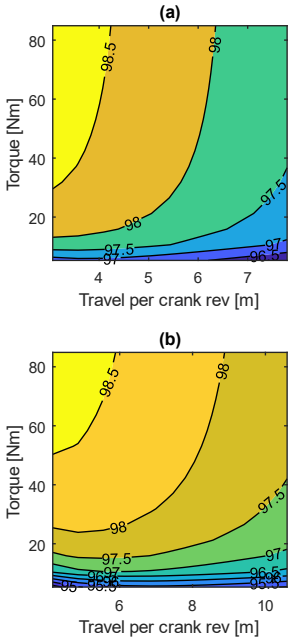

Figure 2. Power efficiency [%] contour map for varying rider torque and gear for 11-28 tooth cassette sprockets engaged with (**a**) 39-tooth chainring; and (**b**) 53-tooth chainring.

3. Variable efficiency within power model

To model how transmission efficiency varies in a race, simulation of typical power input and race profile is necessary since efficiency depends on power and gear selection, themselves having multivariant dependencies. The power required to overcome resistance at steady speed cycling is given in equations (3) – (6), based on work by Martin et al., 1998.

$$P_{in} = (P_a + P_r + P_g)/\eta, \qquad \text{Eq. (3)}$$

where power to overcome aerodynamic drag, P_a, is described in equation (4), power to overcome rolling resistance of the tyres, P_r, is described in equation (5) and power to overcome gradient, P_g is described in equation (6).

$$P_a = 0.5\rho C_d A_f V^3, \qquad \text{Eq. (4)}$$

where ρ is air density, C_d is coefficient of aerodynamic drag, A_f is the frontal area of bicycle and rider, and V is bicycle velocity. Note that wind velocity is assumed to be zero in this analysis.

$$P_r = mgC_{rr}V, \qquad \text{Eq. (5)}$$

where m is total mass of rider and bicycle, g is the gravitational acceleration constant and C_{rr} is the coefficient of rolling friction between tyre and road surface. Upright, straight-line cycling is considered for this analysis.

$$P_g = mg\,sin(\theta)\,V, \qquad \text{Eq. (6)}$$

where θ is the angle of gradient. Typical values for variables shown in equations (4) – (6) are from Wilson, Papadopoulos, and Whitt, 2004.

Steady-state velocity is calculated at many discrete points along a simulated racecourse for a typical bicycle drivetrain. Gearing is selected to maintain cadence within a typical range, with chosen gearing influencing the calculation for efficiency according to the described frictional loss model. Further, a variable power input is applied such that power increases with positive gradient and decreases with negative gradient, shown to be an effective pacing strategy (Wells & Marwood, 2016).

3.1 Efficiency variation by rider type

Transmission efficiency is simulated for an example elite race: part of the UCI 2021 World Road Championships road-race from Antwerp to Leuven (UCI, 2021). Efficiency is illustrated for four different riders in Figure 3, where rider input parameters are summarised in Table 2. The spread of efficiency estimates during simulated race for each case may be seen in Figure 4.

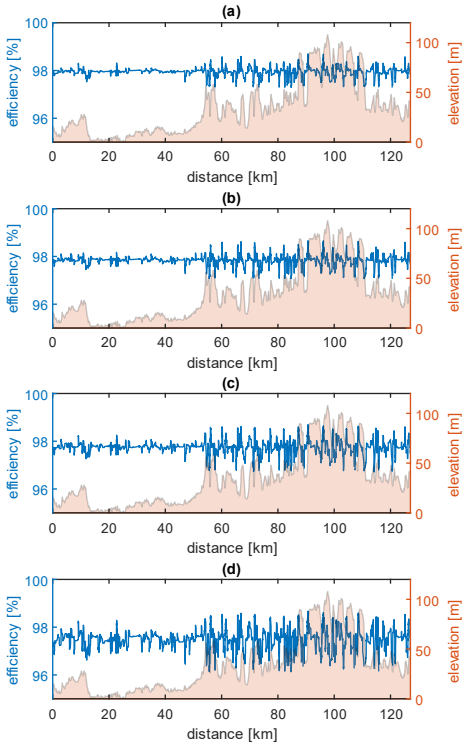

Figure 3. Transmission efficiency overlayed on Leuven 2021 road-race course profile for a (**a**) elite male cyclist, (**b**) elite female cyclist, (**c**) untrained male cyclist, and (**d**) untrained female cyclist.

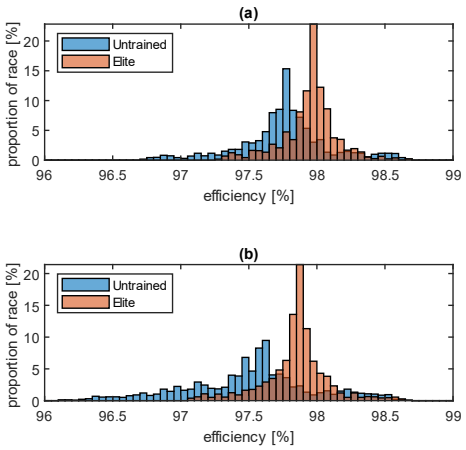

Figure 4. Histogram of simulated transmission efficiency during example race for elite and untrained riders.

Efficiency can be seen to fluctuate with the gradient of the course due to the changing gear and power. Hill climbing gears and a marginal increase in power both result in increased efficiency as has been shown previously. The opposite is true for negative gradients, where smaller sprocket is engaged and power is slightly reduced, decreasing efficiency.

Table 2. Input parameters for four modelled cases, with estimates for elite and untrained male and female riders.

	Elite		Untrained	
	Male	Female	Male	Female
Mass [kg]	70	60	80	65
C_dA [m^2]	0.3	0.25	0.4	0.3
Average power [W]	350	250	150	100
Cadence [rpm]	90±10	90±10	70±15	70±15
Average efficiency (S.D.) [%]	98.0 (0.20)	97.9 (0.24)	97.8 (0.33)	97.6 (0.46)

Comparing the proficient and untrained cases, a larger variance can be seen in the untrained cyclist as well as a slightly lower average efficiency. This is illustrated more clearly in Figure 4. The lower average efficiency is largely due to the reduced power input, and hence lower average torque. The variance is reduced in the trained cyclist due to the responsive gear changes working to maintain a high cadence.

3.2 Efficiency variation in elite riders

In elite level racing, efficiency variance during a race is low and there is little error in determining average velocity, or time to completion, by using a single value efficiency across an entire race. This is determined in simulated races by finding the ratio of total energy input and total energy output, found by integrating the power output and input with respect to time as in equation (7).

$$\eta = \frac{\int P_{in} - P_{lost}\, dt}{\int P_{in}\, dt}, \qquad \text{Eq. (7)}$$

However, there is still dependency of this average efficiency on power input and gearing, which itself is dictated by the elevation profile of a racecourse.

An effective average efficiency is determined by interpolating between results from simulations with varying parameters. Transmission efficiency during 20 different grand tour events is modelled with riders of varying input power (50-550W) and mass (50-80kg). Dependency of average efficiency on the climbing during the race (measured by average metres elevation gain per kilometre travel), and the average power achieved by the rider during the race is illustrated in Figure 5. Mass is less impactful and can be accounted for by applying an additional 0.1% efficiency per 20kg above 65kg. These results are valid for riders with a power-to-weight ratio of between 2 and 6 W/kg.

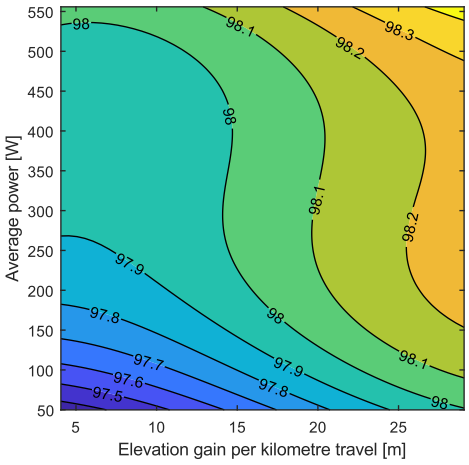

Figure 5. Contour map of example transmission power efficiency [%] as function of average power during a race and its elevation profile.

4. Discussion

The range in efficiency found in previous research is not realised in loading regimes typical in elite racing. This is largely because of the narrow cadence range and high torque in elite racing which results in a low variance, symmetrically distributed spread of transmission efficiencies about a mean value. Provided conditions and input parameters are maintained during a race, there is little error in using a single factor for efficiency.

However, average power and elevation profile are two factors which can vary greatly in elite cycling between different event styles and rider physiologies, leading to consistent changes to efficiency across a race. A mountainous tour stage will see higher efficiency than one which is flat by up to 0.5%-pts, which may be even more extreme if considering specific hill climbing events. Rider power input also will influence average efficiency, meaning that more powerful male riders racing TT courses at maximal effort may experience an average transmission efficiency up to 0.8%-pts higher than a less powerful rider during an endurance event. Female elite riders will inherently experience a reduced transmission efficiency than male elite riders due to applying less power at the crank.

5. Practical Applications

Transmission efficiency may usually be experimentally examined in limited and specific loading regimes. This gives limited insight given the dependencies of efficiency which vary during a bicycle race. This study demonstrates that further applying the results of such tests to contextualise efficiency within the expected loading regimes based on rider and course type may offer additional accuracy in determining an effective average efficiency. This may be applied to future analytical modelling for evaluating equipment upgrades or determining pacing strategies.

Future research to further examine influences on transmission efficiency is needed to confirm the theory presented here, including extensive practical testing which may offer experimental validation.

Funding: This research was funded through an Engineering and Physical Sciences Research Council (EPSRC) NPIF Studentship, with additional support from Renold Plc, and the British Cycling Federation.

Conflicts of Interest: The authors declare no conflict of interest. The funders had no role in the design of the study; in the collection, analyses, or interpretation of data; in the writing of the manuscript, or in the decision to publish the results.

References

1. Barnaby, G. C., Yon, J., & Burgess, S. (2020). Sprocket Size Optimisation for Derailleur Racing Bicycles. *Journal of Science and Cycling*, *9*(2), 36.
2. Lodge, C. J., & Burgess, S. C. (2001). A model of the tension and transmission efficiency of a bush roller chain. *Proceedings of the Institution of Mechanical Engineers, Part C: Journal of Mechanical Engineering Science*, *216*(4), 385-394.
3. Martin, J. C., Milliken, D. L., Cobb, J. E., McFadden, K. L., & Coggan, A. R. (1998). Validation of a mathematical model for road cycling power. *Journal of applied biomechanics*, *14*(3), 276-291.
4. SKF model for calculating the frictional moment (n.d.). Retrieved from https://www.skf.com/binaries/pub12/Images/0901d1968065e9e7-The-SKF-model-for-calculating-the-frictional-moment_tcm_12-299767.pdf
5. Spicer, J. B., Richardson, C. J., Ehrlich, M. J., Bernstein, J. R., Fukuda, M., & Terada, M. (2001). Effects of frictional loss on bicycle chain drive efficiency. *J. Mech. Des.*, *123*(4), 598-605.
6. UCI 2021 Road World Championships Flanders Belgium (2021). Retrieved from https://www.flanders2021.com/en/races
7. Wells, M. S., & Marwood, S. (2016). Effects of power variation on cycle performance during simulated hilly time-trials. *European journal of sport science*, *16*(8), 912-918.
8. Wilson, D. G., Papadopoulos, J., & Whitt, F. R. (2004). *Bicycling science (3rd ed.)*. MIT press.
9. Wragge-Morley, R., Yon, J., Lock, R., Alexander, B., & Burgess, S. (2018). A novel pendulum test for measuring roller chain efficiency. *Measurement Science and Technology*, *29*(7), 075008.

Appendix I

Work done against friction in articulating chain links as derived by Lodge & Burgess, 2001, is summarised here. Eight articulations are considered, at entry to and exit from each engaged sprocket. The work done in articulating these links simultaneously represents the energy lost for the drive advancing by one link, which may be multiplied by the chain speed in link pitch per second to determine the power lost here.

Work done in articulating chain links

The articulation of inner and outer links results in relative sliding of different surfaces between the pin and bushing. Since they must alternate, an average is taken of the two to define work done for one articulation:

$$W = (W_{pin} + W_{bush})/2$$

where work done during pin articulation is described as below:

$$W_{pin} = \frac{F_i}{\sqrt{1+\mu^2}} \mu r_{bi} \alpha_i$$

and work done during bush articulation is:

$$W_{bush} = \frac{\mu F_c r_{bi} [\cos\theta_{RA} - \cos(\theta_{RA} + \alpha_m)]}{\sqrt{1+\mu^2}\sin(\theta_{RA} + \alpha_m)} + \frac{\mu F_c r_{bo}(1 - \cos\alpha_m)}{\sin(\theta_{RA} + \alpha_m)}$$

Lodge & Burgess, 2001 should be consulted for definitions of these terms. These are determined by the geometry of the chain components and sprocket, except for coefficient of friction, μ, which is determined using accurate measurements as described in Wragge-Morley et al., 2017.

Chain tension force

The contact force between each of 8 articulating links is calculated. The high-tension span contact force is from crank torque acting at chainring radius and acts at articulations onto the chainring and off the engaged cassette sprocket. Low-tension span contact force is assumed to be equal for all 6 remaining articulations and resolved from the estimated spring rate of the rear derailleur tension arm and its geometry.